

BARBOUR, A. 1998. *The analysis of airgap eccentricity in three-phase induction motors using finite elements for a reliable condition monitoring strategy*. Robert Gordon University, PhD thesis. Hosted on OpenAIR [online]. Available from: <https://doi.org/10.48526/rgu-wt-2807289>

# The analysis of airgap eccentricity in three-phase induction motors using finite elements for a reliable condition monitoring strategy.

BARBOUR, A.

1998

*The author of this thesis retains the right to be identified as such on any occasion in which content from this thesis is referenced or re-used. The licence under which this thesis is distributed applies to the text and any original images only – re-use of any third-party content must still be cleared with the original copyright holder.*

# **The Analysis of Airgap Eccentricity in Three-Phase Induction Motors using Finite Elements for a Reliable Condition Monitoring Strategy**

**Alexandra Barbour**

A thesis submitted in partial fulfilment of the requirements of The Robert  
Gordon University  
for the degree of the Doctor of Philosophy

This research programme was carried out in collaboration with GEC  
Alstom Engineering Research Centre

October 1998

THE ROBERT GORDON UNIVERSITY



0004469304 ABERDEEN

## Declaration

I hereby declare that the work presented in this thesis is my own and that all sources of reference and assistance have been duly acknowledged. During the duration of the research programme the following conferences were attended and industrial visits were made:

1. Seventh International Conference on Electrical Machines and Drives, 4-6th September, 1995, University of Durham.
2. The Robert Gordon University, Faculty of Science and Technology, Research Conference '96, Engineering Monitoring and Maintenance, March 1996. Paper submitted and presented.
3. Visit to GEC Alstom Engineering Research Centre (Collaborating Company) to meet Dr. T. Preston and Dr. J. Sturgess. A presentation was given on the research to date and discussions were held.
4. IEE Colloquium on Modelling Electrical Machines, April 1997, Savoy Place, London.
5. Visit to Peebles Electric, Edinburgh, regarding design details for the large industrial induction motors, met with Mr. J. Middlemiss Chief of Electrical Machine Design, July, 1997.
6. Eighth International Conference on Electrical Machines and Drives, 1-3th September, 1997, Robinson College, Cambridge to present a paper entitled "Finite Element Analysis and On-Line Current Monitoring to Diagnose Airgap Eccentricity in 3-Phase Induction Motors".

7. On-site visit to BP Dalmeny Oil Tank Farm, South Queensferry. Performed on-site tests on two 1.45MW induction motors.

In addition, in-house courses for researchers were attended and presentations were given to industrialists visiting the Department. The papers published during this research programme can be found in Appendix 6.

Signed

Date

29/10/98

# Abstract

This thesis presents the results of a finite element investigation into airgap eccentricity in three phase induction motors. Airgap eccentricity is an inherent condition in induction motors which if left undetected can result in motor failure. It is therefore of interest to detect and quantify the level of airgap eccentricity.

A literature review is presented which covers the research to date on the detection and quantification of airgap eccentricity using classical and finite element techniques. The classical approach using the mmf and permeance wave approach calculated specific frequency components in the line current spectra which are a function of airgap eccentricity. An attempt was also made using classical techniques to predict the magnitude of these components as a function of the airgap eccentricity severity. Agreements between predicted and measured magnitudes were inconsistent. A critical appraisal of this research is presented to highlight the limitations which resulted in the poor results and the findings that are applicable to the research programme presented in this thesis.

The application of finite element analysis overcomes many of the limitations of the classical mmf and permeance wave approach. The finite element modelling of a motor to investigate these components in the current and predict their magnitude as a function of the airgap eccentricity level is a new contribution to knowledge that this thesis puts forward. The finite element analysis was applied to an 11kW test-rig motor and the expected frequency components were present and increased in magnitude with increasing airgap eccentricity. The comparisons of calculated current magnitudes and those obtained from the test-rig motor for given levels of airgap eccentricity were consistently good. This was an improvement on the classical approach.

The effects of different rotor slot designs and the numbers of rotor bars were also successfully modelled using the finite element analysis. This provided useful information

in terms of monitoring different motors in industry as these parameters have a significant effect on the increases observed in the current magnitudes for the same increase in airgap eccentricity.

To verify the technique in the industrial sense a large 1.45MW industrially based induction motor was modelled. The prediction of the current component magnitudes as a function of the airgap eccentricity level had not been previously attempted by classical or finite element techniques. On-site tests were carried out on two identical motors. The current component magnitudes in the frequency spectra indicated that one motor had a higher level of airgap eccentricity than the other. This concurred with the heavy usage of this motor and the thoughts of on-site personnel which reinforced the application of on-line current monitoring in the industrial situation. The finite element analysis of the motor provided good results with the 50Hz component of the correct magnitude and the airgap eccentricity components being present in the spectra. Although the exact level of airgap eccentricity in the motors was unknown by modelling the motor with several different levels of airgap eccentricity it was found that the current components were in the same region of magnitude as those from the on-site tests.

Conclusions and suggestions for further work are also presented. In summary this thesis contains details of the successful application of finite element analysis to quantify the level of airgap eccentricity in a small test-rig and large industrially based motor.

## **Acknowledgements**

I wish to express my sincere gratitude to my Supervisor, Professor W. T. Thomson for his continued advice and encouragement throughout this project.

I also wish to thank GEC Alstom Engineering Research Centre for providing the finite element package FEMTA and to the engineers there, in particular to Dr. J. Sturgess and Dr. T. Preston for their technical support.

Peebles Electric for providing the design details for the large industrial motor and in particular Mr. J. Middlemiss for his technical support. Mr. J. Wiley and Mr. T. Evans of BP Oil Dalmeny for their co-operation to arrange a site visit and their assistance on the day.

The technical staff within the School of Electrical and Electronic Engineering, in particular Mr. M. Johnstone for setting up the test-rig motor with different airgap eccentricity levels. There are also many others who have lent their assistance over the three years to whom I am also very grateful.

## List of Principal Symbols

### Calculation of the frequency components and associated pole-pairs:

$f_{cc}$  = frequency components which are a function of airgap eccentricity (Hz)

$f_1$  = supply frequency (Hz)

$n_d$  = zero for static and one for dynamic eccentricity

$n_{sa}$  = saturation integer

$n_{ws}$  = time harmonic of the stator mmf

$n_s$  = static eccentricity integer

$n_d$  = dynamic eccentricity integer

$n_{os}$  = stator space harmonic integer

$p$  = pole-pairs

$s$  = slip

$R$  = number of rotor slots

$S$  = number of stator slots

### Induction Motor Parameters:

$R_1$  = stator resistance

$jX_1$  = stator reactance

$R_c$  = core loss resistance

$jX_m$  = magnetising reactance

$R'_2$  = rotor resistance referred to the stator

$jX'_2$  = rotor reactance referred to the stator

### FFT Parameters:

$\Delta f$  = frequency resolution

$f_s$  = sampling frequency of data

$N$  = number of points in FFT

$T$  = total record time of data

$w(n)$  = window coefficients

**All Other Symbols:**

$B$  = flux density

$c$  = integer

$d$  = number of slots/pole/phase

$D$  = stator core bore or denoting a diameter

$e(t)$  = time domain emf waveform (from finite element analysis)

$E_n$  = induced voltage at frequency  $n$

$f_r$  = rotor speed frequency

$F$  = magnetic force

$I_n$  = current flowing at frequency  $n$

$k_p$  = coil pitch factor

$k_d$  = distribution factor

$k_w$  = winding factor

$k_{wn}$  = winding factor for harmonic  $n$

$k_{dn}$  = distribution factor for harmonic  $n$

$k_{pn}$  = coil pitch factor for harmonic  $n$

$l$  = axial length of stator core

$m$  = pole-pair number

$n$  = frequency value

$r_{be} = r'_{be}$  = effective rotor bar resistance

$r_e$  = end-ring resistance

$T_{ph}$  = turns / phase

$V_s$  = supply voltage

$Z_n$  = impedance at frequency  $n$

$X_e$  = Stator end-winding leakage reactance

$X_{sewl}$  = stator end-winding leakage reactance

$\alpha$  = angle

$\lambda_{es}$  = permeance coefficient

$\tau_p$  = pole pitch

$\phi$  = winding pitch

$\sum \lambda$  = sum of permeance coefficients

$\Lambda$  = permeance

$\mu_0$  = permeability of free space

# Contents

<b>Chapter 1</b>	<b>Introduction</b>	<b>Page</b>
1.1	Induction Motors in Modern Industry	1
1.2	Condition Monitoring of Electrical Machines	2
1.3	Airgap Eccentricity and other Induction Motor Problems	
	1.3.1 Review of Induction Motor Problems	4
	1.3.2 Airgap Eccentricity	6
1.4	Research Objectives	7
<b>Chapter 2</b>	<b>Review of Research on Airgap Eccentricity</b>	
2.1	Introduction	11
2.2	Quantification of the UMP	12
2.3	Airgap Eccentricity Diagnosis using Vibration and Flux Signals	13
2.4	On-Line Current Monitoring to Diagnose Airgap Eccentricity	16
2.5	Critical Appraisal of Classical Approach to Diagnose Airgap Eccentricity	
	2.5.1 Introduction	26
	2.5.2 Critical Appraisal of Experimental Observations of Cameron and Thomson	26
	2.5.3 Critical Appraisal of Analysis Technique to Predict Airgap Eccentricity Level by Cameron and Thomson	40
2.6	Finite Element Analysis of Airgap Eccentricity	49
2.7	Conclusion	52
<b>Chapter 3</b>	<b>Finite Element Analysis of the Test-Rig Motor</b>	
3.1	Introduction	55
3.2	Generation of FE Model of Test Rig Motor	59
3.3	Determination of Test-Rig Motor Parameters	
	3.3.1 Test-Rig Motor Specification	61
	3.3.2 Locked Rotor and Open Circuit Tests	63

3.3.3	Performance Tests for Equivalent Circuit Validation	64
3.3.4	Rotor Bar Conductivity Calculation	67
3.3.5	Stator End-Winding Leakage Reactance	68
3.4	Initial Finite Element Result using the Fixed Mesh Model	75
3.5	Initial Time Stepping Analysis of the Test-Rig Motor	
3.5.1	Procedure	77
3.5.2	Initial Time Stepping Analysis, Problems and Conclusion	80

## **Chapter 4 Signal Processing Software Development**

4.1	Introduction and Specification of Spectrum Plot	85
4.2	Investigation of Matlab FFT Function	87
4.3	Correction of Component Magnitudes in the Spectrum	
4.3.1	Investigation of Magnitude Distortion by Matlab FFT	89
4.3.2	Development of Program to Calculate Factor for Component Magnitude Correction	90
4.4	Display of Spectrum on a dB Scale	92
4.5	Application of Windows to Reduce Skirting	94
4.6	Final Tests	97
4.7	Experiment with Increasing the Number of Samples Processed	100
4.8	Conclusion	103

## **Chapter 5 Analysis and Experimental Results for 51 Bar Unskewed Rotor**

5.1	Introduction	105
5.2	Pole Pair Analysis	110
5.3	Static Eccentricity Variations	
5.3.1	Experimental Results	115
5.3.2	Finite Element Analysis Results, Comparison and Discussion	120
5.4	Static and Dynamic Eccentricity Variations Experimental Results	
5.4.1	Experimental Results	131
5.4.2	Finite Element Analysis Results, Comparison and Discussion	136
5.5	Purely Finite Element Results	

5.5.1	Purely Dynamic Eccentricity	143
5.5.2	A Concentric Motor	147
5.5.3	70% Static Eccentricity	148
5.6	Conclusion	152

## **Chapter 6 Finite Element Analysis of the Effects of Rotor Design on the Airgap Eccentricity Frequency Components**

6.1	Introduction	154
6.2	Number of Rotor Bars Investigation	
6.2.1	Introduction	155
6.2.2	50 Bar Rotor	157
6.2.3	43 Bar Rotor	159
6.2.4	44 Bar Rotor	163
6.2.5	Conclusions on the Results for the Number of Rotor Bars	170
6.3	Rotor Slot Design Investigation	
6.3.1	Introduction	171
6.3.2	Rotor Slot Variations at 0%, 5%, 10% and 25% Static Eccentricity	173
6.3.3	Rotor Slot Variations for Combinations of Static and Dynamic Eccentricity	179
6.3.4	Conclusions on the Rotor Slot Design Results	181
6.4	Conclusion	183

## **Chapter 7 Finite Element Analysis of a Large Motor Operating in Industry**

7.1	Introduction	184
7.2	Design Details and Calculation of Finite Element Data	185
7.3	Pole-Pair Analysis	186
7.4	On-Site Test Results	
7.4.1	Introduction	190
7.4.2	Current Spectra for Motors A and B	191
7.4.3	Discussion and Conclusions on On-Site Results	194

7.5	Finite Element Analysis	
7.5.1	Introduction and Initial Result	195
7.5.2	Airgap Eccentricity Results for Finite Element Analysis at 742rpm	196
7.5.3	Airgap Eccentricity Results for Finite Element Analysis at 744rpm	202
7.5.4	Conclusion on Finite Element Analysis of Large Motor	208
7.6	Conclusion	208

## **Chapter 8 Conclusion**

8.1	Achievement of Objectives	210
8.2	Suggestions for Future Work	213

## **References**

## **Appendices**

# Chapter 1

## Introduction

### 1.1 Induction Motors in Modern Industry

The invention of the polyphase induction motor can be largely attributed to Nikolai Tesla (1856-1943), his first US patent in 1888 followed by several others resulted in the induction motor being commercially manufactured by 1896 [1]. The principles of the motor as laid out in his patents are still applied to motors today, over a century later. The induction motor is often called the ‘workhorse’ of industry. This title is fully justified as they are used to drive, for example, fans, compressors, conveyors and hoists. As a result they perform critical duties in areas such as manufacturing industries, oil and gas production, power stations, agriculture and transportation systems. Fixed speed applications such as fans and pumps have always been dominated by induction motors, however, recently, with the advent of reliable, variable frequency inverters they are now used for controlled speed applications [2]. In the UK it is estimated that there are 22 million 3-phase induction motors installed which consume approximately 43% of all the electrical energy generated [1]. In the US an estimated 50 million or more are in use in industry, totalling some 150 million horsepower. Normal yearly production adds 1 million motors to that figure. Another 20 million single-phase fractional horsepower motors are found in domestic appliances such as fans, refrigerators and washing

machines [3]. Clearly the induction motor is destined to play a significant role for many years in the future both socially and industrially.

## **1.2 Condition Monitoring of Electrical Machines**

Due to the critical duties that induction motors and other electrical machines (e.g. generators) perform, condition monitoring of electrical machines has been extensively adopted by machine operators. Condition monitoring involves monitoring a machine over time to gain a picture of its health and to identify the inception of any degradation processes or failure mechanisms. These systems monitor machine parameters such as vibration, temperature, current and voltage signals. The parameter monitored depends on the type of machine and the fault of interest. With the information from condition monitoring systems it is possible to avoid unexpected failures of machines and planned maintenance programmes can be developed. This all leads to reduced machine downtimes and financial savings. Plants are also safer, for example, the sudden failure of a machine in oil and gas production or a power station could have catastrophic consequences to personnel and equipment.

The development of different monitoring techniques, the application of such systems in industry and the general economic viability of condition monitoring strategies have become the focus of considerable research over recent years. This section reviews a selection of the many papers related to general condition monitoring of electrical machines and the assessment of the economic viability of condition monitoring strategies. It is interesting to note that the majority of these papers have been written by people in the front-line of machine operation; electricity generating companies, oil and gas production and machine manufacture, thus, highlighting the direct relevance of condition monitoring in the industrial situation.

Tavner et al [4], reviewed the techniques available for monitoring generators and large motors in an electricity generating company. Motor monitoring techniques discussed

were the sensing of magnetic flux, stator current, rotor current, partial discharges, vibration, speed fluctuations, temperature, chemical analysis of cooling air and bearing oil. Techniques reviewed for monitoring generators were partial discharges, shaft voltages, vibration, gas leakage and chemical techniques to detect insulation degradation. Some successes with monitoring motors and generators were presented. They also stress that a condition monitoring system cannot be relied on solely for an assessment of machine health and that there is still a need for a regular inspection of machines.

Power station plant is the focus of condition monitoring in [5]. HV rotating plant was monitored over time and early ‘fingerprint’ tests on machines were compared to results from regular tests to assess the condition of the plant. Many off-line and on-line techniques were employed amongst which ‘MotorMonitor’ [6] was successfully used to detect rotor bar faults by spectral analysis of the line current to the motor.

The author of [7] from a leading UK oil and gas exploration company describes how condition monitoring fits into the maintenance programme of an oil company. On motor/pump sets, vibration and current analysis was used together with some routine maintenance. Current monitoring for broken rotor bar detection gave a net benefit of 140% of the cost of monitoring. The saving was due to the reduced incidence of damage resulting from failure. This figure did not include additional benefits from increased production.

There are clear benefits to be derived from condition monitoring, as its adoption in industry illustrates, however, a condition monitoring system has to be economically viable, as highlighted in many of the papers on the subject. The benefits and savings which would arise from the installation of a system have to be compared with the initial cost and running. A critical appraisal of these factors was presented in [4] and was the principal subject of [8]. Various maintenance strategies were reviewed [8]; run-to-breakdown, time-based and condition-based. Condition monitoring techniques were

discussed together with the services available from several companies in the field. It concluded that condition monitoring can save money if failures can result in extensive damage, if machine downtime is expensive or if a machine is difficult to reach. It reported the opinion that before installing a system a maintenance audit must be carried out and for a system to be worthwhile it must pay for itself within two years.

Condition monitoring systems clearly play an important part in industry for the detection of many different problems before they become more serious and result in failures for operators. Induction motors, with their critical duties in industry, have been the focus of considerable research on methods for detecting failure mechanisms. The next section briefly reviews the problems of interest before focusing on airgap eccentricity in induction motors.

### **1.3 Airgap Eccentricity and other Induction Motor Problems**

#### **1.3.1 Review of Induction Motor Problems**

Induction motors are relatively reliable, largely due to the simplicity of their design and their rugged construction, however, they are subject to considerable stresses during their operational lifetime and as a result failures can occur. These stresses can be generally grouped into electrical, thermal, mechanical and environmental [9]. The rotor is also subject to dynamic forces due to its rotation and unbalanced magnetic forces due to airgap eccentricity. These stresses can lead to failures as a result of a motor being operated beyond the design specification, anomalies in the manufacturing materials and general wear and tear after years of operation, particularly in hostile environments. As a result a variety of failures do occur which are briefly reviewed in the following paragraphs.

The stator winding insulation of high voltage (HV) induction motors can breakdown as a result of progressive degradation over time [10]. The insulation can fail as a result of

surface contamination causing discharges and also movement of the windings due to electromagnetic forces. The breakdown of insulation in a HV motor can lead to a phase-phase or phase-earth fault and failure.

Broken rotor bars and end-rings can progressively degrade the condition of a motor [6]. The failure of one bar (open circuit) causes the adjacent bars to carry more current which in turn can lead to their failure. A Broken rotor bar/bars does not in itself cause a motor to fail but broken parts of the bars can travel at high velocity and cause stator winding insulation failure. Broken rotor bars are mainly attributed to a motor operating on a strenuous duty cycle or poor quality control during manufacture and not to rotor material faults.

Single-Phasing [11] occurs when one of the supply lines or windings becomes open circuited, this results in high current and vibration levels in the motor. The high current results in the windings overheating due to thermal stress and could result in insulation failure. The vibration levels also damage the insulation around the windings [12].

Bearing failure can be caused by contamination of the bearing lubricant and corrosion of the bearings themselves, incorrect installation and load problems [13]. Bearing failures account for a significant percentage of large industrial motor failures as reported in numerous surveys. Surveys carried out by [14, 15, 16, 17] revealed that as a percentage of the failures in the motors taking part in the survey bearing failures accounted for 41%, 44.7%, 58.9% and 65% respectively. The surveys reported in [15, 16] were specifically for large HV induction motors from 425kW to 6.3MW [15] and 100kW to over 1MW [16]. The surveys reported in [14, 17] dealt with large HV machines (induction, synchronous and DC) with sizes of over 150kW [14] and 300kw to 60MW [17]. The type of bearings in the machines (roller, ball or plain) were not specified. As the next section explains, airgap eccentricity problems can wear the bearings and lead to complete failure. Bearing problems, due to other factors, can in turn result in airgap eccentricity in the motor.

### 1.3.2 Airgap Eccentricity

Airgap eccentricity is an undesirable condition which is inherently present in induction motors where the airgap between the stator (stationary part) and the rotor (rotating part) is not uniform. The condition can take two forms; static airgap eccentricity and dynamic airgap eccentricity and in practice both types are normally present in a motor. Static eccentricity results in a minimum airgap which is fixed in both space and time, whereas, dynamic eccentricity results in the position of the minimum airgap rotating with the rotor. Figure 1.1 illustrates this variation in the airgap length for the two forms.

*Note: In the text when airgap eccentricity is mentioned both forms of the condition are considered. At all other times static or dynamic eccentricity will be specified dependant on the context.*

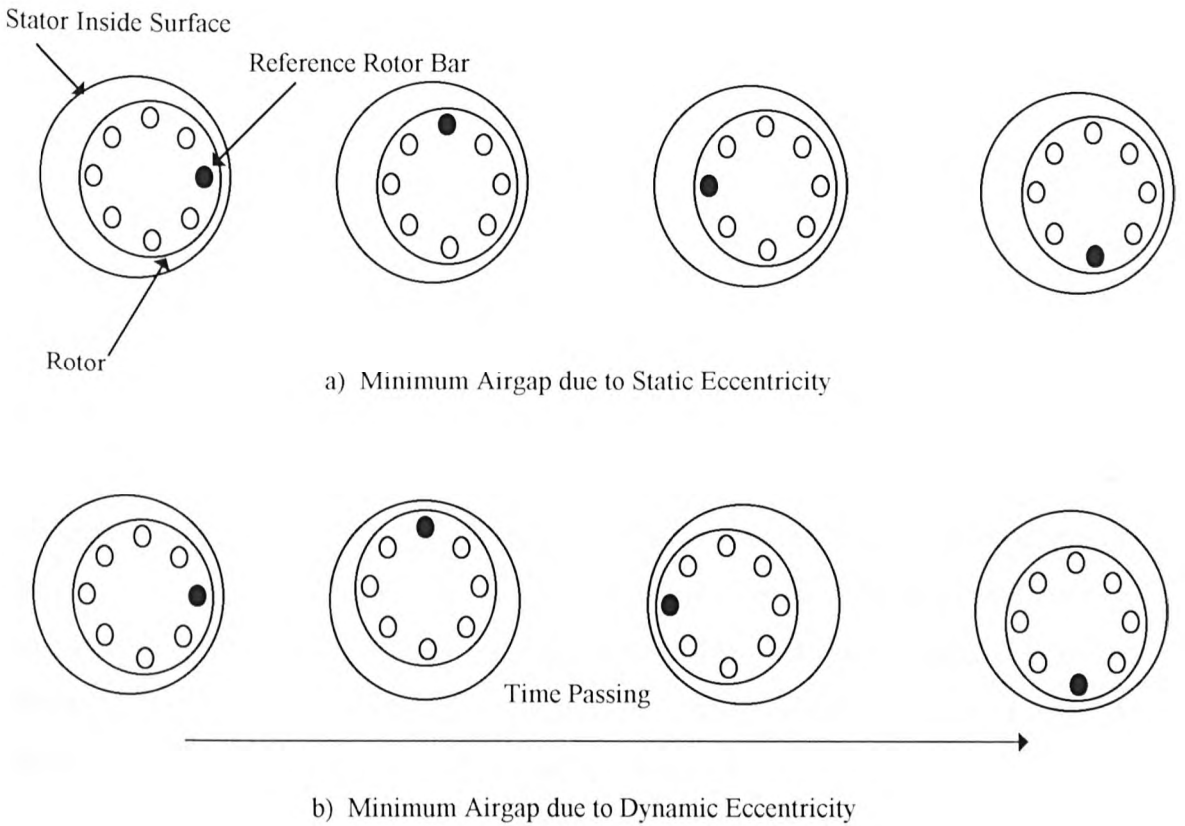


Figure 1.1. Variation in Airgap Length with a) Static and b) Dynamic Eccentricity.

Static eccentricity is caused by a build up of manufacturing tolerances between the stator and bearing centres or incorrect reassembly after repair. Dynamic eccentricity can be caused by worn bearings, thermal bow of the rotor or operation at critical speeds creating rotor whirl. Static eccentricity can also cause dynamic eccentricity due to the resulting unbalanced magnetic forces present in the motor. If high levels (over 20%) of airgap eccentricity remain undetected the severity of the problem may increase since it results in increased vibration and noise from the motor, further wear to the bearings and possibly bearing failure. In a worst case the rotor can actually be pulled onto the stator resulting in extensive damage to the stator windings and complete motor failure. It is this rotor to stator rub which is considered to be a serious failure.

Airgap eccentricity problems are uncommon in new motors due to good designs and manufacturing procedures, a typical level would be 5% airgap eccentricity for a large 1.5 MW motor [18]. However, the application of on-line current monitoring [19, 20] has shown that problems can occur after a motor has been in service for a number of years. Motor operators are therefore interested in being able to determine the level of airgap eccentricity in their motors.

## **1.4 Research Objectives**

Chapter 2 reviews the published literature on airgap eccentricity in induction motors and the reasoning for the project objectives to provide an original contribution to knowledge in this area. However, this section describes what these objectives are and highlights the new contributions to knowledge so that the reader is aware of how this work fits into the overall picture when reading Chapter 2.

This research applies finite element analysis to model an induction motor with airgap eccentricity for predicting specific frequency components and their magnitude in the current signal as a function of airgap eccentricity. It has already been shown by the

classical mmf and permeance wave approach, that specific frequency components in the current are a function of rotor slotting and airgap eccentricity [19, 20]. The magnitudes of these components increase with increasing airgap eccentricity. At present in industry the current spectrum is monitored over time and if these components are clearly visible in the spectrum and are increasing in magnitude then it can be stated that airgap eccentricity is present and that the severity of the problem is increasing [21]. This really requires the motor to be monitored from the commissioning stage in order to have a healthy current spectrum to compare with those from the motor after it has been in service. What would be of considerable value to motor operators is to be able to quantify the level of airgap eccentricity. That is, to say a motor has x% airgap eccentricity from the magnitudes of these current components from a single current spectrum taken at any time during the motor's life. This would greatly aid the development of planned maintenance programmes as discussions with manufacturers suggest that an airgap eccentricity level of 20% is considered to be unacceptable and a level of 50% is considered to be serious enough to immediately remove the motor from service [18].

An attempt was made to predict the fault severity from the current component magnitudes using classical circuit analysis and the mmf and permeance wave approach [19,22]. A critical appraisal of this work is presented in Chapter 2. Several good agreements were obtained between measured and predicted current magnitudes, however, the drawbacks in the analysis resulted in very poor agreement for some components. Consequently, it was thought that by applying a finite element analysis to predict the magnitude of specific current components a better agreement could be obtained compared to the classical approach without actually requiring any more design details than for the classical approach. The actual rotor and stator slot shapes are modelled in the finite element analysis instead of a grossly simplified design with the classical approach. This realistic slot shape modelling allows the accurate calculation of all slot passing frequencies. Saturation effects would also be modelled more realistically using finite element analysis.

There are other factors which may affect the current component magnitudes which were not possible to model using the classical approach. The current component magnitudes are a function of rotor slotting which in turn is dependant on the design of the rotor slots. The finite element analysis accurately models the true rotor slot shape compared to the classical approach model of a simplified shape. The more realistic modelling of the motor, for example, the actual slot design instead of a simplified design, facilitates the investigation of these factors. Consequently, in addition to the accurate calculation of the slot passing frequencies it was possible to investigate the effect of rotor slot design and the number of rotor bars.

In brief the objectives of this research work are:

- Literature review of the monitoring and diagnosis of airgap eccentricity in induction motors and the application of finite element analysis to investigate airgap eccentricity.
- Perform a critical appraisal of the mmf and permeance wave analysis to predict the frequencies and pole-pair numbers of the airgap eccentricity flux waves.
- Apply a time stepping finite element analysis to model a 3-phase induction motor with static eccentricity.
- Use the finite element results to calculate the magnitude of the current components which are a function of static airgap eccentricity, rotor slotting and saturation. Compare the calculated components (frequency and magnitude) in the current with experimental results from the test-rig motor being modelled.
- Use the finite element results to compare with the predictions from the pole-pair analysis as to which current components are compatible with the stator winding harmonic pole-pairs, that is, which frequency components should appear in the

current spectra. This will further investigate the limitations of the mmf permeance wave analysis.

- Repeat the above for dynamic eccentricity and combinations of static and dynamic eccentricity.
- Investigate the effect of open, semi-closed and totally closed rotor slots on the magnitudes of these current components in comparison to the effect of static eccentricity using the finite element analysis. Repeat this for models of dynamic and then combinations of static and dynamic eccentricity.
- Investigate the effect of the number of rotor slots on the current components.
- Apply the analysis to a large induction motor operating in industry and compare with on-site test results.

These investigations will lead to the prediction of the level of airgap eccentricity present in the motor from the magnitudes of these specific components in the current spectrum. A better understanding of the limitations and application of the classical mmf and permeance wave analysis will be obtained. They will also determine how much of an effect the rotor slot shape and the number of rotor bars have on the magnitudes of these current components in comparison to the changes in magnitudes observed when the airgap eccentricity level is increased. This will lead to a better understanding of airgap eccentricity in relation to current monitoring of different types of motors in industry. The verification of the technique to a large industrial induction motor is important as a prediction of the current component magnitudes for a large motor has not previously been attempted. All these objectives contribute to new knowledge in the area.

# Chapter 2

## Review of Research on Airgap Eccentricity

### 2.1 Introduction

This chapter reviews the published literature on the analysis of airgap eccentricity in 3-phase induction motors. A thorough literature search has been undertaken and to the author's best knowledge the objectives of this research contribute to new knowledge in the field. As published literature is reviewed the reasoning behind the development of the research objectives is explained. In particular, as this research is based on a combination of the mmf and permeance wave approach to predict the frequency components in the current and a finite element analysis for the calculation of the component magnitudes, the advantages and disadvantages of the permeance wave approach are fully reviewed. The classical approach is used to calculate the frequency of the current components which are a function of airgap eccentricity and to verify the finite element predictions. The reasoning and advantages behind pursuing the accurate prediction of the component magnitudes by finite element analysis are explained together with a review of published literature on the application of finite element analysis to airgap eccentricity problems.

## 2.2 Quantification of the UMP

Early research on airgap eccentricity was not focused on detecting the problem from a condition monitoring perspective but on the calculation of the forces which result in a motor with a non-uniform airgap. An unbalanced magnetic pull (UMP) results from the non-uniformity of the airgap length with airgap eccentricity. The magnetic forces due to north and south poles on the stator and rotor no longer balance out, consequently, a net force acts in the direction of the minimum airgap. This is a steady pull for static eccentricity but is a rotating force wave with dynamic eccentricity. The quantification of this force is of considerable importance for motor design as it effects the critical speed, shaft flexibility and length and also the bearing specification.

It is not the purpose of this thesis to calculate the UMP, therefore, only a brief review is presented of a selection of the key papers in this area. By 1918 sufficient work had been carried out to allow Gray and Pertsch [23] to review published literature on the analysis of UMP. In the intervening years many different approaches have been taken in the analytical and experimental investigation of UMP up to the present day when finite element techniques have been applied. Before the availability of the computational power to use finite elements, analysis of the UMP was exclusively carried out using classical techniques. For instance, B-H curves were used to quantify the imbalance of airgap flux to calculate the UMP [24, 25]. Space vectors were used [26] to represent the rotating fields in the airgap and Swann [27] developed a method whereby a motor with an eccentric rotor and symmetrical windings could be transformed into a motor with a concentric rotor with asymmetrical windings. Freise and Jordan [28] modelled a machine representing the airgap permeance by a constant plus a sinusoidal component. This modulates the fundamental rotating flux and leads to UMP. Osama and Lipo [29] used an approach based on multiple coupled circuits to calculate all the self and mutual inductances of the motor to obtain the electromagnetic force expressions. This technique was verified experimentally and used to study the dependence of UMP on supply voltage, eccentricity and load. A two-dimensional time-stepping finite element

analysis was used by Arkkio and Lindgren [30] to calculate the UMP. The analysis based on the principle of virtual work was used to calculate the forces acting on the rotor for a 30kW 2-pole and 15kW 4-pole motor. The effect of supply frequency, loading and the level of airgap eccentricity on the UMP were investigated.

Although the quantification of the UMP both theoretically and experimentally is important, it cannot be used as an indication of the presence or the degree of airgap eccentricity in terms of a condition monitoring system. As the work of [31, 32, 33, 34, 35] showed it is not practical to measure the force resulting from UMP in an industrial situation. Attempts to measure the forces in these references involved the use of either strain gauges, load cells, or piezoelectric transducers and in all cases specially adapted test rig motors in a laboratory situation. Consequently, research has been carried out on the diagnosis of airgap eccentricity using other parameters which are affected by airgap eccentricity as reviewed in the next section.

### 2.3 Airgap Eccentricity Diagnosis using Vibration and Flux Signals

The non-uniformity of the airgap length with eccentricity distorts the flux, similar to the effect of slotting and saturation, which results in high frequency fluxes rotating in the airgap. The magnetic forces which act on the inside of the stator can be determined from Equation (2.1), [12]:

$$F = \frac{B^2}{2\mu_o} \quad (2.1)$$

where  $F$  = magnetic force ( $N/m^2$ ),  $B$  = flux density and  $\mu_o$  = permeability of free space

Consequently, these high frequency fluxes can be detected as vibrations in the stator core and frame because they result in forces that act on the inside of the stator which are then transmitted through the mechanical structure. The magnitude of these vibrations are dependant on the electromagnetic waves and the mechanical response of the stator.

These high frequency flux components can also be detected directly in the motor flux and they can induce currents at these frequencies in the current signal dependant on the pole-pairs of the flux components and the stator winding factors. The flux signals that can be used are: airgap flux, stray flux from the end-windings, leakage flux outside the motor and axial flux. The following paragraphs review the diagnosis of airgap eccentricity using vibration and the various flux signals before focusing on the use of on-line current monitoring in the next section.

Bearing vibration is commonly monitored in the industrial situation to detect bearing wear and rotor dynamic problems. Airgap eccentricity does cause an increase in the level of vibration at the bearings, however, the vibration components monitored are not purely a function of static or dynamic eccentricity. Uncertainty can exist when interpreting the vibration spectrum, for example, the vibration component at the rotational speed frequency can increase due to airgap eccentricity, mechanical imbalance in the rotor or because of load problems [36]. Hence, diagnosing the real cause of the increase can be difficult.

Rai [33] verified that low frequency vibratory forces change due to airgap eccentricity/UMP. However, these components at 50Hz, 100Hz and 200Hz can also be effected by dynamic imbalance [20] and the 100Hz 200Hz 300Hz stator core vibration components are also effected by interturn stator winding faults, single phasing and voltage supply imbalance [12]. Therefore, these components cannot be used to unambiguously diagnose airgap eccentricity.

It was not until later that Cameron et al [19, 20] and Thomson et al [37] showed that the stator core vibration spectrum can be used to diagnose static and dynamic eccentricity. High frequency vibration components due to rotor slotting increase in magnitude with increasing static eccentricity and unique components appear due to dynamic eccentricity. It is very complex to model the electromagnetic forces and the mechanical response of each motor being monitored so a prediction of the severity of

the problem has not been attempted. The magnitude of the vibration components also increase with load adding to the complexity. It can also be difficult to fit the vibration transducers to the stator core back in an industrial installation.

Ellison and Yang [38] showed that eccentricity causes an increase in the acoustic noise levels of an induction motor. He predicted, using an analysis of the airgap magnetic field that the magnitude of the slot passing frequencies would be effected by eccentricity. Experimental verification of the analysis using an anechoic chamber was successful. This technique is very difficult to apply in an industrial installation due to the high background acoustic noise.

Early work by Verma and Natarajan [39] used search coils in the stator to study the effect on the airgap field with changing eccentricity. Fruchtenicht et al [40] showed that frequency components in the airgap flux signal can be used to diagnose airgap eccentricity and Penman et al [41] achieved the same by the use of axial flux signals. In both cases the magnitude of the components in Webers was not quantified as a function of the severity of the fault. To fit search coils to detect airgap flux requires a motor to be removed from service which is not a popular option with motor users. It also requires design modifications and approval by the insurers of the plant. Access to the motor is also required to fit axial flux search coils. In order to sense a reliable signal the coil must be fitted on the shaft inside the steel outer frame because the frame attenuates the flux signal by acting as a magnetic shunt. This again means removing the motor from service temporally and is not really popular with motor operators. In addition, no on-site case histories have been presented on the successful application of axial flux monitoring to detect a serious airgap eccentricity problem.

Although the aforementioned signals can be used to diagnose airgap eccentricity they are invasive to monitor and therefore not particularly practical to implement in the industrial situation. Motor operators prefer a non-invasive monitoring system that does

not disturb the drive. Current monitoring meets this criteria as explained in the next section.

## **2.4 On-Line Current Monitoring to Diagnose Airgap Eccentricity**

The application of current monitoring, versus other motor signals, to detect induction motor problems and failure mechanisms is popular within industry. The current is monitored via a clip-on current transformer around an input line to the motor and as this can be done from the switchgear room access to the drive is not required. On-line current monitoring has already been successfully used to detect broken rotor bars [42, 43, 44] and operators are keen that airgap eccentricity can be diagnosed and its level quantified using the same signal and a current transformer which may already be in place.

The motor current is also the principal signal being used in the development of automated condition monitoring systems using artificial neural networks where an operator does not have to interpret the information gathered. Scheon et al [45] used stator current monitoring and a neural network to monitor already established specific frequency components in the current spectrum which are indicative of airgap eccentricity, broken rotor bars and bearing problems. The system successfully detected problems by monitoring the magnitude of specific frequency components compared to 'learned' magnitudes from a healthy motor, however, this has not yet been applied in industry. Penman and Yin [46] used neural networks in the laboratory situation to identify unbalanced supply conditions, spectral components in the current and frame vibration signals were monitored. A neural network was also trained to detect rotor asymmetries by monitoring the current signal [47].

The breakthrough in the application of on-line current monitoring to diagnose airgap eccentricity in induction motors was a result of the work by Cameron and Thomson

[19, 20, 22]. This work, based on the mmf and permeance wave approach, also investigated stator core vibration and stray flux signals for detecting airgap eccentricity as reported in [19] and [20] respectively. The investigation of these signals will not be discussed in detail as this research is solely concerned with the application of on-line current monitoring to diagnose airgap eccentricity. The remainder of this section briefly discusses the work of Cameron and Thomson and other research published after the work of Cameron and Thomson which is also based on using the current signal as a means of diagnosing airgap eccentricity. Two successful applications of on-line current monitoring in an industrial installation are also reviewed. Section 2.5 presents an in-depth critical review of the analysis developed by Cameron and Thomson as an appraisal of their work was an objective of this research.

Cameron and Thomson predicted the airgap flux waveform by the mmf and permeance wave approach which was proposed by Yang [48]. The airgap flux distribution is calculated from the product of the mmf distribution of the windings and the permeance of the airgap. The expression for the permeance wave takes into account the effect on the airgap permeance of rotor and stator slotting, static and dynamic eccentricity and magnetic saturation. The series expression for the mmf includes the fundamental and stator and rotor mmf harmonics. The resulting flux density distribution varies in both space and time. From the time components in the airgap flux density expression the frequency of components which are a function of airgap eccentricity can be predicted as Equation 2.2 illustrates [19, 20, 48]:

$$f_{ec} = f_1 \left[ (R \pm n_d) \left( \frac{(1-s)}{p} \right) \pm 2n_{sa} \pm n_{ws} \right] \quad (2.2)$$

$f_{ec}$  = frequency components which are a function of airgap eccentricity (Hz)

$f_1$  = supply frequency (Hz)

$R$  = number of rotor slots

$n_d$  = zero for static and one for dynamic eccentricity

$s$  = slip

$p$  = pole-pairs

$n_{sa}$  = 0, 1, 2, saturation integer

$n_{ws} = 1, 3, 5, 7$ , time harmonic of the stator mmf (usually taken as 1 for the principal components)

The pole-pairs associated with these frequencies in the airgap flux can be calculated from the space component, as Equation 2.3 illustrates [19, 20, 48]:

$$m = (R \pm S \pm n_s \pm n_d \pm 2n_{sa}p \pm n_{\theta_s}p) \quad (2.3)$$

$m$  = pole-pair number of flux waves

$R$  = number of rotor slots

$S$  = number of stator slots

$n_s$  = static eccentricity integer

$n_d$  = dynamic eccentricity integer

$p$  = pole-pairs

$n_{sa}$  = saturation integer

$n_{\theta_s}$  = stator space harmonic integer

The high frequency flux waves as predicted by Equation 2.2 move relative to the stator winding and may induce corresponding currents provided that the pole-pairs of the flux waves are compatible with the stator winding design harmonic pole-pair numbers. Consequently, the current spectrum can be used to diagnose airgap eccentricity. Cameron and Thomson predicted and verified experimentally that these specific frequency components are present in the current signal and are dependant on the level of airgap eccentricity in the motor. However, in some of their experimental results certain components did not increase significantly in magnitude with increasing airgap eccentricity as expected. Several explanations were proposed for this but it will be shown later in this thesis that their explanations were only partially valid. Cameron and Thomson did calculate the pole-pairs of the flux waves at the frequencies they were investigating but they never calculated the harmonic pole-pair numbers of the stator winding to check for compatibility. They did not realise that the pole-pairs of certain

frequency components in the flux waveform which are a function of airgap eccentricity were incompatible with the stator winding harmonic pole pair numbers. Consequently, other than by second order effects such as winding asymmetry or saturation (as explained later) these components could not induce currents at those frequencies in the stator winding. A detailed review of these problems and the pole-pair analysis carried out in this work to explain their observations is presented in Section 2.5. The pole-pair analysis is also taken further to understand the limitations of the approach for predicting the pole-pairs of frequency components in the flux waveform. In Equation 2.3 Cameron only considered  $n_s = 1/n_d = 1$  which is a gross simplification of the analysis.

Despite these points, by looking for all the frequencies components predicted by Equation 2.2 they did include in their investigations the frequency components which were truly compatible with the stator winding and they did increase in magnitude with increasing airgap eccentricity. Generally, there are frequency components which are a function of slotting and static eccentricity (principal slot passing frequencies - PSPF) and new components appear either side of the principal slot passing frequencies which are a function of dynamic eccentricity. The magnitude of the dynamic eccentricity components can also be effected by the level of static eccentricity [21].

The method proposed by Cameron and Thomson has been successfully applied in industry [20, 21]. In industry, at present, the current spectrum is monitored over time and if these frequency components are clearly visible and increasing in magnitude then airgap eccentricity is deemed to be present and the level is increasing. This really requires the motor to be monitored from the commissioning stage. To be able to quantify the fault severity from a single measurement of the component magnitudes would be of considerable value to motor operators. In most applications, but particularly in hazardous environments, it would be valuable to know how close the airgap eccentricity is to the critical level at which motor failure (rotor to stator rub) might occur.

An attempt was made by Cameron and Thomson to predict the fault severity from the magnitudes of the current components [19, 22]. This approach was based on the mmf and permeance wave approach, empirical approximations and classical circuit analysis. In some cases the agreement obtained between measured and calculated magnitudes was good (difference less than 1.9 dB), this was for components whose pole-pair numbers were compatible with the stator winding which were not due to any second order effects like saturation and winding asymmetries. However, when it came to components due to second order effects the agreement was not good (difference of 13dB). Section 2.5 discusses in detail the analysis developed by Cameron and Thomson with quantitative results from their work explaining the limitation of the approach and how the finite element method used in this research overcomes these limitations.

Stavrou and Penman [49] also adopted the rotating wave and permeance approach to quantify the magnitudes of the high frequency current components due to purely static eccentricity. The permeance expression for the airgap included slotting and static eccentricity, however, saturation was not taken into account. The flux density was again taken as the product of the permeance wave and winding mmf which was used to calculate the resultant flux linking the stator winding. Having determined the inductances and resistances of the test-rig motor they used a space vector theory to define a matrix for the voltage equations of the motor from which the current magnitudes were calculated. By introducing an effective eccentricity level, damping effects, saturation and airgap fringing were incorporated. The graphical presentation of the calculated and measured current magnitudes does indicate reasonable agreement, however, the presentation prevents a numerical comparison of the results to be made. They clearly show from experimental results the increase in magnitude of the current components with increasing eccentricity as shown by previous work. This technique was not applied to an industrially based motor. They also attributed the appearance of rotational speed side-bands ( $f_1 \pm f_r$ ) around the fundamental supply component of current as being due to equalising currents in the parallel connected stator winding. In

fact, it has been shown by Dorrell et al [50] and Salon et al [51] that these are due to the combination of static and dynamic eccentricity.

Toliyat et al [52] used a winding function approach to model the steady state and dynamic performance of an induction machine with static eccentricity. The method is based directly on the geometry of the induction machine and the physical layout of all the windings. The expressions derived for the machine inductances incorporated an airgap factor in which static eccentricity was included. The model was used to predict the shaft speed during run-up with zero and 50% static eccentricity, showing that with eccentricity the run-up time was longer due to the generation of the backward MMF due to eccentricity. The stator phase current for 0% and 50% static eccentricity was calculated and the frequency spectrum computed. The high frequency current components due to slotting and static eccentricity determined by Cameron and Thomson were investigated. An increase in one of these components was clearly visible in the modelled current with the 50% increase in static eccentricity. They did not carry out any experimental work themselves and compared their results with the experimental results of Cameron et al [20]. The prediction of the current component magnitudes as a function of the fault severity was not attempted.

Hiroven [53] reviewed the application of on-line condition monitoring to detect faults in squirrel cage induction motors. The use of current, speed, flux and vibration signals to detect broken rotor bars and airgap eccentricity were reviewed and experimental investigations carried out on test-rig motors (with skewed/unskewed rotors) with broken bars and airgap eccentricity. The equations derived by Cameron to predict the airgap eccentricity frequency components in the stator current, stator core vibration and axial flux were used. The level of airgap eccentricity in the test-rig motor had to be increased to 60% before any significant increase in the current component magnitudes were observed. It was noted by the authors that this phenomenon was also observed by Cameron and Thomson. In both cases the pole-pairs of the flux waves at these frequencies and the stator winding harmonic pole-pairs were not calculated to confirm

that these components could be induced in the stator winding. This is a possible reason for the insignificant increase observed until very high levels of airgap eccentricity where second order effects (saturation) could predominate. This will be discussed in more detail in Section 2.5.

Cardoso and Saraiva [54] used computer-aided monitoring of the stator current Park's Vector to detect static airgap eccentricity. The Park's Vector describes the machine in two dimensions by the use of d and q Park's Vectors. These trace out a circular locus with time and the effect of eccentricity can be seen in the distortion of this locus. The splitting of the current Park's Vector provides qualitative information about the severity of the fault, however, this can be very difficult to interpret and has not been applied in industry.

In addition to the high frequency current components which are dependant on airgap eccentricity, low frequency components around the fundamental are a function of both static and dynamic eccentricity [55, 56] as predicted by Equation 2.4:

$$f_{ec} = f_1 \pm f_r \quad (2.4)$$

$f_1$  = supply frequency (Hz)

$f_r$  = rotor speed frequency (Hz)

The original theory on these components [57, 58] assumed that they were only due to dynamic eccentricity and that the flux waves associated with them had pole-pairs of  $p \pm 1$ . These would not induce components in a  $p$  pole-pair stator winding. It was first shown experimentally by Thomson [55] and then theoretically verified by Dorrell et al [56] that dynamic eccentricity with an inherent level of static eccentricity can result in these components appearing in the current spectrum. The magnitude of the components are a function of both static and dynamic eccentricity. An inherent level of static eccentricity is realistic in an industrial based motor due to manufacturing tolerances and incorrect reassemble after repair. The analysis presented by Dorrell et al [56] showed

that flux waves with  $p$  pole-pairs can occur at the frequencies given by Equation 2.4 due to airgap modulation of mmf waves caused by both types of airgap eccentricity being present simultaneously. The magnitude of these components as a function of the severity of the airgap eccentricity was not predicted and it is difficult to determine which form of airgap eccentricity is causing the increase in component magnitudes. However, this work provided new knowledge as to the real cause of the  $(f_1 \pm f_r)$  Hz components when static and dynamic eccentricity are being modelled.

Monitoring these low frequency airgap eccentricity components in the presence of an oscillating load torque can be problematic. Torque oscillations at multiples of the rotational speed can excite the static/dynamic eccentricity frequencies at  $(f_1 \pm f_r)$  [59]. Torque oscillations can also cause problems when monitoring the classical twice slip frequency sidebands  $(1 \pm 2s)f_1$  (Hz) which are a function of broken rotor bars. The presence of a load torque oscillation can increase the magnitude of the frequency components of interest giving a false impression of the fault severity. It is possible to remove arbitrary load effects from the current spectrum by comparing the actual stator current to a model reference value excluding the load effect. The difference between these two signals provides a filtered current independent of load variations [60]. The high frequency current components due to airgap eccentricity investigated by Cameron and Thomson [19, 20] are unique to airgap eccentricity and are not prone to the effects of load variations [61].

As mentioned earlier, on-line current monitoring to diagnose airgap eccentricity has been successfully applied to large high voltage induction motors operating in industry. Cameron et al [20] applied the technique to two 11kV, 1.2 MW 3-phase induction motors in a power station. The high frequency current components predicted by Equation 2.2 were investigated. Although these motors were identical in design, it was known that motor B had stator core ovality. This would give rise to a static eccentricity condition. In this case the dynamic eccentricity components in motor B were 7-13 dB higher than the corresponding components in motor A. This validated the technique

when applied to large, industrially based motors. As the analysis in this thesis shows it is important to calculate the pole-pair numbers of the frequencies of interest to check for compatibility with the stator winding. This ensures that the optimum components in the current spectrum are monitored and not those dependent on second order effects. Cameron and Thomson did not do this in the results presented for the large motors. The magnitude of the principal slot passing frequency, which is a function of static eccentricity, was only 2.1 dB higher for motor A than for motor B. With stator core ovality in motor B this suggested that the static eccentricity level in motor B would be higher, which was not seen from the current spectrum results. It could be the case again that the pole-pairs of the flux-waves at this frequency were not compatible with the stator winding and hence showed no difference in magnitude between the two motors. The fact that the dynamic eccentricity components were higher for motor B suggests that they were a function of static eccentricity in this motor [19, 20]. The pole-pair analysis could be used to confirm if this was the case.

Thomson et al [21], used a combination of monitoring the high frequency components predicted by Equation 2.2 together with the low frequency sidebands around the fundamental as described in [56]. This approach was applied to three 1.45MW, 11kV industrially based motors driving pumps in an oil-tank farm. Motor A exhibited high vibration levels at the bearings which was resulting in overheating of the bearing oil. An acceptable level of vibration set by a manufacture for this size and speed of motor would be 1.5mils (pk-pk), however, vibration levels on motor A were 4.8 and 4.4mils at the drive end for the vertical position displacement and the horizontal position displacement, respectively. There were obviously very large forces acting on the bearings but vibration and temperature measurements could not identify the problem. On-site personnel thought that the problem could be due to broken cage bars or airgap eccentricity. To determine which or both was the cause required on-line current monitoring to be applied. On-line current monitoring was applied and motor A was observed to have high magnitude dynamic eccentricity components around the 1019Hz rotor slot passing frequency. The dynamic eccentricity component at 1031Hz was 13dB

down on the 1019Hz for motor A but 40dB down for motor C which was deemed to have a normal level of airgap eccentricity. For motor A the  $(f_1 \pm f_r)$  components were also predominant around the 50Hz, 20dB above the noise level compared to motors B and C where these components were in noise. This suggested that both static and dynamic eccentricity were present in motor A. The  $f_1(1 \pm 2s)$  broken bar frequency components were insignificant being 64dB down on the 50Hz. Motors B and C were deemed to have a normal inherent level of airgap eccentricity but motor A was removed from service to realign the airgap. Airgap measurements taken during the realignment showed that the airgap was non-uniform (35% airgap eccentricity). Motor A was reinstalled and the vibration levels were normal. The current spectrum also showed that the high frequency dynamic eccentricity components were 8-10dB smaller in magnitude and that the  $(f_1 \pm f_r)$  were not present, 25dB smaller than before.

In conclusion, it has been shown that an analysis of the current signal can successfully diagnose airgap eccentricity in induction motors both in the laboratory and industrial situation without having to disturb the drive. This is a very advantageous feature of current monitoring as industry is not interested in a technique that requires special modifications to a motor or removal of a motor from service to fit transducers etc. The accurate prediction of the level of airgap eccentricity is most likely to be successfully achieved by predicting the magnitudes of the current components. This has been only partially achieved by Cameron et al [22] and the limitations in their approach, which are explained in the next section, can be overcome by the application of finite element analysis. A finite element analysis of an induction motor as a function of airgap eccentricity and the prediction of the current waveform will produce new knowledge for the reliable on-line detection of airgap eccentricity via current monitoring.

## **2.5 Critical Appraisal of Classical Approach to Predict Fault Severity**

### **2.5.1 Introduction**

The section presents a critical review of the work of Cameron and Thomson since the research presented in this thesis is partially based on their analysis. Equation 2.2 is used to calculate the frequency components in the flux waveform which are a function of airgap eccentricity. However, in this work the pole-pairs of the flux waves are recalculated and checked for compatibility with the stator winding harmonic pole-pair numbers. This is necessary to ascertain whether the flux waves can induce a voltage and current in the stator winding. Cameron and Thomson did calculate the pole-pairs of the flux waves at the frequencies of interest but they did not calculate the stator winding harmonic pole-pair numbers to check for compatibility. As a result they found it difficult to explain some of their experimental observations. A basic pole-pair analysis is presented in this section, firstly, to explain some of their experimental results and secondly, as an introduction to the pole-pair analysis which is presented for the motors used in this research project. It also assists in the explanation of the limitations in the approach to calculate the pole-pairs of the frequency components. The analysis method developed by Cameron and Thomson to predict the current magnitudes as a function of the airgap eccentricity level will then be discussed highlighting the limitations of the approach, therefore, accounting for some of the poor agreements that were obtained between measured and predicted current magnitudes. The advantages of applying a finite element analysis to investigate the frequency components predicted by Equation 2.2, the prediction of their magnitudes as a function of the airgap eccentricity level and an investigation of other factors which effect their magnitude are discussed

### **2.5.2 Critical Appraisal of Experimental Observations of Cameron and Thomson**

Cameron carried out extensive experimental tests [19] on a specially designed test-rig motor; static eccentricity, dynamic eccentricity and then combinations of both forms of

the problem were investigated and the current component magnitudes, at the frequencies predicted by Equation 2.2, were observed on a high quality spectrum analyser (80dB dynamic range). Tests were carried out on a 36 slot stator with a 51 and then a 28 bar rotor. The 28 bar rotor was of a double cage design and both rotors had skew. More results were taken using the 51 bar rotor and it was also used in the analysis to predict the magnitudes of the current components. Therefore, the 51 bar rotor results will be used to highlight the importance of calculating the pole-pairs of the flux waves at the frequencies predicted by Equation 2.2. These calculated pole-pairs can then be compared to the stator winding harmonic pole-pair numbers to check for compatibility, that is, will the flux waves be able to induce a voltage and current in the stator.

Firstly the frequency components to be detected in the flux were calculated using Equation 2.2, Table 2.1 shows the components that Cameron investigated and the parameters used in Equation 2.2 to calculate them.

Type	Frequency (Hz)	$f_1$	R	$n_d$	s	p	$n_{sa}$	$n_{ws}$
pspf	1178	50	51	0	0.037	2	0	-1
pspf	1278	50	51	0	0.037	2	0	1
pspf	1378	50	51	0	0.037	2	1 (0)	1 (3)
de	1154	50	51	-1	0.037	2	0	-1
de	1202	50	51	1	0.037	2	0	-1
de	1254	50	51	-1	0.037	2	0	1
de	1302	50	51	1	0.037	2	0	1

de: dynamic eccentricity component; pspf: principal slot passing frequency also a function of static eccentricity

Table 2.1 Frequency Components Investigated by Cameron [19] for 51 Bar Rotor

In Table 2.1 there are two possible combinations of  $n_{sa}$  and  $n_{ws}$  to calculate the frequency at 1378Hz. Cameron [19, 20] never specified what values he used in

Equation 2.2. Both combinations are valid as the 1378Hz can be a function of the third time harmonic of the stator mmf and/or a function of the first time harmonic of stator mmf with first order saturation present. It can be shown that the pole-pairs associated with this frequency, calculated from Equation 2.3, are the same for each combination of  $n_{sa}$  and  $n_{ws}$ .

Figures 2.1 to 2.6, on pages 31-33, show the changes in magnitude of these components (Table 2.1) for increasing airgap eccentricity as presented in [19]. Mr. Cameron's permission was granted to copy these figures from his thesis.

Figure 2.1 illustrates the effect of increasing static eccentricity on the principal slot passing frequencies (PSPF). These frequencies are a function of rotor slotting and static eccentricity and therefore should increase in magnitude with increasing static eccentricity. The components at 1178Hz and 1378Hz substantially increased in magnitude even at the lower levels of static eccentricity, for example, the 1178Hz increased from 2.4mA to 4.3mA when the static eccentricity increased from 0% to 40%. The 1278Hz component stayed fairly constant in magnitude (to within 1.2dB up to 40% static eccentricity) until very high levels of static eccentricity were introduced, that is, 60% and in particular 80% static eccentricity. Static eccentricity levels of 60% to 80% are extremely high and in a large, industrial motor this would probably result in a rotor to stator rub. If you consider a large rotor with an inherent dynamic eccentricity present and such a high static eccentricity level a rub would be highly likely. At these high levels of static eccentricity the magnetic circuit would be very unbalanced resulting in much increased localised saturation in the region of the minimum airgap. It is justified to say that the 1278Hz component did not increase significantly with increasing static eccentricity until extraordinary high levels of static eccentricity. It also has to be considered that both rotors Cameron investigated were skewed which could reduce the magnitude of this component. Cameron [19] did not comment on the difference between the increases in the principal slot passing frequencies for the 51 slot rotor result, other than saying that the trend in the increase of the frequency components

between 0% and 60% static eccentricity was considerably different for the 51 bar rotor compared to the 28 bar rotor. For the 28 bar rotor none of the components showed any increase in magnitude as the static eccentricity increased until 60% to 80% levels were introduced. This difference was accounted for in the different rotor designs and bar numbers remembering that the 28 bar rotor was a double cage. The pole-pair analysis presented after an appraisal of Cameron's results shows that the pole-pairs of the flux waves associated with the 1278Hz component are incompatible with the pole-pair harmonic numbers of the stator winding. Therefore, other than by second order effects the component should not have induced a current at this frequency. This ties in with the experimental observations in that only at very high levels of static eccentricity, where second order effects were probably present, did the component really become visible in the current spectrum.

A similar trend is noticed with the frequency components which are a function of dynamic eccentricity, Figure 2.2. Only the 1202Hz component showed a significant increase with increasing dynamic eccentricity (4.6dB of an increase with the dynamic eccentricity increasing from 0% to 50% compared to less than 1dB of an increase for the other components). Cameron did not comment on this. Figure 2.3 shows the effect on the principal slot passing frequencies of increasing static eccentricity with a fixed level of dynamic eccentricity of 12.5%. As for the case of purely static eccentricity increasing, the 1178Hz and the 1378Hz increased in magnitude as expected, however, the 1278Hz remained at the same level. For a constant level of 12.5% dynamic eccentricity the dynamic components would not be expected to increase in magnitude unless they were a function of static eccentricity as well. Figure 2.4 shows that the dynamic eccentricity components remained steady until a high static eccentricity level of 60% when they did increase (except the 1302Hz). Cameron did not comment on this other than to say that the high increase in the 1202Hz component at 60% static eccentricity (Figure 2.4) was due to the combined action of the static and dynamic eccentricity permeance variations on the current component. These results will be

discussed again after the pole-pair analysis is presented which aids in the explanation of the observations.

Figure 2.5 shows the effect on the principal slot passing frequencies of increasing static eccentricity with 25% dynamic eccentricity present. These results differ considerably to those in Figure 2.3 with 12.5% dynamic eccentricity present. The dynamic eccentricity components in Figure 2.6 showed no overall increase with increasing static eccentricity. It is possible that they would have increased if Cameron had introduced 60% static, as in Figure 2.4, however, this would have been too high a level combined with 25% dynamic eccentricity. Cameron explained the decrease in the 1178Hz and 1378Hz at the 20% static eccentricity level as being due to localised saturation effects in the region of the minimum airgap. Localised saturation effects partially explain these unusual results, however, Cameron neglected to consider the effect of skimming the rotor. The rotor was skimmed to introduce dynamic eccentricity which would alter the magnetic circuit of the rotor. This would have had more of an effect at 25% dynamic eccentricity compared to 12.5% dynamic eccentricity, hence, explaining how the principal slot passing frequencies behaved differently at 25% dynamic eccentricity. When comparing the results for 12.5% and 25% dynamic eccentricity Cameron was not comparing the results from the same rotor in magnetic circuit terms.

Tests carried out on the 28 slot rotor also yielded some strange observations. For increasing static eccentricity the principal slot passing frequencies investigated (736Hz and 936Hz) did not increase until more than 60% static eccentricity was introduced. This compared with the increase in the corresponding components after 20% static eccentricity was introduced with the 51 bar rotor. As mentioned earlier, Hiroven [53] noticed the same effect, of components not increasing until very high values of airgap eccentricity, on a test rig motor he investigated. Cameron attributed the effect to the difference in the rotor cage design, the 28 slot being of a double cage design and the 51 bar a single cage design. The pole pair analysis presented after Figures 2.1 to 2.6, for the 51 bar rotor was also carried out for the 28 bar rotor and it can be shown that the

pole pairs of the flux waves at 736Hz and 936Hz were not compatible with the pole - pair numbers of the stator winding. Corresponding currents would not have been induced other than by second order effects such as saturation, which could become present with the extraordinary high levels of static airgap eccentricity or by stator winding asymmetry.

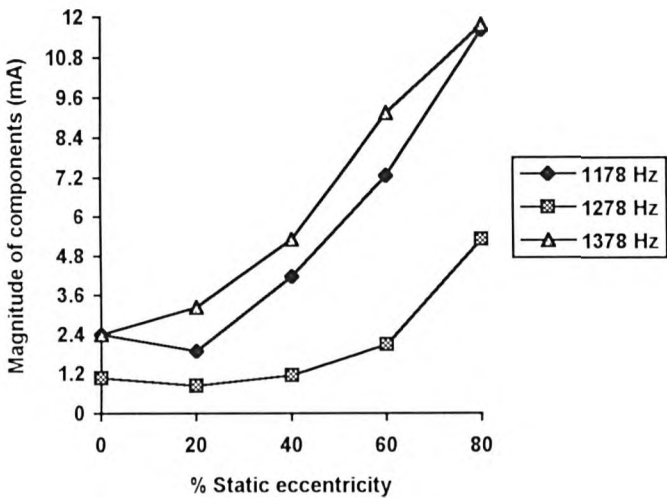


Figure 2.1 Effect on Principal Slot Passing Frequencies of Increasing Static Eccentricity

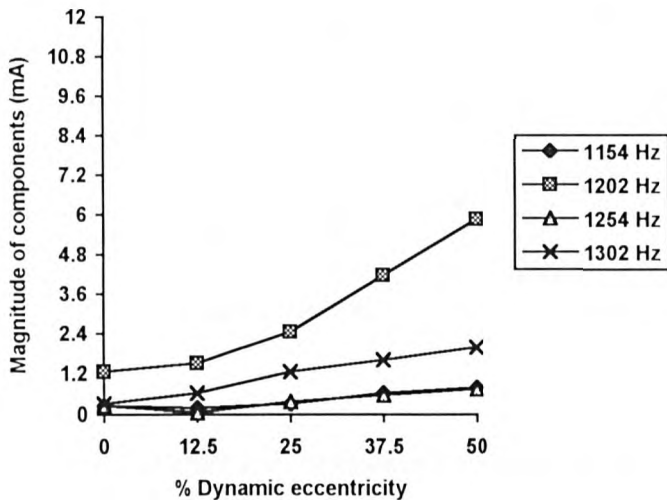


Figure 2.2 Effect on Dynamic Eccentricity Components of Increasing Dynamic Eccentricity

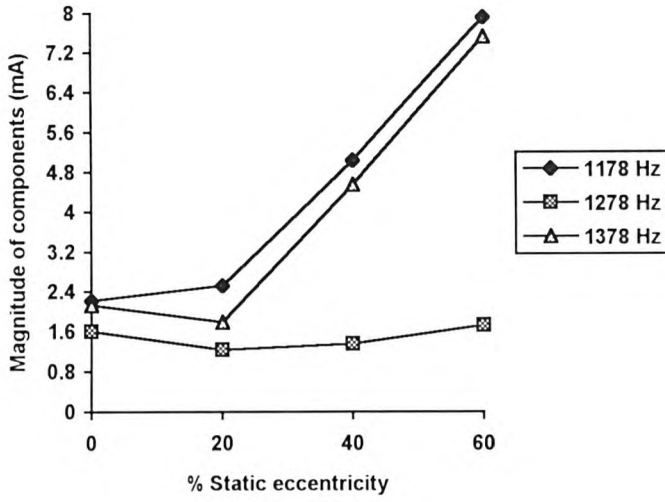


Figure 2.3 Effect on PSPF of Increasing Static Eccentricity with 12.5% Dynamic Eccentricity

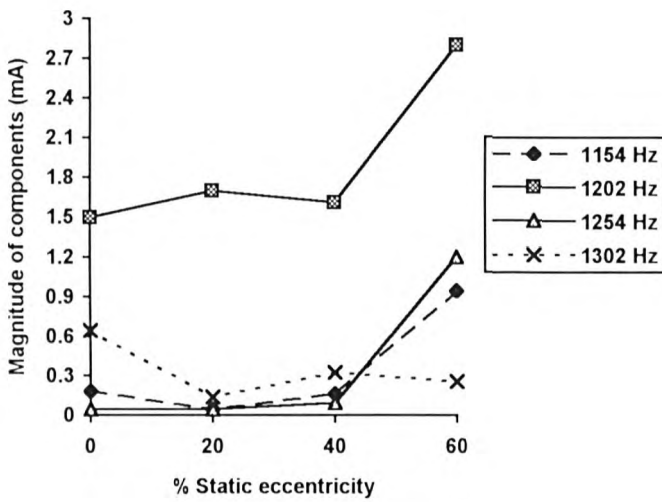


Figure 2.4 Effect on Dynamic Eccentricity Components of Increasing Static Eccentricity with 12.5% Dynamic Eccentricity

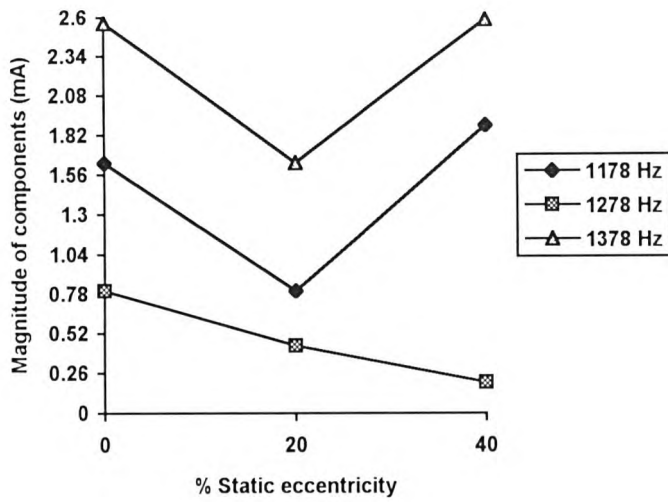


Figure 2.5 Effect on PSPF of Increasing Static Eccentricity with 25% Dynamic Eccentricity

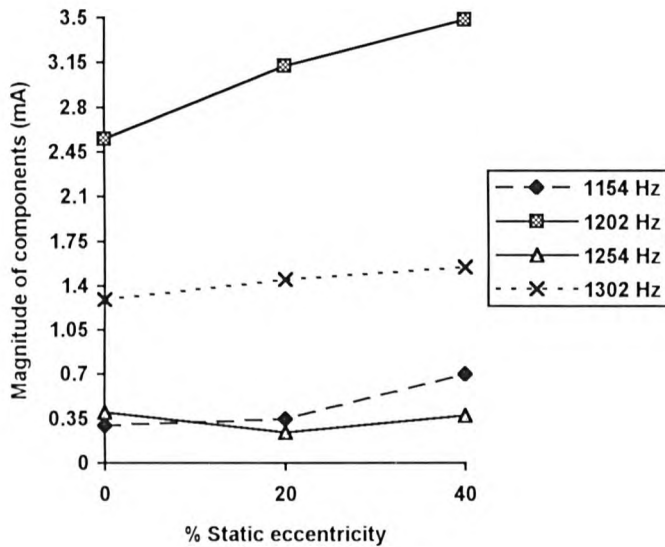


Figure 2.6 Effect on Dynamic Eccentricity Components of Increasing Static Eccentricity with 25% Dynamic Eccentricity

The pole-pair analysis performed as part of this research explains the effects noticed in Cameron's results, in that some frequency components are more responsive to changes in airgap eccentricity levels than others. In the pole-pair analysis the harmonic pole-

pairs of the stator winding are calculated as shown in Table 2.2. To calculate the first order harmonic pole pairs for a 3-phase winding layout as shown in Table 2.2, only odd harmonics of the fundamental are considered which are not divisible by three (1, 5, 7, 11, 13, 17 ...). In a balanced three phase winding only odd harmonics can be present [62] and triple harmonics do not appear in a normally designed star or delta connected motor [3] as the winding factors of these harmonics equate to zero so no current can be induced for flux waves with pole-pairs of 6, 12, 18 etc.

Stator winding data: 4 pole, 36 slot, 8/9 pitch, 3 slots/pole/phase, star connected.																
<b>Harmonic pole-pairs m:</b> Fundamental - 2 pole-pairs $m = p(6c \pm 1)$ where $c = 0, 1, 2, 3...$																
2	10	14	22	26	34	38	46	50	58	62	70	74	82	86	94	98 etc

Table 2.2 Harmonic Pole-Pair Numbers for Stator used by Cameron and Barbour

The pole-pair analysis calculates the pole-pairs of the flux waves at the frequencies predicted by Equation 2.2. By using Equation 2.3 the pole-pairs are calculated and can then be compared to the pole-pair harmonic numbers of the stator winding to see if currents at those particular frequencies will be induced. The harmonic pole-pairs of the stator winding shown in Table 2.2 are first order harmonic pole-pair numbers. If winding asymmetry is present (unbalanced supply) then pole-pairs due to even harmonics of the fundamental ( $m = p(6c \pm 2)$ ) can be present resulting in the stator winding being compatible to flux waves with pole-pairs of 8, 16, 20 etc.

When calculating the pole-pairs associated with the frequencies calculated by Equation 2.2 the same values for  $n_s$ ,  $n_{sa}$  etc. are used in both equations corresponding to a specific frequency. For instance, for the 1178Hz component  $n_{sa} = 0$  and  $n_{os} = -1$  corresponding to  $n_{os} = -1$ . As already mentioned the 1378Hz component can be a function of the third time harmonic of the stator mmf or of the first time harmonic of stator mmf and first order saturation. The pole-pairs calculated are the same for each case which is expected as the third time harmonic of the stator mmf is a function of

saturation, this component is clearly a function of saturation. The 1278Hz component is not a function of saturation and a flux wave at 1278Hz will occur when there are no saturation effects. However, with saturation present the pole-pairs of the 1278Hz flux wave could be modified. To calculate the effect of saturation it is possible to apply  $n_{sa}=1$  to the pole-pairs calculated for the 1278Hz component. These points will become apparent as the analysis is worked through.

The pole-pair analysis is built up in stages for ease of interpretation, the simplest case of a perfect motor is assumed first, then static and dynamic are incorporated separately and finally the two forms of airgap eccentricity are considered together.

*Case 1: No static or dynamic eccentricity*

$$m = (R \pm S \pm n_s \pm n_d \pm 2n_{sa}P \pm n_{\theta s}P) \quad \text{where } n_s = 0, n_d = 0; n_{sa} = 0, n_{\theta s} = \pm 1, p = 2,$$

$$R = 51 \text{ and } S = 36.$$

$$\therefore m = R \pm S \pm 2$$

$$m = 51 \pm 36 \pm 2$$

$$= 87 \pm 2 \quad \text{and} \quad 15 \pm 2$$

Which gives 89 and 17 for +2 which corresponds to  $n_{\theta s} = +1$  and component 1278Hz and also 85 and 13 for -2 which corresponds to  $n_{\theta s} = -1$  and component 1178Hz. Also  $m = 87 + 4 + 2$  and  $15 + 4 + 2 = 93$  and 21 which corresponds to  $n_{\theta s} = +1$  and  $n_{sa} = 1$  for component 1378Hz

This result shows that the pole-pairs of the flux waves at the principal slot passing frequencies are odd and not compatible with the stator winding, Table 2.2. This means that in an absolutely perfect motor these components should not be present in the frequency spectrum of the current.

*Case 2: Static eccentricity present but no dynamic eccentricity*

$$m = (R \pm S \pm n_s \pm n_d \pm 2n_{sa}p \pm n_{\theta s}p) \text{ where } n_s = \pm 1, n_d = 0; n_{sa} = 0/1, n_{\theta s} = \pm 1, p = 2$$

$$R = 51 \text{ and } S = 36.$$

Giving  $85 \pm 1$  and  $13 \pm 1 \Rightarrow 86, 84$  and  $14, 12$  pole-pairs for 1178Hz

$89 \pm 1$  and  $17 \pm 1 \Rightarrow 90, 88$  and  $18, 16$  pole-pairs for 1278Hz

$93 \pm 1$  and  $21 \pm 1 \Rightarrow 94, 92$  and  $20, 22$  pole-pairs for 1378Hz

This result shows that the 1278Hz flux component should not be able to induce a current in the stator winding, however, the 1178Hz and the 1378Hz are compatible with the stator winding and therefore the magnitude of these components should increase with static eccentricity.

*Case 3: Dynamic eccentricity present but no static eccentricity*

$$m = (R \pm S \pm n_s \pm n_d \pm 2n_{sa}p \pm n_{\theta s}p) \text{ where } n_s = 0, n_d = \pm 1, n_{sa} = 0, n_{\theta s} = \pm 1, p = 2,$$

$$R = 51 \text{ and } S = 36.$$

From earlier analysis the pole-pairs for the slot passing frequencies were:

85 and 13 for  $n_{\theta s} = -1$  for the 1178Hz component

89 and 17 for  $n_{\theta s} = +1$  for the 1278Hz component

Now with  $n_d = \pm 1$ :

-1 for the lower dynamic eccentricity components 1154Hz and 1254Hz

+1 for the upper dynamic eccentricity components 1202Hz and 1302Hz

The pole-pairs associated with these frequencies are:

1154Hz:  $85 - 1$  and  $13 - 1 \Rightarrow 84, 12$

1254Hz:  $89 - 1$  and  $17 - 1 \Rightarrow 88, 16$

1202Hz:  $85 + 1$  and  $13 + 1 \Rightarrow \underline{86}, \underline{14}$

1302Hz:  $89 + 1$  and  $17 + 1 \Rightarrow 90, 18$

The above result shows that only the flux waves associated with the 1202Hz component are compatible with the stator winding. This implies that only this component should be affected by changes in the dynamic eccentricity level.

#### *Case 4: Both static and dynamic eccentricity present*

The pole-pairs of the dynamic eccentricity components with dynamic eccentricity present were calculated in Case 3, static eccentricity is now included  $n_s = \pm 1$  and this is applied to the pole-pair values obtained in Case 3:

1154Hz:  $84 \pm 1$  and  $12 \pm 1 \Rightarrow 83, 85$  and  $11, 13$

1254Hz:  $88 \pm 1$  and  $16 \pm 1 \Rightarrow 87, 89$  and  $15, 17$

1202Hz:  $86 \pm 1$  and  $14 \pm 1 \Rightarrow 85, 87$  and  $13, 15$

1302Hz:  $90 \pm 1$  and  $18 \pm 1 \Rightarrow 89, 91$  and  $17, 19$

This result (all odd pole-pairs) indicates that with static and dynamic eccentricity the dynamic eccentricity components are not a function of static eccentricity in this motor. A limitation of the pole-pair analysis now becomes apparent, in that with static and dynamic eccentricity how are the pole-pairs of the principal slot passing frequencies calculated. The above procedure only calculates the pole-pairs associated with the dynamic eccentricity components, however, this does not include the principal slot passing frequencies. It could be argued to return to the pole-pairs calculated in Case 2 for only static eccentricity and then apply the  $\pm n_d$  to them to include dynamic eccentricity. This would result in all odd pole-pairs (87, 91, 17, 19 etc) and would imply that with static and dynamic eccentricity the principal slot passing frequencies would not be affected by increases in airgap eccentricity of either form. However, it is known

from experimental observations that with static and dynamic eccentricity combinations, the principal slot passing frequencies increase with increasing static eccentricity just as they did when nominally only static eccentricity was present. This is a limitation in the mmf and permeance wave analysis that has to be appreciated when applying it to an induction motor. This will be discussed further later in the thesis.

A summary of the findings of the pole-pair analysis is given below before reviewing again the experimental observations of Cameron in light of these new findings:

*Summary:* 1178Hz and 1378Hz should increase with increasing static eccentricity, the 1278Hz should not show any increase.

With increasing dynamic eccentricity only the 1202Hz should increase with increasing dynamic eccentricity.

With combinations of static and dynamic eccentricity, the dynamic eccentricity components should not increase with either form of the fault increasing. As already mentioned it is ambiguous as to what happens to the pole-pairs of the principal slot passing frequencies (1178Hz, 1278Hz etc).

Returning to Figure 2.1, it can be seen that the experimental results confirm the pole-pair analysis. The 1178Hz and 1378Hz increase with increasing static eccentricity. The 1278Hz component does not increase until after 60% static eccentricity. At this high level of static eccentricity saturation would be more prominent and it can be shown using the pole-pair analysis that if first order saturation is included for the 1278Hz component (Case 2) the pole-pairs of the flux waves at that frequency become: 94, 86, 92, 84 and 22, 14, 20, 12 which makes this component compatible with the stator winding. This explains the increase in the magnitude of this component with the higher level of static eccentricity where localised saturation would increase considerably.

The experimental results again agree with the pole-pair analysis, Figure 2.2, in that only the 1202Hz component increases significantly with increasing dynamic eccentricity. The

1302Hz component does show more of an increase than the 1154Hz and the 1254Hz components, although the pole-pairs associated with these frequencies are only compatible with the stator winding if second order effects are present. In this situation the winding factors at these frequencies have to be calculated and it can be shown that the winding factors are larger for certain frequencies. It is these frequencies which are more prominent in the current when considering second order effects. Winding factors are calculated for the pole-pair analysis presented later for the motors used in this research project.

In Figure 2.3 the principal slot passing frequencies increase with increasing static eccentricity with 12.5% dynamic eccentricity present just as they did in Figure 2.1 with only static eccentricity present. As already mentioned the pole-pair analysis is limited when trying to unambiguously decide the pole-pairs of the flux waves at the principal slot passing frequencies for combinations of static and dynamic eccentricity. The experimental results suggest that the principal slot passing frequencies are independent of dynamic eccentricity in this motor. Figure 2.4 confirms the pole-pair analysis that with static and dynamic eccentricity the dynamic eccentricity components are independent of increases in static eccentricity as they do not increase in magnitude until over 40% static eccentricity. The increase in these components at the higher level of static eccentricity could be due to the interaction of the high static eccentricity with the distorted field resulting from the skimmed rotor.

The results in Figures 2.5 and 2.6 have to be really questioned as it was not truly dynamic eccentricity present due to for instance a mechanical defect like a bearing problem but was created by skimming the surface of the actual rotor. It is appreciated that there will be a very slight ovality of any rotor, however, to introduce 25% dynamic eccentricity in this fashion involved removing a relatively substantial part of the rotor core. This would have affected the rotor slots by making them more open at the slot gap, this affects the permeance due to the rotor slots and also the magnetic circuit. With less magnetic material at the teeth localised saturation would increase. As explained

later dynamic eccentricity was not introduced into the test-rig motor in this research project by skimming the rotor. Despite the unusual results of Figure 2.5, the dynamic components behave as predicted in Figure 2.6 with increasing static eccentricity.

In conclusion, in this instance, the basic pole-pair analysis carried out to calculate the pole-pairs of the flux waves at the frequencies of interest can to a certain degree provide a more thorough explanation for the experimental observations of Cameron [19]. However, this basic approach does not provide a fully accurate picture as to the pole-pairs associated with the frequency components in the flux due to inherent simplification in the analysis. This is a result of a gross simplification assumed in Equation 2.3 ( $n_s = 1$ ) and is fully explained towards the end of the next section. The next section reviews the method developed by Cameron and Thomson [22] to calculate the severity of airgap eccentricity from the current component magnitudes.

### **2.5.3 Critical Appraisal of Analysis Technique to Predict Airgap Eccentricity Level by Cameron and Thomson**

Cameron and Thomson used the rotating mmf and permeance wave approach together with empirical formulae and equivalent circuit analysis to predict the current component magnitudes as a function of the airgap eccentricity severity. The advantages and disadvantages of this approach are reviewed in this section together with the gains expected from applying a finite element analysis to the problem.

In this analysis the airgap flux density due to the stator winding was calculated using the mmf and permeance wave approach where the permeance wave expression took into account airgap factors, slotting, airgap eccentricity and saturation. The high frequency flux waves dependent on airgap eccentricity induced emf's in the rotor resulting in currents flowing in the rotor. The damping effects of these rotor currents were modelled when evaluating the resultant airgap flux waveform. The resultant high

frequency airgap flux components which are a function of airgap eccentricity induced emf's in the stator winding and using an equivalent circuit of the stator, the current components due to airgap eccentricity were calculated. The flow chart in Figure 2.7 as presented in [22] illustrates the salient points of the approach.

This method, despite limitations to be expanded upon later, provided some good agreement between predicted and measured current component magnitudes. Quantitative examples of the agreement obtained are now presented. Table 2.3 shows the difference between calculated and measured values for the principal slot passing and dynamic eccentricity frequencies with different levels of static and dynamic eccentricity as presented in [19].

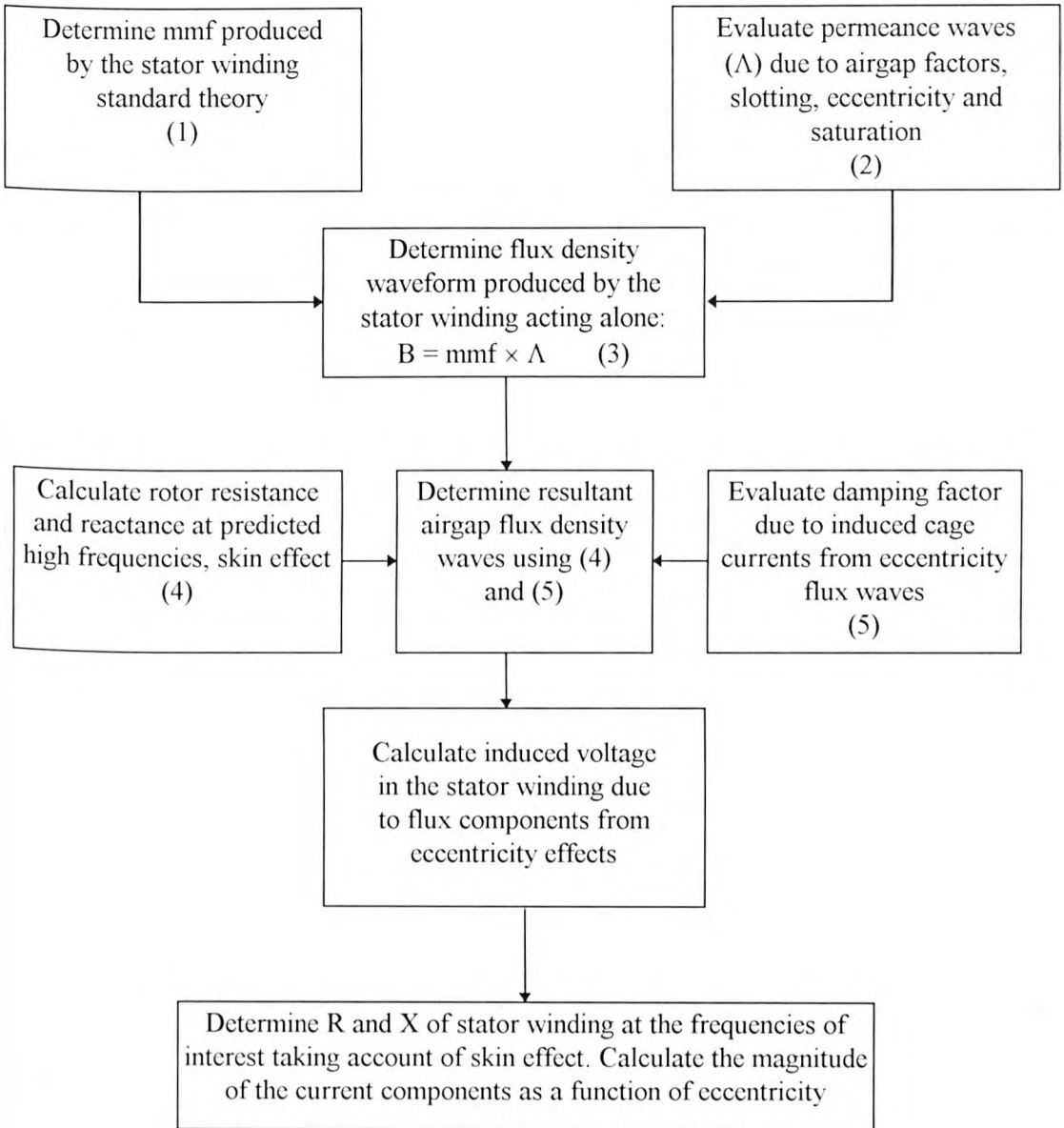


Figure 2.7 Flow Chart for Calculating Current Component Magnitudes

Frequency (Hz)	% static	% dynamic	I calculated (dB)	I measured (dB)	dB difference	% difference
1178 pspf	20	0	28.9	28.4	+0.5	+5.9
	60	0	40.1	40.3	-0.2	-1.9
1278 pspf	20	0	29.3	20.9	+8.4	+163
	60	0	40.6	29.3	+11.3	+266
1378 pspf	20	0	29.7	33.1	-3.4	-32.2
	60	0	40.9	42.2	-1.3	-13.5
1154 dynamic	0	12.5	-1.5	8.4	-9.9	-68.4
	0	25	4.6	12.4	-7.8	-60.0
1202 dynamic	0	12.5	24.6	26.5	-1.9	-20
	0	50	30.8	30.8	0.0	0
1178 pspf	20	12.5	28.9	30.7	-1.8	-18.5
	60	12.5	40.1	40.7	-0.6	-6.4
1278 pspf	20	12.5	29.3	24.4	+4.9	+76.3
	60	12.5	40.6	27.6	+13.0	+346
1378 pspf	20	12.5	29.7	27.8	+1.9	+24.7
	60	12.5	40.9	40.2	+0.7	9.0
1154 dynamic	20	12.5	4.6	4.5	+0.1	0.0
	60	12.5	15.4	22.2	-6.8	-53.3
1202 dynamic	20	12.5	17.1	27.2	-10.1	-68.5
	60	12.5	28.3	32.3	-4.0	-36.6
1254 dynamic	20	12.5	12.8	2.9	+9.9	+210
	60	12.5	23.9	24.2	-0.3	-3.5

Table 2.3 Comparison of calculated and measured current magnitudes for PSPF and dynamic eccentricity components with different levels of static and dynamic eccentricity [19]

It can be seen from the results in Table 2.3 that the analysis developed by Cameron and Thomson provided good agreement between predicted and measured current

component magnitudes for some of the frequency components. For static eccentricity variations with 0% dynamic eccentricity the most consistently close agreement was obtained for the 1178Hz component (difference less than 0.5dB), followed by the 1378Hz component (difference less than 3.4dB), and finally the 1278Hz component (difference more than 8.4dB). Cameron attributed the poor agreement for the 1278Hz component to localised saturation effects at that particular frequency which the analysis could not take into account. For the 1278Hz the analysis was over predicting the magnitude of this component, by over 8dB, compared with the experimental result. It could be that for this component the pole-pairs are not compatible with the stator winding as the basic ( $n_s = 1$ ) pole-pair analysis suggested. However, as explained later, this basic pole-pair analysis grossly simplifies the situation and it cannot be relied upon to calculate the pole-pairs associated with the static frequencies. This component may very well be compatible, however, the fact remains that these results illustrate that the classical approach cannot model all the factors accurately enough to provide a consistent level of agreement between calculated and measured current magnitudes.

Dynamic eccentricity variations with 0% static eccentricity follow the same pattern, the agreement was consistently good for the 1202Hz component but not for the 1154Hz, however, in the case (1154Hz) the calculated current was less than the measured current (by over 7.8dB). Cameron investigated possible reasons for the disagreement and localised saturation effects were one possible reason suggested which the analysis could not incorporate. To improve the agreement between calculated and measured current magnitudes Cameron tried incorporating a low level of static eccentricity into the analysis based on there being an inherent level of static eccentricity present with the dynamic eccentricity. Cameron also varied whether saturation effects were modelled or not to see what combination gave the best agreement. This was really resorting to guess work as to selecting the best permeance combination.

Combinations of static and dynamic eccentricity revealed further limitations in the analysis when both forms of the fault were considered together as the agreement for the

principal slot passing frequencies and the dynamic eccentricity components was not as good for when static and dynamic eccentricity were considered separately. The percentage difference between calculated and measured current magnitudes varied between 0% to 210%. This suggests that the analysis was predicting current components that occasionally happened to agree with the measured values.

In spite of the reasonable agreement obtained for certain components the analysis has several limitations in the representation of motor behaviour and it was never verified by application to a large, three phase industrial induction motor. The remainder of this section reviews the disadvantages of the classical analysis and how these can be overcome with a finite element analysis approach. Firstly, disadvantages effecting the current magnitude calculation are considered and then secondly factors affecting the prediction of the pole-pairs associated with the frequencies are considered.

The analysis was based on empirical formulae and techniques to represent the airgap permeance in terms of rotor and stator slotting, saturation and airgap eccentricity. The motor impedances for the equivalent circuit, the damping and skin effect factors were also computed. Locked rotor and no-load tests were performed on the test-rig motor to determine experimentally the motor parameters. These experimental values were then compared to calculated values to verify the equations used. The percentage difference between calculated and experimental values for the motor resistance and reactance was 7% and 14% respectively. This was not considered to introduce a significant error in the prediction of the current magnitudes. The method for calculating the skin effect gave good agreement between calculated and experimental tests. The accuracy of the current magnitude prediction at certain frequencies verified that the techniques used to model damping and skin effect were reasonably reliable.

When the permeance wave was computed several non-ideal assumptions and simplifications were made. Most significant of these involved the permeance variation due to saturation and slotting which will now be discussed. Saturation causes a

flattening of the airgap waveform in the region of maximum flux density [62]. This can be modelled as a fictitious radial airgap length with twice the number of poles and twice the frequency of the fundamental flux density. This gives a fully rectified sinusoidal distribution with an average value corresponding to the product of the radial airgap length and the saturation factor. The permeance of this fictitious airgap and hence saturation was derived by Fourier analysis. This model for the permeance due to saturation is approximate as the fictitious airgap length is not a true sinusoidal distribution. This is due to the saturation curve being non-linear and the saturation increasing more significantly as the flux density reaches its peak value [19]. The average value of the waveform is also dependant on the accuracy of the saturation factor used.

Airgap eccentricity leads to localised saturation in the region of the minimum airgap. This saturation region is fixed in space for static eccentricity but rotates with dynamic eccentricity. The classical approach did not take this form of saturation into account due to the complexity of modelling. A finite element analysis of a motor models the true B-H curve of the motor and therefore non-linearities are accurately modelled. Instantaneous flux densities are computed for each element in the mesh, therefore, localised saturation effects are modelled. This is one of the main advantages of a finite element approach over classical techniques.

When calculating the permeance terms due to stator and rotor slotting the work of Heller and Hamata [63] was referenced to model the variation in permeance due to the stator and rotor slots. Heller and Hamata considered the flux density to vary over a slot as shown in Figure 2.8. For constant mmf the flux density is proportional to the permeance, therefore, the permeance distribution due to slotting takes the form as that of the flux density distribution.

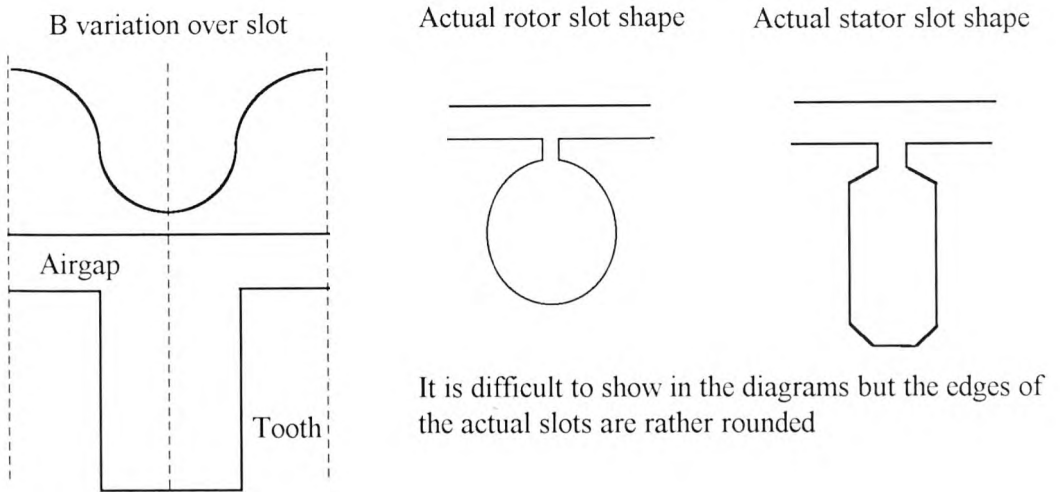


Figure 2.8 Permeance Variation over a Rotor or Stator Slot

However, the simplified slot shape used in the analysis is considerably different from the stator and rotor slots in the test-rig motor that was modelled by Cameron and Thomson. A very square sided totally open slot shape is assumed which differs from the semi-closed more rounded reality. Therefore, the slotting terms in the overall permeance wave do not include the permeance variations in the airgap due to the actual slot designs. A finite element analysis can model the actual permeance variation due to the true slot shape and not a simplified shape.

The non-representation of the true slot shape is also a drawback in Equation 2.3 for calculating the pole-pairs of the frequencies. The term  $n_s$  is the static eccentricity integer which in the basic analysis shown thus far has been equal to 1. Cameron also considered it only equal to 1. It is used to describe the permeance variation due to static eccentricity as Equation 2.4 illustrates [20]:

$$\Lambda_{se}(\theta) = \sum_{n_s=0}^{n_s=\infty} \Delta n_s \cos n_s \theta \quad (2.4)$$

where  $n_s = 1, 2, 3, 4, \dots$

Taking  $n_s = 1$  (basic analysis) models the permeance variation as if the slots were sinusoidal in shape. As  $n_s$  approaches infinity the permeance variation becomes more like that due to a square sided totally open slot (square wave shape) which is *more* representative of the true slot shape. It is therefore a gross simplification to only calculate the pole-pairs based on  $n_s = 1$  as was performed for the basic analysis. If the analysis is taken further and  $n_s = 2$  or 3 etc. it is possible for other frequency components in the flux waveform to now be compatible with the stator winding harmonic pole-pair numbers. As an example take the 1278Hz component in Cameron's results. With the basic analysis  $n_s = 1$ ,  $m = 90, 88, 18, 16$ , which was not compatible with the stator winding. With saturation also included :  $m = \underline{94}, 92, \underline{86}, 84, 22, 20, \underline{14}, 12$  which makes it compatible. This provided a plausible explanation for his experimental results as the component did not really increase significantly until very high static eccentricity levels where saturation might have an effect. However, the fact remains that the component was present in the spectrum when the basic pole-pair analysis predicted it was incompatible. It could be said that its presence was a result of winding asymmetries, however, if the pole-pair analysis is revisited with  $n_s \neq 1$  then another explanation presents itself.

If  $n_s = 2$  then the pole-pairs at the 1272Hz component are all odd:  $89 \pm 2$  and  $17 \pm 2$ , not compatible with the stator winding.

However, if  $n_s = 3$  then the pole-pairs are 92, 86, 20, 14 which are compatible with the stator winding so this component would present in the current.

If saturation is then included with  $n_s = 3$  and  $n_{sa} = 1$  then the pole-pairs are: 92, 86, 20 and 14 all  $\pm 4 = 96, 90, \underline{88}, 82, 24, 18, 16, 10$ .

So even if saturation is present at high static eccentricity levels the component is still compatible with the stator. This more in depth analysis also ties in with the experimental observations.

As discussed later, the basic pole-pair analysis ( $n_s = 1$ ) has predicted that the pole-pairs of certain flux components would not be compatible with the stator winding when they

have been clearly present experimentally. This was in another motor which was considered to be symmetrical, so second order effects would be minimal. This gross simplification in the pole-pair analysis is a major drawback. There is also the limitation when trying to calculate the pole-pairs of the static eccentricity components (principal slot passing frequencies) when static and dynamic eccentricity are considered together. This is where a finite element analysis has a significant advantage over the classical mmf and permeance wave approach. The actual slot shape is modelled and it therefore predicts the true frequency components which will be present in the current. This completely models what happens experimentally and it can also cope with combinations of static and dynamic eccentricity.

In addition to these limitations in the representation of saturation effects and actual slot shape, the classical approach required extensive design details so there is no advantage over a finite element analysis approach in this respect. The technique was not applied to a large industrial induction motor to predict the current component magnitudes. The verification of a technique on a large industrial motor is an important part of the development process [20, 21]. The finite element approach reported in this thesis has been applied to a large industrial motor.

## **2.6 Finite Element Analysis of Airgap Eccentricity**

Recently with the advent of more powerful computers finite element analysis of induction motors has become a feasible option and it has been extensively used for motor design and investigations of various fault conditions. Chapter 3 presents a brief background to finite element analysis and its application to induction motor analysis. The finite element analysis technique applied in this research is also discussed, therefore, the purpose of this section is to review the application of finite element techniques to the analysis of airgap eccentricity problems in induction motors. The following paragraphs review published literature in this area, there has not been an

abundance of work carried out on this topic hence the small number of papers discussed.

Much of the published work has concentrated on the calculation of the forces present in a motor with airgap eccentricity. As mentioned in the section on UMP a two-dimensional time-stepping finite element analysis was used by Arkkio and Lindgren [30] to calculate the UMP due to static eccentricity. The analysis based on the principle of virtual work was used to calculate the forces acting on the rotor of a 30kW 2-pole and a 15kW 4-pole motor and was verified by comparing measured and computed forces. The effects of equalising currents, slotting and saturation were taken into account in the analysis. The effect of supply frequency, loading and the level of airgap eccentricity on the UMP were investigated. Lower supply frequency caused the UMP to be larger as the flux variation was too slow to induce effective equalising currents which tend to reduce the magnitude of the UMP. The UMP was also found to increase with load and the level of airgap eccentricity.

Arkkio [64] then extended this analysis to include dynamic eccentricity, however, static and dynamic eccentricity were considered separately and the forces in the motor due to the combination of static and dynamic eccentricity were not computed. For both types of eccentricity parallel connections in the stator winding resulted in a reduction in the UMP compared to the series connected levels and this reduction was most noticeable for dynamic eccentricity. Increases in supply frequency with fixed dynamic eccentricity showed that, as for static eccentricity, the UMP decreased. An increase in the load with dynamic eccentricity initially caused the UMP to decrease and then increase slightly again, showing that the UMP was highest at starting, this was most noticeable for the 4-pole motor. Investigations into the UMP with closed and semi-open rotor slots revealed that a motor with closed rotor slots may produce a larger UMP than a motor with semi-closed slots.

Mercier et al [65] used a two-dimensional time-stepping finite element analysis to calculate the average forces in the airgap due to static or dynamic eccentricity. The analysis assumed that all the space harmonics vanish in the airgap except the fundamental. This simplified the complexity of the analysis and lead to a fast solution time. The justification provided for neglecting the other space harmonics was that machines are designed to reduce the other space harmonics and another paper by the authors showed this to be true if the winding and space harmonics are much smaller than the fundamental. This approach is satisfactory for quickly determining the principal force within the airgap, however, it could not be used to analyse the high frequency effects due to higher order harmonics. An industrial 2-pole 900kW motor was modelled and the electrical parameters obtained validated the analysis. The average airgap forces were calculated for static and then dynamic eccentricity, computed results were not compared to experimental measurements.

DeBortoli et al [66] used finite elements to investigate the effect of series and parallel connections on the airgap flux density and airgap force distribution with static or dynamic eccentricity. The finite element analysis used included the effects of induced currents, saturation, circuit coupling, an external power system, rotor motion and slotting. The classical permeance wave approach was used to predict low frequency components in the airgap flux density (less than 200Hz) and the airgap force was taken as the square of the airgap flux density. The low frequency components which they predicted were found in the FFT of the finite element computed waveform for the airgap flux density and airgap force wave. Investigations revealed that circulating currents resulting from parallel connections of the stator reduce the UMP and the harmonic components associated with it for both static and dynamic eccentricity. This correlated with the results obtained by Arkkio. The trends were also in good agreement with experimental results published by the authors in another paper. The study also showed that a finite element analysis could successfully generate the expected harmonics in the airgap flux density waveform. An attempt was not made to predict the

eccentricity level from the magnitude of these flux density or force wave frequency components.

Salon et al [67], also part of the group with DeBortoli, used the same finite element analysis technique to investigate the effect of stator and rotor ovality on the airgap flux density and magnetic force waves. The classical permeance wave approach was used to modify the airgap permeance taking into account stator or rotor ovality. The flux density was taken as the product of the mmf and permeance wave and unique components due to ovality were predicted. The finite element analysis was applied to models of the motor with a round stator and rotor, an oval rotor and then an oval stator. These components due to ovality were not present in the FFT of the flux density computed by the finite element analysis for the round rotor/stator model, however, they were present when rotor or stator ovality was introduced. A similar trend was observed with the predicted components in the airgap force waveform. The components in the airgap flux density and airgap force waveform were primary harmonics of 200Hz or less. The finite element analysis was used to look at the relative effects of ovality on induction motor behaviour and an attempt was not made to predict the degree of ovality from the magnitudes of the components.

## **2.7 Conclusion**

The literature review revealed that the presence of airgap eccentricity can be detected by on-line current monitoring and that by classical techniques it is possible to predict the magnitude of some of the current components as a function of the airgap eccentricity severity. However, this analysis has several limitations in terms of further investigating airgap eccentricity. Specifically, due to simplifications in the classical analysis, more realistic modelling of the stator winding, saturation and the actual slot designs is not possible. This limits the application of the analysis to very basic attempts at predicting the current component magnitudes as a function of the airgap eccentricity.

A finite element analysis does not have to rely on permeance wave and pole-pair analysis to predict which frequencies components will induce current in the stator winding. By detailed modelling of the motor by finite element analysis the pole-pairs of the flux waves in the airgap are calculated along with the stator winding harmonic pole-pairs and the stator winding factors. The finite element analysis therefore correctly predicts which frequency components will appear in the current spectrum. This overcomes the gross simplifications that the pole-pair analysis makes when calculating the pole-pairs of the flux waves associated with the airgap eccentricity frequencies.

As explained in the previous section a finite element analysis models saturation effects more realistically and localised saturation effects can be computed. The actual rotor slot shape is modelled allowing investigations into the effect of different rotor slot designs and the numbers of rotor bars on the current components which are a function of airgap eccentricity. A literature survey revealed that finite elements had been applied to problems like the optimum rotor slot shape for maximum efficiency, however, they have not been used to investigate the effect of different rotor slot designs and numbers of rotor bars on the current components. This work is presented in Chapter 6 where the papers covered by the literature survey are discussed.

The classical approach will still be used to calculate the frequency components (Equation 2.2) and the pole-pairs associated with them (Equation 2.3) to compare the pole-pair analysis results with the finite element analysis. The finite element analysis will also be used to bring out the limitations of Equation 2.3 for calculating the pole-pairs associated with the frequency components. This research focuses on the high frequency current components due to rotor slotting and airgap eccentricity. It was decided not to investigate the low frequency rotational speed frequency components (25, 75 Hz) which are more prone to load effects. Thomson [68] showed that these components can also be affected by shaft misalignment. In addition these components can easily be hidden in an FFT spectrum due to skirting effects around the high 50Hz component. Although this is not a problem for a high quality industrial spectrum analyser, it was uncertain at

the onset of the project if the MATLAB based FFT programs to be written to process the finite element generated emf / current signal would be able to achieve this degree of signal processing.

The literature search has revealed that finite elements have been used to model airgap eccentricity, however, they have not been used to predict the magnitudes of the frequency components in the current spectrum which are a function of rotor slotting, saturation and airgap eccentricity for either a small test-rig motor or a large, industrial motor. The effects of rotor slot design and rotor bar number on these components have not been investigated using finite elements. These are the principal objectives of this research project as outlined in Chapter 1.

# Chapter 3

## Finite Element Analysis of the Test-Rig Motor

### 3.1 Introduction

This chapter presents a brief background to finite element analysis. The finite element analysis software used in this research work is discussed together with the two types of analysis available; fixed mesh and time-stepping. The motor design details and experimental tests performed to calculate the motor parameters required for the finite element solution are presented. Initial results using the fixed mesh and then the time-stepping finite element analysis are presented with a discussion on the relative merits of each. This research is based on the application of a finite element package to model an induction motor. A finite element method has not been developed, consequently, an in-depth discussion of finite element theory in this chapter was deemed to be inappropriate.

The application of finite element analysis to engineering problems is relatively recent and can largely be attributed to the aeronautical industry of the 1950's [69]. Finite elements were applied to structural analysis problems in aircraft and the work of Turner et al [70] really heralded the start. As explained shortly, finite element analysis involves

large algebraic problems and hence requires substantial computational power. In the early days of the 1950's only the large aircraft companies had main frame computers to work through the solution and the relatively slow spread of such a versatile technique to other areas can be attributed to the non-availability of fast, economic, computational power. Today this is increasingly less of a problem with workstations now capable of running finite element packages. However, for some more complex problems, especially 3-dimensional modelling, the time and money involved in the computational aspect is still a prohibitive consideration until the next generation of computers arrive. Work by Zienkiewicz and Cheung [71] introduced finite elements to electrical engineers in the 1960's. Finite element analysis has been applied to induction motors for the last fifteen years and over the last five years has been taken on board by motor manufacturers [1]. In today's highly competitive market the edge provided by finite element analysis to design more efficient, quieter and more robust motors is considerable and finite element analysis is seen as a productivity enhancing tool [72].

The basic theory behind finite elements is the assumption that any continuous function over a global domain can be approximated by a series of functions operating over a finite number of small sub-domains. These series of functions are piecewise continuous and approach the exact solution as the number of sub-domains approach infinity [73]. The global domain (e.g. cross section through a motor or a mechanical structure) is divided into sub-domains called elements, the points defining and connecting the elements are called nodes. The function that exists over the domain is explicitly solved for all the nodal points and the value of the function inside the elements is defined in terms of the element's nodal variables. This makes finite elements particularly useful for the analysis of fields. Originally these types of problems were described using differential equations but due to their complexity only simple geometric shapes could be analysed. However, with finite elements the difficulty of mathematically solving large complex geometric problems is transformed from a differential equation approach to an algebraic problem, wherein the finite elements have all the complex equations solved for their simple shape (e.g. triangle). The differential equations describing the variables

within an element are transformed to matrix form and is now a linear algebraic relation and not a differential equation. The entire problem can be cast as a larger algebraic equation by assembling the element matrices within a computer in much the same way that the real problem is built with many simple pieces of material [69]. These basic concepts can be applied to electromagnetic fields and hence the application of finite element analysis to electrical machine design and analysis.

In addition to airgap eccentricity analysis, finite elements have been applied to virtually every other area of motor design and analysis that had once been solely the domain of classical techniques or impossible to model classically. These areas are not relevant to the work of this thesis so a very brief resumé of selected papers from the literature review is given to gain an appreciation of the wide spread use of finite element analysis. Motor faults such as broken rotor bars [74] and phase failure conditions [75] have been modelled. A considerable amount of work has focused on the design aspect of induction motors. For instance, finite elements have been used to calculate the equivalent circuit parameters [76], the resistance and inductance of the end rings [77], [78] respectively. Losses have been estimated including resistive and eddy current loss [79] and saturation effects have been investigated [80, 81]. Finite elements have also been used to investigate the optimum rotor slot shape and the effects of slot shape on harmonics, these papers are reviewed in detail in Chapter 6.

Finite element methods applied to induction motor analysis are based on the same fundamental principles. They differ in the way the rotor movement is incorporated and how the rotor currents are calculated. Basically there are two types of solution available; fixed mesh where the rotor is fixed in space and time stepping where rotor movement is incorporated. The rotor currents can be calculated by either an eddy current or a circuit model for both forms of rotor movement. Williamson [82] presents an excellent review of the theory behind the different methods available for induction motor analysis. Two finite element methods were used in this research project. Initially a fixed mesh model using an eddy current model to calculate the rotor currents was

used. An early result using this method is presented then the limitations of the method compared to a time stepping approach are discussed. The results presented in this thesis are based on a time stepping method using an eddy current model to calculate the rotor currents.

The finite element packages used in this research have been developed by the collaborating company. A selection of the papers published on the development of these methods will be reviewed. It is appreciated that others have taken the fundamental principles and developed finite element methods. However, the research presented in this thesis has not involved the development of a finite element method but the application of methods already developed. Therefore, a review of published literature on finite element methods was deemed irrelevant. The reader is directed to Williamson's review paper [82] for references to other finite element methods.

The methodology behind the fixed mesh analysis that was initially used to model airgap eccentricity is outlined by Parkin et al [83]. The method used was based on a 2-dimensional finite element current formulation linked to an external circuit to enable the solution to be driven from a constant voltage source. All functions are assumed to vary sinusiodally with time. This results in a fixed value of permeability for each element in the model. To obtain an average reluctance through the time cycle, the permeability of each element is based on the peak flux density. This value was calculated from an a.c. B-H curve. End effects are modelled by increasing the conductivity of the rotor bars to include the effects of temperature and the rotor end-rings. The stator end-winding is included in the external circuit linked to the finite elements using a value of the stator end-winding leakage reactance. The stator resistance is also included in this external circuit. Both these values are per phase. The method was validated by modelling test - rig motors ranging from a few hundred watts to tens of kilo-watts and good agreement was obtained between experimental and modelled values of stator current and torque/speed. The time stepping method is described in [84]. It was also driven from a constant voltage source. Rotor movement was incorporated by restitching the rotor and

stator meshes in the airgap at each new position of the rotor with the stator remaining stationary. The method was successfully validated on induction motors used in rail traction applications. There are significant advantages of a time stepping formulation compared to the fixed mesh approach which will be expanded upon later in this chapter.

### **3.2 Generation of the Finite Element Model of the Test-Rig Motor**

The fixed mesh and the time-stepping formulations both required a 2-dimensional cross sectional model of the motor. The 2-dimensional cross section was known as the finite element mesh and in it were defined nodes at positions relating to the motor dimensions. Other nodes were positioned within the mesh to ensure well shaped elements between the nodes. The optimum shape was a triangle with sides of equal lengths and in areas such as the tooth tips and the airgap more nodes and hence elements were defined to give as accurate a representation of the flux distribution as possible. The number of nodes used had to be considered in terms of the mesh size and consequent processing time. Figure 3.1 shows the distribution of nodes in the mesh for the test-rig motor. The mesh contained 6406 nodes and 11,105 elements. In order to define the material properties of the various parts of the motor each element was assigned a label. For instance, all the elements in the airgap were given material label 'A' and the magnetic properties of that label were defined in the control files as those of air. Appendix 1, Sections A1.1 to A1.4 detail all the motor dimensions used to generate the finite element mesh. The phase bands of the stator winding were also defined in the mesh using labels R, r, Y, y, B, b, this defined the direction of the current flow in the stator winding and also the direction of the rotating magnetic field.

The software also required control files which contained motor parameters such as supply voltage, number of poles, stator and rotor winding design, speed of operation and the material label properties. The type of solution and program outputs required were also specified. The finite element analysis calculated a program output for each node and element in the mesh. These outputs, for example, were the magnetic vector

potential, current density and eddy current loss. Post analysis software allowed these outputs to be displayed on top of the mesh. For example, as shown later, a flux plot could be obtained for the motor. In addition to these features the time-stepping analysis outputted a file containing the data points for the variation in stator current and stator emf with time. It was these outputs that were utilised in this research to investigate the frequency components of interest. Results for this will be shown later. The next section details the calculations and experimental investigations undertaken to acquire the motor parameters for the control files. Early results using the fixed mesh and the time-stepping methods are then presented.

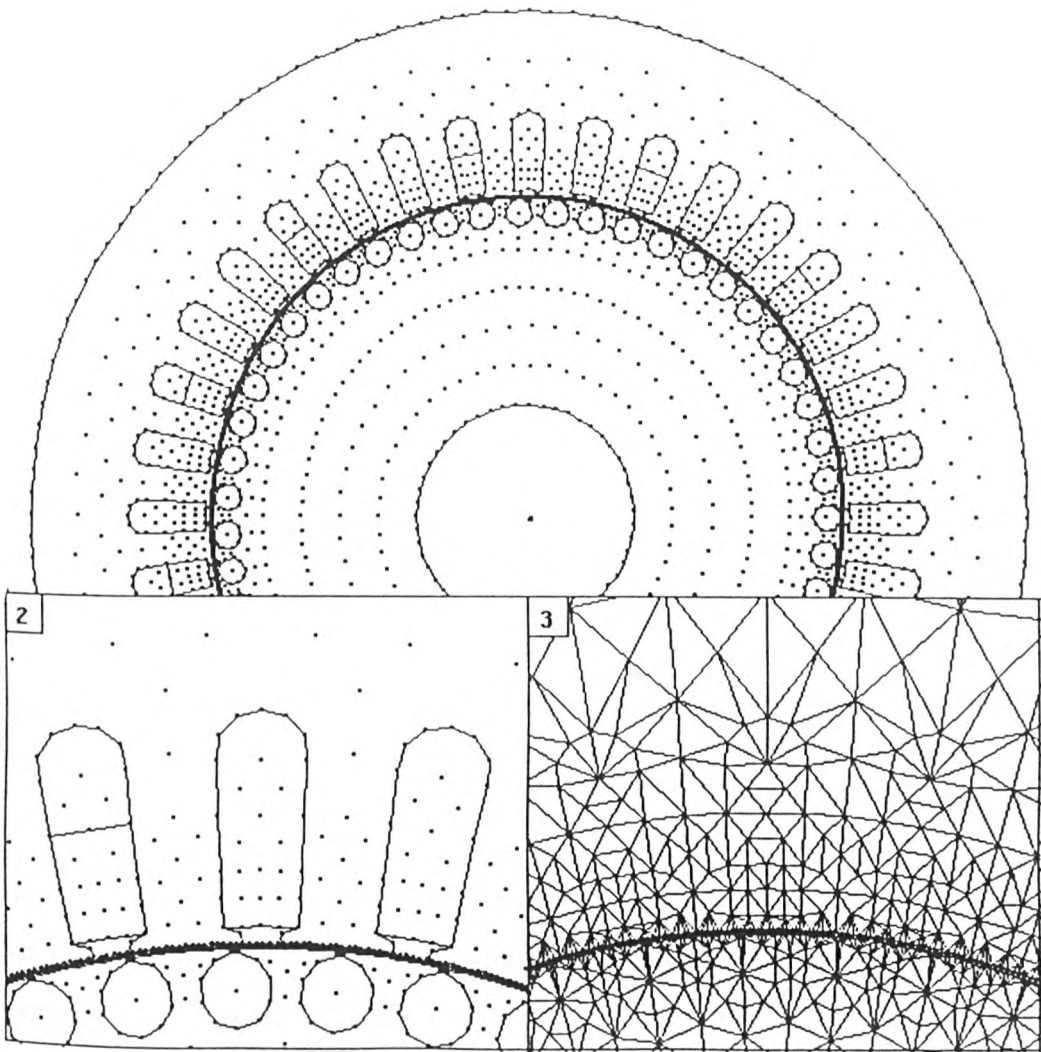


Figure 3.1 Finite Element Mesh of Test-Rig Motor

### 3.3 Determination of Test-Rig Motor Parameters

#### 3.3.1 Test-Rig Motor Specification

The complete test-rig motor specification including winding and distribution factors can be found in Appendix 1, however, the main parameters are shown in Table 3.1.

Parameter	Value
Power	11 kW
Frequency	50 Hz
Phase	3
Line Voltage	415 V
Full load current	20 A
Speed	1420 rpm
Poles	4
Connection	delta
Airgap length	22 thou $\pm$ 2 thou (0.56mm $\pm$ 0.05mm)
Number of stator slots	36
Number of rotor slots	51
Skew	none

Table 3.1 Test- Rig Motor Specification

The motor was rated at 415V line for a delta connection of the phases, however, the vast majority of large high voltage induction motors are connected in star hence the laboratory test-rig motor was connected for this mode of operation. This resulted in the motor operating at reduced voltage and power, however, the results were perfectly valid as the full load current was still being circulated. The test-rig motor had 240V

phase (415V line to line) applied in a star connected configuration which resulted in a full-load current of 11.5A at a speed of 1322 rpm. An unskewed rotor was used, again to model as closely as possible the configuration of larger motors. The rotors used by Cameron were both skewed so his results would have been affected as skew is introduced in a motor to reduce the magnitude of high frequency fluxes. The specially fabricated unskewed copper rotor had been previously designed and fabricated in house as reported in [85]. The rest of the test-rig had been constructed using parts provided by a manufacturer, e.g. the stator core assembly, 51 slot rotor laminations, rotor shaft etc. The stator in this motor was exactly the same as that used by Cameron, hence, values of stator parameters he calculated were referenced. The airgap length was nominally 22 thou, however, a  $\pm 2$  thou tolerance existed when the rotor was in the motor. The gap was measured using feeler gauges at both the drive and non drive end of the test-rig and at N, S, E and W positions. The airgap length measured varied from 21-22 thou, therefore, including an error in measurement of at least 1 thou the resultant tolerance was  $\pm 2$  thou. The copper rotor was also found to expand in diameter with prolonged running especially with high airgap eccentricity levels adding to the heating effect. This further reduced the airgap length and did effect the magnitudes of the current components, this is discussed later.

Static and dynamic eccentricity were introduced into the test-rig motor in a controlled fashion. Shims of known thickness (11 thou for 50% static) were inserted between blocks on the base plate and the feet of the stator frame. This offset the stator core by a certain amount therefore introducing static eccentricity. Dynamic eccentricity was introduced by fitting heat shrink collars to the rotor shaft where it sat in the bearings. These collars were then skimmed on one side so that when rolling in the bearings the offset introduced caused the rotor to trace out a path which resulted in a rotating minimum airgap. This modelled dynamic eccentricity due to a mechanical problem, for instance bearing wear. This was a more realistic modelling of the condition compared to skimming the actual rotor as performed by Cameron which would effect the magnetic symmetry of the rotor.

### 3.3.2 Locked Rotor and Open Circuit Tests

This section presents the results of locked rotor and open circuit tests to calculate the motor parameters required for the finite element solution. Reference [86] was used for calculating the parameters from the test results. (The individual equations in this process have not been assigned numbers as they were too numerous and were not referenced again. Non standard equations which were referenced within the thesis such as for the referred rotor resistance and the stator end-winding leakage reactance have been assigned numbers). The locked rotor and open circuit tests and the performance tests carried out to validate the equivalent circuit developed were carried out for the motor in delta connection with 415 V line to line. The parameters derived are no different from those if the tests had been carried out in star as the full load current was circulated in each case.

#### *No-Load Test Results*

The exact equivalent circuit on no-load was used since the stator resistance  $R_1$  and the stator reactance  $jX_1$  were obtained experimentally and calculated from design details respectively. An accurate stator resistance measurement was made when the motor was at normal operating temperature ( $80^\circ\text{C} \pm 2^\circ\text{C}$ ). Values of motor resistance required by the finite element analysis had to be the resistance value at operating temperature, not  $21^\circ\text{C}$ , as the finite element analysis could not incorporate temperature effects. The value of stator resistance was  $2\Omega \pm 0.01\Omega$ . The value of the stator inductance had been calculated from design details by Cameron [19] using well established empirical methods. The value obtained was  $j2.27\Omega$ . Cameron validated all his calculated equivalent circuit parameters by experimental investigations. He found that calculated and experimentally derived resistances differed by 7% and calculated and experimentally derived reactances differed by 14%. Also taking into account the accuracy of certain predicted current component magnitudes these factors suggested that Cameron's calculated values for the required parameters such as  $jX_1$  could be used with reasonable

confidence. Appendix 2, Section A2.1 details of the calculation performed to acquire the no-load equivalent circuit parameters. Values obtained were  $R_1 = 2\Omega$ ,  $jX_1 = 2.27\Omega$ ,  $R_c = 513.14\Omega$  and  $jX_m = 63.86\Omega$ .

### ***Locked Rotor Test Results***

A locked rotor test was performed with measurements taken per phase and the results are shown in Appendix 2, Section A2.2. The motor was known to be slightly unbalanced between phases hence the reason for testing each phase. The temperature of the motor during these tests was normal operating temperature  $80^\circ\text{C} \pm 2^\circ\text{C}$ . This meant that the value of effective rotor bar conductivity calculated from  $R'_2$  incorporated the effects of temperature. This conductivity is calculated in the next subsection. Appendix 2, Section A2.2 details the calculations performed to acquire the locked rotor equivalent circuit parameters. Values obtained were  $R'_2 = 2.254\Omega$ ,  $jX'_2 = 1.615\Omega$ .

### **3.3.3 Performance Tests for Equivalent Circuit Validation**

To verify the accuracy of the above equivalent circuit, performance tests were carried out at different loads and the measured values of parameters like the input power, current and power factor were compared to calculated values using the equivalent circuit. The calculation for full load using the equivalent circuit is presented in Appendix 2, Section A2.3. The calculated values were then compared to the measured values. A summary of calculated and measured values for full load is shown in Table 3.2. The same process was carried out at different loads and the comparison of calculated and measured results for input power, current and power factor are shown in Figures 3.2 to 3.4.

Parameter	Calculated from Equivalent Circuit	Measured Experimental	Difference	% Difference
Input Power	11.94 kW	11.775 kW	165 W	1.4
Input I (phase)	11.5 A	11.05 A	0.45 A	3.9
Input I (line)	19.92 A	19.14 A	0.78 A	4
power factor	0.834 lag	0.86 lag	0.026	3

Table 3.2 Summary of calculated and measured values for full load condition

The results calculated using the equivalent circuit are reasonably accurate with the percentage differences between calculated and measured values relatively low (below 4%) in comparison to experimental uncertainties in reading meters and meter accuracy. For example, the measured phase current was 11.05A. A combined meter and reading error of 0.25A was present which was 2.3%. Indeed, later experimental results measured 11.5A for the full load current using the same meter. The validation of the equivalent circuit was important as the value of referred rotor resistance  $R'_2$  was used to calculate a value of effective rotor bar conductivity for the finite element analysis.

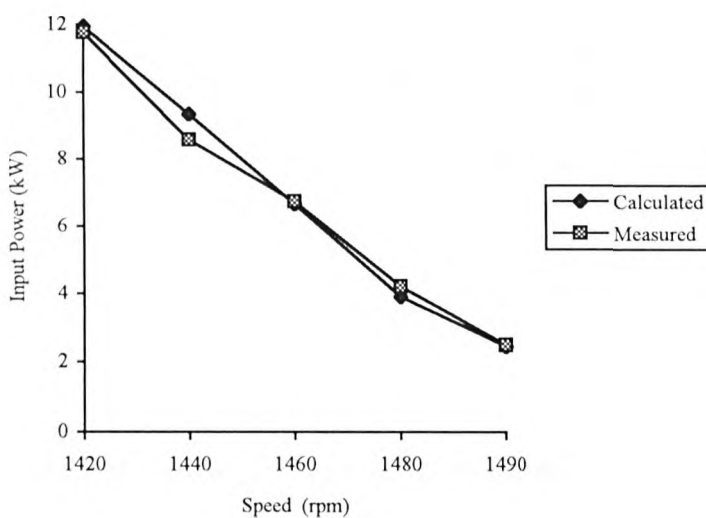


Figure 3.2 Comparison of Calculated and Measured Input Power

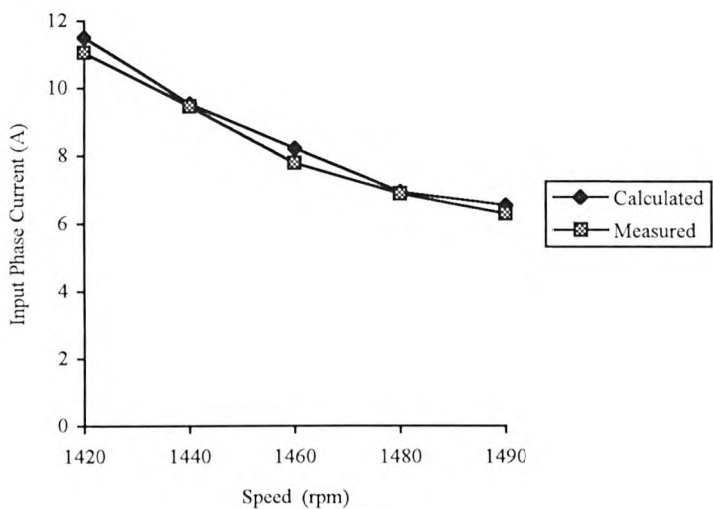


Figure 3.3 Comparison of Calculated and Measured Input Phase Current

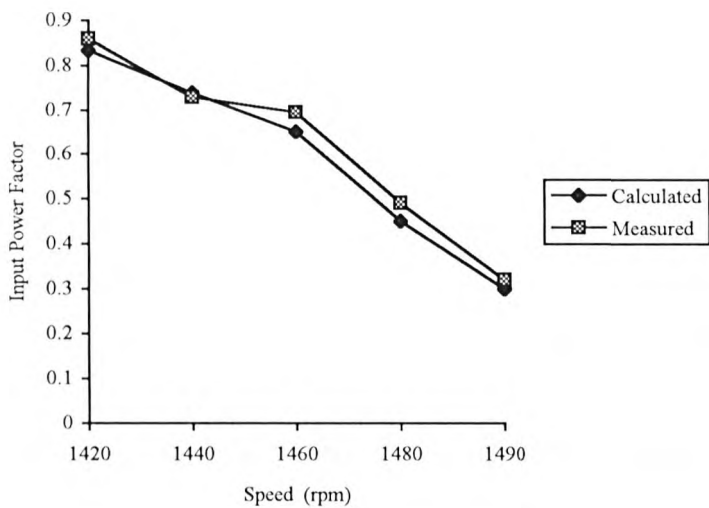


Figure 3.4 Comparison of Calculated and Measured Input Power Factor

### 3.3.4 Rotor Bar Conductivity Calculation

The finite element analysis required a value for the effective rotor bar conductivity. This had to include the 3-dimensional effects of the end-rings as only a 2-dimensional finite element analysis was performed. The value of rotor bar conductivity entered into the analysis had to be increased to give an effective value for rotor bar conductivity taking into account the end-rings. The value entered also had to relate to the value at the operating temperature of the motor. As explained earlier that was the reason for performing the locked rotor tests with the motor at normal full load operating temperature. Equation 3.1 [88] was used to calculate the effective rotor bar conductivity.

$$R'_2 = \frac{12(k_p k_d T_{ph})^2}{R} \left\{ r_{be} + \frac{R}{2p^2 \pi^2} r_e \right\} \quad (3.1)$$

where  $k_p$  = coil pitch factor = 0.9848

$k_d$  = distribution factor = 0.96

$T_{ph}$  = turns / phase = 180

$R$  = number of rotor bars = 51

$r_{be} = r'_{be}$  = effective rotor bar resistance

$p$  = pole pairs = 2

$r_e$  = end-ring resistance

$R'_2$  = referred rotor resistance = 2.254  $\Omega$  from locked rotor test

By equating the end-ring resistance to zero in this equation the value of  $r'_{be}$  calculated included the resistance of the end-ring. From this effective bar resistance the effective rotor bar conductivity was calculated taking account of end-ring effects as required by the finite element analysis. This calculation is shown in Appendix 2, Section A2.4.

The value obtained was  $1.115 \times 10^7$  S/m and was the value used for the effective rotor bar conductivity in the finite element analysis. Originally the standard science data book value of conductivity for copper was used with temperature effects taken into account. At that stage a method to accurately include the effects of the end-ring into the rotor bar conductivity had not been decided upon. It was not thought that the end-winding would make a huge difference so for the first run the standard value of conductivity of copper ( $5.8 \times 10^7$  S/m), recalculated at  $80^\circ\text{C}$  ( $4.42 \times 10^7$  S/m) was used. The first run would confirm if the high frequency components were being modelled and that the mains current was not of a ridiculous value, the current calculation could then be refined. This value of conductivity resulted in the phase current calculated by the finite element analysis being too high. It was discovered that the main cause of the problem was that soft soldered joints at the joints between the bar ends and the end-rings were increasing the resistance of the rotor considerably. This is discussed in more detail in Section 3.5 which details early problems and results using the time-stepping model.

### 3.3.5 Stator End-Winding Leakage Reactance

The stator end-winding leakage reactance was required for the finite element analysis in order to calculate the stator current resulting from the airgap emf. A circuit diagram explaining where this parameter was used is presented in Section 3.5. The section solely details the calculations performed. To obtain as realistic a value as possible was very important as it had direct bearing on the magnitude of the current components. This was particularly the case at the high airgap eccentricity frequencies where the inductive reactance  $X_L = 2\pi fL$  was larger. As mentioned earlier this test-rig stator was the same as that used by Cameron, therefore, his calculations could be referenced. He calculated the stator slot and stator end-winding leakage reactance using a method developed by Kostenko and Piotrovsky [89]. This approach calculated the permeance of the stator slots and the stator end-winding as seen by the leakage flux. These permeance coefficients were then summed and applied to another Kostenko and Piotrovsky equation to calculate the total reactance for the stator slot and stator end-winding. This

method was reapplied to confirm Cameron's value for the permeance term for the stator end-winding and then to calculate the reactance for only the stator end-winding. As Cameron showed [19] the permeance coefficient for the stator end-winding can be calculated from Equation 3.2:

$$\lambda_{es} = 0.57 \frac{d\tau_p}{l} \left( \frac{3\phi - 1}{2} \right) \quad \text{where} \quad \tau_p = \frac{2D}{2p} \quad (3.2)$$

where:

$\lambda_{es}$  = permeance coefficient

d = number of slots/pole/phase = 3

$\tau_p$  = pole pitch

$\phi$  = winding pitch = 8/9

l = axial length of stator core = 0.146m

p = pole pairs = 2

D = stator core bore = 0.1662m

Substituting these values gives a value of the permeance coefficient for the stator end-winding of  $\lambda_{es} = 1.27$ .

The reactance is obtained from Equation 3.3:

$$X_e = \frac{4\pi\mu_o T^2 \ell}{pd} \sum \lambda_{es} \quad (3.3)$$

$X_e$  = Stator end-winding leakage reactance

f = frequency = 50Hz

T = turns/phase = 180

l = axial length of stator = 0.146m

p = pole pairs = 2

d = number of slots/pole/phase = 3

$\Sigma\lambda$  = sum of permeance coefficients (Only the stator end-winding was of interest  $\lambda_{es} = 1.27$ )

Substituting these values gives  $X_e = 0.78\Omega$  as  $X_e = 2\pi fL$  then the stator end-winding leakage inductance = **2.5mH**. Reasonable confidence could be assumed with this value as mentioned earlier as Cameron did verify the accuracy of his calculated motor parameters experimentally. However, it was decided to investigate another method to calculate the stator end-winding leakage reactance as a comparison. The Kostenko and Piotrovsky method is a simplified approach which had the advantage of not requiring extensive design details. The stator flux was solely considered and no account was taken of rotor end-ring to stator end-winding mutual flux. The finite element software did not model the interaction of flux between the stator and the rotor end-rings, therefore, to include this effect in the value of the stator end-winding leakage reactance used in the finite element analysis would model the end-winding leakage effects more accurately.

A review was carried out of techniques to calculate the stator end-winding leakage reactance. The calculation of this parameter has been the focus of considerable research. The majority of early methods, pre-finite elements, used classical techniques and empirical approximations, Barnes [90] presents a review of these traditional techniques as does Lloyd et al [91]. These techniques are all based on a permeance expression approach along the same principles as the Kostenko and Piotrovsky technique. Honsinger [92] adopted a different approach in that the inductance of the end-winding was computed directly. The end-winding field was defined in three dimensions with boundaries representing the frame etc. Volume integrals were used to relate the inductance to the potential within the boundaries. More recently finite elements have been used to calculate the end-winding inductance (stator and rotor). A 3-dimensional model of the entire end region was developed by De Weerd [93] and the inductance calculated by evaluating the stored energy in the model.

A finite element analysis approach to calculate the stator end-winding leakage reactance was not a practical option as a 2-dimensional or 3-dimensional finite element study would be a project within itself. Therefore, the classical techniques were considered. It was decided to use the method proposed by Alger, the derivation of which is presented in [62]. This method is often used by electrical machine designers in industry. This approach also took into account the mutual flux between the stator and rotor end-rings, however, the disadvantage was that extensive end-winding design details were required. The end-winding leakage flux was resolved into axial and radially directed components in order to simplify the analysis. The two components were then summed to compute the resultant field. The reactance was then calculated from the current and induced voltage in the end-winding. The equation proposed by Alger is shown below (Equation 3.4):

$$X_{es} = \frac{1.84qN_1^2 K_{p1}^2 K_{d1}^2}{P^2 10^6} \times \left\{ D_1 \log \frac{0.695D_1}{r_1} - D \log \frac{0.541D}{R} \right\} + \frac{2fqD_1 N^2 K_d^2 \tan \alpha}{P^2 10^6} \left\{ \left( \frac{p\pi - \sin p\pi}{\pi} \right) \left( 1 - \left( \frac{0.8D_2}{D_1} \right)^P \right) \right\} \quad (3.4)$$

where

$$Y_1 = \frac{\pi p D_1}{8P} \left( 1 + \frac{P^2}{5} \right) \tan \alpha \quad \text{and} \quad R = \sqrt{[0.25(D_1 - D_2)^2 + (Y_1 - Y_2)^2]}$$

$$r_1 = \frac{1}{2} \text{ depth of stator slot}$$

The motor dimensions described in this equation can be found in Appendix 1, Section A1.5. The only new terms not previously defined are:  $q$  = number of phases = 3 and  $p$  = pitch factor = 8/9. In this equation  $P$  = pole-pairs. The term on the left hand side of the plus sign is the peripheral end-winding leakage reactance and the term on the right is the end-winding leakage reactance produced by axial end currents. The disadvantage in Alger's analysis was in the definition of the angle  $\alpha$  used in determining the stator end-winding leakage reactance. This angle defined the angle at which the coil bends towards the coil end. Alger's analysis was based on a coil shape that differed somewhat from the actual coil shape in the test-rig motor end-winding as shown in Figure 3.5. The shape of the test-rig motor coil was obtained by tracing out the path of a coil with a

length of wire and then marking out the bend of the wire on paper. The diamond shape end-winding assumed by Alger clearly defined  $\alpha$ . The value chosen for this angle had a considerable effect on the reactance value calculated.

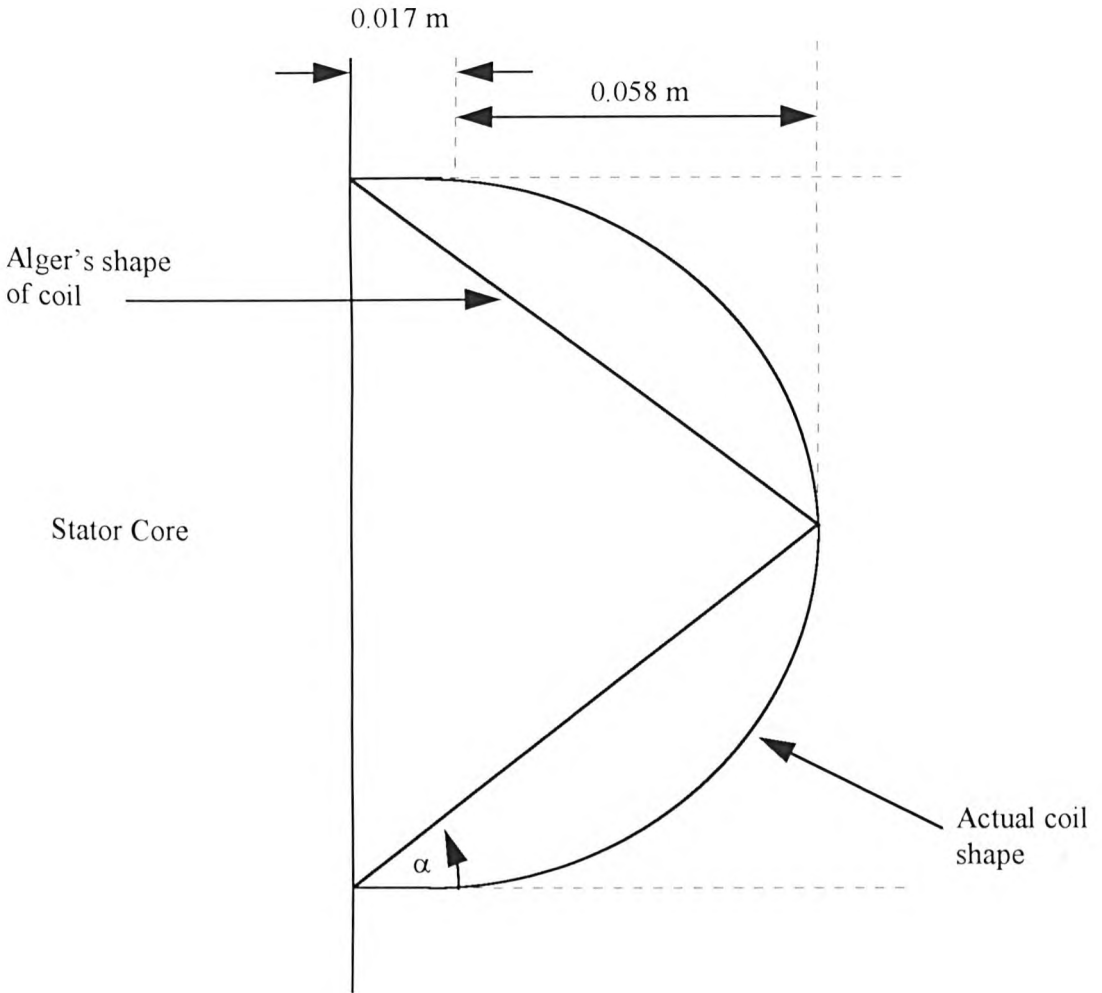


Figure 3.5 Definition of the Angle of Bend  $\alpha$  of the Stator End-Winding Coils

With reference to Figure 3.6 the angle is important in the calculation as it determined the proportion of axial and radially directed flux at each point along the coil. For instance in the region marked X in Figure 3.6 the angle  $\alpha = 0$  there was no axial flux component in this region. By using a protractor to measure the angle of bend of the

test-rig motor coil it was decided that a value of  $\alpha = 30^\circ$  was a reasonable estimate of the average angle of bend. It is appreciated that this introduces an error into the calculation of the end-winding leakage inductance.

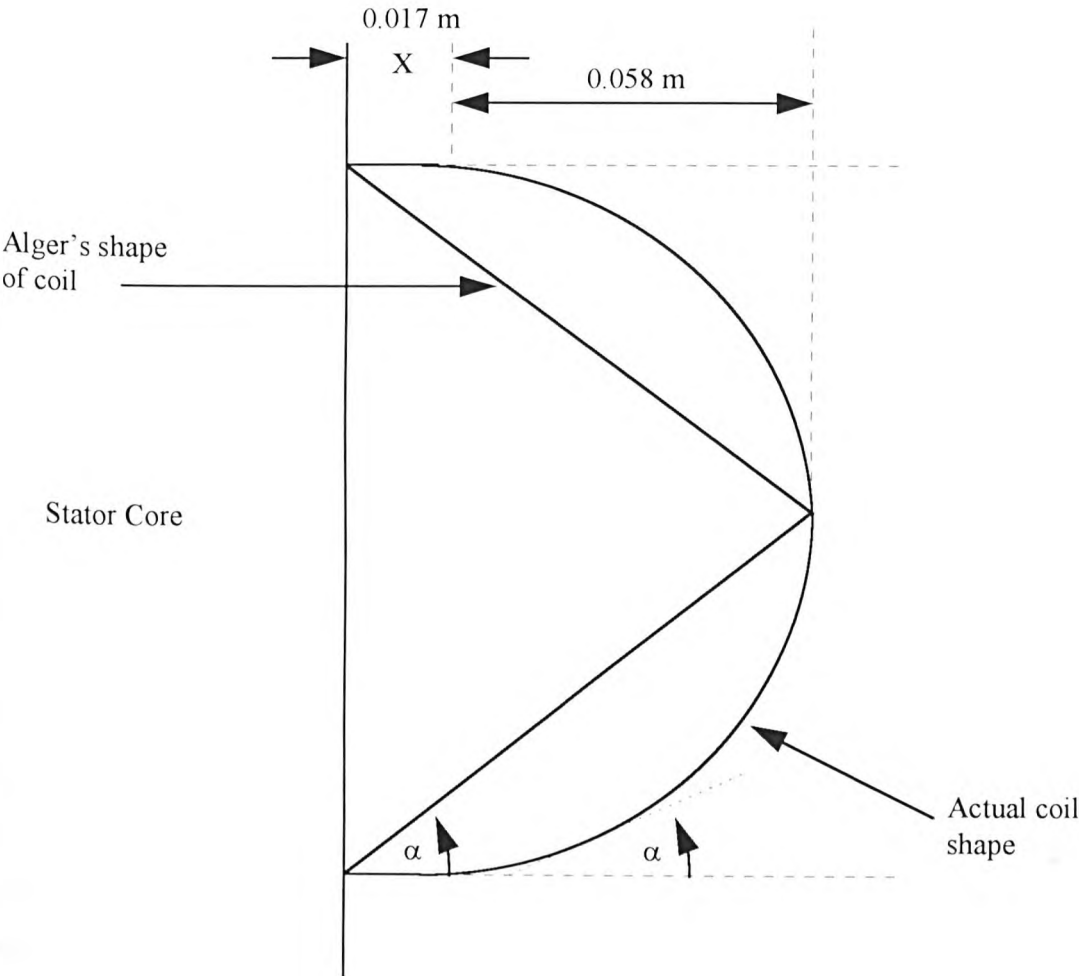


Figure 3.6 Selection of the Angle of Bend  $\alpha$  for the Test-Rig Motor Coil

Table 3.3 shows the inductance value calculated for the chosen value of  $\alpha$  and other values to provide an idea of the error introduced by the selection of the angle.

Value of $\alpha$ ( $^{\circ}$ )	$L_{es}$ (mH)
20	1.22
25	1.33
<b>30</b>	<b>1.45</b>
35	1.60
40	1.90

Table 3.3 Effect of  $\alpha$  on the Value of  $L_{es}$

As can be seen from Table 3.3 that the value of stator end-winding leakage inductance was considerably less than was calculated by Kostenko and Piotrovsky method, 1.45 mH compared to 2.5 mH. The lower value obtained via Alger's method was attributed to the difference in the test-rig motor coil shape compared to that assumed by Alger. In addition to the uncertainty for the best value for  $\alpha$  an error was also introduced as the straight part of the test-rig motor coil (region  $x = 0.017\text{m}$  in Figure 3.6) was not included in the analysis. In this region an additional flux due to peripherally directed components of the end-winding current was present and there was no axial flux in this region. The peripherally directed flux in this region increased the value of the stator end-winding inductance, however, by not including it the calculated inductance value was lower. It was decided to use 2.5mH as calculated by the Kostenko and Piotrovsky method in the finite element analysis. This value could be assumed to be reasonably accurate as Cameron verified by experimental tests that the difference between the calculated and measured total motor reactance was 14%. If the unrealistic scenario of all this error being associated with the stator end-winding leakage reactance was taken then the value of inductance was  $2.5\text{mH} \pm 3.5 \times 10^{-4} \text{ mH}$  which was a relatively small error.

### 3.4 Initial Finite Element Result using the Fixed Mesh Model

Initially a fixed mesh solution was performed. Rotor movement was not incorporated during the analysis so the solution obtained was for one position of the rotor and one instance in time. Two meshes of the motor were created, one for a concentric motor (uniform airgap) and a second for the test-rig motor with 40% static eccentricity. The static eccentricity was introduced into the model by moving the stator away from the centre axis of the motor. Figures 3.7 and 3.8 show the plots of the variation in magnetic vector potential for a concentric airgap and the motor with 40% static eccentricity, respectively. The plots were interpreted, in that where there were more lines of magnetic vector potential and they are closer together then the flux density was greater. Therefore, in Figure 3.7 with the uniform airgap the flux was distributed uniformly over the four poles of the motor. However, in Figure 3.8 where the minimum airgap was at the 3 o'clock position there was clearly more flux flowing. This is expected as the side of the minimum airgap offers the path of least reluctance to the flux. This was a very early result which confirmed that the finite element software was capable of modelling the effects of static airgap eccentricity on the motor.

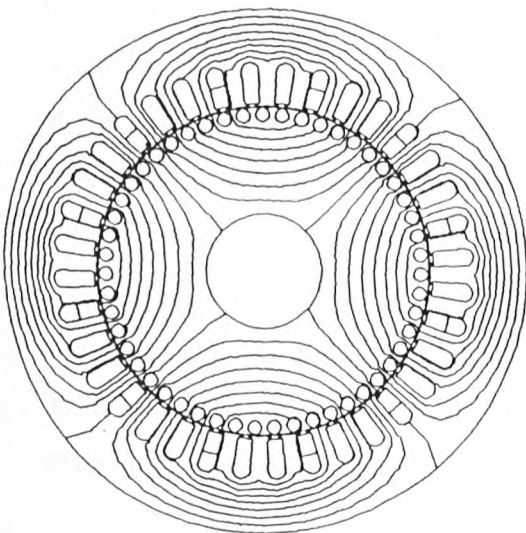


Figure 3.7 Distribution of Flux for the Motor with 0% Static Eccentricity

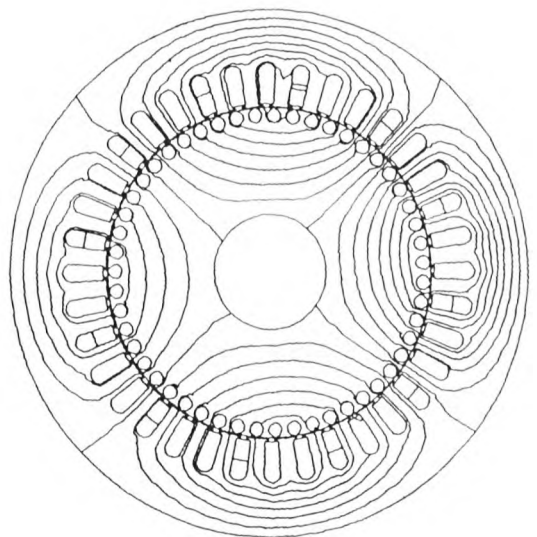


Figure 3.8 Distribution of Flux for the Motor with 40% Static Eccentricity

These investigations also showed that the fixed mesh analysis was not capable of modelling the motor to the sophistication required to properly investigate airgap eccentricity. In reality this fact was already known without carrying out these investigations, however, at that point in time the University had not received the time-stepping package. There were considerable advantages with a time-stepping finite element analysis in comparison to a fixed mesh solution. The most important of these was the automatic incorporation of rotor movement in the solution. In this research work the objective was to produce a frequency spectrum of the airgap emf and motor current signals generated by the finite element analysis. This required a continuous time series of points to make up a waveform to perform an FFT. The only practical method of doing this was by a time-stepping formulation with each point in the waveform relating to a new position of the rotor. There was of course the penalty of the CPU time to perform a full finite element analysis at each time-step, however, there were other significant advantages as outlined below [82].

With a fixed mesh model in order to incorporate rotor movement via slip frequency transformations, variables (e.g. flux) are assumed to vary in time sinusoidally. The drawback of this is that magnetic saturation is accounted for using localised values of reluctivity that are time averaged. By redoing the finite element analysis at each position of the rotor sinusoidal variation of the field quantities does not have to be assumed. Therefore, instantaneous values of reluctivity are used rather than time averaged values. Airgap permeance variations due to slotting, the movement of the rotor teeth past the stator teeth, are included in the time-stepping field model. This was of considerable importance in this work as the frequency components of interest were a function of both static eccentricity and rotor slotting. The next section details the time-stepping analysis of the test-rig motor.

## 3.5 Initial Time Stepping Analysis of the Test-Rig Motor

### 3.5.1 Procedure

A time stepping analysis of the test-rig motor resulted in two time domain waveforms; the motor phase current and the induced stator emf. The induced stator emf is the voltage across the stator as if the winding was open circuited. For both signals the stator winding factors have been taken into account. The current can be calculated from the stator emf by applying it to an equivalent circuit modelling the stator resistance and end-winding leakage inductance. An FFT algorithm in a mathematical package was the basis of software developed to produce the frequency spectrums of the finite element generated time domain phase current and induced emf. The induced emf was used to calculate the magnitude of the fundamental and airgap eccentricity current components and the current signal was used to verify the magnitude of the 50Hz component calculated from the emf signal. The procedures for these calculations are now explained.

#### *Current Spectrum:*

In Figure 3.9, similar to that presented in reference [84], the procedure to obtain the current spectrum is shown. The finite element analysis computes the airgap emf which is then applied to the equivalent circuit modelling the stator resistance and the stator end-winding leakage reactance to calculate the current. Software was developed by the author based on MATLAB to perform and display the current spectrum. The frequency and dB scaling were set to exactly model the spectrum produced on the test-rig motor current by the calibrated laboratory spectrum analyser. This resulted in the dB current magnitudes of the finite element current being directly comparable with the dB magnitude of the test-rig motor current components. The development and testing of this software is described in Chapter 4. The software was thoroughly tested using MATLAB to ensure that the magnitudes and frequencies displayed in the spectrum

were representative of the original time domain signal. This testing eliminated the FFT software as a potential problem if the finite element results were not as expected and was therefore very important.

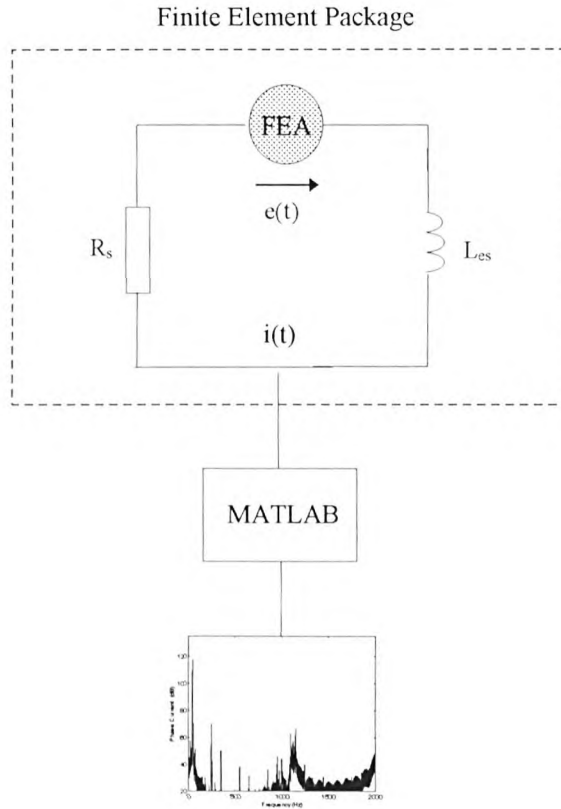


Figure 3.9 Procedure to Obtain the Current Spectrum from the Finite Element Analysis

*EMF Spectrum and Calculation of Current Component Magnitudes*

In this case the stator emf spectrum was obtained from an FFT of the time domain emf signal generated by the finite element analysis, Figure 3.10. To calculate the magnitude of the current at any of the frequencies of interest the specific components were identified in the emf spectrum. The emf magnitude in volts was then applied to the equivalent circuit modelling the stator to calculate the magnitude of the current at those

frequencies. The principle of superposition was used to calculate the current magnitude for each frequency component in turn. At the high frequencies of interest the supply voltage source was effectively a short circuit and it was only the stator emf which drove a current at the frequencies due to airgap eccentricity. An example of this calculation is presented later.

The time domain stator emf signal was scaled down by a factor of 2000 and a reference of  $10^{-6}$  applied to display the spectrum in dB. To compute the magnitude of any component in volts the reverse process was applied. This scaling was chosen only on the bases of displaying the spectrum on a sensible scale. Unlike the current the emf spectrum from the finite element analysis was not being compared to experimental results from the test-rig motor.

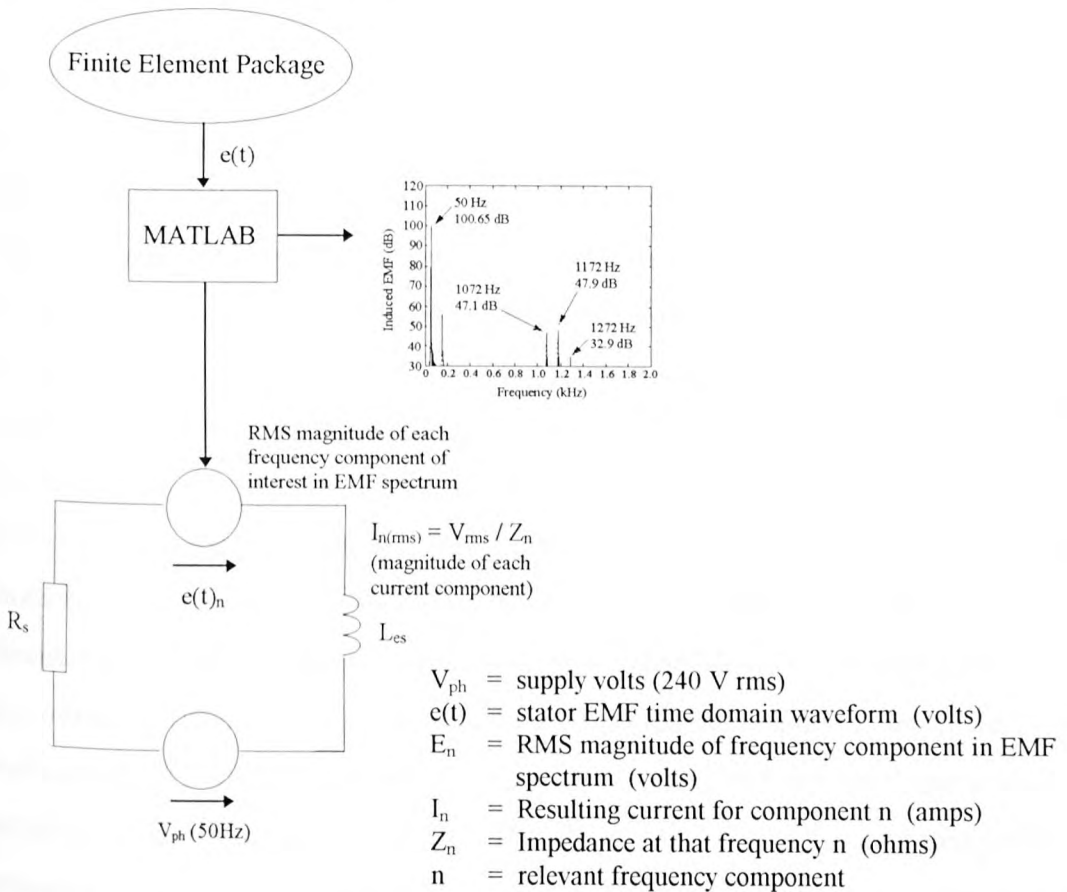


Figure 3.10 Procedure to Obtain the EMF Spectrum from the Finite Element Analysis and Calculate the Current Component Magnitudes

### 3.5.2 Initial Time Stepping Analysis, Problems and Conclusion

The purpose of initial solutions using the time stepping analysis was to get the calculated fundamental current at the same value as measured on the test-rig motor. The current and the emf were also checked to ensure that the expected airgap eccentricity components were present in the spectrums predicted by equations 2.1 and 2.2. They also provided an opportunity to fine tune the spectrum analysis software for the best spectrum possible. The length of the timestep, that is, the time between each finite element solution and hence the number of points making up a cycle of current or emf in the time domain was investigated. The value used was important and a compromise between a short enough timestep to model the high frequency permeance effects and CPU time had to be reached.

For a more conventional analysis where only stator quantities would be of interest a timestep of 0.002s was recommended by the package developers. This would result in each cycle of emf/current having ten points. However, to include high frequency effects like permeance variations a much shorter timestep was required. A value of  $7.843 \times 10^{-5}$  s was initially used resulting in each cycle of emf/current containing 255 points, that is, 5 solutions per rotor slot tooth. This was less than a suggested value of approximately 15 solutions per rotor tooth, However, these early runs were mainly to check that the finite element analysis was modelling the motor correctly (correct 50Hz magnitude) without taking too long to solve. Investigations with shortening the timestep length, as described later, were performed after the analysis was confirmed to be working. Five timesteps per rotor tooth was considered more than adequate initially to model the permeance variations. It must be mentioned that the developers of the finite element software (GEC Alstom, Engineering Research Centre) had not used the package to model an induction motor in this way. Therefore, there was no predetermined optimum timestep length already established other than less than 0.002s. This meant that to a certain degree it was only as the runs were performed that information was obtained to decide on the best timestep length.

The first time stepping solution was of a mesh of the test-rig motor with 5% airgap eccentricity. A good result was obtained with the frequency components predicted by equation 2.1 present in the emf. The magnitude of the fundamental 50Hz in the current spectrum was equivalent to 15.8A, higher than the 11.48A measured on the test-rig motor spectrum. Investigations led to the main cause of the difference being due to the value of conductivity used for the rotor bars. This had a significant effect on the value of the current. The value of the stator resistance and the stator end-winding leakage reactance were also important in determining the current magnitude, especially the inductance at the high frequencies which were a function of airgap eccentricity. However, as explained earlier reasonable confidence was had with the values calculated for these parameters and at 50Hz the stator end-winding leakage inductance was relatively small. For instance, as  $L_{es} = 2.5\text{mH}$  then at 50Hz,  $X_{les} = 0.78 \Omega$  whereas at 1072Hz,  $X_{les} = 16.8 \Omega$ . The focus of investigation was therefore the rotor bar conductivity.

The copper cage had been fabricated in house some years previously from copper bars and end-rings. Investigations discovered that the bars had been joined onto the end-rings by using soft solder joints. It had not been possible to apply enough heat to use hard solder. These soft solder joints were effectively increasing the resistance of the rotor cage. Initially the standard data book value for the conductivity of copper corrected for temperature effects had been used in the finite element analysis. This value was not a true reflection of the conductivity of the rotor bars as the effect of the soft solder joints on the conductivity was not taken into account. The resistivity of soft solder is  $15 \times 10^{-8} \Omega/\text{m}$  this is significantly higher than  $1.7 \times 10^{-8} \Omega/\text{m}$  for copper. By using the value of referred rotor resistance from the locked rotor test and Equation 3.1 it was possible to recalculate a value for the conductivity of the rotor bars taking into account the effect of the soft solder joints, temperature and the end-ring. This calculation was explained in Section 3.3.4.

The recalculated value of effective conductivity for the rotor bars was  $1.115 \times 10^7 \text{ S/m}$ , considerable less than the  $4.42 \times 10^7 \text{ S/m}$  originally used. This explained how the

calculated 50Hz component of current was larger than the experimental. The original higher value of conductivity resulted in the resistivity being lower and therefore the rotor resistance being lower. For the same supply voltage this resulted in the higher current flowing. The analysis was rerun with the new value of conductivity and the magnitude of the 50Hz component was now 11.3A (121dB) which was deemed to be in agreement, within experimental errors, with the experimental value of 11.48A (121.2dB). Note: These figures are for the 50Hz component in the current spectrum and cannot be directly compared to the current meter readings as the meter measured the magnitude of the harmonic current components in addition to the 50Hz.

To further investigate how inaccurate the standard value of conductivity of copper was, the referred rotor resistance was calculated using design details and the standard value for the conductivity of copper. Using the rotor dimensions shown in Appendix 1, Section A1.3 the resistance of the bars and the end-ring were calculated using the resistivity value obtained from the standard value of conductivity for copper. This calculation is shown in Appendix 2, Section A2.5. The value obtained was  $0.79\Omega$  at  $21^{\circ}\text{C}$ , by using Equation A2.2 [94] this was transferred to  $80^{\circ}\text{C}$  to be comparable with the value from the locked rotor test. This resulted in a value of  $1.04\Omega$ . By using the standard value for the conductivity of copper the referred rotor resistance of  $1.04\Omega$  was considerably less than the  $2.254\Omega$  obtained from the locked rotor test, therefore, confirming that the soft solder joints were dramatically increasing the rotor resistance.

During these investigations the same procedure was repeated for the 51 bar cast aluminium rotor that was also used within the Department. The referred rotor resistance measured from a locked rotor test was  $1.9\Omega$ . This was obtained from another test-rig motor with the aluminium rotor. Using the rotor dimensions and the standard conductivity value for aluminium the bar and end-ring resistance was calculated. The referred rotor resistance was then calculated using Equation 3.1 and found to be  $2.14\Omega$ . Both values were at  $80^{\circ}\text{C}$ . This investigation increased confidence in the equation to calculate the referred rotor resistance and also confirmed the effect of the soft solder

joints on the copper rotor, that is, with a cast aluminium rotor (no joints) the standard conductivity value for aluminium can be used.

After the mains current was of the correct magnitude it was decided that the motor parameters entered in the finite element analysis were sufficiently representative of the test-rig motor and with the 50Hz component at the expected level the airgap eccentricity components would also come into line. The only parameter in which accuracy would be more apparent at the higher frequencies was the stator end-winding leakage reactance which resulted in a higher inductance value at the higher frequencies compared to at 50Hz. The accuracy of this was investigated as various finite element solutions were performed with different levels of static/dynamic eccentricity and the calculated current magnitudes compared to the magnitudes obtained experimentally. It was found that the value used was accurate as good agreement was obtained between experimental and predicted current magnitudes.

The timestep length and the length of continuous data (continuous cycles of I/emf) were investigated to optimise the quality of the FFT whilst minimising the CPU time required to complete a solution. CPU power and time were limited so after the initial runs to verify the mains current it was decided to only halve the timestep to  $3.952 \times 10^{-5}$  s, that is, 510 solutions per cycle or 10 solutions per rotor tooth. The timestep of  $7.843 \times 10^{-5}$  s provided a reasonable spectrum and all the expected high frequency components were modelled. However, it was thought that by halving the timestep again that the resulting spectrum would be much sharper as a result of the improved sampling frequency. This did result in excellent spectrum quality as seen in the results sections. To decrease the timestep further was deemed unnecessary in terms of spectrum quality and would have resulted in runs having taken more than the approximate two weeks already. Reducing the timestep from  $7.843 \times 10^{-5}$  s to  $3.952 \times 10^{-5}$  s did not affect the magnitude of the components displayed in the spectrums.

Investigations were also carried out on how to further reduce CPU time by taking x cycles of continuous current/emf and then copying the x cycles and adding them into

the end of the first  $x$  cycles. The same record length as before could be obtained without the same CPU time penalty. Intensive tests were carried out using MATLAB to ensure that the accuracy (frequency and magnitude) of the FFT spectrums were not adversely affected by this procedure. Chapter 4 details the FFT software development and testing.

These early results confirmed that the parameters inputted to the finite element analysis were correct, that the airgap eccentricity components were being modelled and they provided an opportunity to fine tune the FFT software. After this the finite element analysis was used to model the test-rig motor with varying degrees of static and/or dynamic eccentricity. These results were then compared to the magnitude of the components measured experimentally. The limitations of the pole-pair analysis for predicting the pole-pairs associated with the frequencies were also further investigated using these results. This part of the research is presented in Chapter 5.

# Chapter 4

## Signal Processing Software Development

### 4.1 Introduction and Specification of Spectrum Plot

This chapter summarises the work carried out to develop an accurate procedure for the spectrum analysis of the induced airgap emf or phase current signal produced by the time stepping finite element analysis. This software was based on the FFT algorithms in Matlab, a computer based mathematical package. At the time this software was developed it was unknown if the finite element analysis would model the frequency components of interest, this would only be discovered after a complete run of the test-rig motor had been performed and the FFT software had been written. It was therefore important that the software based FFT process was capable of accurately processing all the possible components that should appear. This would eliminate Matlab as being the problem if these components did not appear in the emf/current spectrums or if their magnitudes were not at the expected level. Consequently, the signal processing software was thoroughly tested to ensure its correct operation by processing Matlab generated signals composed of known frequency and magnitude. At the time of developing this software, before the finite element package was fully investigated, it was thought that the FFT would be applied to only the current signal. In the explanations in this Chapter the current signal is considered, however, the emf had the

same FFT procedure applied to it other than the pre-FFT scaling which did differ from the current. The processing of both signals was thoroughly tested.

To allow the resulting spectrum plots for the experimental and modelled currents to be directly compared, the plot produced by Matlab had to be the same as that produced by the laboratory spectrum analyser in terms of the range of frequency components shown and the magnitude (rms values on a dB scale). The following sections describe how this was achieved. As explained in Chapter 3, the induced airgap emf spectrum was displayed on an arbitrary but sensible scale as a direct comparison with the airgap emf from the test-rig motor was not required. As the development stages progressed various limitations of the FFT algorithm became apparent. The FFT algorithm distorted the magnitude of components in the spectrum and skirting effects severely affected the performance. The investigations into these problems and their solutions are also presented.

The FFT had to be capable of displaying components up to 2000Hz with a resolution of 0.25Hz to reproduce the specification of the laboratory spectrum analyser. In reality such a fine resolution was not required as the components of interest were never closer than  $\approx 25\text{Hz}$  apart. The FFT also had to process components which could be up to 80dB down on the fundamental component, that is, possess a dynamic range of 80dB. The spectrum had to be displayed on a dB scale to allow the small airgap eccentricity components to be visible on the same spectrum as the 50Hz component. The test-rig motor current was monitored via a clip on current transformer (CT) with a linear output of 0.1V/A. Therefore, a 15A phase current produced an output voltage of 1.5V from the CT. A reference voltage of 100mV = 100dB was applied to display these voltages on a dB scale. The software in Matlab also had to process the current signal in this manner by multiplying it by 0.1, converting each peak value to rms and applying the same reference voltage. This process led to a direct comparison of the experimental and modelled current spectrums. The emf values were divided by 2000, converted from

peak to rms and then the same reference of 100mV = 100dB was applied. This resulted in the dB display scale as shown on the emf spectrums later in the thesis.

## 4.2 Investigation of the Matlab FFT Function

Matlab had a built in function that performed a Fast Fourier Transform [96]. The FFT function employed a radix-2 fast Fourier Transform algorithm if the length of the data sequence was a power of two, and a slower mixed-radix algorithm if it was not. The number of points (N) in the FFT could be specified using  $y = \text{fft}(x,N)$ . If the data sequence  $x$  was less than N, the FFT padded  $x$  with trailing zeros to length N. If the length of  $x$  was greater than N, the FFT truncated the sequence  $x$ . As described below, it was advantageous to be able to set N to a specific value, so it was decided to use the above form of FFT compared with  $y = \text{fft}(x)$  in which Matlab set the value of N. To avoid the data being truncated the number of points in the FFT was always greater than the number of data samples. The frequency resolution of the spectrum, i.e. the frequency between each line in the plot was defined by the Equation 4.1, [97].

$$\Delta f = \frac{f_s}{N} = \frac{1}{T} \quad (4.1)$$

where  $\Delta f$  = frequency resolution

$f_s$  = sampling frequency of data

N = number of points in FFT

T = total record time of data

From this equation it can be seen that if the sampling frequency of the data was predefined (due to the time-stepping software), then the ability to control N was vital if a specific resolution was required. If the FFT function had to add zeros to the end of the data then the total record time also increased thus the above equation always remained true.

The operation of the FFT function and the presentation of the resulting spectrum plots were investigated. A simple sine wave was generated and an FFT applied to it. A frequency axis was produced and the magnitude of the frequency components graphed. This procedure is explained in more detail with the program code shown in Appendix 3, Section A3.1. The spectrum generated by this code is shown in Figure 4.1.

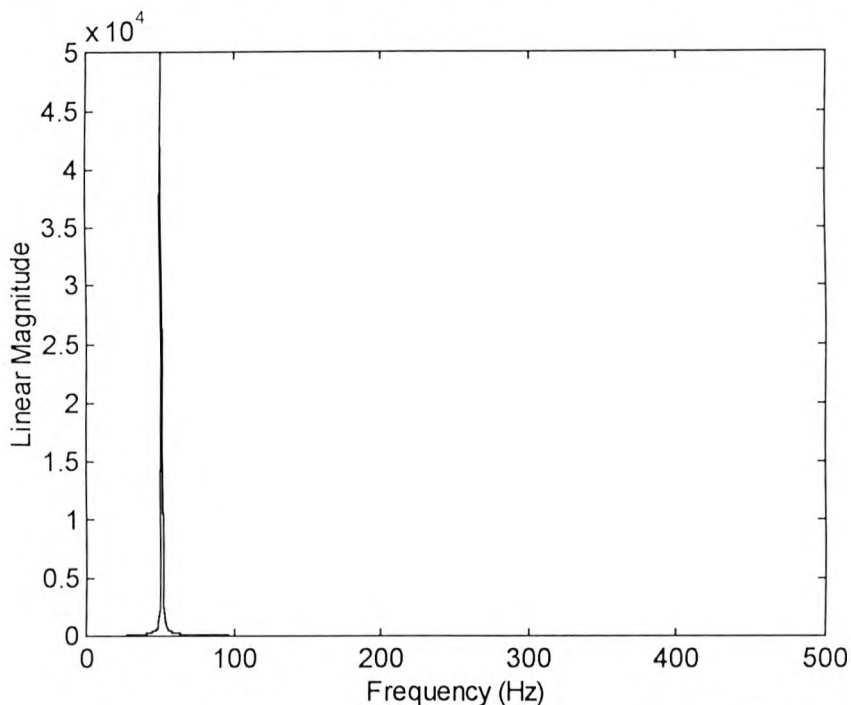


Figure 4.1. Spectrum of a 50 Hz Sine Wave with Peak Mag. of 100 ( $\Delta f \approx 1$  Hz)

Only the first half of the spectrum was displayed (up to 500 Hz) this was because the FFT algorithm produced an amplitude spectrum which was symmetrical about harmonic  $N/2$  [98]. All the signal components were fully represented in an amplitude spectrum plotted up to harmonic  $N/2$  and it was unnecessary to plot further points.

At this point it was observed that the FFT was distorting the magnitude of the frequency components displayed by defaulting to a large linear scale. The magnitude scaling of the components produced by Matlab was meaningless, the magnitudes being much larger than the magnitude of the original signal. The next section discusses the

effects noticed and the software written to compensate for the distortion of the component magnitudes.

### 4.3 Correction of Component Magnitudes in the Spectrum

#### 4.3.1 Investigation of Magnitude Distortion by Matlab FFT

As Figure 4.1 shows, the original magnitude of 100 was increased by the FFT algorithm. The signal (50 Hz sine wave peak magnitude 100) was transformed using FFTs of various lengths  $N$ . This revealed that the magnitude of the component in the resulting spectra depended on the number of points in the FFT. The number of points ( $N$ ) in the FFT was then kept constant and signals of the same frequency but different magnitudes were transformed. It was noted that the multiplying factor applied to the magnitude of the signal was constant as Table 4.1 illustrates.

$f = 50 \text{ Hz}$

Mag. of Original Signal	Mag. Displayed on Plot	Multiplying Factor
100	10,000	100
200	20,000	100
300	30,000	100
400	40,000	100

Table 4.1. Estimation of Multiplying Factor at Constant Frequency & Different Magnitudes

Several signals of different frequencies but constant magnitude were then transformed. The effect on the magnitude was not constant as Table 4.2 illustrates.

Magnitude = 200

Frequency of Signal	Mag. Displayed on Plot	Multiplying Factor
50	20,000	100
500	19,500	97.5
1000	18,500	92.5
1500	17,000	85

Table 4.2. Estimation of Multiplying Factor at Constant Magnitude & Different Frequencies

These investigations showed that if the multiplying factors could be calculated then the magnitudes obtained in the plot could be divided by these factors to return them to their original size. This would therefore provide a proper spectral display, i.e. for a 50 Hz sine wave of peak magnitude 100 one would expect to see a peak in the spectrum at 50 Hz and magnitude 100 as a rms conversion was not performed. These conversion factors would operate for that size of FFT (N). They would have to be recalculated if N changed as earlier investigations revealed that the magnitudes in the plot were affected by the length of FFT used.

#### 4.3.2 Development of Program to Calculate Factors for Component Magnitude Correction

The aforementioned investigations revealed that the conversion factor changed with frequency but stayed constant for any magnitude at any one frequency. With this in mind a program was written which calculated the conversion factors for each frequency of interest in the spectrum plot. Since the set of conversion factors was different for different lengths of FFT, at this point a value of N was selected for experimental purposes. It was decided to process a data sequence sampled at  $f_s = 5000$  Hz,  $\Delta f = 0.25$  Hz  $\therefore N = 20,000$ . It was thought that 0.25 Hz was more than adequate resolution

considering the closest components would be 25 Hz apart and initially it was thought that 5000 samples in the emf/current signals from the finite element analysis was realistic.

The methodology behind the program for calculating the factors is now explained before the code is presented. When a sine wave of a certain frequency was Fast Fourier Transformed then the resulting spectrum plot had one peak at that frequency as Figure 4.1 illustrated. By finding the value of that peak and dividing it by the original magnitude the conversion factor was found. It was then possible to change the frequency of the wave, Fast Fourier Transform it, find the size of the peak in the spectrum plot at this new frequency and calculate the conversion factor for this frequency. By doing this for all the frequencies of interest the conversion factors were calculated and stored in a matrix. They could then be applied to the magnitude values in the plot to return them to the correct size.

The values could be calculated for the range of frequencies displayed in the spectrum and at the intervals defined by  $\Delta f$ . For this case the range would be 0 - 2000Hz at 0.25Hz intervals. Therefore, a conversion factor was calculated for each line in the spectrum, so the values of magnitude due to the analysis of any signal could be divided by the corresponding factor for that line to calculate the original magnitude which was then displayed.

It had to be remembered when applying an FFT to the signal of interest to have the same sampling frequency for the data and the same number of points  $N$  so that  $\Delta f$  was the same as that used for calculating the conversion factors. This ensured that the conversion factors consecutively corresponded to each line in the plot therefore allowing the data to be divided by the conversion factors point by point.

The code shown in Appendix 3, Section A3.2 generates the conversion factors for a spectrum where  $N = 20,000$ ,  $f_s = 5000$  Hz and  $\Delta f = 0.25$ . This resulted in a matrix of

length  $8001 \times 1$  containing the conversion factors. Another short program was written to apply the conversion factors to the magnitudes of a spectrum plot (contained in matrix 'Plot') to return them to their original values and display the spectrum on the correct frequency scale. This code is shown in Appendix 3, Section A3.3.

Tests were performed to verify the correct operation of the program. The original signal of Figure 4.1 was transformed and the correct plot displayed (peak of magnitude 100 at 50 Hz as expected). At this point signals were generated which modelled the type of signal that the test-rig motor and hopefully the finite element analysis would generate. The expected frequencies and magnitudes appeared in the spectrum which verified that the program for generating and applying the conversion factors was working. These signals contained components of high magnitude with sidebands which were of low magnitude in comparison; a factor of 100 or more down on the magnitude of the larger components. With the spectrum shown on a linear scale it was impossible to display such a plot in a manner similar to the commercial analyser which was clear to see. To check the magnitude of the smaller high frequency test components the linear scale was zoomed into. The next section describes how the linear plot was converted to a dB display. There also seemed to be considerable skirting in the plot. It was decided to investigate this after the dB conversion had been performed in case this might reduce it.

#### **4.4 Display of Spectrum on a dB Scale**

As mentioned in Section 4.1, the current signal was multiplied by 0.1 (CT output 0.1V/A), converted to rms and the reference chosen for the dB scale was selected to be the same as the analyser, i.e.  $100\text{dB} = 100\text{mV}$ . After the signal was FFT and the corrected magnitudes for the plot calculated they were transformed to a dB scale using Equation 4.2.

Since  $100\text{dB} = 100\text{mV}$

$$100 \text{ dB} = 20 \log_{10} \frac{100 \text{ mV}}{V_{ref}} \quad (4.2)$$

$$\therefore V_{ref} = 10^{-6}$$

When  $V_{ref}$  was known the equation could be used to calculate the dB magnitude of any linear component. A small program was written to implement this equation on the values in the matrix containing the magnitudes as shown in Appendix 3, Section A3.4. This was applied initially to a simple sinewave and the correct magnitude at 50Hz was displayed. However, there were still the degrading effects due to excessive skirting (picket fence effect), as Figure 4.2 illustrates.

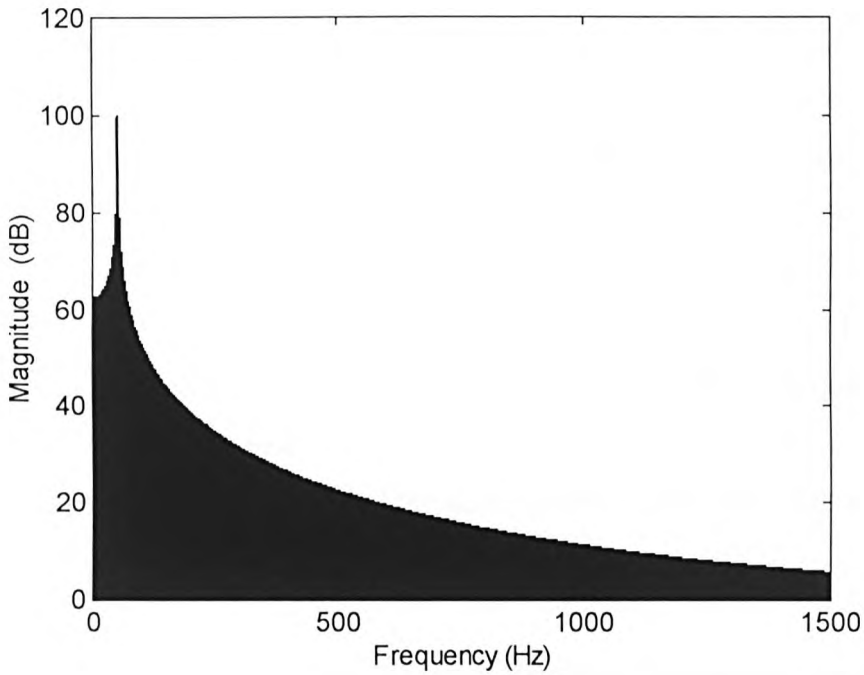


Figure 4.2. Spectrum of 50 Hz Sine Wave Magnitude 10A

A huge skirt was present around the component which extended up the frequency range which would have affected the display of components in this region. Smaller components due to slotting and airgap eccentricity could have been hidden by the skirt.

A procedure was required to remove the skirting to allow components to be displayed with minimum interference. The next section describes the solution obtained.

## 4.5 Application of Windows to Reduce Skirting Effects

Signal processing techniques were investigated [97, 98, 99] which highlighted that the skirting could be reduced by applying a window to the data in the time domain before the FFT. The sampled data values were multiplied point by point by the sampled values of the selected window function. The skirting or picket fence effect was an unavoidable limitation of FFT analysis. It occurs when a component in the signal falls between two adjacent frequency lines in the spectrum. Its energy is shared between neighbouring harmonics and nearby spectral amplitudes are distorted.

Various types of windows exist, each applying a weighting to different parts of the time data dependant on the shape of the window, they effectively filter the data. Consequently, each window when applied to data, will give a slightly different spectrum. The shape of a window can be adjusted by varying the value of a particular parameter  $\alpha$ , part of the technique of windowing is to select by experimentation the value of  $\alpha$  which gives the best results for a particular application. The variation of  $\alpha$  changes the width of the main lobe and the sidelobe fall-off rate, thus emphasising parts of the signal in different ways.

Matlab had built in window functions, Hanning, Hamming, Rectangular and Kaiser, that could be applied to the data. Each window had different characteristics and as a result were more suited for some applications than others. Research revealed that the Kaiser window is favoured for trying to identify between components that are close together with large differences in magnitudes (similar to those found in the motor current). Due to its good selectivity it can fully separate two components over a dynamic range of over 60 dB. Adjusting  $\alpha$  (increasing it) increases the definition between frequencies, i.e.

the level of skirting reduces. A Kaiser window was generated using Matlab. The length of the window generated was equal to the length of the time data to be processed and the values were multiplied point by point. The value of  $\alpha$  was experimented with and for the skirting to reduce sufficiently required  $\alpha = 9$ .

During these investigations it was noticed that the magnitudes of the components were reduced. The higher the value of  $\alpha$  the more the components decreased from the expected value as Table 4.3 shows.

Window Applied $\alpha =$ window correction factor	Expected Magnitude	Magnitude from plot
no window	100	100.0
	40	40.0
$\alpha = 4$	100	96.9
	40	36.4
$\alpha = 9$	100	92.5
	40	32.02

Table 4.3 Effects of Windowing on Plot Magnitudes

The reduction in magnitude of the components could not be avoided when the window was applied [98]. This was caused by the window reducing the signal energy which was to be expected as it acted rather like a filter. From [98] a formula (Equation 4.3) could be used which calculated a factor which the data could be multiplied by. The derivation of this formula can be found in [98]. This factor restored the signal power to the original level and was applied to the data prior to windowing. The formula for the factor is:

$$x = \left[ \frac{N}{\sum_{n=0}^{N-1} w^2(n)} \right]^{\frac{1}{2}} \quad (4.3)$$

where N = Number of data points

w(n) = window coefficients

A program was written to generate this factor x as shown in Appendix 3, Section A3.5. The operation of the program was verified using a smaller matrix with numbers that allowed the result produced by the program to be checked manually. Running the program generated a value of  $x = 1.832$  for window data where  $\alpha = 9$ . The data was multiplied by this value before the window was applied. A signal was generated with several components and the spectral analysis process applied. Applying x greatly improved the magnitude of the components, increasing them to just below the levels they should be. The value of x was experimented with until the magnitudes were closer to their expected values. Table 4.4 shows a summary of the results of this. The ideal magnitudes of the components are: 25, 75, 760 and 780 Hz - 40 dB, 50 and 750 Hz - 100 dB.

	Magnitude (dB) of Various Frequency Components (Hz)					
x	25	50	75	750	760	780
1.832	37.52	97.7	37.52	97.38	37.2	37.5
2.3	39.15	99.97	39.47	99.65	38.8	39.15
2.5	40.76	100.62	40.76	100.62	40.11	40.11

Table 4.4 Effect on Magnitudes due to Different Values of x

It was concluded that 2.3 brought the values to within close enough range of the ideal magnitudes. The compensation for the reduction in energy levels due to windowing had worked successfully, the figure from the formula gave an initial value from which to adjust the data. Table 4.5 shows the results of the FFT of another test waveform.

Freq. Component	Voltage Mag. (V)	Expected dB Mag.	Spectrum dB Mag.
25	0.0001	40	39.47
50	0.1	100	99.97
75	0.01	80	79.91
750	0.1	100	99.65
760	0.001	60	59.85
780	0.01	80	79.91

Table 4.5 Magnitude Values from Spectrum of Test Signal

### 4.6 Final Tests

To finally test the software a complex signal was generated that modelled all the components that would be expected in a signal from the finite element analysis modelling a real motor. This contained ‘real motor’ components at 50 Hz, odd and even harmonics of the fundamental and high frequency components due to eccentricity at the rotor slot passing frequencies. The magnitude of the components were also realistic as obtained from experimental tests.

Before this signal was processed the data values were converted to rms and to volts ( $\times 0.1$ ) as performed by the commercial analyser, together with multiplying the data by 2.3 to compensate for the reduction due to windowing, this was equivalent to multiplying the data by 16.263455976.

All the small programs were combined to create one large program. To generate a spectrum all that was required was for the data samples to be in a matrix (y) and to have generated the window coefficients (w1) and the conversion factors (Conv). The final program is shown in Appendix 3, Section A3.6. A flow chart of the entire processing procedure is presented in Figure 4.3.

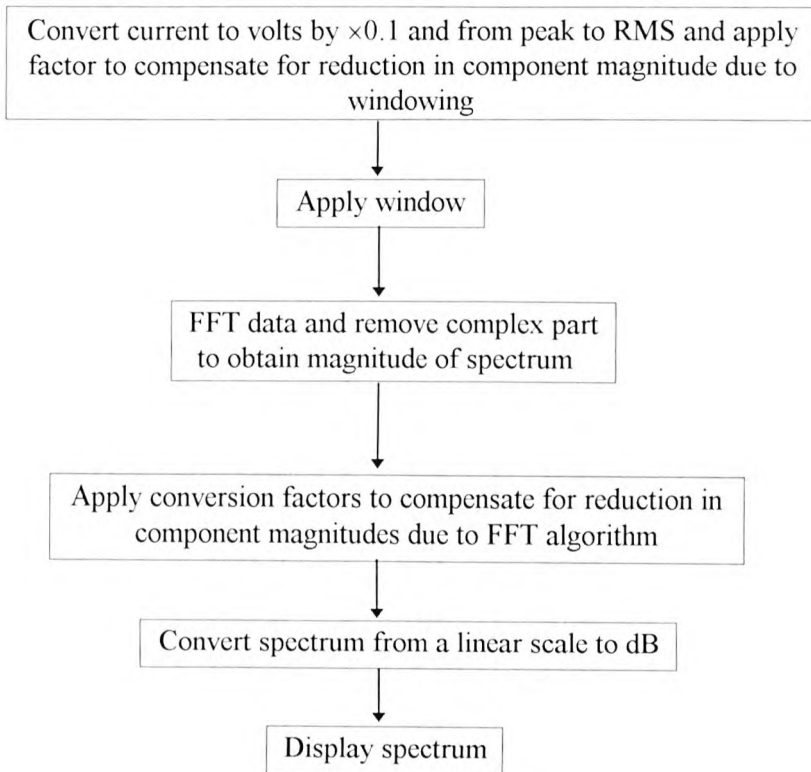


Figure 4.3 Flow Chart of Spectrum Analysis Process

This was run several times with different data and worked successfully, one set of results is shown below in Table 4.6 and Figure 4.4. The magnitudes of the components were found using the command: `[f,k] = ginput(1);` This positioned a cursor on the plot and allowed any point to be selected, it then displayed the frequency and magnitude of that point. There was a small degree of inaccuracy in the positioning of the cursor on the peak of a component but not enough to be of concern.

Frequency comp. (Hz)	Magnitude (volts)	Frequency of cursor on plot	% difference ideal freq. vers. plot freq.	Calculated ideal RMS mag. (dB)	Spectrum RMS mag. (dB)	% difference ideal RMS mag. vers. plot mag.
50	0.1	50.46	0.92	96.98	96.73	0.25
100	3.162E-06	99.88	0.12	6.98	6.80	2.57
150	1.778E-04	150.11	0.07	41.98	41.41	1.35
200	3.162E-06	200.46	0.23	6.98	6.79	2.72
250	0.0001	249.88	0.05	36.98	36.88	0.27
300	3.162E-06	300.36	0.12	6.98	6.47	7.31
350	5.623E-05	349.88	0.03	31.98	32.03	0.16
400	3.162E-06	399.76	0.06	6.98	6.47	7.31
450	3.162E-05	449.88	0.02	26.98	26.53	1.67
500	3.162E-06	500.46	0.09	6.98	6.47	7.31
550	1.778E-05	549.88	0.18	21.98	21.68	1.36
600	3.162E-06	600.46	0.07	6.98	6.47	7.31
650	0.00001	649.88	0.02	16.98	16.82	0.94
1050	3.162E-05	1050.10	9.5E-03	26.98	26.52	1.70
1074	0.0001	1074.20	0.02	36.98	36.88	0.27
1098	3.162E-05	1098.40	0.04	26.98	26.52	1.70
1150	3.162E-05	1150.10	8.7E-03	26.98	26.52	1.70
1174	0.0001	1174.20	0.02	36.98	36.88	0.27
1198	3.162E-05	1198.40	0.03	26.98	26.52	1.70
1250	3.162E-05	1250.10	8.0E-03	26.98	26.52	1.70
1274	0.0001	1274.20	0.01	36.98	36.88	0.27
1298	3.162E-05	1298.40	0.03	26.98	26.52	1.70

Table 4.6 Spectrum Results for a FFT of a Signal Modelling Real Motor Components

The following spectrum in Figure 4.4 corresponds to the results in Table 4.6.

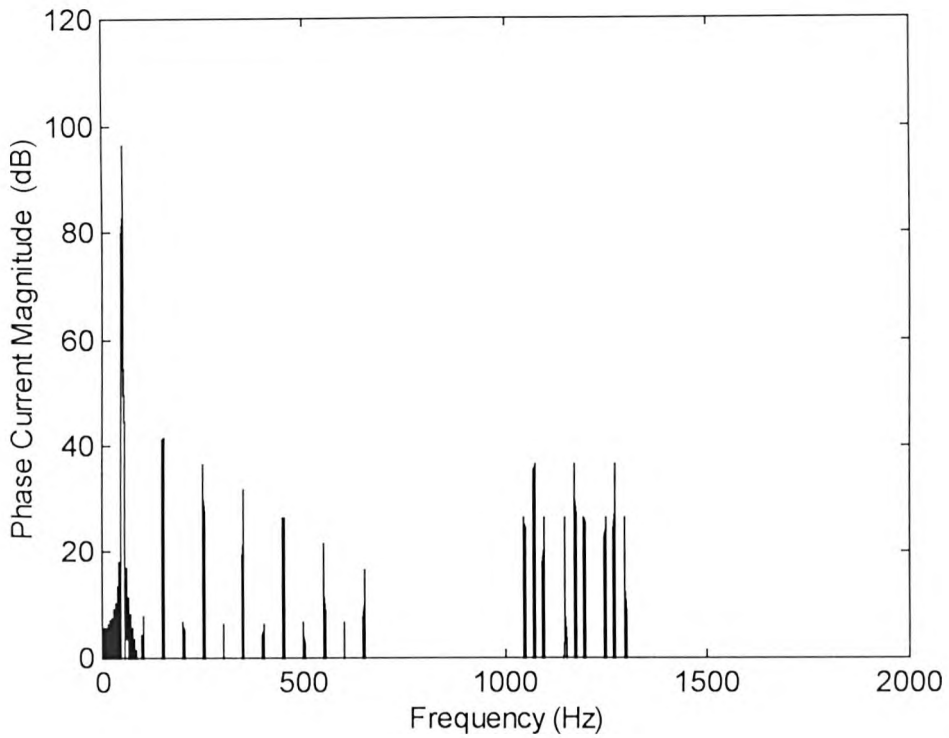


Figure 4.4 Spectrum of Modelled Machine Signal

#### 4.7 Experiment with Increasing the Number of Samples Processed

Up to this point, data where  $f_s = 5000$  Hz, was being processed, this was increased to 10000 Hz. This was to check the operation of the procedure for processing increased numbers of data samples. To maintain  $\Delta f = 0.25$ Hz,  $N$  had to increase from 20,000 to 40,000. The programs for calculating the conversion factors and producing the plot were modified, modified values are shown in bold in the two programs presented in Appendix 3, Section A3.7. A longer window had to be generated since increasing  $f_s$  increased the number of samples to process. It was thought and proved correct that as  $\alpha = 9$  was staying constant then 2.3 would still work as the correction factor despite the longer data length.

A waveform was generated, successfully transformed and the spectrum accurately displayed as shown in Table 4.7.

Frequency Component (Hz)	Magnitude (Volts)	Freq. defined in plot (Hz)	Calculated RMS magnitude (dB)	Spectrum mag. (dB)
25	0.0001	25.29	36.98	36.88
50	0.1	50.11	96.98	96.73
75	0.001	74.94	56.98	56.62
1050	0.0001	1049.70	36.98	36.88

Table 4.7 Results from Spectrum using Increased Number of Samples

This verified that the alterations that had been made for increasing the sampling frequency (i.e. more data points) had worked successfully. At that point in time this was important to ensure changes in the number of data points (sampling frequency) as a result of the initial runs using the time-stepping analysis could easily be handled. As Chapter 3 explained two timesteps were used, initially  $7.843 \times 10^{-5}$  s for testing and finally  $3.9215 \times 10^{-5}$  s for all the analysis results. In both cases the aforementioned procedure was carried out to thoroughly test the programs with the new sampling rates. As good agreement as shown in Tables 4.6 and 4.7 was obtained in both cases. The final programs for calculating the conversion factors and displaying the emf and the current spectrums for the timestep of  $3.9215 \times 10^{-5}$  s are shown in Appendix 3, Section A3.8.

As explained in Chapter 3, experiments were carried out after initial runs had been performed using the time-stepping analysis to see if it was possible to block cycles of emf or current together as Figure 4.5 illustrates. This would reduce the CPU time needed to produce the required data length.

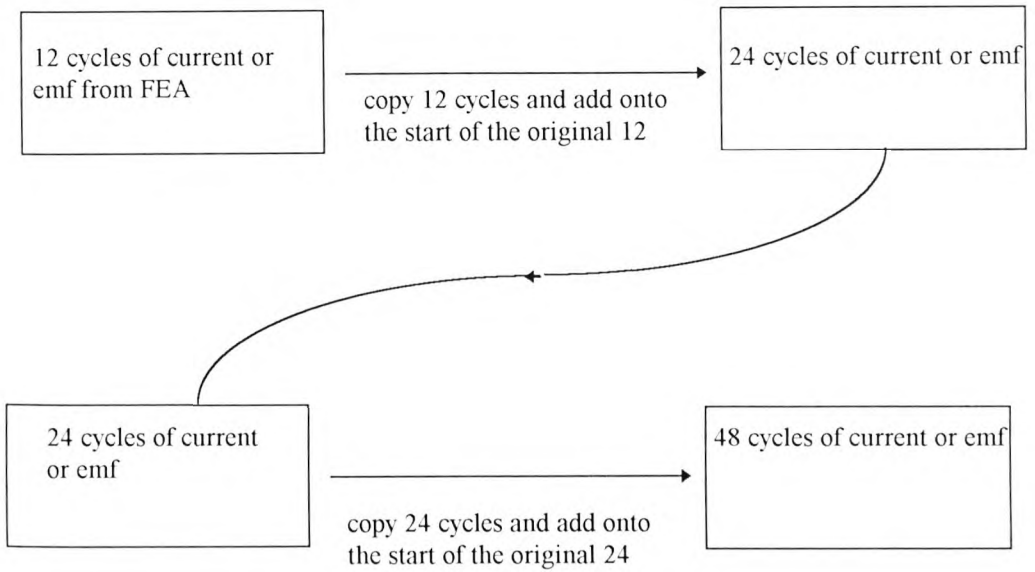


Figure 4.5 Blocking of Data to Reduce Computation Time

The actual execution of this process was easy as the finite element signal was read from an UNIX text file into a matrix in Matlab. Using Matlab matrix manipulation functions the data was blocked as shown above. Investigations focused on the minimum number of continuous cycles required from the finite element analysis, the number of times the data could then be blocked and also the effect, if any, on the spectrum quality in terms of skirting and distortion of the component magnitudes displayed. The testing was performed in Matlab by generating signals of 12 cycles and then blocking that to 24/48 or generating 24 cycles and blocking that to 48. These spectra were then compared to one produced from a waveform of 48 continuous cycles.

It was found that it was possible to take 12 cycles of continuous data from the finite element analysis and block that up to 48 cycles without affecting the magnitude of the components displayed. The only drawback was a slight increase in the skirting around each rotor slot passing frequency but this was not large enough to hide, for instance, smaller dynamic eccentricity components. Any less than 12 cycles of continuous data began to effect the spectrum quality too much with skirting effects. The skirting was

occurring as a result of the join between the blocks of data. There was a slight step between the last point in the first block and the first point in the start of the copied block. Adding together too many blocks increased the number of steps present and hence the level of skirting.

These investigations were performed both in Matlab and then on the current and emf from the finite element analysis. The predictions from Matlab were proved to be correct as it was found that trying to block too few continuous cycles of data resulted in a very poor spectrum. This verified Matlab as a very powerful and accurate testing tool. In relation of the 50Hz component, the rotor slot passing frequencies, even with high airgap eccentricity levels were relatively small compared to the 50Hz magnitude for the 51 slot rotor. However, a finite element analysis on a 44 bar rotor revealed that the combination of 36 stator slots with 44 rotor slots result in very high magnitude rotor slot passing frequencies. In this instant the skirting present round these components was so large that smaller dynamic eccentricity components either side were being lost. In this case 24 continuous cycles were blocked to 48 (instead of 12 to 48 as before) to remove the skirting. This allowed all components of interest to be visible.

## **4.8 Conclusion**

Software was successfully developed based on Matlab that allowed a spectral analysis to be performed on the emf and the current produced by the time-stepping finite element analysis. The software was written to produce a spectrum as close to that generated by the commercial analyser thus facilitating the comparison of spectra from experimental and modelled data. The length of the data sequence to be processed could be easily increased as could the frequency resolution, if required. Testing the software with a signal similar to that generated by the test-rig motor and the finite element analysis showed that it was capable of processing a more complex signal in terms of the number of components and proximity of components to one another. It also

successfully processed and displayed the large differences in magnitude between components.

Various limitations of the FFT and windowing became apparent during the development of the software. These were due to the inherent limitations of the FFT itself and the effects of windowing the data to reduce skirting. These drawbacks, which affected the magnitude of the components, were successfully overcome by original ideas and techniques developed from the references.

# Chapter 5

## Analysis and Experimental Results for 51 Bar Unskewed Rotor

### 5.1 Introduction

This chapter presents the results of both an experimental and a finite element analysis study of airgap eccentricity in the 51 bar test-rig motor. An in-depth pole-pair analysis is presented for this motor based on Equation 2.3 and the limitations of the approach as suggested in Chapter 2 are expanded upon with the aid of the experimental results and the finite element analysis. The Chapter is composed, firstly, of a basic pole-pair analysis which is developed further both within that section and as the experimental and finite element results are discussed. The experimental and finite element results are then presented together in sections relating to the type of fault modelled. For instance, static eccentricity variations and then another section for static and dynamic eccentricity variations. Comparisons between the finite element and experimental results and discussions are presented. There is also a section on purely finite element results, for instance, a truly concentric motor, to which no experimental comparison could be made.

The main objective of this part of the research was to compare the modelled and experimental current frequency spectra (frequency and magnitude of components) for the 51 bar test-rig motor for varying levels of static and/or dynamic eccentricity. The experimental and finite element results were also used to further expand on the pole-pair analysis and its limitations. In the ideal case for a perfectly symmetrical motor (supply, windings and magnetic circuit) the frequency components present in the test-rig motor current should be in total agreement with those in the finite element analysis current as the finite element analysis models a perfectly symmetrical motor. However, as previously discussed the test-rig motor was considerably unbalanced and this had to be considered when investigating the results. In practice the three-phase line voltages differed by 1% to 2% and the third, fifth, seventh and ninth harmonics were each 1% of the actual supply frequency voltage to the test-rig.

The processing of the finite element results was explained in Chapter 3, the test-rig motor set-up will now be explained. The phase current was monitored via a clip on current transformer (CT) whose voltage output (0.1V/A via an internal shunt) was fed directly into the laboratory spectrum analyser as Figure 5.1 illustrates. The linearity of the CT was  $\pm 5\%$  over 0 to 2kHz.

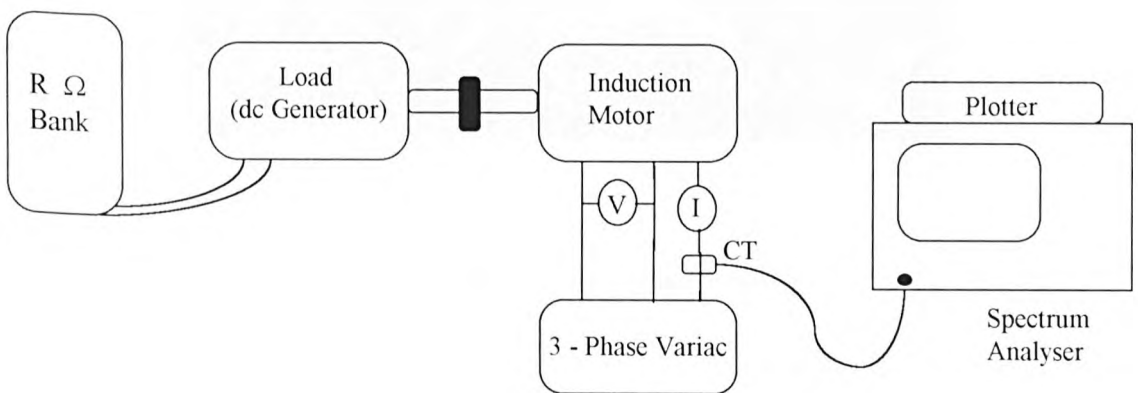
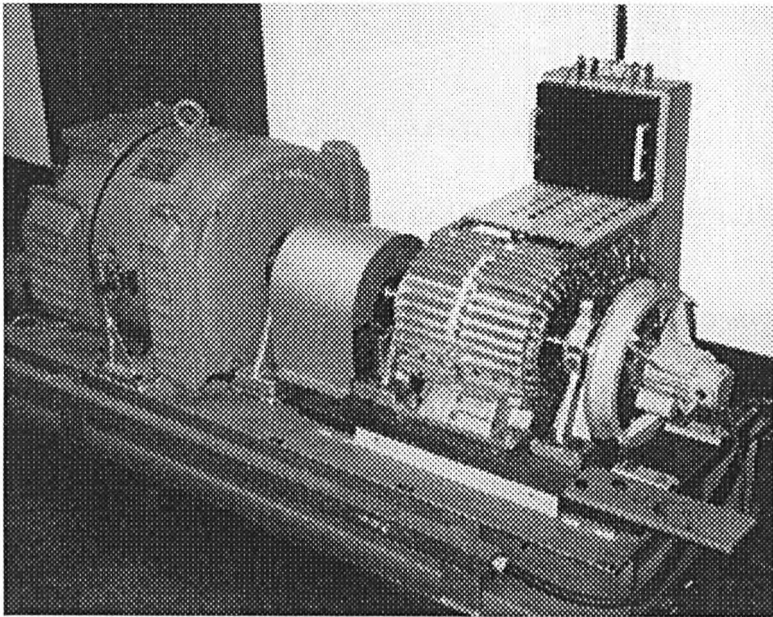


Figure 5.1 Experimental Set-Up

Photographs of the test-rig motor, CT and spectrum analyser and the copper fabricated rotor are shown in Photographs 5.1, 5.2 and 5.3 respectively.

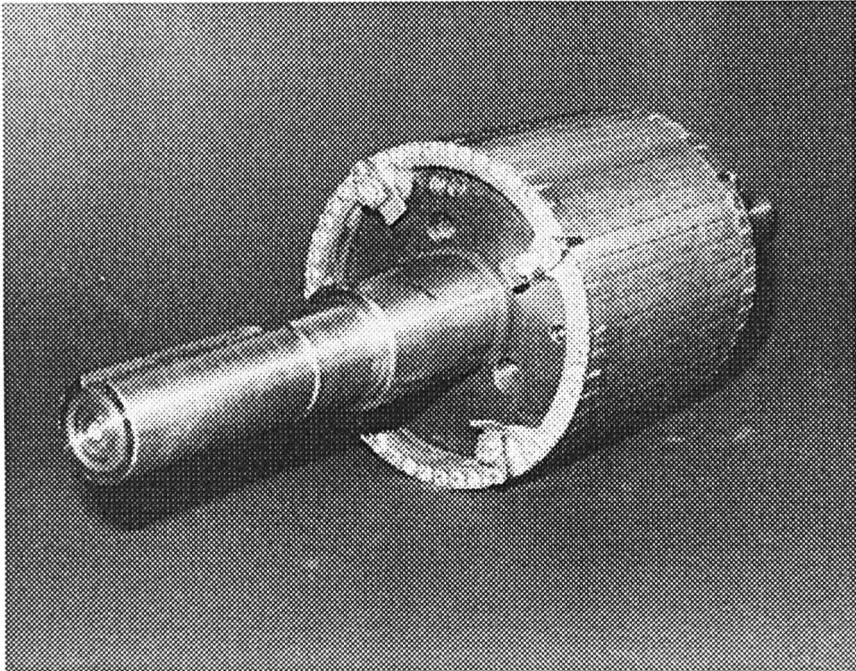
The majority of tests were performed at full-load (1322 rpm), however, as motors often operate at less than full-load, current spectra were obtained for 25% static eccentricity at lighter loads to compare with finite element analysis results at lighter loads. This provided an opportunity to investigate the finite element analysis ability to model the components at lighter loads. The test-rig motor was loaded via a dynamometer (dc generator) whose output was fed into a bank of resistors.



Photograph 5.1 Test-Rig Motor



Photograph 5.2 Current Transformer and Spectrum Analyser with Plotter



Photograph 5.3 51 Bar Copper Fabricated Rotor used in Tests

Various levels of static and/or dynamic eccentricity were introduced into the test-rig. The test-rig motor had an inherent degree of airgap eccentricity of approximately 5 % - 10% static and 5% dynamic eccentricity. Therefore, this combination was the lowest airgap eccentricity level that was investigated. For safety reasons a maximum value of 50% airgap eccentricity was introduced, this could be as 50% static eccentricity or 25% static and 25% dynamic. In the finite element analysis it was decided not to attempt to include in the model the inherent level of static and/or dynamic eccentricity. It was known that after the test-rig had been adjusted, for instance, taking the rotor in and out, that this inherent level could change slightly ( $\approx \pm 5\%$ ). This contributes to the tolerance on the experimental results in terms of the exact level of airgap eccentricity present. Therefore, when the motor is said to have 10% static and 25% dynamic eccentricity, these are the introduced levels in addition to the variable inherent level. With the finite element analysis, 10% static and 25% dynamic eccentricity means 10% static and 25% dynamic in the model and in general the finite element analysis was modelling slightly less airgap eccentricity than was present experimentally which had to be taken into account when discussing the results.

## 5.2 Pole-Pair Analysis

The frequency components which were observed in the test-rig current spectra were calculated from Equation 2.2 and are shown in Table 5.1.

Type	Frequency (Hz)	$f_1$	R	$n_d$	s	p	$n_{sa}$	$n_{ws}$
pspf	1072	50	51	0	0.1187	2	0	-1
pspf	1172	50	51	0	0.1187	2	0	1
pspf	1272	50	51	0	0.1187	2	1	1
de	1050	50	51	-1	0.1187	2	0	-1
de	1094	50	51	1	0.1187	2	0	-1
de	1150	50	51	-1	0.1187	2	0	1
de	1194	50	51	1	0.1187	2	0	1
de	1250	50	51	-1	0.1187	2	1	1
de	1294	50	51	1	0.1187	2	1	1

de: dynamic eccentricity component; pspf: principal slot passing frequency also a function of static eccentricity

Table 5.1 Frequency Components Investigated by Barbour for 51 Bar Rotor

The pole-pairs of the flux waves associated with these frequencies for different combinations of airgap eccentricity were calculated using Equation 2.3. As for the example in Chapter 2 the analysis is presented in stages for ease of interpretation and will be further added to as the results are discussed. Table 5.2 shows the stator winding harmonic pole-pair numbers including some higher ones compared to those shown in Table 2.2.

Stator winding data: 4 pole, 36 slot, 8/9 pitch, 3 slots/pole/phase, star connected.																	
<b>Harmonic pole-pairs m:</b> Fundamental - 2 pole-pairs $m = p(6c \pm 1)$ where $c = 0, 1, 2, \dots$																	
2	10	14	22	26	34	38	46	50	58	62	70	74	82	86	94	98	106
110	118	122	130	134.....etc.													

Table 5.2 Harmonic Pole-Pair Numbers for Stator used by Cameron and Barbour

*Case 1: No static or dynamic eccentricity*

$$m = (R \pm S \pm n_s \pm n_d \pm 2n_{sa}p \pm n_{os}p) \quad \text{where } n_s = 0, n_d = 0; n_{sa} = 0, n_{os} = \pm 1, p = 2,$$

$$R = 51 \text{ and } S = 36.$$

$$\therefore m = R \pm S \pm 2$$

$$m = 51 \pm 36 \pm 2$$

$$= 87 \pm 2 \quad \text{and} \quad 15 \pm 2$$

Which gives 89 and 17 for +2 which corresponds to  $n_{os} = +1$  and component 1172Hz and also 85 and 13 for -2 which corresponds to  $n_{os} = -1$  and component 1072Hz

For the 1272Hz component:

$$m = 51 \pm 36 + 4 + 2 = 87 + 6 \text{ and } 15 + 6$$

Which gives 93 and 21 which corresponds to  $n_{sa} = 1, n_{os} = 1$  and component 1272Hz

This result showed that the pole-pairs of the flux waves at the principal slot passing frequencies were odd and not compatible with the stator winding. In actual fact the coil pitch factor for the 1272Hz component was 0 since the pole-pairs associated with it are divisible by three. This meant that in an absolutely perfect motor (0% airgap eccentricity) these components should not be present in the current frequency spectrum. The finite element analysis was used to model this condition and a result is presented later. The condition could never be achieved experimentally due to the inherent eccentricity levels in the motor.

*Case 2: Static eccentricity present but no dynamic eccentricity*

$$m = (R \pm S \pm n_s \pm n_d \pm 2n_{sa}p \pm n_{\theta s}p) \quad \text{where } n_s = \pm 1, n_d = 0; n_{sa} = 0/1, n_{\theta s} = \pm 1, \\ p = 2, R = 51 \text{ and } S = 36.$$

Giving  $85 \pm 1$  and  $13 \pm 1 \Rightarrow 86, 84$  and  $14, 12$  pole-pairs for 1072Hz  
 $89 \pm 1$  and  $17 \pm 1 \Rightarrow 90, 88$  and  $18, 16$  pole-pairs for 1172Hz  
 $93 \pm 1$  and  $21 \pm 1 \Rightarrow 94, 92$  and  $20, 22$  pole-pairs for 1272Hz

This result showed that the 1172Hz should not be able to induce a current in the stator winding, however, the pole-pairs of the flux waves for the 1072Hz and the 1272Hz are compatible with the stator winding and therefore the magnitude of these components should increase with static eccentricity. It should be noted that if saturation effects are included for the 1172Hz component then the pole-pairs become: 94, 86, 84, 92 and 14, 22, 12, 20. The pole-pairs at this frequency are now compatible with the stator winding.

As explained in Chapter 2.5.3 this basic analysis ( $n_s = 1$ ) is a gross simplification of the actual situation where the permeance variation is being modelled as if the slots were sinusoidal in shape. If for example  $n_s = 3$  (with or without saturation included) the pole-pairs associated with the 1172Hz component are now compatible with the stator winding, (86 and 14 with no saturation or 88 with saturation). It can be seen from the experimental and finite element results that this component was actually the largest in magnitude of the three principal slot passing frequencies. This is further discussed later.

*Case 3: Dynamic eccentricity present but no static eccentricity*

$$m = (R \pm S \pm n_s \pm n_d \pm 2n_{sa}p \pm n_{\theta s}p) \quad \text{where } n_s = 0, n_d = \pm 1, n_{sa} = 0, n_{\theta s} = \pm 1, p = 2, \\ R = 51 \text{ and } S = 36.$$

From earlier analysis the pole-pairs for the slot passing frequencies were:

85 and 13 for  $n_{ws} - 1$  for the 1072Hz component  
 89 and 17 for  $n_{ws} + 1$  for the 1172Hz component  
 93 and 21 for  $n_{ws} + 3$  for the 1272Hz component

Now with  $n_d = \pm 1$ :

-1 for the lower dynamic eccentricity components 1050Hz, 1150Hz and 1250Hz

+1 for the upper dynamic eccentricity components 1094Hz, 1194Hz and 1294Hz

The pole-pairs associated with these frequencies are:

1050Hz: 85 - 1 and 13 - 1  $\Rightarrow$  84, 12

1150Hz: 89 - 1 and 17 - 1  $\Rightarrow$  88, 16

1250Hz: 93 - 1 and 21 - 1  $\Rightarrow$  92, 20

1094Hz: 85 + 1 and 13 + 1  $\Rightarrow$  86, 14

1194Hz: 89 + 1 and 17 + 1  $\Rightarrow$  90, 18

1294Hz: 93 + 1 and 21 + 1  $\Rightarrow$  94, 22

The above result shows that only the flux waves associated with the 1094Hz and the 1294Hz component are compatible with the stator winding. This implies that only these components should be affected by changes in the dynamic eccentricity level. Again the analysis is grossly simplified when  $n_d = 1$ . Purely dynamic eccentricity was modelled using the finite element analysis and this result, discussed later, differs from the predictions shown above.

#### *Case 4: Both static and dynamic eccentricity present*

The pole-pairs of the dynamic eccentricity components with dynamic eccentricity present were calculated in Case 3, with static eccentricity now included ( $n_s = \pm 1$ ) this was applied to the pole-pair values obtained in Case 3:

1050Hz:  $84 \pm 1$  and  $12 \pm 1 \Rightarrow 83, 85$  and 11, 13

1150Hz:  $88 \pm 1$  and  $16 \pm 1 \Rightarrow 87, 89$  and 15, 17

1250Hz:  $92 \pm 1$  and  $20 \pm 1 \Rightarrow 93, 91$  and 21, 19

1094Hz:  $86 \pm 1$  and  $14 \pm 1 \Rightarrow 85, 87$  and 13, 15

1194Hz:  $90 \pm 1$  and  $18 \pm 1 \Rightarrow 89, 91$  and 17, 19

1294Hz:  $94 \pm 1$  and  $22 \pm 1 \Rightarrow 95, 93$  and 23, 21

This basic result (all odd pole-pairs) indicated that with static and dynamic eccentricity the dynamic eccentricity components were not a function of static eccentricity in this motor. As explained in Chapter 2 there is the limitation with this analysis in that the pole-pairs of the static eccentricity components cannot be predicted with static and dynamic eccentricity combined. In addition the experimental and finite element results do not follow the predictions as all the upper dynamic eccentricity components (1094Hz etc.) were clearly visible.

This analysis will be further developed and referred to as the experimental and finite element results are presented.

## 5.3 Static Eccentricity Variations

### 5.3.1 Experimental Results

In these experimental investigations the level of static eccentricity introduced into the test-rig was varied from 10% to 50%. On average the inherent dynamic eccentricity level was approximately 5% so these investigations focused on the effects of static eccentricity variations. The current spectra from the motor with 10% and then 50% static eccentricity are shown in Figures 5.2 and 5.3 on the next page. This was for the full load condition of 11.5A at 1322 rpm. The components which are a function of static eccentricity (principal rotor slot passing frequencies) are at 1072Hz, 1172Hz and 1272Hz as predicted by Equation 2.2. The increase in the magnitude of the components with increasing static eccentricity is illustrated in Figure 5.4.

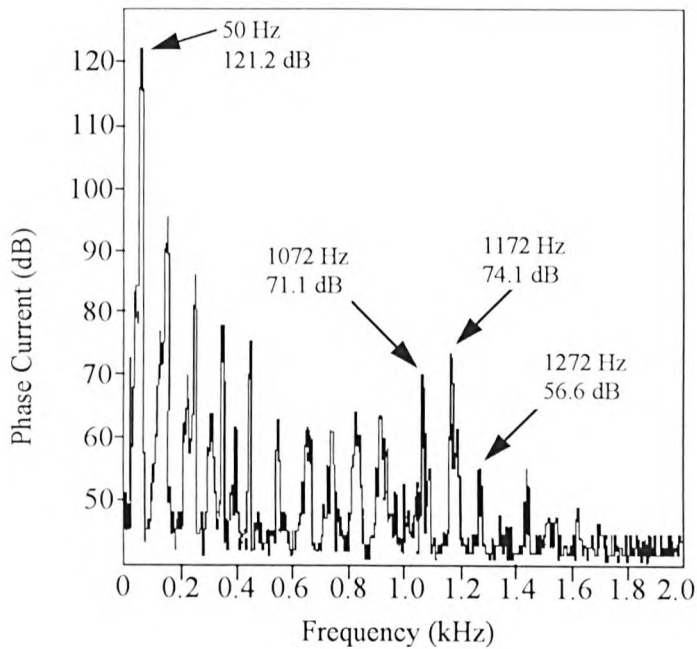


Figure 5.2 Current Spectrum from Test-Rig for 10% Static and 5% Dynamic Eccentricity, Full-Load, 1322 rpm

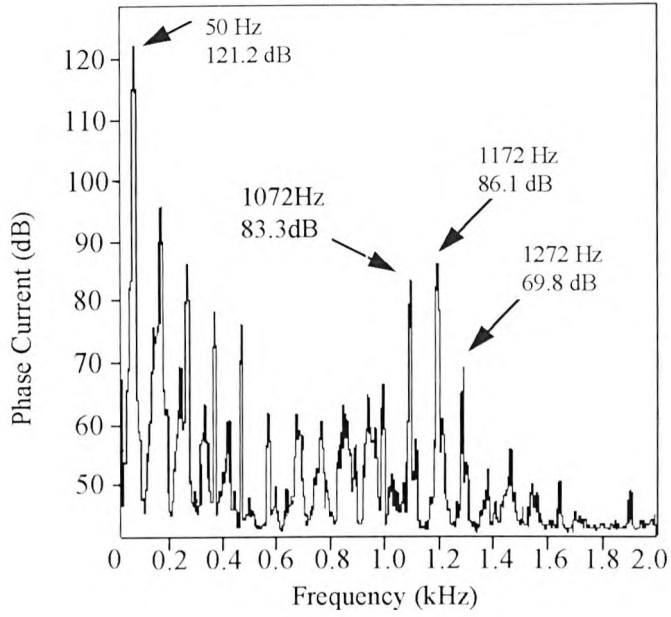


Figure 5.3 Current Spectrum from Test-Rig for 50% Static and 5% Dynamic Eccentricity, Full-Load, 1322 rpm

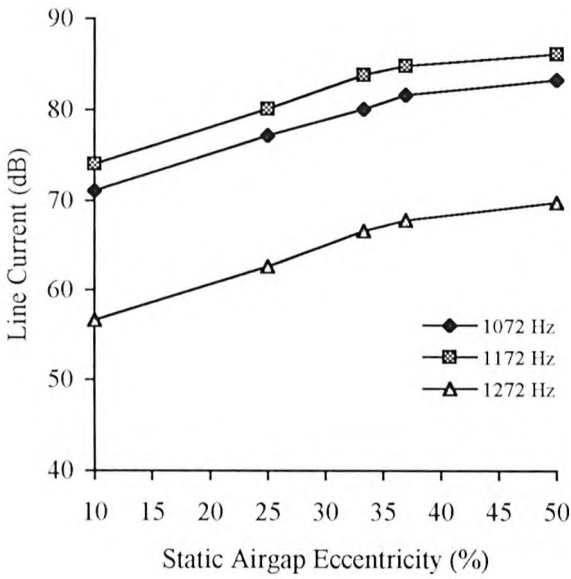


Figure 5.4 Magnitude of Current Components versus Static Eccentricity in Test-Rig

With reference to Figures 5.2 and 5.3, each component increased in magnitude by more than 10dB (a range of 12.2dB to 13.2dB) which is a linear increase of more than 3.16 times the original magnitude. This illustrated that these components were clearly a function of static eccentricity and could be used to quantify the degree of static eccentricity.

The dynamic eccentricity components were present in the spectra due to the inherent level of dynamic eccentricity in the test-rig motor. Table 5.6 in the next section on static and dynamic combinations shows the magnitude that they occurred at for 10% static and the estimated 5% inherent dynamic eccentricity level. Their magnitude was checked at 10% and then 50% static eccentricity and the upper dynamic eccentricity components (1194Hz etc.) did not increase in magnitude with the increase in static eccentricity (stayed constant to within 1dB). As explained in the next section the lower dynamic eccentricity components (1050Hz etc.) behaved very erratically. This showed that the upper dynamic eccentricity components, at least, were independent of the level of static eccentricity. In a motor with a long shaft the high static eccentricity, hence, the unbalanced forces, could result in dynamic eccentricity increasing due to mechanical problems with the shaft flexing or bearing wear. This was not happening in the experimental case primarily because the motor was not allowed to run for long enough for problems to develop and because the shaft was short.

From these results it can be seen that the 1172Hz component was consistently the largest in magnitude, generally 3dB higher at each static eccentricity level than the next largest at 1072Hz. The basic pole-pair analysis predicted that the pole-pairs associated with this frequency were incompatible with the stator winding harmonic pole-pair numbers compared to those for 1072Hz and 1272Hz. This prediction was based on only considering the simplified case of static eccentricity ( $n_s = 1$ ) and dynamic eccentricity was not incorporated.

These results clearly show the presence of the 1172Hz component in the spectra. Its presence could have been due to the pole-pairs actually being compatible. This was possible due to the limitations of Equation 2.3 in considering the actual slot shape and when trying to consider static and dynamic eccentricity together. The other reason was that even modelling the true motor behaviour the pole-pairs at this frequency were not compatible with the stator. In this case the component was only appearing because second order effects such as winding asymmetry or supply imbalance meant that the stator winding was receptive to frequencies with pole-pairs at, for example, 88 and 16. The test-rig motor winding and supply were not perfect so second order effects would be present. Stator winding factors now had to be considered. If the winding factors associated with second order pole-pairs were larger than those associated with first order pole-pairs then components with second order pole-pairs would be noticeably present. As shown in Appendix 4.1, Section A4.1, the winding factors were calculated for the above situation using the pole-pairs predicted by the basic analysis as an example.

First order pole-pairs at 14 and 86 possibly associated with the 1072Hz  $k_w = 0.06$

Second order pole-pairs at 16 and 88 possibly associated with the 1172Hz  $k_w = -0.263$

The winding factor for the second order pole-pairs is 4.4 times larger than that for the first order pole-pairs. This shows that when second order effects (winding asymmetry) are present the pole-pairs associated with the 1172Hz are compatible with the stator winding. The larger winding factor (4.4 times) for the 1172Hz compared to the 1072Hz winding factor confirms why the current component at 1172Hz is higher ( $\approx 3\text{dB}$ ).

The result of this discussion is that it becomes evident when only the basic pole-pair analysis was used together with experimental results it could not be unambiguously predicted or explained which components were really compatible with the stator and therefore the best to track from a condition monitoring perspective. By including a finite element analysis into the investigation a better understanding was possible. For example, Equation 2.3 cannot reliably predict the pole-pairs of the frequency components in the flux waveform so this leads to one area of uncertainty. In addition,

because second order effects were present in the motor, components could appear in the current spectrum which would not otherwise be compatible with the stator.

However, a finite element analysis should accurately predict the pole-pairs of the frequency components even with static and dynamic eccentricity together and because a perfect motor was modelled, second order effects were removed from the equation. If a finite element analysis revealed that the 1172Hz component was clearly present in the spectrum then it can be assumed that the pole-pairs associated with this frequency were indeed compatible with the stator and that the pole-pair analysis was very limited.

Figure 5.5 shows the effect of load variation on the magnitudes of the components for a fixed value of 25% static and nominal 5% dynamic eccentricity. The components change in frequency with load so they are referred to as the components calculated with  $n_{ws} = 1$ ,  $n_{ws} = -1$  and  $n_{ws} = 1$ ,  $n_{sa} = 1$ .

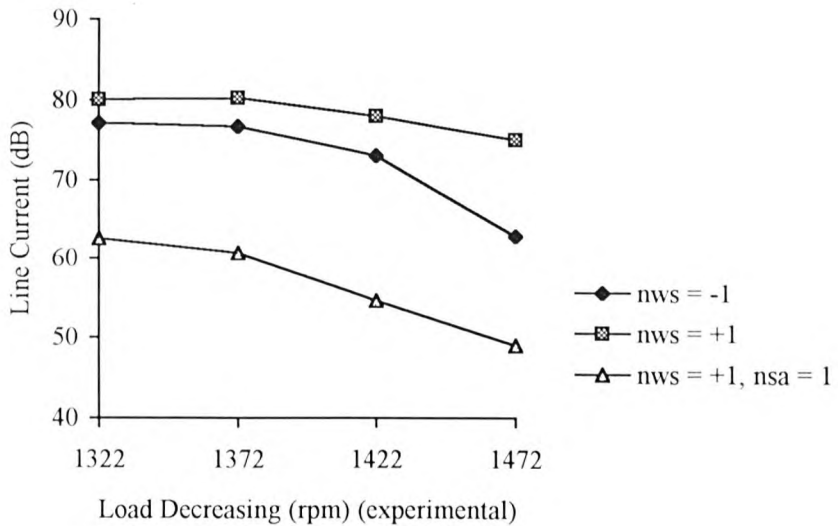


Figure 5.5 Effect of Load on Static Eccentricity Components in the Test-Rig Motor

As expected, with reduced current flowing in the rotor winding the magnitude of the components decreased, however, the initial rate of decrease was low between 1322rpm to 1372 rpm. This result was important as motors do not always operate at full-load in industry. A comparison is made later with finite element results for lighter loads.

### **5.3.2 Finite Element Analysis Results, Comparison and Discussion**

The finite element analysis was used to model variations of 10, 25 37 and 50% static eccentricity and 0% dynamic eccentricity. The small level of inherent dynamic eccentricity was not included in these models as later results focussed on combinations of static and dynamic eccentricity. It was not thought that this would make a great deal of difference and it provided an opportunity to model purely static eccentricity which is impossible to achieve experimentally, that is, only one variable parameter. Also, at the time these results were obtained the collaborating company was modifying the time stepping program to incorporate dynamic eccentricity. The analysis was performed for the full-load speed of 1322rpm. The time domain waveforms of the induced stator emf for 10% and then 50% static eccentricity are shown in Figures 5.6 and 5.7 respectively.

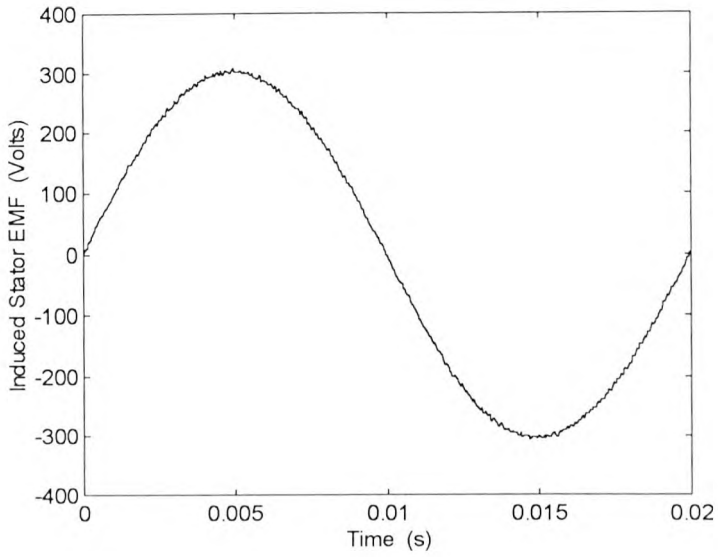


Figure 5.6 Time Domain Representation of Induced EMF for 10% Static Eccentricity

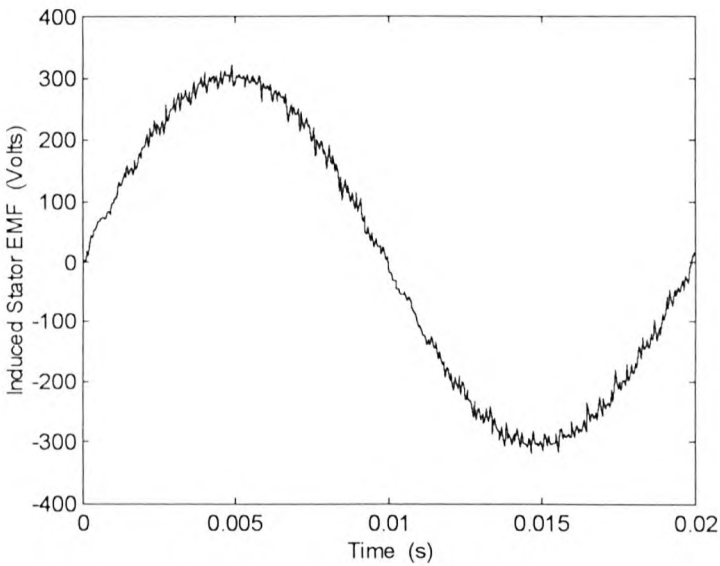


Figure 5.7 Time Domain Representation of Induced EMF for 50% Static Eccentricity

Since a purely sinusoidal voltage supply was applied to the finite element model the harmonic content was minimal, however, the effect of increased static eccentricity is clearly visible. In terms of saturation, with either waveform there was no visible

flattening of the peaks or a change in the slope in between the peaks which are indications of saturation being present due to the third harmonic in the flux [100, 101]. However, it is reasonable to say that with 50% static eccentricity some localised saturation would be present.

The induced stator emf spectra for 10% and then 50% static eccentricity are shown in Figures 5.8 and 5.9 respectively. With regard to the previously mentioned imbalance of supply to the test-rig motor, it can be seen in the finite element spectra that the fifth, seventh... harmonics are negligible in the finite element analysis compared to the magnitudes of the components due to static eccentricity. This was due to the pure sinusoidal and perfectly symmetrical voltage modelled in the finite element analysis.

There was more skirting in the spectrum for 50% static eccentricity as a result of the blocking of data as explained in Chapter 4. With the higher harmonic content in the 50% static eccentricity waveform there was a larger step between each point on the waveform. As a result of this there was a larger glitch at the zero crossing line when continuous cycles of data were blocked onto each other. This resulted in more spectrum noise being present, however, thorough testing revealed that this did not affect the magnitude of the components displayed.

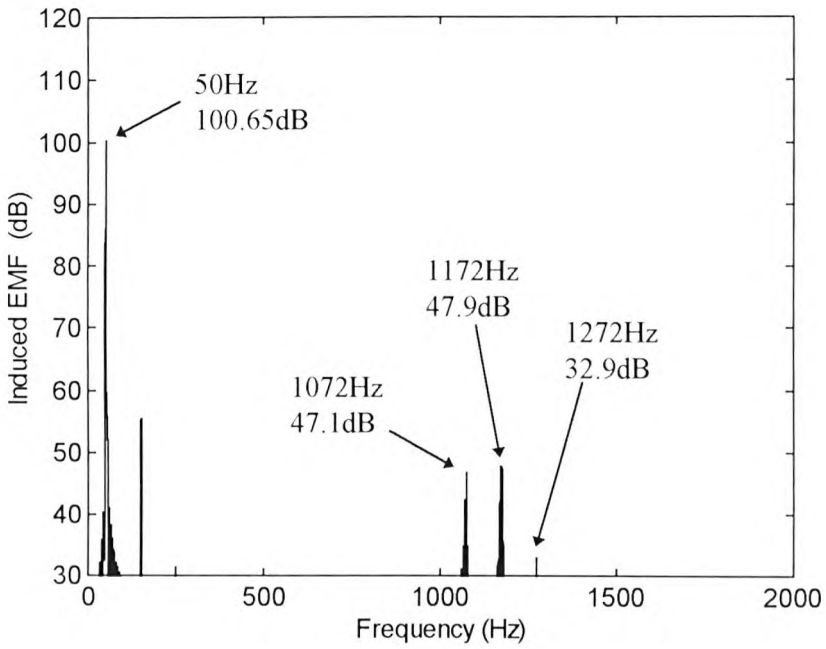


Figure 5.8 EMF Spectrum from FE Analysis for 10% Static, Full-Load, 1322 rpm

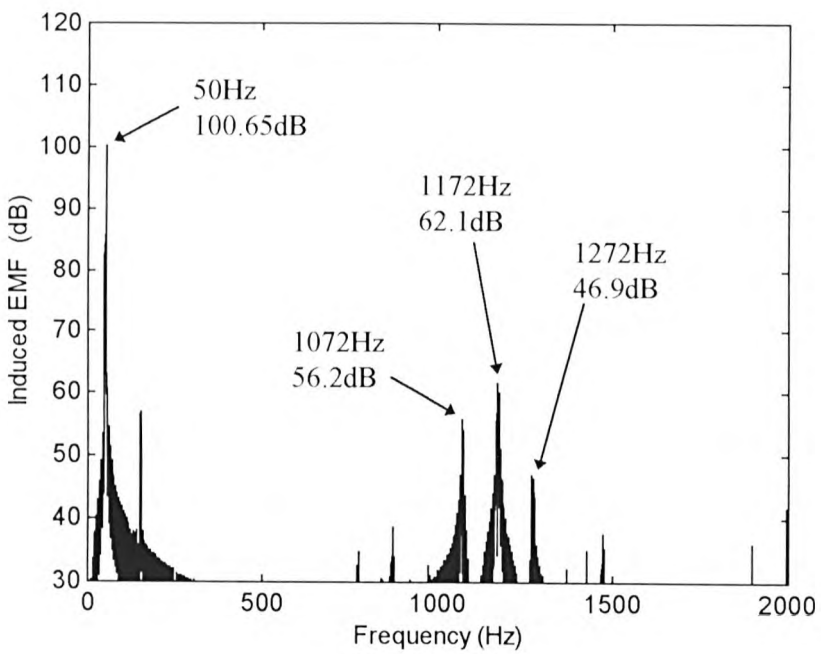


Figure 5.9 EMF Spectrum from FE Analysis for 50% Static, Full-Load, 1322 rpm

The components predicted by Equation 2.2 and obtained experimentally were present in the spectra and they clearly increased in magnitude with the 40% rise in static eccentricity. The dynamic eccentricity components were not present in the spectra as dynamic eccentricity was not modelled. The current magnitude of each component of interest was calculated from the emf spectrum using the equivalent circuit explained in Chapter 3. An example of the calculation for the 50Hz and the 1072Hz component is shown in Appendix 4, Section A4.2. The comparison between measured and predicted magnitudes of the current components which are a function of static eccentricity is shown in Table 5.3 at the end of this subsection, page 130.

Inspection of Table 5.3 reveals that the difference between the experimental and predicted fundamental 50Hz component was only 0.2dB (0.28A) which confirmed the finite element analysis of the test-rig motor. The differences between the magnitudes for the static eccentricity components varied from 2.6dB to 6.2dB. This could still be thought of as a considerable difference in real current terms, however, the agreement was consistently closer than was obtained using the mmf and permeance wave approach and in terms of on-line current monitoring to predict the severity of the fault was a good agreement. It also has to be remembered that there is a  $\pm 1$ dB tolerance on the experimental results and a  $\pm 1$ dB tolerance on the finite element results from a measurement perspective. The range of increase for the components with a 40% increase in static eccentricity was similar. For the experimental components this range was 12.0 to 13.2dB and was 9.2 to 14.1dB for the finite element results.

The finite element results followed a similar pattern to the experimental results in that the 1172Hz component was largest in the spectra followed by the 1072Hz and then the 1272Hz. As the finite element model of the motor had a symmetrical winding and supply then second order effects could not have been resulting in the 1172Hz component appearing in the spectra which was a possibility in the test-rig motor due to asymmetries. This result suggested that the pole-pairs in the flux waveform associated with the 1172Hz component were after all compatible with the stator winding which the

basic pole-pair analysis failed to predict. The only factor still to be discussed is saturation. It could be that the pole-pairs for the 1172Hz component were compatible whether saturation was present or not. If saturation was present it could alter the pole-pair numbers and make them compatible. It could equally be said that saturation could result in the pole-pairs being incompatible. It was impossible to isolate which of the aforementioned possibilities was resulting in the 1172Hz appearing. The finite element analysis accurately models saturation effects including localised saturation due to high airgap eccentricity, therefore, for this non-ideality, the modelled and real motor cases were the same. It was possible that in both the finite element analysis and the test-rig motor that saturation was affecting the pole-pairs associated with the 1172Hz component and this was how it was compatible with the stator. This cannot be determined other than to say that for normal operation the flux density in the motor was not in the saturation region. Localised saturation due to airgap eccentricity, although undoubtedly present at 50% static eccentricity, would be insignificant at 10% static eccentricity where the 1172Hz component was still clearly visible in the spectrum. This suggested that saturation did not play a part in the 1172Hz component appearing in the current spectra. These discussions tend to indicate that the pole-pairs associated with the 1172Hz component were actually compatible with the stator. If the pole-pair analysis (pg. 112) is revisited and by taking the analysis further and not assuming the simple case of  $n_s = 1$  then the pole-pairs of the 1172Hz can become compatible with the harmonic pole-pairs of the stator winding. If  $n_s = 3$  the pole-pairs become 92, 86, 20, 14 which are compatible with the stator winding. This is the major advantage of the finite element analysis in that the true rotor slot shape is modelled and therefore takes into account second order and third order static eccentricity ( $n_s = 2, 3$  etc.).

The fact the finite element analysis with no dynamic eccentricity was agreeing with the experimental result with inherent dynamic eccentricity present also suggested that the presence of dynamic eccentricity was not affecting the static eccentricity components. This was confirmed with a finite element result for 10% static with 5% dynamic eccentricity presented in the next section. For this condition the dynamic eccentricity

components appeared in the spectrum but the static eccentricity components stayed at their purely static eccentricity levels to within 0.9dB (within the 1dB tolerance).

It is interesting to note that in comparing modelled with experimental results the relative difference between the 1072Hz and the 1172Hz was slightly different. At 10% static eccentricity the measured 1172Hz component was 3dB larger than the 1072Hz whereas the predicted 1172Hz component was only 0.1dB larger. At 50% static eccentricity the measured 1172Hz component was 2.8dB larger than the 1072Hz whereas the predicted 1172Hz component was now 5dB larger. An initial thought was that the presence of dynamic eccentricity in the test-rig was causing this, although the aforementioned result removed this possibility.

Although the finite element analysis was providing consistently closer agreement between measured and predicted current component magnitudes reasons were still investigated for the remaining discrepancy between the current magnitudes. It had to be taken into account that there was a slightly higher level of static eccentricity present in the test-rig motor compared to the finite element model due to the inherent level of static eccentricity. This was estimated at 5 to 10%, therefore, the measured magnitudes would always be slightly higher than predicted. From Table 5.3 it can be estimated that the experimental results would be 1 to 2dB higher due to the extra static eccentricity.

Initial investigations into the remaining difference in the components focused on the motor parameters inputted into the finite element analysis, in particular the stator resistance and stator end-winding leakage reactance. As explained in Chapter 3 considerable care was taken to ensure the most accurate values were obtained. The fact that the agreements for the 50Hz component and many of the high frequency components were good, further increased confidence in these values and it was not thought that these could be realistically improved upon. The main cause of the difference was later found to be associated with the test-rig motor. Further experimental

investigations revealed that temperature effects were causing the rotor structure to expand which was affecting the magnitudes of the current components measured.

The experimental results shown in Figures 5.2, 5.3, 5.4 and in Table 5.3 were taken after a 3 hour run up of the test-rig motor (continuous operating conditions). During another set of experiments it was observed that as the motor was left to run the magnitude of the static eccentricity components increased. The motor was stopped and feeler gauges used to measure the airgap which was found to have reduced in length from 22 thou to approximately 20 thou. This reduction in the airgap length was effectively increasing the static eccentricity level in the motor. Investigations revealed that the dynamic eccentricity components were unaffected. It was thought that the copper fabricated rotor was expanding in diameter with prolonged heat. The current component magnitudes were measured again after the motor was up to operating temperature (80°C). This was after 20 minutes running as it was a small motor (11kW). Table 5.4 shows the effect that these different conditions had on the magnitude of the current components at 10% static eccentricity.

Frequency component (Hz)	Measured magnitude after 3 hour run up (80°C) (dB)	Measured magnitude after 20 minutes (motor up to temperature 80°C)) (dB)	Calculated magnitude from the FEA (dB)
1072	71.1	<b>67.0</b>	68.5
1172	74.1	<b>70.8</b>	68.6
1272	56.6	<b>55.6</b>	52.9

Table 5.4 Improvement in Agreement between Measured and Predicted Results for 10% Static Eccentricity after the Over Heating Problem was Identified

In summary, the temperature of the copper rotor was the same after 20 minutes and 3 hours but in the latter the iron infrastructure had risen to the same temperature. This

resulted in the expansion of the rotor and an increase in static airgap eccentricity (decrease in minimum airgap length). This is the reason for the higher levels after 3 hours.

It can be seen from these results that the measured current magnitudes were now significantly closer to the predicted levels, 1072Hz now only 1.5dB different compared to 4.1dB before. The differences shown in Table 5.3 are actually less than shown for the static eccentricity variations at 10, 25, 37 and 50% eccentricity. All results from this point forward (static and dynamic eccentricity combinations) were taken after a 20 minute run up.

Finally, a finite element analysis was performed at 25% static eccentricity for lighter loads to compare with the experimental results and to investigate the ability of the analysis to model the components. The component magnitudes decreased in magnitude as the speed increased. Tests were performed at 1372, 1422 and 1472rpm. A comparison between measured and modelled current magnitudes for 1372rpm is shown in Table 5.5 and the decrease in magnitude for the component calculated with  $n_{ws} = -1$  with increasing speed (lighter load) is shown in Figure 5.10. (The experimental results shown are higher than actual as they were taken after the 3 hour run up). These results further confirmed the finite element analysis ability to model the motor accurately under a wide variety of conditions.

Frequency Component (Hz)	Measured Magnitude (dB)	Calculated Magnitude (dB)	Difference (dB)
50	117.8	118.2	0.4
1116	76.7	74.7	2.0
1216	80.3	76.0	4.3
1316	60.7	54.4	6.3

Table 5.5 Comparison of Measured and Predicted Current Component Magnitudes at 1372rpm ( $s = 0.085$ )

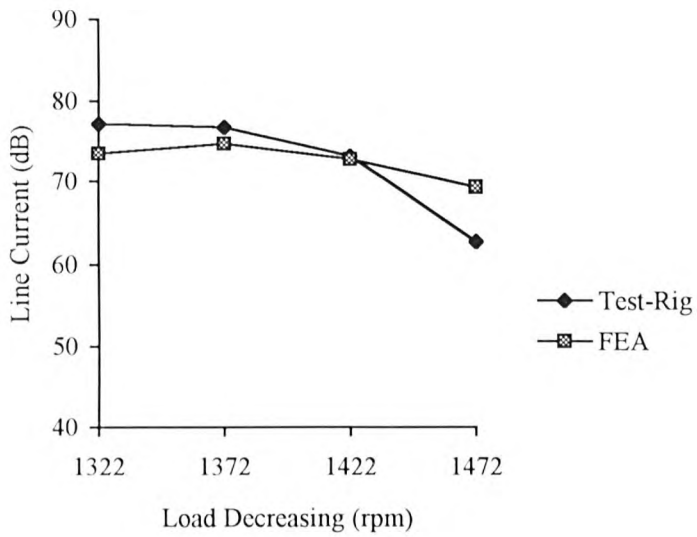


Figure 5.10 Decrease in Magnitude of the Current Component Calculated with  $n_{ws} = -1$  with Load for the Measured (Test-Rig) and Calculated (FEA) Cases

m - measured (x% se with 5% de)		c - calculated (se only)				se - static eccentricity (%)				diff. - difference		
se (%)	50 Hz (m) (dB)	50 Hz (c) (dB)	<i>dB diff</i> (dB)	1072 (m) (dB)	1072 (c) (dB)	<i>dB diff</i> (dB)	1172 (m) (dB)	1172 (c) (dB)	<i>dB diff</i> (dB)	1272 (m) (dB)	1272 (c) (dB)	<i>dB diff</i> (dB)
10	121.2	121.0	0.2	71.1	68.5	2.6	74.1	68.6	5.5	56.6	52.9	3.7
25	121.2	121.0	0.2	77.2	73.5	3.7	80.1	76.5	3.6	62.6	59.9	2.7
37	121.2	121.0	0.2	81.6	75.4	6.2	84.8	79.5	5.3	67.8	63.6	4.2
50	121.2	121.0	0.2	83.3	77.7	5.6	86.1	82.7	3.4	69.8	66.8	3.0

Table 5.3 Comparison between the measured and predicted (FE analysis) magnitudes of the 50 Hz supply component of current and current components which are a function of static airgap eccentricity

## 5.4 Static and Dynamic Eccentricity Variations

### 5.4.1 Experimental Results

This section investigates the effects of combinations of static and dynamic eccentricity on the current spectra. The static eccentricity results were for an inherent level of 5% dynamic eccentricity, for these investigations this level was increased to 25% dynamic eccentricity and two levels of static eccentricity (10% and 25%) were investigated. As previously mentioned all results now presented were taken after a 20 minute run-up by which time the motor was at its operating temperature of 80°C. Dynamic eccentricity was introduced into the test-rig by eccentrically machining heat shrink collars where the rotor runs in the bearing housing. This procedure was more valid than machining the actual rotor as was the case with Cameron's work [19] which would affect the magnetic circuit of the rotor. When the rotor collars were machined to introduce 25% dynamic eccentricity it was possible that the inherent level of 5% dynamic eccentricity could be affected (reduced) by this procedure. Consequently, the results for dynamic eccentricity at 25% could be at 25% dynamic eccentricity or at a slightly higher level. When discussing the results the inherent level is taken as 5% and results for introduced dynamic eccentricity are taken at 25%.

When dynamic eccentricity was present ( $n_d = \pm 1$  in Equation 2.2) additional components appeared either side of the components which are a function of static eccentricity. In the previous results with 5% dynamic eccentricity these components were present although they were not prominent enough to be highlighted in the spectra. The magnitude of the dynamic components for 10% static eccentricity and 5% dynamic eccentricity are shown in Table 5.6, these will be further discussed shortly.

Frequency Component (Hz)	$n_{ws}$ $n_{sa}$ $n_d$ Equation 2.2	Magnitude (dB)	Magnitude (dB)	Magnitude (dB)
		10% se 5% de	10% se 25% de	25% se 25% de
50	-	121.0	121.0	121.0
de 1050	-1 0 -1	50.8	44.4	41.8
se 1072	-1 0 0	67.0	66.4	75.9
de 1094	-1 0 +1	54.6	75.0	74.3
de 1150	+1 0 -1	40.4	39.7	42.8
se 1172	+1 0 0	70.8	69.0	78.8
de 1194	+1 0 +1	59.0	77.0	76.5
de 1250	+3 1 -1	31.1	44.6	37.7
se 1272	+3 1 0	55.6	52.4	61.8
de 1294	+3 1 +1	51.2	59.3	60.4

Table 5.6 Magnitudes of the Current Components from the Test-Rig Motor for Combinations of Static (se) and Dynamic (de) Eccentricity

Table 5.6 shows the increase in the dynamic eccentricity components with the change from 5% to 25% dynamic eccentricity (fixed static of 10%) in the test-rig motor. These components, in particular those with  $n_d = 1$ , were clearly dependant on the dynamic eccentricity level, for instance, the component at 1094 Hz increased by 20.4dB and the 1194Hz component increased by 18.4dB for a 20% increase in dynamic eccentricity. This was clear evidence of the effect of dynamic eccentricity (20dB = 10 times linear). (The lower dynamic eccentricity components (1050Hz etc.) were present in the spectra but they were too small to be clearly highlighted). The effect on the components with a fixed level of dynamic (25%) with increasing static was investigated, Figures 5.11 and 5.12 and Table 5.6 show the spectra of the current for 10% static with 25% dynamic and 25% static with 25% dynamic respectively. With a 15% increase in static and a fixed dynamic of 25% the static eccentricity components increased in magnitude and the dynamic components remained approximately at the same level. For instance, the 1172 Hz (static component) increased by 9.8dB and the 1194Hz decreased by 0.5dB, whereas the 1194Hz component increased by 18.0dB when dynamic eccentricity was increased from 5% to 25%.

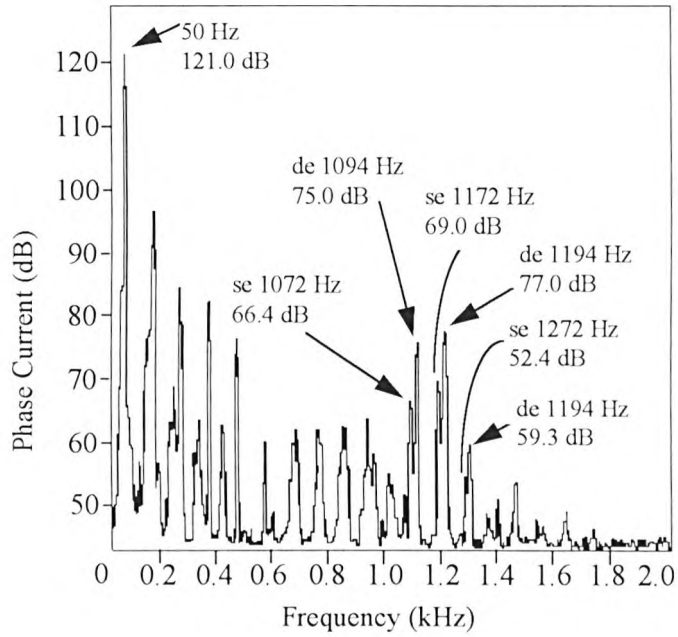


Figure 5.11 Current Spectrum from Test-Rig for 10% Static and 25% Dynamic Eccentricity, Full-Load, 1322 rpm

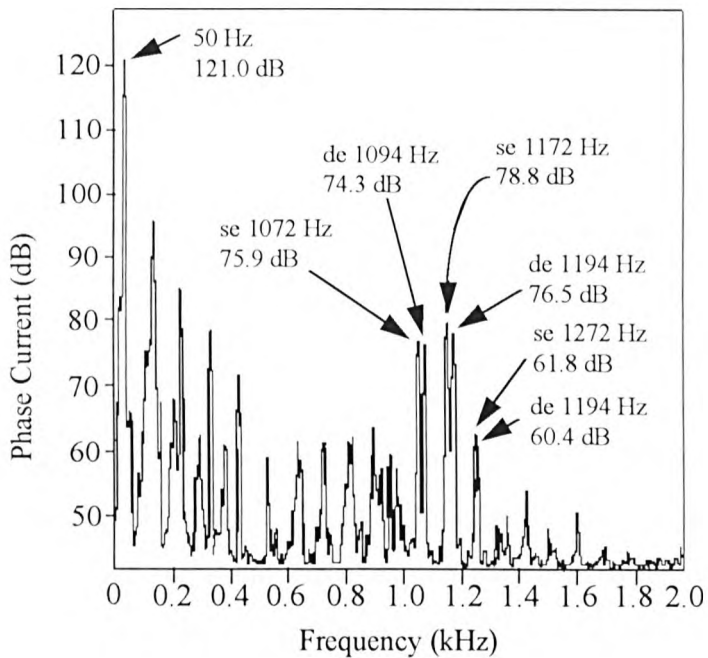


Figure 5.12 Current Spectrum from Test-Rig for 25% Static and 25% Dynamic Eccentricity, Full-Load, 1322 rpm

These results indicated that the static and dynamic eccentricity components in the test-rig motor were not a function of each other. For instance, increasing the static eccentricity with fixed dynamic eccentricity (25%) did not result in the dynamic eccentricity components increasing nor did increasing the dynamic with fixed static result in the static eccentricity components increasing. The basic pole-pair analysis predicted that the dynamic eccentricity components would not be compatible with the stator winding. In terms of the lower dynamic eccentricity components this appears to be correct as these components are not immediately visible in the spectrum and at a level of 40 to 50dB are 70 to 80dB down on the magnitude of the fundamental component. In this region they are just about at noise level. From Table 5.6 it can be seen that unlike the higher dynamic eccentricity components, these lower frequency components did not clearly increase in magnitude with the jump from 5% to 25% dynamic with a fixed static level of 10% or stay constant in magnitude with the change in static eccentricity with fixed dynamic eccentricity. For instance, with the change from 10% static and 5% dynamic to 10% static and 25% dynamic, the 1050Hz decreased 6.4dB, the 1150Hz decreased 0.7dB, only the 1250Hz increased by 13.5dB. However, with constant dynamic eccentricity and an increase in the static eccentricity the 1250Hz decreased 6.9dB.

Contrary to the pole-pair analysis prediction, all the upper dynamic components were clearly present in the spectra. As explained for the 1172Hz component for the static eccentricity variations, their presence could be due to them actually being compatible with the stator which the basic pole-pair analysis failed to predict or to second order effects (winding asymmetry) in the test-rig motor. The finite element analysis leads to further understanding of this result. The basic pole-pair analysis could not predict the pole-pairs associated with the static eccentricity components when dynamic and static eccentricity were present together, however, each static eccentricity component was clearly present in the spectra for the test-rig motor. The pole-pair analysis is further investigated as the finite element results are discussed.

The effect of load variations on the components, which at 1322 rpm occurred at 1150Hz, 1172Hz and 1194Hz, for fixed static (25%) and dynamic (25%) eccentricity level is shown in Figure 5.13.

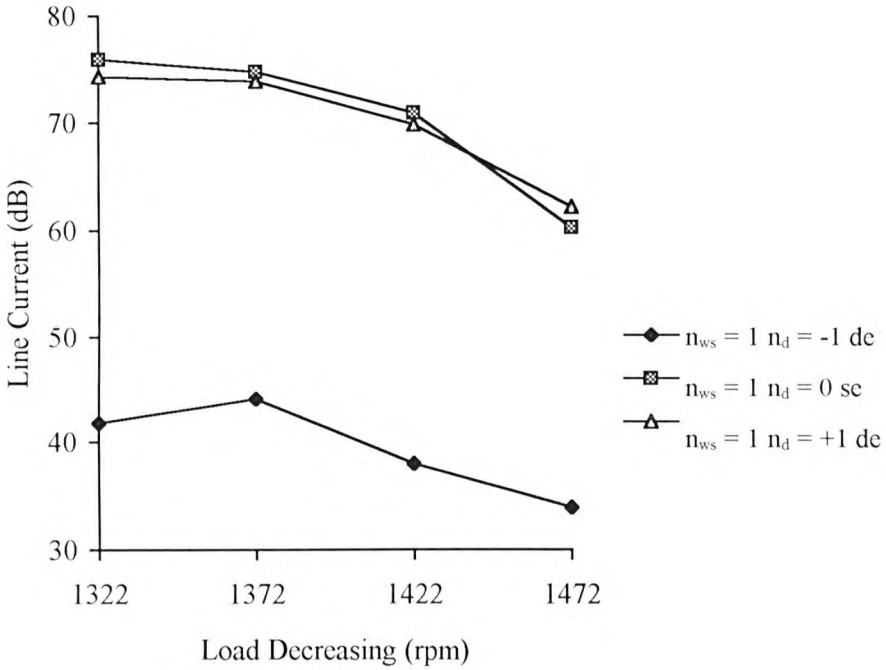


Figure 5.13 Effect of Load on Static (se) and Dynamic (de) Eccentricity Components

As expected the current component magnitudes decreased with lighter loads. A similar trend as for the static eccentricity components was noticed in that the fall off was least between 1322 and 1372rpm (the 1150Hz actually increased slightly). A finite element analysis was not performed for static and dynamic eccentricity combinations at reduced load. This was partly a CPU time consideration and also the results for lighter loads with static eccentricity at 25% had proved that the analysis was capable of modelling the motor on lighter load, there was no reason to presume that it could not do the same for the dynamic eccentricity components.

#### 5.4.2 Finite Element Analysis Results, Comparison and Discussion

Initially purely dynamic eccentricity was modelled at 1322rpm using the finite element analysis to confirm that the condition was being modelled correctly. Also, the effects of purely dynamic eccentricity were investigated to see if the components behaved differently from when static and dynamic eccentricity were considered together. The results for 5% and then 25% dynamic eccentricity are presented in the next section, “Purely Finite Element Analysis Results.” In brief, the dynamic eccentricity components were present in the spectra and at the same level as when static eccentricity was also present. This confirmed the independence of the static and dynamic eccentricity components on each other.

A finite element analysis was performed at 10% static and 5% dynamic, 10% static and 25% dynamic and finally 25% static and 25% dynamic eccentricity for the full load condition, 1322rpm. Figures 5.14 and 5.15 show the induced stator emf for 10% static with 25% dynamic and 25% static with 25% dynamic eccentricity, respectively. The frequencies of the components were the same as predicted by Equation 2.2 and obtained experimentally. The same trend was followed, with the static eccentricity components clearly present and increasing with the 15% increase in static eccentricity. The upper dynamic components were clearly present and remained approximately constant in magnitude. Similarly, the lower dynamic components, although present, were not immediately visible in the spectra. (The author apologies for the poor quality of the y axis label in Figure 5.15).

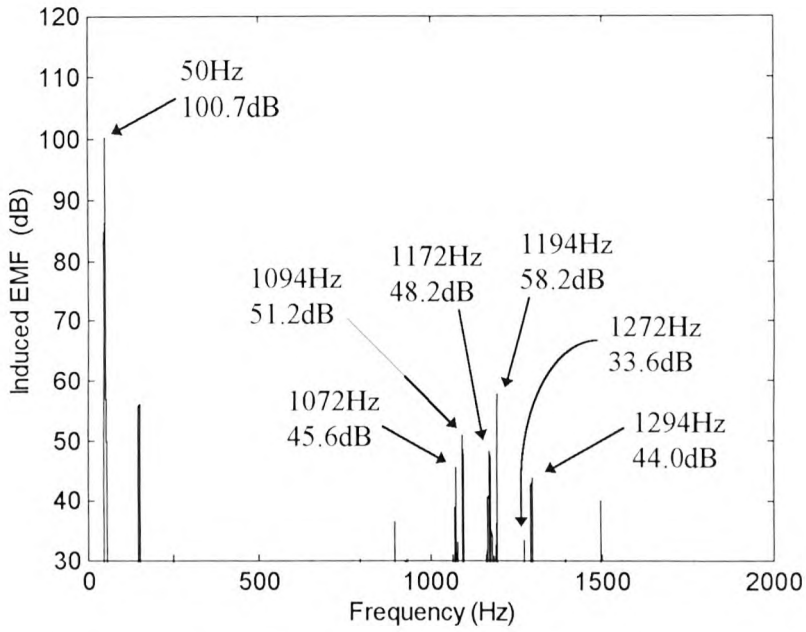


Figure 5.14 EMF Spectrum from FE Analysis for 10% Static and 25% Dynamic Eccentricity, Full-Load, 1322 rpm

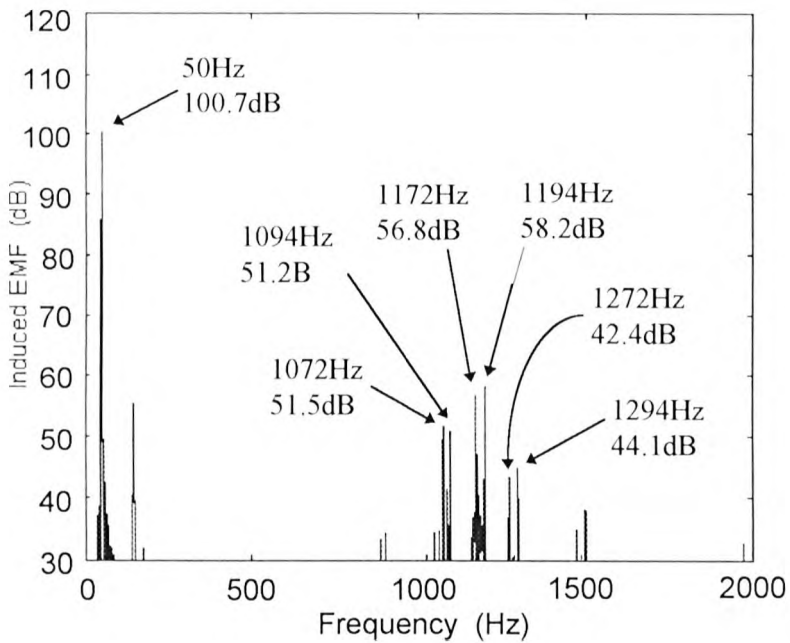


Figure 5.15 EMF Spectrum from FE Analysis for 25% Static and 25% Dynamic Eccentricity, Full-Load, 1322 rpm

The finite element analysis current magnitudes for the three modelled fault conditions are shown in Table 5.7. Direct comparisons with the test-rig motor current magnitudes will be made later.

Frequency Component (Hz)	$n_{ws}$ $n_{sa}$ $n_d$ Equation 2.2	Magnitude (dB) 10% se 5% de	Magnitude (dB) 10% se 25% de	Magnitude (dB) 25% se 25% de
50	-	120.7	120.7	120.7
de 1050	-1 0 -1	45.1	46.6	52.2
se 1072	-1 0 0	67.6	67.0	72.9
de 1094	-1 0 +1	57.7	72.4	72.4
de 1150	+1 0 -1	40.5	39.9	48.7
se 1172	+1 0 0	68.3	68.9	77.4
de 1194	+1 0 +1	63.7	78.7	78.7
de 1250	+3 1 -1	33.1	31.1	46.8
se 1272	+3 1 0	53.5	53.5	62.3
de 1294	+3 1 +1	48.0	63.7	63.9

Table 5.7 Magnitudes of the Current Components from the Finite Element Analysis for Combinations of Static (se) and Dynamic (de) Eccentricity

In relative terms this table illustrates a favourable comparison with the trends exhibited by the test-rig motor components (Table 5.6). For instance, the 1094Hz component increased by 20.4dB in the test-rig when the eccentricity levels were changed from 10% static with 5% dynamic to 10% static with 25% dynamic, in comparison the calculated component increased by 14.7dB. The 1194Hz increased 18.4dB experimentally and 15dB calculated for the same change. The finite element analysis was clearly modelling the effect of increasing dynamic eccentricity. As for the experimental results the static eccentricity components remained steady in magnitude with constant 10% static despite the 25% increase in dynamic eccentricity. When the dynamic eccentricity remained at 25% and the static eccentricity increased from 10% to 25%, the static eccentricity component at 1172Hz increased by 8.5dB which is a favourable comparison with the measured increase of 9.8dB. The upper dynamic eccentricity components remained

steady, less than 0.2dB of a change, however, as for the test-rig motor the lower dynamic eccentricity components exhibited a very random pattern.

Tables 5.8, 5.9 and 5.10 present comparisons for the measured and calculated current magnitudes for 10% static with 5% dynamic, 10% static with 25% dynamic and 25% static with 25% dynamic eccentricity, respectively. Inspection of these tables reveal excellent agreement between the measured and calculated current magnitudes for all frequencies the only exception being some of the lower dynamic eccentricity components. The range of differences for the static eccentricity components was 0.6dB to 3dB, for the upper dynamic components 1.7dB to 4.7dB and finally for the lower dynamic eccentricity components 0.1dB to 13.5dB. The finite element results agreed with the experimental results and once again these results differed from the basic pole-pair analysis predictions.

Frequency Component (Hz)	Current Magnitude from Test-Rig (dB)	Current Magnitude from FEA (dB)	dB Difference (dB)
50	121.0	120.7	0.7
1050	50.8	45.1	5.7
1072	67.0	67.6	0.6
1094	54.6	57.7	3.1
1150	40.4	40.5	0.1
1172	70.8	68.3	2.5
1194	59.0	63.7	4.7
1250	31.1	33.1	2.0
1272	55.6	53.5	2.1
1294	51.2	48.0	3.2

Table 5.8 Comparison between the Measured (test-rig) and Calculated (FEA) Current Components for 10% Static and 5% Dynamic Eccentricity, Full-Load 1322rpm

Frequency Component (Hz)	Current Magnitude from Test-Rig (dB)	Current Magnitude from FEA (dB)	dB Difference (dB)
50	121.0	120.7	0.3
1050	44.4	46.6	2.2
1072	66.4	67.0	0.6
1094	75.0	72.4	2.6
1150	39.7	39.9	0.2
1172	69.0	68.9	0.1
1194	77.0	78.7	1.7
1250	44.6	31.1	13.5
1272	52.4	53.5	1.1
1294	59.3	63.7	4.4

Table 5.9 Comparison between the Measured (test-rig) and Calculated (FEA) Current Components for 10% Static and 25% Dynamic Eccentricity, Full-Load 1322rpm

Frequency Component (Hz)	Current Magnitude from Test-Rig (dB)	Current Magnitude from FEA (dB)	dB Difference (dB)
50	121.0	120.7	0.3
1050	41.8	52.2	10.4
1072	75.9	72.9	3.0
1094	74.3	72.4	1.9
1150	42.8	48.7	5.9
1172	78.8	77.4	1.4
1194	76.5	78.7	2.2
1250	37.7	46.8	9.1
1272	61.8	62.3	0.5
1294	60.4	63.9	3.5

Table 5.10 Comparison between the Measured (test-rig) and Calculated (FEA) Current Components for 25% Static and 25% Dynamic Eccentricity, Full-Load 1322rpm

These results with regard to the pole-pair analysis will now be discussed. In terms of the static eccentricity components with static and dynamic eccentricity together the basic pole-pair analysis could not predict the pole-pairs of the static eccentricity components. Both the experimental and the finite element results indicate that they are indeed compatible with the harmonic pole-pairs of the stator winding. The basic analysis predicted that with static and dynamic eccentricity the pole-pairs associated with the dynamic eccentricity components were all odd and therefore not compatible with the stator winding. The upper dynamic eccentricity components were clearly present in both the experimental and finite element spectra with the lower dynamic components 70 to 80dB down on the fundamental.

Similar reasoning as applied to the 1172Hz static eccentricity component can be used for the appearance of the upper dynamic eccentricity components. In the test-rig motor

their presence could have been put down to second order effects such as winding asymmetry but this could not be the reason for their presence in the finite element results as a perfectly symmetrical winding is modelled. It is fair to assume that these components are actually compatible with the stator (first order harmonic pole-pairs). If the basic pole-pair analysis is extended and  $n_s/n_d$  is not just assumed to be one then compatibility can occur. The only other factor to be considered is saturation. As explained earlier the effect or not of saturation on the pole-pairs of the components cannot be determined. However, they were clearly present at 10% static with 5% dynamic where localised saturation would be low if at all present. Generally good agreement was obtained for the upper dynamic eccentricity components.

The lower dynamic eccentricity components presented a slightly different picture. The basic pole-pair analysis predicted that they would not be compatible with the stator,  $n_s/n_d = 1$ . The experimental and the finite element results agreed with this as they were very low in magnitude (at noise level) for both cases. In the comparison between finite element and experimental results there was no consistent trend, for instance, the experimental magnitudes always being larger than the finite element current magnitudes. If that were the case then the large disagreements could be attributed to the components appearing experimentally due to second order effects (supply imbalance, winding asymmetry) which were not modelled in the finite element analysis. The agreement is generally good at 10% static with 5% dynamic but with 25% dynamic and 10% or 25% static eccentricity some poor results were obtained. For instance, at 10% static with 25% dynamic the 1250Hz component was 13.5dB larger experimentally and at 25% static with 25% dynamic it was 9.1dB larger in the finite element results. This could perhaps have been an effect of the higher dynamic eccentricity level. An explanation for this was difficult to find especially as there was no trend to the differences for the lower dynamic eccentricity components and the good agreement obtained for the upper dynamic components.

The next section presents the results of finite element investigations into models of purely dynamic eccentricity, a concentric motor and an extremely high level of static eccentricity. The analyses were based on the model of the test-rig motor, however, no experimental comparisons could be made as the situations modelled could not be attained in the test-rig motor. Conclusions on the results presented in this Chapter will then follow.

## **5.5 Purely Finite Element Investigations**

### **5.5.1 Purely Dynamic Eccentricity**

The finite element analysis was performed on a model of the test-rig motor for 5% and then 25% dynamic eccentricity (no static present). This was to check that the modified version of the finite element analysis program was correctly modelling dynamic eccentricity. It also provided an opportunity to investigate the effect, if any, of purely dynamic eccentricity on the frequency components in the motor. This could not be performed experimentally as there was an inherent level of static eccentricity present. The stator induced emf spectra for 5% and then 25% dynamic eccentricity are shown in Figures 5.16 and 5.17, respectively.

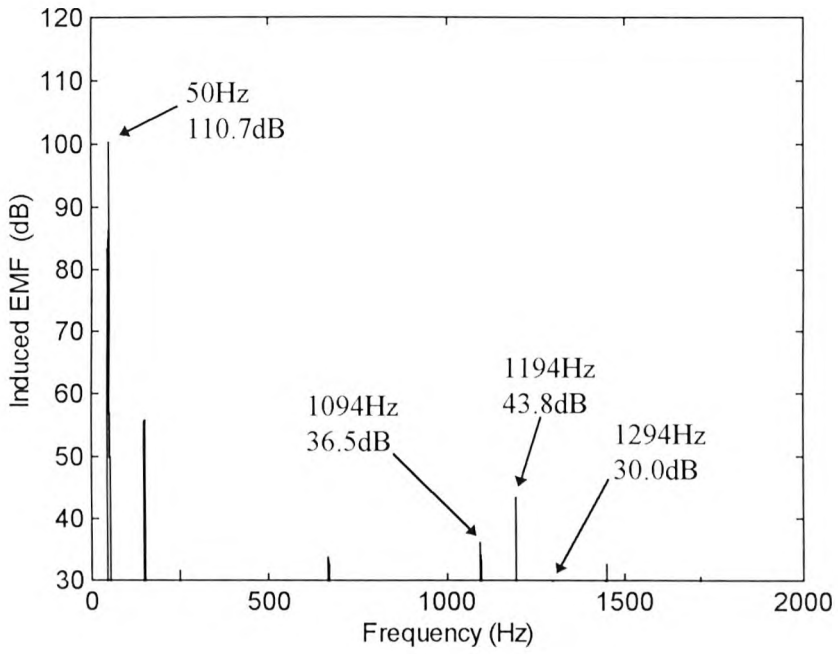


Figure 5.16 EMF Spectrum from FE Analysis for 5% Dynamic Eccentricity, Full-Load.

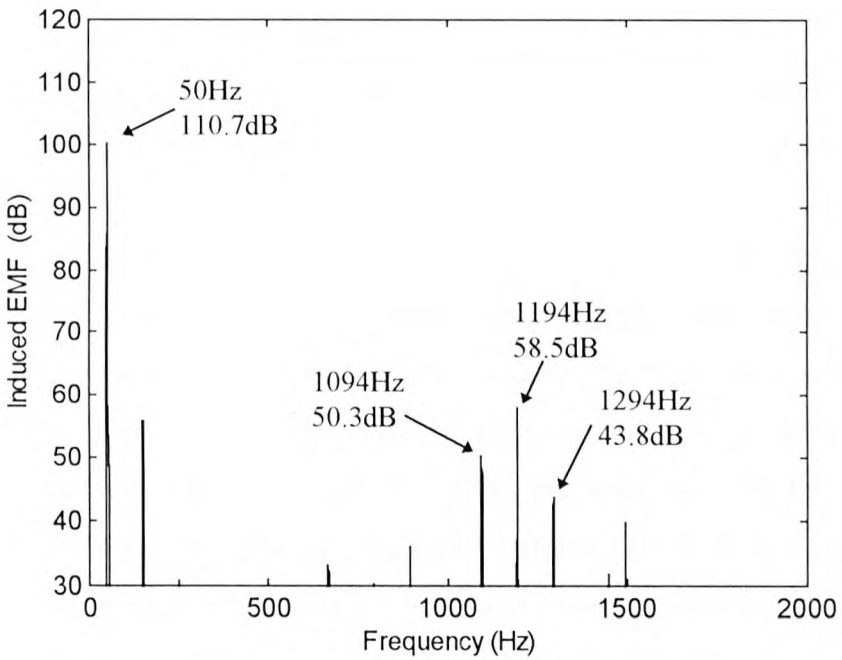


Figure 5.17 EMF Spectrum from FE Analysis for 25% Dynamic Eccentricity, Full-Load.

The current magnitudes of these components were calculated from the emf spectra and are shown in Table 5.11, the current component magnitudes from the finite element analysis for combinations of static and dynamic eccentricity as shown in Table 5.7 are also presented for comparison.

Dynamic Eccentricity Frequency Component (Hz)	Dynamic Eccentricity Level (%)	EMF Magnitude from FEA (dB)	Calculated Current Magnitude (dB)	Current Mag. shown in Table 5.7 (% de / % se) (dB)
1094	5	36.5	57.7	57.7 (5/10)
1194	5	43.8	64.3	63.7 (5/10)
1294	5	30.0	49.8	48.0 (5/10)
1094	25	50.3	71.6	72.4 (25/10)
1194	25	58.5	79.0	78.7 (25/10)
1294	25	43.8	64.3	63.7 (25/10)

Table 5.11 Current Magnitudes of the Dynamic Eccentricity Components from the Finite Element Analysis with 5% and then 25% Dynamic Eccentricity.

These results clearly showed that the modifications to the finite element analysis program were correctly modelling dynamic eccentricity. The components were occurring at the correct frequencies as predicted by the Equation 2.2 and obtained experimentally. They also clearly increased in magnitude with a 20% increase in dynamic eccentricity. The basic pole-pair analysis predicted that only the 1094Hz and the 1294Hz components would be compatible with the first order harmonic pole-pair numbers of the stator winding. The 1194Hz was clearly present in the spectra once again revealing the limitations of the analysis. For this component with  $n_d = 1$  the pole-pairs were  $89 + 1$  and  $17 + 1 = 90$  and  $18$  which were not compatible with the stator.

However, if the dynamic eccentricity integer is taken as 5 then the pole-pairs become 94 and 22, both of which are compatible.

The magnitude of the upper dynamic eccentricity components remained at the same level (to within processing tolerances) whether static eccentricity was present or not. Even the higher level of static eccentricity had no effect. For instance the 1194Hz had a magnitude of 79.0dB for 25% dynamic eccentricity, and 78.7dB for both 10% static with 25% dynamic and 25% static with 25% dynamic. This was confirmation of the independence of the upper dynamic eccentricity components on the level of static eccentricity.

The lower dynamic eccentricity components were not present in the spectra. For combinations of static and dynamic eccentricity they occurred at induced emf levels of 26 to 30dB, however, for purely dynamic eccentricity even when the spectra was displayed from 0dB to 110dB they were still not visible. In linear terms 0dB compared to 100dB is 100,000 times less in magnitude. For the case of the lower dynamic eccentricity components the presence of static eccentricity did have an effect as only with static eccentricity present did they appear in the frequency spectra. This was a very interesting result that could not have been predicted experimentally or by the pole-pair analysis. It is also further evidence that tracking the lower dynamic eccentricity components from a condition monitoring perspective is not advisable.

The principal slot passing frequencies which are a function of static eccentricity and slotting were not present in the spectra. This suggested that the pole-pairs associated with these frequencies were incompatible with the stator winding. It could be that the presence of dynamic eccentricity was affecting the pole-pairs of the principal slot passing frequencies or that they were not compatible unless static eccentricity was present. This will be further discussed in the next subsection.

### 5.5.2 A Concentric Motor

A finite element analysis was performed on the test-rig motor model for a totally concentric rotor, that is, 0% static and 0% dynamic eccentricity. The static or dynamic eccentricity components were not present in the spectrum for the induced stator emf. The non-appearance of the dynamic eccentricity components was expected as they are only a function of dynamic eccentricity. The principal slot passing frequencies could have been present due to slotting effects, however, as they were not present, the pole-pairs associated with these frequencies were obviously not compatible with the first order harmonic pole-pair numbers of the stator winding. In this case the basic pole-pair analysis predicted this outcome correctly. The pole-pairs for the principal slot passing frequencies are always odd:

$$\begin{aligned}m &= R \pm S \pm n_{0s} p \\ &= 51 \pm 36 \pm 2 \times 1 \\ &= 87 \pm 2 \text{ or } 15 \pm 2\end{aligned}$$

The presence of saturation would not result in the pole-pairs of these frequencies being compatible as they would always remain odd. The combination of 51 rotor bars with 36 stator slots reduced the harmonic content of the stator emf which from a motor design point of view is desirable. The next chapter presents the results of a finite element study into the effects of different numbers of rotor bars on the principal slot passing frequencies which revealed that some combinations of stator and rotor slots are particularly undesirable.

### 5.5.3 70% Static Eccentricity

The highest level of introduced airgap eccentricity into the test-rig motor was 50% either as 50% static or 25% static and 25% dynamic. This limited the investigation of the effects of very high airgap eccentricity on the motor due to safety reasons. However, the finite element analysis could be used to model the effects of high airgap eccentricity in an electrical and magnetic sense. It was found that in order to still create decent shaped elements in the airgap that a maximum level of 70% airgap eccentricity could be modelled. As computation time was only available to perform one solution in this area it was decided to introduce this as static eccentricity in the model as in reality a higher static eccentricity level would be more likely to develop than a high dynamic eccentricity level due to very severe bearing wear and noise. Even with the test-rig motor, 50% static was noticeable but not as noticeable as the noise and vibration from 25% static with 25% dynamic eccentricity.

The main focus of interest was if the high static eccentricity resulted in the components behaving differently from at 10% to 50% static eccentricity. Saturation effects could play a part in this as localised saturation around the minimum airgap would be significantly higher than before. The time domain waveform for the induced stator emf is shown in Figure 5.18.

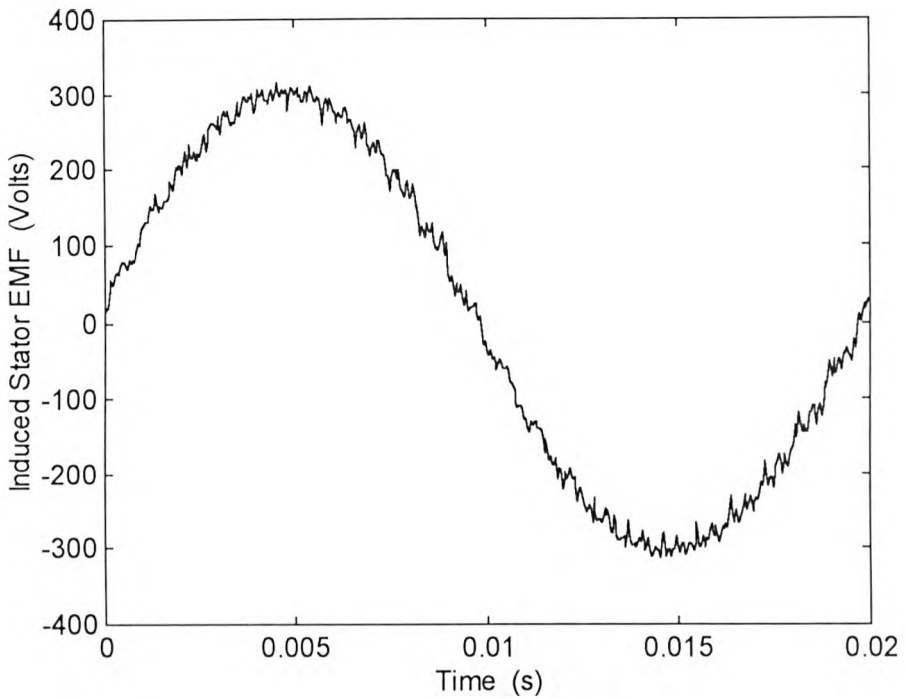


Figure 5.18 Time Domain Representation of Induced EMF at 70% Static Eccentricity

Inspection of this signal reveals a higher harmonic content than was present in the time domain signal for 50% static eccentricity. Saturation is also more visibly present with the form of the waveform either side of the mid cycle zero crossing. The spectrum of the signal is shown in Figure 5.19.

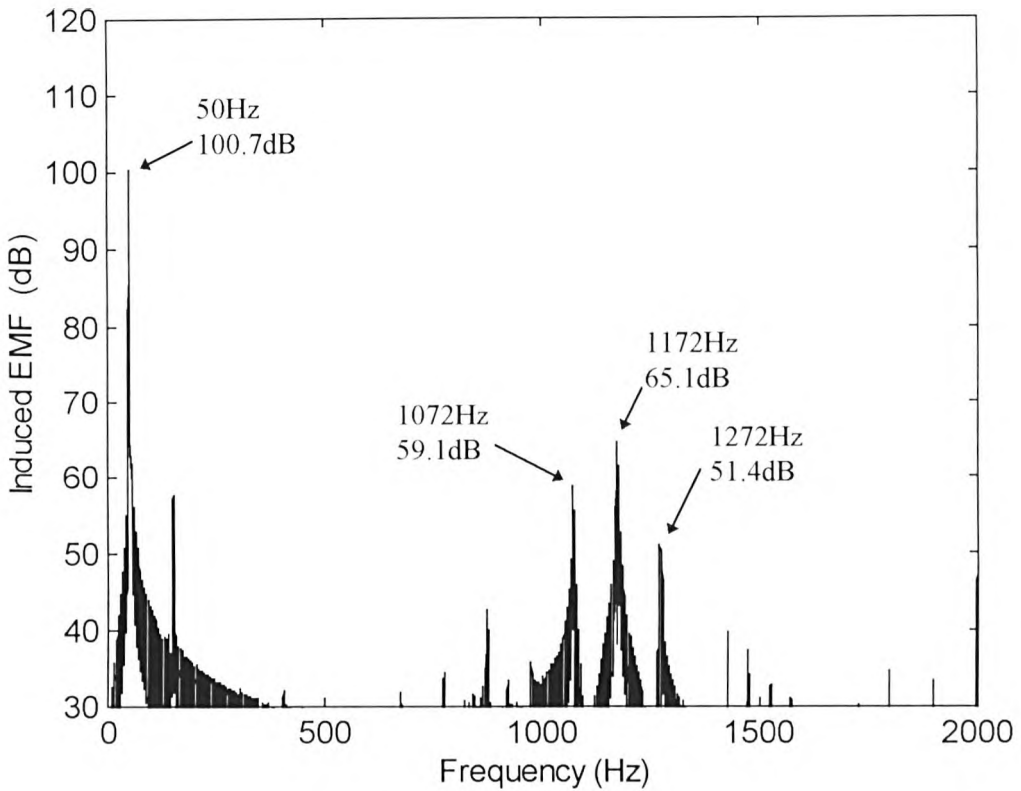


Figure 5.19 EMF Spectrum from FE Analysis for 70% static eccentricity, full-load, 1322 rpm

The components increased again in magnitude from their levels at 50% static eccentricity: the 1072Hz by 2.9dB, the 1172Hz by 3.0dB and the 1272Hz by 4.5dB. They still took on the same trend in that the 1172Hz was largest then the 1072Hz and finally the 1272Hz. It is interesting to note that the 1272Hz component showed the biggest increase from 50% to 70% static eccentricity. This component was a function of the third stator mmf harmonic ( $n_{ws} = 3$ ) which is predominantly produced by saturation effects [100, 101]. Hence, the 1272Hz component was more dependant on saturation than the 1072Hz ( $n_{ws} = -1$ ) or the 1172Hz ( $n_{ws} = 1$ ). Table 5.12 shows the percentage of the 1272Hz magnitude as part of the magnitude of the 1172Hz component at 10%, 50% and 70% static eccentricity. These are based on the current component magnitudes calculated from the emf magnitudes shown in the spectra.

Static Eccentricity (%)	% of the 1172Hz Current Magnitude
10	76.7
50	84.4
70	83.2

Table 5.12 Percentage of the 1272Hz Magnitude with Respect to the 1172Hz Magnitude for 10%, 50% and 70% Static Eccentricity (Finite Element)

This table indicates that as the eccentricity level increased the 1272Hz not only increased in general terms with the others but also became more prominent in the spectrum relative to the other components. This can be attributed to the increase in saturation present at the higher levels of static eccentricity. This was also borne out by the experimental results at 10% static and then 50% static with nominal 5% dynamic eccentricity as Table 5.13 illustrates. (These magnitudes were obtained after a 20 minute run-up).

Frequency (Hz)	Current Magnitude at 10% static (dB)	Current Magnitude at 50% static (dB)	1272Hz magnitude as a % of the 1172Hz (%)
1172	70.8	84.8	78.5 at 10%
1272	55.6	69.1	81.5 at 50%

Table 5.13 Percentage of the 1272Hz Magnitude with Respect to the 1172Hz Magnitude for 10% and 50% Static Eccentricity with Nominal 5% Dynamic for the Test-Rig Motor

With the higher level of static eccentricity the 1272Hz component became slightly more prominent as a percentage of the 1172Hz component in the spectrum. The percentages shown above were also in close agreement with those calculated for the finite element analysis which suggested that the modelling of saturation in the finite element analysis

was close to that in the test-rig motor. Overall, this result showed that saturation definitely increased with the higher levels of airgap eccentricity but not to the point where the general form of the spectra changed, for instance, the 1272Hz became the largest present.

## 5.6 Conclusion

The results presented in this Chapter have illustrated the successful application of a finite element analysis to model a three-phase induction motor with airgap eccentricity. The frequency and magnitude of the components which are a function of static and dynamic eccentricity have been successfully modelled and are in good agreement with those obtained experimentally. Consistently closer agreement has been obtained between measured and calculated current component magnitudes than was achieved using classical methods. The successful modelling of combinations of static and dynamic eccentricity is particularly significant as the two forms of the condition are present in all industrially based motors.

Although there is still a difference in absolute terms between the measured and calculated current component magnitudes, in terms of the increase in the magnitude of the components with increasing airgap eccentricity the relative difference is negligible. For instance, the experimental results showed that the dynamic eccentricity component at 1194Hz increased by 18dB when the dynamic eccentricity was increased by 20% with a fixed static of 10%. The finite element analysis predicted that the 1194Hz dynamic eccentricity component was 78.7dB compared to the measured value of 77dB. Hence, the difference of 1.7dB between experimental and calculated absolute values for a given static and dynamic combination was negligible compared to the increase of 18dB due to the increase in dynamic eccentricity. In terms of a monitoring strategy this is an excellent agreement.

In addition to the reliable prediction of the current components which are a function of airgap eccentricity the purpose of this research was also to use the finite element analysis to further the understanding of the fault mechanism and investigate the limitations of the classical mmf and permeance wave approach. These objectives have been achieved as fault conditions such as purely static or dynamic eccentricity, a concentric motor and very high static eccentricity have been modelled using the finite element analysis. These conditions could not be obtained in reality, however, the finite element analysis provided some interesting information which could not have been obtained experimentally or by the classical approach. For instance, the lower dynamic eccentricity components only become more prominent if static eccentricity is also present. This result and other observations both experimentally and from the finite element analysis revealed that the monitoring of the lower dynamic eccentricity components for airgap eccentricity detection is not recommended.

The limitations of the basic pole-pair analysis were confirmed by the finite element results which agreed with the experimental results. The basic pole-pair analysis has its place to give an approximation of the pole-pairs associated with the frequency components, however, as these results have shown it is the finite element analysis which provided the explanations for the experimental observations.

Overall, the test-rig motor was successfully modelled and the application of finite element analysis to model airgap eccentricity was verified. This was a good foundation for applying the finite element analysis to a large (over a 1 MW) industrially based motor to predict the magnitude of the current components as a function of airgap eccentricity. The prediction of the magnitude of the current components for a large motor had not been previously attempted either by classical techniques or by a finite element analysis approach. This was performed as part of this research, details of which are presented in Chapter 7. Chapter 6 details finite element investigations into the effect on the current components of the number of rotor bars and the rotor slot design.

# Chapter 6

## Finite Element Analysis of the Effects of Rotor Design on the Airgap Eccentricity Frequency Components

### 6.1 Introduction

This chapter presents a finite element investigation into the effects of the rotor design on the frequency components in the current which are a function of airgap eccentricity. This was based on the finite element model of the test-rig motor and the number of rotor bars were varied for the 36 slot stator. The rotor slot design was altered for the 51 bar rotor with the 36 slot stator. The finite element analysis and experimental tests for the test-rig motor and the large industrial based motor were the main focus of this research. However, these investigations were worthwhile to further increase knowledge of the factors affecting the components which are a function of airgap eccentricity. The information gained would be valuable in terms of the on-line monitoring of different motors in industry. For instance, in comparison to the overall increase in the magnitude of the components with increasing airgap eccentricity, how significant are the

magnitude differences of components for different slot designs at a given level of airgap eccentricity.

These investigations could only be carried out using a finite element analysis as classical methods were limited in their modelling of the actual motor design, for instance, the true rotor slot design, hence the effects of different slot designs could not be modelled. This work further contributes to new knowledge in the area as these investigations have not been previously performed.

## **6.2 Number of Rotor Bars Investigation**

### **6.2.1 Introduction**

The effect of rotor/stator slot number combinations has been well documented in terms of induction motor behaviour: crawling, cogging, stray losses, noise and vibration [62, 63, 88] and certain rotor/stator combinations have been proven to be very undesirable. For instance, if the number of rotor bars equals the number of stator slots a motor may refuse to start due to cogging, whereby the slot harmonic fluxes give rise to strong alignment forces when the machine is at rest which may exceed the tangential accelerating forces. The effect of different number of rotors bars on the magnitude of the UMP was also investigated by Arkkio [102] using a finite element analysis of a motor. The findings concurred with the knowledge that odd numbers of rotor bars tend to increase the UMP more than an even number of rotor bars [62, 63].

Ferrah et al [103] carried out an experimental investigation of the effect of rotor design on the magnitude of the rotor slot passing frequencies. This was in connection with non-invasive speed estimation by tracking the rotor slot passing frequencies. The number of rotor bars, skew and the rotor slot design were investigated for a nominally healthy 30kW motor, airgap eccentricity was not introduced. The rotor slot passing

frequencies and associated pole-pairs were calculated using the same classical approach as explained in this research, but only the components with  $n_{ws} = \pm 1$  were investigated and a basic concentric rotor pole-pair analysis performed to calculate the associated pole-pairs. The experimental results obtained clearly showed the effect of the number of rotor bars on the magnitude of the rotor slot passing frequencies. The appearance of frequency components whose pole-pairs were otherwise not compatible with the stator winding was attributed to inherent static eccentricity and third order effects. The results also confirmed the fact the skew reduces the magnitude of the rotor slot passing frequencies. Of interest to the next part of this Chapter were the results for semi-closed and open slot designs. The magnitude of the current components were higher for the semi-closed slot than for the open slot (tunnel slot). As explained later this experimental result was in line with other finite element work and the results obtained in this research.

The aforementioned literature was reviewed and a selection of the different rotor bar numbers to be investigated was made in conjunction with a pole-pair analysis for each rotor. In addition to investigating the introduction of static and dynamic eccentricity with different rotors these investigations also provided an opportunity to further investigate the limitations of the basic pole-pair analysis and the ability of the finite element analysis to overcome these limitations. With respect to these objectives three different rotors were investigated: 50, 43 and then 44 bars, with the 44 bar rotor forming the main focus of the airgap eccentricity variations. The reasons for the selection of these rotors are explained in the following sections, each dedicated to one particular rotor.

The 36 slot model of the test-rig motor stator was used and rotors were investigated with 50, 43 and 44 bars. The overall conductor area for the 51 bar rotor was calculated and this was kept constant with each rotor. Therefore the 44 bar rotor had bars of diameter 7.54mm compared to 7.0mm for the 51 bar rotor. All other rotor parameters such as the conductivity, slot opening width and end-ring dimensions remained the

same. Only the slot diameter and the number of rotor bars were changed. A relative comparison could be made between the magnitudes of the current components for the different rotors as the permeance and hence their magnitude would alter dependant on the number of rotor bars.

### 6.2.2 50 Bar Rotor

The 50 bar rotor was modelled to further investigate the pole-pair and the finite element analysis. A concentric 50 bar rotor was modelled at full load (1322rpm) and a pole-pair analysis performed for this case. The rotor slot passing frequencies occurred at 1052Hz, 1152Hz and 1252Hz and the associated pole-pairs occurred at:

$$m = (R \pm S \pm n_s \pm n_d \pm 2n_{sa}P \pm n_{ts}P) \quad \text{where } n_s = 0, n_d = 0; n_{sa} = 0, n_{ts} = \pm 1, p = 2,$$

$$R = 50 \text{ and } S = 36.$$

$$\therefore m = R \pm S \pm n_{ts} p$$

$$m = 50 \pm 36 \pm 2$$

$$= 86 \pm 2 \quad \text{and} \quad 14 \pm 2$$

Which gives 84 and 12 which corresponds to  $n_{ts} = -1$  and component 1052Hz and also 88 and 16 which corresponds to  $n_{ts} = 1$  and component 1152Hz

For the 1252Hz component:  $n_{sa} = 1, n_{ts} = 1,$

$$m = 50 \pm 36 + (2 \times 1 \times 2) + 2 = 88 + 4 \text{ and } 16 + 4$$

Which gives 92, and 20 for component 1272Hz

For the 51 bar rotor the basic pole-pair analysis predicted that the pole-pairs for the concentric case were all odd and/or divisible by three and therefore not compatible with the stator winding. The result was confirmed by the finite element analysis in that the components were not present in the spectrum. With the 50 bar rotor the components again were predicted to be incompatible. In a balanced winding pole-pairs of harmonic numbers which are even or triplen (2, 3, 6, 8 etc.) should not occur and consequently

for the 50 bar rotor the components should not appear in the stator current. Obviously in a practical motor asymmetries are present allowing the possibility of components with otherwise non-compatible pole-pairs to induce an emf, however, the finite element analysis modelled a perfectly symmetrical winding and supply. Figure 6.1 shows the induced emf spectrum for a concentric 50 bar rotor at 1322rpm.

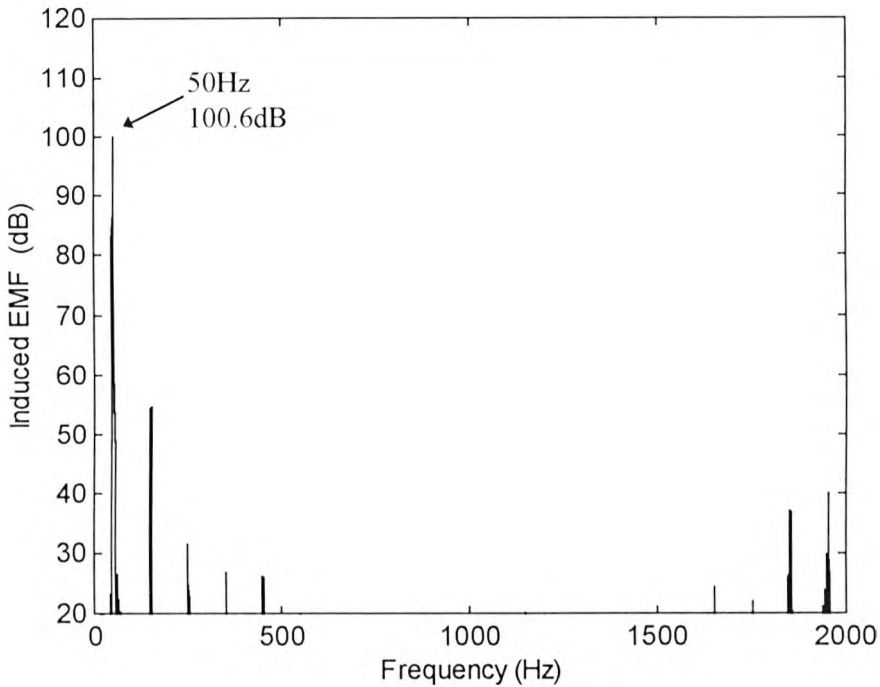


Figure 6.1 EMF Spectrum from FE Analysis for a 50 Bar Concentric Rotor, 1322 rpm

Inspection of the spectrum reveals that the predicted frequency components were not present. The dB display scale was reduced from the normal 30dB to 20dB and they were still not present. Below 20dB was considered to be in the noise region as 20dB is 10,000 times less than the 100dB level or fundamental emf in linear terms.

Further investigations were not carried out for the 50 bar rotor as CPU time was limited and the 43 and 44 bar rotors provided the opportunity for more interesting investigations when static and dynamic eccentricity were included.

### 6.2.3 43 Bar Rotor

It is generally considered that a rotor with an even number of bars (for all but some combinations of stator and rotor slot numbers) is preferable to using a rotor with an odd number of bars [63]. This is due to the possible occurrence of one sided rotating forces with an odd number of bars. However, experimental investigations by Muller [63] showed that motors with odd numbers of rotor slots operated satisfactorily. For instance, 36 stator slots with 43 rotor bars or 48 stator slots with 19 or 33 rotor bars for a four pole motor. The test-rig motor with 36 stator slots and 51 rotor bars was another example of designers using an odd number of rotor bars successfully. Consequently, a 43 bar rotor was modelled with a concentric rotor and then 25% static with 25% dynamic eccentricity was introduced. This provided an opportunity to investigate the behaviour of the frequency components with airgap eccentricity for the 43 bar rotor compared to the 51 bar and to further investigate the pole-pair analysis.

The frequency components which were are a function of slotting and static eccentricity (principal slot passing frequencies) and dynamic eccentricity are shown in Table 6.1 for the 43 bar rotor. Additional components which were not prominent in the spectrum for the 51 bar rotor are highlighted in bold. These components were clearly visible in the emf spectrum for 25% static with 25% dynamic eccentricity with the 43 bar rotor.

Type	Frequency (Hz)	$f_1$	R	$n_d$	s	p	$n_{sa}$	$n_{ws}$
<b>pspf</b>	<b>797</b>	<b>50</b>	<b>43</b>	<b>0</b>	<b>0.1187</b>	<b>2</b>	<b>-1</b>	<b>-1</b>
pspf	897	50	43	0	0.1187	2	0	-1
pspf	997	50	43	0	0.1187	2	0	1
pspf	1097	50	43	0	0.1187	2	1	1
<b>pspf</b>	<b>1197</b>	<b>50</b>	<b>43</b>	<b>0</b>	<b>0.1187</b>	<b>2</b>	<b>2</b>	<b>1</b>
<b>de</b>	<b>775</b>	<b>50</b>	<b>43</b>	<b>-1</b>	<b>0.1187</b>	<b>2</b>	<b>-1</b>	<b>-1</b>
<b>de</b>	<b>819</b>	<b>50</b>	<b>43</b>	<b>1</b>	<b>0.1187</b>	<b>2</b>	<b>-1</b>	<b>-1</b>
de	875	50	43	-1	0.1187	2	0	-1
de	919	50	43	1	0.1187	2	0	-1
de	975	50	43	-1	0.1187	2	0	1
de	1019	50	43	1	0.1187	2	0	1
de	1075	50	43	-1	0.1187	2	1	1
de	1119	50	43	1	0.1187	2	1	1
<b>de</b>	<b>1175</b>	<b>50</b>	<b>43</b>	<b>-1</b>	<b>0.1187</b>	<b>2</b>	<b>2</b>	<b>1</b>
<b>de</b>	<b>1219</b>	<b>50</b>	<b>43</b>	<b>1</b>	<b>0.1187</b>	<b>2</b>	<b>2</b>	<b>1</b>

de: dynamic eccentricity component; pspf: principal slot passing frequency also a function of static eccentricity

Table 6.1 Frequency Components Investigated for the 43 Bar Rotor

Before the results for the concentric and combination of static and dynamic eccentricity are discussed a summary of the pole-pair analysis for the 43 bar rotor is presented. For the concentric rotor the pole-pairs associated with the frequencies were always odd as was obtained for the 51 bar rotor:

For the 897Hz and the 997Hz components:  $n_{sa} = 0$ ,  $n_{os} = \pm 1$ ,

$$m = 43 \pm 36 \pm (2 \times 1)$$

Which gives 5, 77 for component 897Hz ( $n_{os} = -1$ )

and 9, 81 for component 997Hz ( $n_{os} = 1$ )

For the 797Hz and the 1097Hz components:  $n_{sa} = \pm 1$ ,  $n_{\theta s} = \pm 1$ ,

$$m = 43 \pm 36 \pm (2 \times 1 \times 2) \pm 2$$

Which gives 1 and 73 for component 797Hz ( $n_{sa} = -1$ ,  $n_{\theta s} = -1$ )

and 13 and 85 for component 1097Hz ( $n_{sa} = 1$ ,  $n_{\theta s} = 1$ )

For the 1197Hz component:  $n_{sa} = 2$ ,  $n_{\theta s} = +1$

$$m = 43 \pm 36 + (2 \times 2 \times 2) + 2$$

Which gives 1 and 89 for component 1197Hz

Therefore, for the concentric case none of these frequency components should appear. A finite element analysis was performed for a concentric rotor and these components were not present in the spectrum even reducing the dB display to 20dB as explained earlier. This result again confirmed the finite element analysis method and the usefulness of the pole-pair analysis for very basic situations. However, when static and dynamic eccentricity were considered the limitations of the pole-pair analysis once again became apparent.

When the pole-pair analysis was extended to incorporate static eccentricity ( $n_s = 1$  on to the aforementioned pole-pair numbers) the associated pole-pairs were even, some of which were compatible with the stator winding. If the pole-pairs associated with dynamic eccentricity were then calculated by applying  $n_d = 1$  onto the even static eccentricity pole-pairs then the associated dynamic eccentricity pole-pairs when both forms of the condition are present were odd and therefore not compatible with the stator. However, as the spectrum in Figure 6.2 illustrates, with static and dynamic eccentricity, the upper dynamic components were clearly present which the basic analysis failed to predict. This is a similar situation as to the analysis for the 51 bar rotor. Assuming  $n_s$  and  $n_d$  to be 1 is a gross simplification and it can be shown that if  $n_s = 1$  and then second order dynamic eccentricity  $n_d = 2$  is considered that the majority of the dynamic eccentricity components become compatible and  $n_d = 4$  for the remainder

to be compatible. It is in this type of situation that the results of the pole-pair analysis had to be treated with caution.

Inspection of Figure 6.2 reveals that the 43 bar rotor responded differently to 25% static and 25% dynamic eccentricity compared to the 51 bar rotor. As a comparison with experimental data was not being made the current components magnitudes were not calculated, comparisons were made based on the emf magnitudes. The static and upper dynamic eccentricity components were clearly visible in the spectrum. The pole-pairs associated with the lower dynamic eccentricity components were compatible but they were not clear in the spectrum. It is possible that they were present and like the 51 bar rotor were low in magnitude and therefore did not appear above the spectral noise. As explained in Chapter 5, spectral noise due to blocking the cycles of continuous data was more pronounced as the components were larger in magnitude.

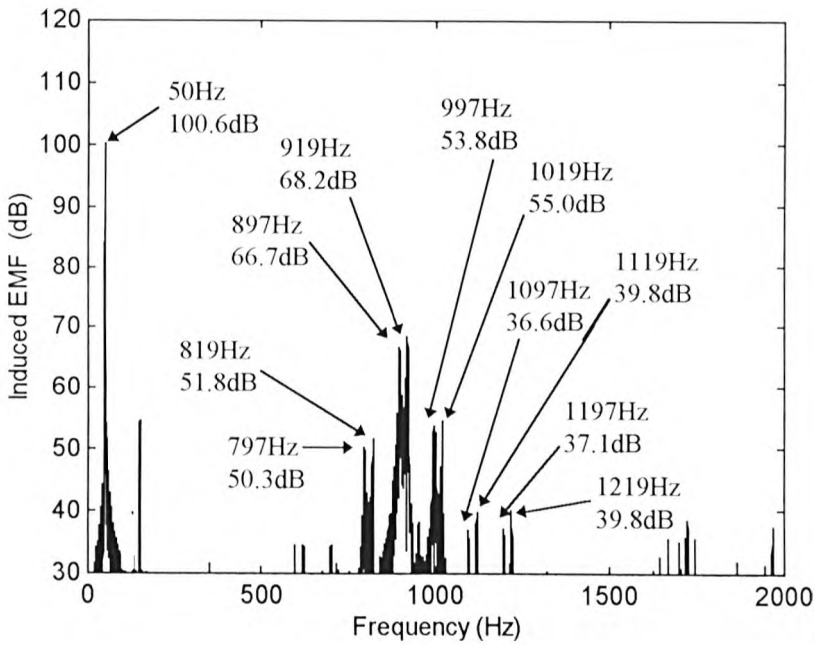


Figure 6.2 EMF Spectrum from FE Analysis for a 43 Bar Rotor with 25% Static and 25% Dynamic Eccentricity, 1322 rpm

Generally the component magnitudes for the 43 bar rotor were higher than for the 51 bar rotor with the same level of airgap eccentricity. For instance, the largest static and dynamic components in the induced emf spectrum for 25% static with 25% dynamic eccentricity for the 51 bar rotor were 1172Hz - 56.8dB and 1194Hz - 58.2dB respectively. The largest static and dynamic components for the 43 bar were 897Hz - 66.7dB and 921Hz - 68.2dB which were 9.9dB up for the static component and 10.0dB up for the dynamic eccentricity component. In linear terms the largest 43 bar rotor components were 3 times greater than the 51 bar rotor for the same airgap eccentricity level. This was a very clear indication of the effect of the rotor bar number and slot design combined with airgap eccentricity remembering that for both the 51 and 43 bar rotors the components were not present in the spectra for the concentric cases.

For the 51 bar rotor only three principal rotor slot passing frequencies and their associated dynamic eccentricity components were clearly present (1072Hz ( $n_{ws} = -1, n_{sa} = 0$ ), 1172Hz ( $n_{ws} = 1, n_{sa} = 0$ ) and 1272Hz ( $n_{ws} = 1, n_{sa} = 1$ )). However, for the 43 bar rotor in addition to the equivalent components above (897Hz, 997Hz, 1097Hz) two other principal rotor slot passing frequencies became prominent at 797Hz ( $n_{ws} = -1, n_{sa} = 1$ ) and 1197Hz ( $n_{ws} = 1, n_{sa} = 2$ ). It is also interesting to note that 1172Hz ( $n_{ws} = 1, n_{sa} = 0$ ) was the largest for the 51 bar rotor but 897Hz ( $n_{ws} = -1, n_{sa} = 0$ ) was the largest for the 43 bar rotor. This again illustrated the effect on the permeance of a different number of rotor slots.

#### **6.2.4 44 Bar Rotor**

A 44 bar rotor with a 36 slot stator has been documented as being an unfavourable combination in terms of large synchronous parasitic torques [63]. The pole-pair analysis also predicted that the pole-pairs for the rotor slot passing frequencies would be compatible with the stator winding for the concentric case unlike for the other rotors investigated in which they were not compatible. Consequently, an investigation into the effects of airgap eccentricity on a motor with a 44 bar rotor would be interesting. Four

different cases were investigated: concentric, 10% static eccentricity, 25% dynamic eccentricity and finally 10% static with 25% dynamic eccentricity. A summary of the pole-pair analysis for this rotor is presented as each result is discussed and the frequencies of interest are shown in Table 6.2.

Type	Frequency (Hz)	$f_1$	R	$n_d$	s	p	$n_{sa}$	$n_{ws}$
pspf	819	50	44	0	0.1187	2	-1	-1
pspf	919	50	44	0	0.1187	2	0	-1
pspf	1019	50	44	0	0.1187	2	0	1
de	797	50	44	-1	0.1187	2	-1	-1
de	841	50	44	1	0.1187	2	-1	-1
de	897	50	44	-1	0.1187	2	0	-1
de	941	50	44	1	0.1187	2	0	-1
de	997	50	44	-1	0.1187	2	0	1
de	1041	50	44	1	0.1187	2	0	1

de: dynamic eccentricity component; pspf: principal slot passing frequency also a function of static eccentricity

Table 6.2 Frequency Components of Interest for the 44 Bar Rotor

As explained in Chapter 4, due to the large magnitude of the rotor slot passing frequencies the data points processed comprised of a longer period of continuous cycles to remove the problem of spectral noise obscuring smaller frequency components. This resulted in reduced skirting around the 50Hz component and for the 10% static with 25% dynamic eccentricity the components at approximately 25Hz and 75Hz became visible. It was not the focus of the work to investigate these components, suffice to say that the finite element analysis was capable of modelling them.

The time domain waveform of the induced emf for the 44 bar concentric rotor is shown in Figure 6.3. The harmonic content is visibly high.

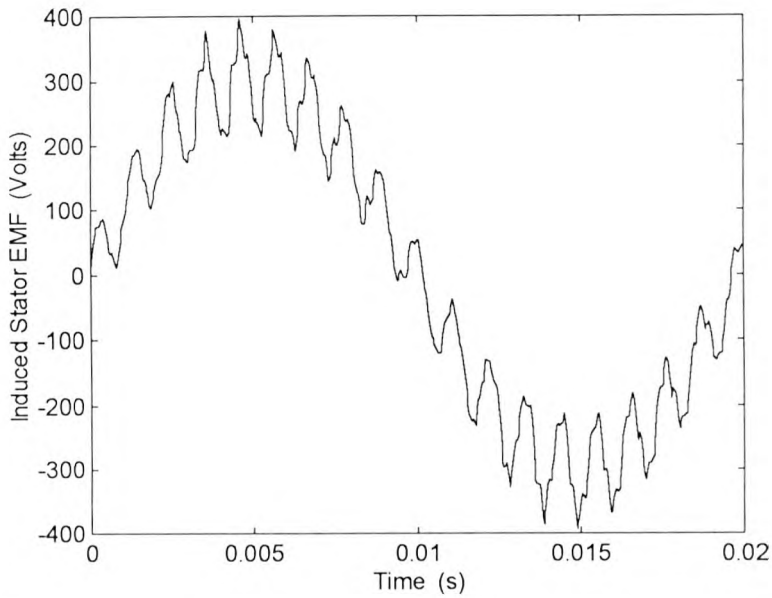


Figure 6.3 Time Domain Representation of Induced EMF for a Concentric 44 Bar Rotor

The induced emf spectrum for the concentric case is presented in Figure 6.4. It can be seen that the rotor slot passing frequencies at 819Hz, 919Hz and 1019Hz were very prominent. Other frequencies at 719Hz, 1119Hz etc. (marked with a \*) were also visible, however, discussion will be focused on the aforementioned three. The component magnitudes were significantly larger than for any of the other rotors investigated. For example, the largest rotor slot passing frequency (919Hz - 87.1dB) was 20.dB higher than the largest rotor slot passing frequency for the 43 bar (897Hz - 66.7dB). The basic pole-pair analysis predictions were not entirely accurate. The pole-pairs associated with the 819Hz (2, 74) and the 1019Hz (10, 82) were compatible with the stator winding harmonic pole-pairs. The finite element result tied in with this prediction. However, the pole-pair analysis predicted the 919Hz component to have pole-pairs at 6 and 78 which were not compatible. This component was clearly present in the spectrum which questioned the accuracy of the pole-pair analysis bearing in mind that the finite element and the experimental results tied up for the 51 bar rotor. Components were present in the experimental and finite element results that the pole-pair analysis predicted would not appear.

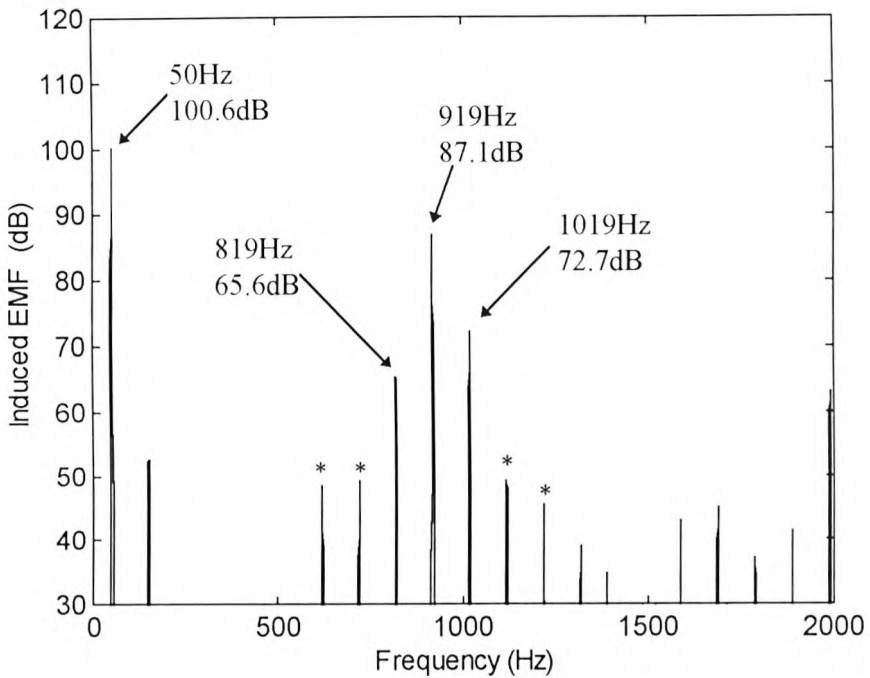


Figure 6.4 EMF Spectrum from FE Analysis for a 44 Bar Concentric Rotor, 1322 rpm

Static eccentricity was then introduced at 10% and the emf spectra investigated. It was found that the magnitudes of the rotor slot passing frequencies which are a function of static eccentricity were the same to within processing tolerances as those obtained for the concentric case. This is shown in Table 6.3

Frequency Component (Hz)	EMF Magnitude Concentric (dB)	EMF Magnitude 10% Static (dB)	dB Difference
819	65.6	65.6	0.0
919	87.1	87.0	0.1
1019	72.7	72.6	0.1

Table 6.3 Difference between EMF Magnitudes for 44 Bar Rotor with Concentric and 10% Static Eccentricity

The presence of static eccentricity was not having any effect on the magnitudes of the principal slot passing frequencies. This suggested that the pole-pairs associated with the principal slot passing frequencies with static eccentricity present were not compatible with the stator winding or the components would have increased in magnitude. The pole-pair analysis predicted this up to a point in that if  $n_s = 1, 2$  or  $3$  the pole-pairs were not compatible. However, if  $n_s$  was taken as  $4$  then the pole-pairs became compatible which suggested that the magnitudes should have increased with the 10% static eccentricity. A possible explanation for the magnitudes not increasing was that in this instance the effect of fourth order static eccentricity was negligible or that it was not until a higher static eccentricity level that the components would show any increase. This could be a result of the effects of the already high magnitude rotor slot passing frequencies for the concentric case. Time did not permit an analysis at a higher level of static eccentricity to be performed and it was thought that the other solutions would aid in the explanation of this observation.

An analysis at 25% dynamic eccentricity was performed and the induced emf spectrum is shown in Figure 6.5.

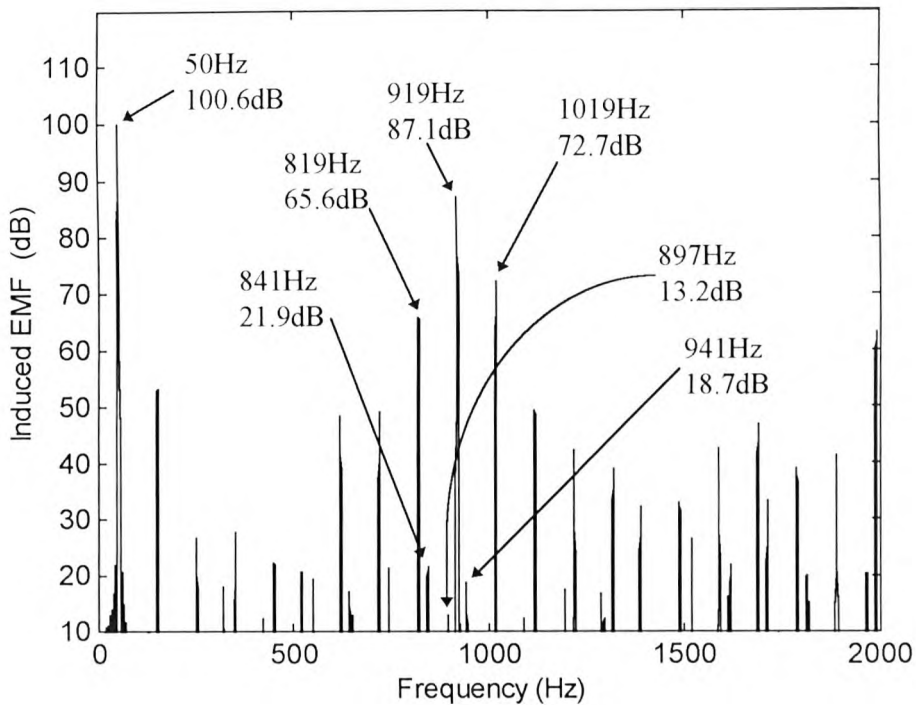


Figure 6.5 EMF Spectrum from FE Analysis for a 44 Bar Rotor with 25% Dynamic Eccentricity, 1322 rpm

The rotor slot passing frequencies remained at the same magnitude as for the concentric and 10% static eccentricity cases. The dynamic eccentricity components did appear in the spectra but at very low magnitudes. The scale was reduced to 10dB to show them. At this magnitude they were considered to be at noise level being over 80dB down on the fundamental component. For the concentric cases components were totally not present at 20dB or below, however, here they were visible although small in magnitude. Dynamic eccentricity of 25% was a high level of airgap eccentricity which for the other rotors results in the components being clearly present (over 50dB). If the pole-pairs associated with the dynamic eccentricity components for the 44 bar rotor were calculated then it was found that they were incompatible for  $n_d = 1, 2, \text{ or } 3$  but compatibility existed when  $n_d = 4$ . This could suggest that fourth order dynamic eccentricity was resulting in the components appearing but at negligible magnitude.

The final solution performed was at 10% static eccentricity with 25% dynamic eccentricity the spectrum of which is shown in Figure 6.6.

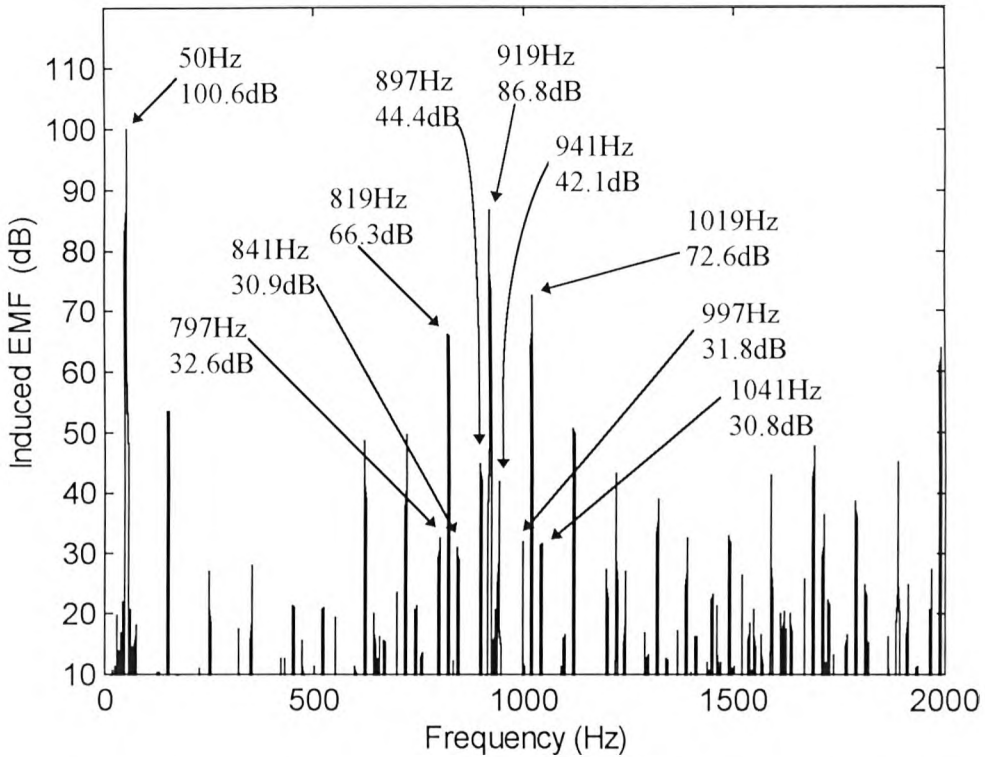


Figure 6.6 EMF Spectrum from FE Analysis for a 44 Bar Rotor with 10% Static and 25% Dynamic Eccentricity, 1322 rpm

The rotor slot passing frequencies were again at the same level, however, the dynamic eccentricity components clearly increased in magnitude from their purely 25% dynamic eccentricity levels. They were all now over 30dB in magnitude, for example, the 841Hz increased from 21.9dB to 30.9dB and the 897Hz from 13.2dB to 44.4dB. These results showed that for the 44 bar rotor dynamic eccentricity was clearly a function of static eccentricity, however, the components which are a function of static eccentricity were totally independent of the dynamic eccentricity level. This is where the pole-pair analysis is even more limited, suffice to say that the pole-pairs associated with the dynamic eccentricity components were compatible when static eccentricity was present could be obtained when the basic pole-pair analysis was extended. For instance,  $n_s = 1$

and then  $n_d = 3$  or when  $n_s = 2$  and then  $n_d = 2$  compatibility occurred. In practice it is probably doubtful that a 44 bar rotor would be combined with the 36 slot stator for a four pole motor, however, it can be seen that monitoring airgap eccentricity for such a combination would be difficult. The magnitudes of the components did not clearly increase with airgap eccentricity (especially static) as occurred for the 51 or 43 bar rotors.

### **6.2.5 Conclusions on the Results for the Number of Rotor Bars**

These investigations have revealed that the number of rotor bars together with changes in the rotor slot design have a considerable effect on the magnitude of the rotor slot passing frequencies. The effects of the introduction of airgap eccentricity also vary dependant on the number of rotor bars. For instance, the 43 bar rotor magnitudes were 10dB higher for the same level of airgap eccentricity than for the 51 bar rotor. The 44 bar rotor is definitely an unfavourable combination with the 36 slot stator due to the very high rotor slot passing frequencies. In addition, the effect of increasing airgap eccentricity does not directly transfer itself to an increase in the component magnitudes as was the case for the other rotors investigated. This is important when monitoring the current components of different motors in industry as it is possible that in some motors the current components do not increase significantly with increasing airgap eccentricity. The ability of the finite element analysis to model a wide variety of motor/airgap eccentricity situations has been further highlighted together with the limitations in the pole-pair analysis. Admittedly, in addition to the effects of different number of rotor bars, the rotor slot diameter also changed. For instance for the 51 bar rotor the diameter was 7mm whereas for the 44 bar rotor it was 7.54mm, the slot opening remained unchanged. This was not a large change in the rotor slot design and it was reasonable to assume that the effect of the different numbers of rotor bars was the significant factor in the effects observed. The remainder of this Chapter details finite element investigations into the effects of different rotor slot designs for a fixed number of rotor bars.

## 6.3 Rotor Slot Design Investigation

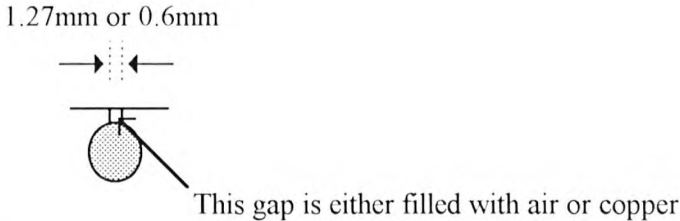
### 6.3.1 Introduction

This section details the investigations into the effects of the rotor slot design on the current components which are a function of airgap eccentricity. These components are also a function of rotor slotting and saturation, consequently, their magnitude is effected by the rotor slot design which in turn alters the permeance of the airgap. The purpose of this investigation was to apply the finite element analysis to determine what effect the rotor slot design has on the magnitudes of these components as a factor of the overall changes observed with increasing airgap eccentricity. This would lead to a better understanding of airgap eccentricity in terms of monitoring different motors in industry.

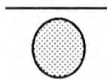
This research contributes to new knowledge as the effect of the rotor slot design on these components with increasing airgap eccentricity has not been investigated. The effect of rotor slot design on the rotor slot passing frequencies for a nominally healthy motor was investigated experimentally by Ferrah et al [103]. The magnitude of the components were higher for a semi-closed slot than for an open rotor slot. Airgap eccentricity was not introduced into the motor. Finite element analysis has been used to investigate the optimum rotor slot design for maximum efficiency [104] and the effects of slanted stator and rotor teeth on torque and electromagnetic losses [105]. Salon et al [106] used a finite element model to investigate the effects of stator slot closure on the permeance variations in the airgap. The airgap flux density and force waves produced by the finite element analysis revealed that when the stator slots were closed the airgap flux density and force waves due to slotting decreased and those due to saturation increased. However, finite element analysis has not been used to investigate the current components which are a function of airgap eccentricity with variations in the airgap eccentricity level and different rotor slot designs.

The rotor slot designs modelled are shown in Figure 6.7. The model of the test-rig motor was used with the 51 bar rotor and the 36 slot stator. The cross-sectional area of the rotor bars remained the same and only the slot opening was altered. The semi-closed slot was modelled in several different configurations with a gap of 1.27mm or 0.6mm and air or copper filling the gap between the copper conductor and the rotor surface. The finite element analysis was performed for the different rotor slot designs at 0%, 5%, 10% and 25% static eccentricity and then combinations of static and dynamic eccentricity (10% static with 25% dynamic and then 25% static with 25% dynamic). All solutions were performed for the full load case of 1322 rpm.

*Semi-closed slot*



*Totally enclosed slot*



*Totally open slot*

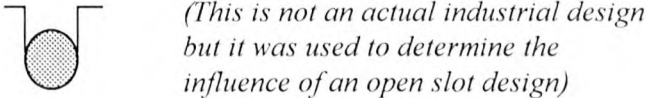


Figure 6.7 Rotor Slot Designs Investigated.

The actual rotor slot design in the test-rig motor as shown in Appendix A1.3 was a semi-closed slot of gap 0.6mm filled with air. All the finite element results for dynamic eccentricity and combinations of static and dynamic eccentricity were performed for this rotor slot design. However, the first set of static eccentricity variations in Chapter 5.3.2 were unintentionally performed for a semi-closed rotor slot of width 1.27mm with copper filling the gap. The results presented later show that there is negligible difference

for the magnitude of the components between these two slot designs. Only the 1272Hz component showed any significant difference of a few dB and as expected the agreement between experimental and calculated current magnitudes for the 1272Hz component was better with the 0.6mm air filled slot. Another point to note is that in the paper included at the end of the thesis entitled, “Finite Element Study of Rotor Slot Designs with Respect to Current Monitoring for Detecting Static Airgap Eccentricity in Squirrel-Cage Induction Motors,” the results for rotor slot variations at 0% static eccentricity are actually for a level of 5% static eccentricity, this was discovered with further research after the paper was submitted. Results are presented in this section for a concentric rotor with different rotor slot designs and the results labelled in the paper at 0% static eccentricity are presented for 5% static eccentricity. Results in the paper at 10% and 25% static eccentricity were for these levels.

### **6.3.2 Rotor Slot Variations at 0%, 5%, 10% and 25% Static Eccentricity**

#### **6.3.2.1 The Concentric Rotor**

As explained in Chapter 5, for a totally concentric rotor with a semi-closed rotor slot design the emf spectrum did not contain the rotor slot passing frequencies at 1072Hz, 1172Hz and 1272Hz. Finite element analysis was then performed for the closed and open rotor slots and the same result was obtained, that is, the components were not present in the emf spectrum even reducing the display scale to less than 20dB. This was expected as changing the rotor slot design would affect the permeance in terms of the magnitude of the components, however, the number of rotor slots did not change so the pole-pairs associated with the frequencies remained the same (incompatible with the stator).

### 6.3.2.2 Static Eccentricity at 5%

Three slot designs were modelled at 5% static eccentricity and the variation in magnitudes of the components is shown in Table 6.4.

5% static	Slot design		
Frequency (Hz)	Semi- closed 1.27mm Cu	Totally open	Totally closed
1072	62.1	56.3	62.3
1172	54.3	56.5	57.4
1272	44.8	47.7	47.0

Table 6.4 Magnitude of Components due to Different Slot Designs Modelled at 5% Static Eccentricity

Inspection of Table 6.4 shows that changing the slot design affected the magnitude of the components in different ways. For instance, the 1072Hz component decreased by 5.8dB when the slot design was changed from semi-closed to totally open, however, when the design was changed from semi-closed to totally closed it increased by 0.2dB. The 1172Hz and the 1272Hz increased in magnitude by 2.2dB and 2.9dB respectively when the design changed from semi-closed to totally open but comparing totally open and totally closed slot magnitudes they remained constant to within 1dB. The open slot magnitudes were smallest as the reluctance of the airgap was higher because of more air being present.

### 6.3.2.3 Static Eccentricity at 10%

The analysis performed at 10% static eccentricity focused on the effects of variations in the design of the semi-closed slot as Table 6.5 illustrates.

10% static	Slot design		
Frequency (Hz)	Semi- closed 1.27mm Cu	Semi- closed 1.27mm air	Semi- closed 0.6 mm air
1072	68.5	68.2	67.9
1172	68.6	68.6	68.6
1272	52.9	52.9	54.4

Table 6.5 Magnitude of Components due to Different Semi-Closed Slot Designs  
Modelled at 10% Static Eccentricity

Inspection of the results indicate that changing the material in the gap between the rotor conductor and the rotor surface from copper to air obviously had a very small or no effect on the magnitudes of the components. This was expected as the magnetic properties of copper are very similar to those of air, hence, the finite element analysis was confirmed to be modelling this change accurately. The reduction in the width of the slot gap from 1.27mm to 0.6mm had an insignificant effect on the 1072Hz and the 1172Hz components, however, the 1272Hz increased in magnitude by 1.5dB. The 1272Hz component was calculated when saturation was included hence the 1272Hz component magnitude was dependant on saturation to a greater extent than the 1072Hz and 1172Hz. Decreasing the slot width (i.e. closing the slot more) increased the magnitude of the component due to saturation.

A comparison of the component magnitudes for the 1.27mm copper filled semi-closed slot modelled with 5% and then 10% static eccentricity revealed that the magnitude of the components for 5% static eccentricity (Table 6.4) were considerably less than those for 10% static eccentricity (Table 6.5) as would be expected. Each frequency component increased in the magnitude by a different amount when the static eccentricity level increased from 5% to 10%. The 1072 Hz increased by 6.4dB whereas the 1172Hz increased by 12.3 dB. Inspection of Table 5.3 in Chapter 5 shows that the increase in each component for the 10% to 25% static eccentricity was less spread out

ranging from 5dB to 7.9dB. A similar trend is noticed when the static eccentricity increased from 25% to 50% each component increased in the range of 4.2 to 6.9dB. These results revealed that in the earlier stages of the fault each component increased by a considerably different amount for the same increase in static eccentricity but at higher levels of the fault, each component increased by approximately the same amount for the same increase in static eccentricity.

#### 6.3.2.4 Static Eccentricity at 25%

The results for variation in rotor slot designs modelled at 25% static eccentricity are shown in Table 6.6.

25% static	Slot Design			
Frequency (Hz)	Semi- closed 1.27mm Cu	Semi- closed 0.6 mm air	Totally open	Totally closed
1072	73.5	72.9	63.0	72.3
1172	76.5	76.5	63.6	74.5
1272	59.9	61.7	51.8	55.9

Table 6.6 Magnitude of Components due to Different Rotor Slot Designs Modelled at 25% Static Eccentricity

Changing the slot gap from copper to air with a constant gap of 1.27mm was not repeated as it clearly had no significant effect on the component magnitudes and it only served as a check on the finite element modelling of the motor. The results for the variation in the width of the semi-closed slot at 25% eccentricity confirmed the observations at 10% static eccentricity in that only the magnitude of the 1272Hz component was affected which increased by 1.8dB. Changing the slot design from semi-closed 1.27mm copper to totally open decreased the 1072Hz component by 10.5dB. This was a considerably larger change than was noticed at 5% static when it decreased

by 5.8dB. The 1172Hz and the 1272Hz decreased at 25% by 12.9dB and 8.1dB respectively compared to an increase of 2.2dB for the 1172Hz and 2.9dB for the 1272Hz at 5% static eccentricity.

Changing the rotor slot from semi-closed 1.27 mm copper to totally closed at 25% static decreased the 1072Hz component by 1.2dB, decreased the 1172Hz by 2dB and decreased the 1272Hz by 4dB. At 5% eccentricity this change in slot design increased the 1072Hz by 0.2dB, increased the 1172Hz by 3.1dB and increased the 1272Hz by 2.2dB. Changing the slot from totally open to totally closed at 25% resulted in the 1072Hz increasing by 9.3dB, the 1172Hz increasing by 10.9dB and the 1272Hz increasing by 4.1dB. This is in comparison to the results at 5% static where changing the slot from open to closed increased the 1072Hz by 6dB, the 1172Hz increased by 0.9dB and the 1272Hz decreased by 0.7 dB.

A comparison of the range of increase for the components with the semi-closed 1.27mm copper and the totally open and totally closed slot designs can be made from Tables 6.4 and 6.6. Table 6.7 shows the increase in magnitude of each component as the static eccentricity level increases from 5 to 25% for the different rotor slot designs.

Increase in component magnitudes			
5-25% Static Increase	Semi-closed 1.27 mm copper	Totally Open	Totally Closed
1072 Hz	11.4	6.7	10.0
1172 Hz	22.2	7.1	17.1
1272 Hz	15.1	4.1	8.9

Table 6.7 Comparison of The Increases in Component Magnitudes for a 20% Increase in Static Eccentricity for the Different Rotor Slot Designs

Table 6.7 shows that the design of rotor slot has a large effect on how much the component magnitudes increase for an increase in static eccentricity from 5 to 25%. The 1072Hz for the semi-closed and totally closed were the only components that increased a similar amount. The totally open slot showed considerably less of an increase than the totally closed and in particular the semi-closed slot design.

The design of the rotor slot does not just affect the magnitude of the rotor slot passing frequencies, as Figures 6.8 to 6.10 illustrate multiples of the fundamental are also effected. The induced emf spectra at 25% static eccentricity for a semi-closed, open and closed rotor slots are shown in Figures 6.8 to 6.10 respectively.

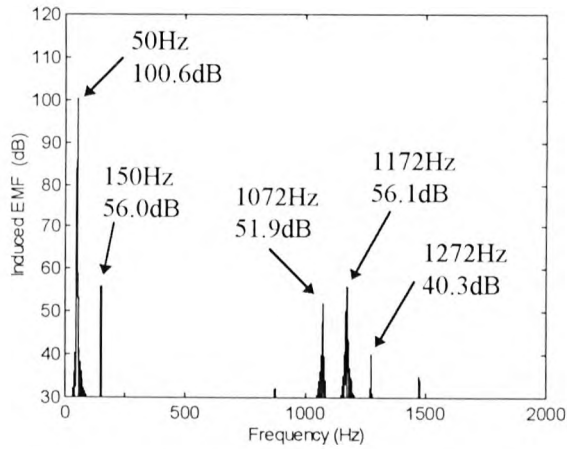


Figure 6.8 EMF from FE Analysis for 25% Static Eccentricity with a Semi-Closed Rotor Slot (1.27mm copper)

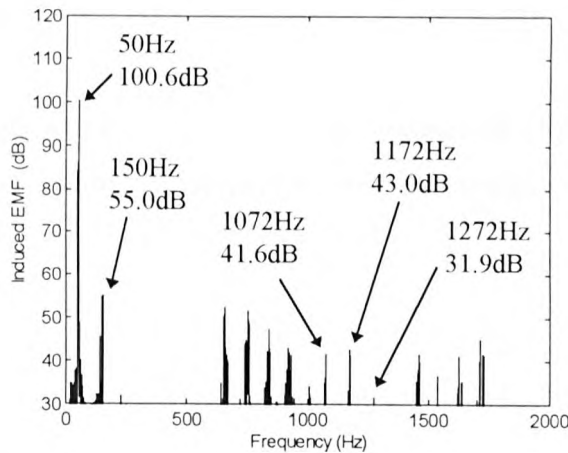


Figure 6.9 EMF from FE Analysis for 25% Static Eccentricity with an Open Rotor Slot

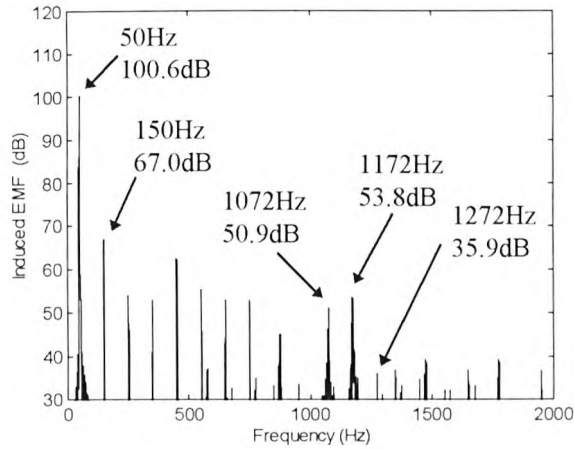


Figure 6.10 EMF from FE Analysis for 25% Static Eccentricity with a Closed Rotor Slot

Inspection of these figures reveals that there is no difference to within processing tolerances between the magnitude of the 150Hz component for the semi-closed and open rotor slots. However, this component increased considerably (by 12dB) for the closed rotor slot. The 150Hz is a function of saturation in the motor and its increase suggests that localised saturation levels increased with the closed rotor slots. This is expected as more flux will flow through the iron versus the air that filled the slot gap for the semi-closed and open rotor slots. Overall the airgap permeance is higher for the closed rotor slots as the reluctance has decreased.

### 6.3.3 Rotor Slot Variations for Combinations of Static and Dynamic Eccentricity

Tables 6.8 and 6.9 show the current component magnitudes for 10% static with 25% dynamic and 25% static with 25% dynamic eccentricity, respectively.

10% se 25% de		Slot design		
Frequency (Hz)	Semi- closed 0.6 mm air	Totally open	Totally closed	
1072	67.0	57.4	66.7	
1172	68.9	58.8	67.2	
1272	53.5	46.4	48.4	
1050	46.6	32.2	63.0	
1094	72.4	59.7	70.4	
1150	39.9	40.6	52.2	
1194	78.7	61.1	76.1	
1250	31.1	35.3	50.5	
1294	63.7	45.9	60.2	

Table 6.8 Magnitude of Components due to Different Rotor Slot Designs Modelled at 10% Static with 25% Dynamic Eccentricity

25% se 25% de		Slot Design		
Frequency (Hz)	Semi- closed 0.6 mm air	Totally open	Totally closed	
1072	75.6	61.2	72.5	
1172	78.8	62.1	75.6	
1272	61.8	50.7	56.5	
1050	41.8	39.1	53.0	
1094	74.3	58.1	70.0	
1150	42.8	43.8	41.8	
1194	76.5	60.9	75.8	
1250	37.7	36.6	46.3	
1294	60.4	46.0	58.6	

Table 6.9 Magnitude of Components due to Different Rotor Slot Designs Modelled at 25% Static with 25% Dynamic Eccentricity

The investigation into the different slot designs with combinations of static and dynamic eccentricity revealed that the same trends as observed with static eccentricity were followed. At a given level of airgap eccentricity the current component magnitudes for the open slot design were least in comparison to the closed and semi-closed magnitudes. With increasing static eccentricity and fixed dynamic the open slot current magnitudes showed the smallest increase, for instance, the 1172Hz component increased by 9.9dB for the semi-closed slot, 8.4dB for the closed slot and only 3.3dB for the open slot. The lower dynamic eccentricity components behaved as erratically for the open and closed slot designs as they did for the semi-closed design. With the closed slot the 1150Hz lower dynamic component decreased by 10.4dB for a fixed level of dynamic eccentricity with increasing static eccentricity. In contrast, the upper dynamic eccentricity components remained constant in magnitude to within processing tolerances. The 1194Hz for the closed slot only decreased by 0.3dB and the 1294Hz for the open slot increased by 0.1dB. This would be expected as the changing slot design affected the permeance wave in terms of magnitude but not the pole-pairs.

### **6.3.4 Conclusions on the Rotor Slot Design Results**

The investigations into the effects of rotor slot design on the components which are a function of rotor slotting, saturation and static eccentricity revealed that changes in rotor slot design had a significant effect on the magnitudes of these components. There was clearly a complex relationship between rotor slotting, saturation and static eccentricity and their combined effect on the magnitudes of the current components. The difference in the magnitude of the components for the different rotor slot designs was less at 5% static eccentricity than at 25% static. For instance, the 1172Hz component increased by 0.9dB at 5% as the slot design changed from totally open to totally closed, whereas, at 25% this component increased by 10.9dB. The higher levels of static eccentricity had a significant effect on the behaviour of the component magnitudes.

The investigations of the semi-closed slot design at 10% and then 25% static eccentricity revealed that (as expected) changing the slot gap filling from copper to air had no significant effect on the components and when the slot gap was reduced from 1.27mm to 0.6mm it was only the 1272Hz which was effected - increased by 1.5dB and 1.8dB respectively. This is small in comparison to the increases in component magnitudes with static eccentricity and it is also very close to the tolerance of approximately  $\pm 1$ dB for the experimental measurement of the component magnitudes.

The results in Table 6.7 show that the amount each component increased for the same increase in static eccentricity was very dependant on the rotor slot design. In an industrial situation if a motor with a totally open rotor slot design was being monitored then the increase in the component magnitudes would be considerably less than that observed for a motor with a semi-closed rotor slot.

The presence of dynamic eccentricity with static eccentricity did not alter the trends noticed for the static eccentricity variations with the open slot design being the least in magnitude. With increasing static eccentricity and fixed dynamic the components for each respective design behaved as for the semi-closed slot results with the static eccentricity components increasing in magnitude and the upper dynamic components remaining constant in magnitude.

The finite element investigation of the rotor slot designs has revealed that the rotor slot design has a considerable effect on the magnitudes of the current components. The rotor slot design also effects the size of the increase in the magnitudes of the components for the same increase in airgap eccentricity. For an increase of 20% (5 to 25%) static eccentricity the 1172Hz component increased by 22.2dB for the semi-closed slot compared to an increase of only 7.1dB for the totally open slot. The information gained from this analysis is of considerable value in terms of on-line current monitoring of different motors in industry.

## 6.4 Conclusion

This part of the research has provided valuable information on the effects of the rotor slot design on the magnitude of the airgap eccentricity components in the current spectra. This information is important in terms of monitoring different motors in industry as it has been shown that the rotor design has a considerable effect on the magnitudes of the components and also on the increase in their magnitude with increasing airgap eccentricity. The finite element analysis successfully modelled the effects of the different rotor bar numbers and rotor slot designs and the limitations of the pole-pair analysis were further highlighted.

# Chapter 7

## Finite Element Analysis of a Large Motor Operating in Industry

### 7.1 Introduction

This Chapter details an experimental and finite element study of airgap eccentricity in a large high voltage industrial based 3-phase induction motor. Monitoring of the current components to detect the presence of airgap eccentricity has been successfully applied in the industrial situation [19, 20, 21]. This has involved monitoring over time to ascertain if the current component magnitudes increased and hence the airgap eccentricity level. However, the prediction of the current component magnitudes as a function of the eccentricity level for a large, high voltage squirrel cage induction motor has not been attempted either by the classical method proposed by Cameron [19, 22] or by a finite element approach. The verification of the finite element method to model and predict the magnitude of these current components was an important part of this research. The application of finite element analysis to a large motor to model airgap eccentricity has not been previously attempted. The motor design details and pole-pair analysis are presented before the on-site test results are discussed. The finite element

analysis of the motor is then presented together with comparisons with the on-site test results.

## **7.2 Design Details and Calculation of Finite Element Data**

The induction motor investigated was a 1.45MW, 11kV, 103A, 742 rpm, 50Hz, 8-pole cage motor. The complete motor specification can be found in Appendix 5, Section A5.1, all design details were obtained from the motor manufacturers [107]. The motor was situated on an oil tank farm and used to drive a pump (directly coupled) to pump oil from oil storage tanks through a pipe to tankers on loading jetties approximately 2 miles away. There were four pumps to be driven by four motors three of which were of the design modelled and a fourth of a slightly different design which was not considered. As explained later the current spectra was obtained from two motors, 'A' and 'B' of nominally identical specification.

A finite element mesh of the large motor was constructed from detailed design drawings [107]. The two dimensional mesh contained 9837 nodes and 17,954 elements. Detailed design details are not presented for this motor to preserve manufacturers confidentiality.

Certain parameters had to be calculated for the finite element analysis control files. The large motor had cooling ducts situated in the core which had to be taken into account when calculating the effective machine length and effective stacking factor for the core. This was not required for the test-rig motor as cooling ducts were not present. Section A5.2 details the calculation of these parameters as required by the finite element analysis [108]. The rotor bar conductivity also had to be calculated taking into account temperature and end-ring effects. The same procedure as performed for the test-rig motor was followed. With the control files and finite element mesh complete initial solutions for the larger motor were performed the results of which are described later in this Chapter.

### 7.3 Pole-Pair Analysis

The frequency components in the current spectrum for the large motor were calculated from Equation 2.2 and are shown in Table 7.1.

Type	Frequency (Hz)	$f_1$	R	$n_d$	s	p	$n_{sa}$	$n_{ws}$
pspf	819	50	62	0	0.008	4	0	1
pspf	919	50	62	0	0.008	4	1	1
pspf	1019	50	62	0	0.008	4	2	1
de	807	50	62	-1	0.008	4	0	1
de	831	50	62	1	0.008	4	0	1
de	907	50	62	-1	0.008	4	1	1
de	931	50	62	1	0.008	4	1	1
de	1007	50	62	-1	0.008	4	2	1
de	1031	50	62	1	0.008	4	2	1

de: dynamic eccentricity component; pspf: principal slot passing frequency also a function of static eccentricity

Table 7.1 Frequency Components Investigated for Large Motor

The frequency components shown above were based on a speed of 744rpm which corresponded to those observed in the current spectra of motors A and B during the on-site tests. The full load speed is 742rpm corresponding to components at 1016Hz, 1004Hz and 1028Hz etc. Finite element results were obtained at both speeds for different airgap eccentricity levels. Other components with  $n_{ws} = -1$  exist (519Hz, 619Hz and 719Hz). These were present in the on-site and finite element spectra in addition to those shown in Table 7.1. However, for clarity of presentation of the results and subsequent discussion they are not included, suffice to say that the behaviour they exhibited followed that of the components which are discussed. They were also the least significant in the on-site test spectra with the 1019Hz and the 919Hz being the most significant.

The pole-pairs associated with these frequencies for different combinations of airgap eccentricity were calculated using Equation 2.3. Table 7.2 shows the stator winding harmonic pole-pair numbers for the stator.

Stator winding data: 8 pole, 84 slot, 3.5 slots/pole/phase, star connected.																	
<b>Harmonic pole-pairs:</b> Fundamental - 4 pole-pairs																	
4	8	16	20	28	32	40	44	52	56	64	68	76	80	88	92	100	104
112	116	124	128	136	140	148	152	160	164	172	176	184	etc.				

Table 7.2 Harmonic Pole-Pair Numbers for Large Motor Stator

*Case 1: No static or dynamic eccentricity*

$$m = (R \pm S \pm 2n_{sa}P \pm n_{os}P)$$

$$\therefore 819\text{Hz: } m = 62 \pm 84 + 2 \times 0 \times 4 + 1 \times 4 = 150, \text{ -18 corresponding to } n_{sa} = 0 \text{ and } n_{os} = 1$$

$$919\text{Hz: } m = 62 \pm 84 + 2 \times 1 \times 4 + 1 \times 4 = 158, \text{ -10 corresponding to } n_{sa} = 1 \text{ and } n_{os} = 1$$

$$1019\text{Hz: } m = 62 \pm 84 + 2 \times 2 \times 4 + 1 \times 4 = 166, \text{ -2 corresponding to } n_{sa} = 2 \text{ and } n_{os} = 1$$

This result shows that the pole-pairs of the flux waves at the principal slot passing frequencies were not compatible with the stator winding. This meant that in an absolutely perfect motor (0% airgap eccentricity) these components should not be present in the frequency spectrum of the current. This condition could never be achieved experimentally due to the inherent airgap eccentricity levels in the motor.

*Case 2: Static eccentricity present but no dynamic eccentricity*

$m = (R \pm S \pm n_s \pm 2n_{sa}P \pm n_{os}P)$  where  $n_s = 1$ , the associated pole-pairs are all odd and therefore not compatible with the stator:

$$\text{e.g.: } 819\text{Hz: } m = 62 \pm 84 \pm 1 + 2 \times 0 \times 4 + 1 \times 4 = 149, 151, -19, -17$$

The same applied for the 919Hz and 1019Hz components. This assumed the basic case of  $n_s = 1$  which was a simplification of the situation. If  $n_s = 2$  the pole-pairs became compatible:

$$819\text{Hz: } m = \underline{148}, \underline{152}, \underline{-20}, \underline{-16}$$

$$919\text{Hz: } m = \underline{160}, 156, -12, \underline{-8}$$

$$1019\text{Hz: } m = \underline{164}, 168, \underline{-4}, 0$$

*Case 3: Dynamic eccentricity present but no static eccentricity*

When only dynamic eccentricity was considered ( $n_d = 1$ ) the same results as for purely static eccentricity were obtained. The pole-pairs of the flux-waves associated with the dynamic eccentricity components were not compatible with the stator winding.

*Case 4: Both static and dynamic eccentricity present*

If  $n_s = 1$  was applied to the concentric pole-pairs obtained in Case 1 the pole-pairs associated with the components were:

$$819\text{Hz: } m = 149, 151, -17, -19$$

$$919\text{Hz: } m = 157, 159, -11, -9$$

$$1019\text{Hz: } m = 165, 167, -3, -1$$

To obtain the pole-pairs of the dynamic eccentricity components with static also present  $n_d = 1$  was applied to the above pole-pairs resulting in:

$$807\text{Hz: } m = \underline{148}, 150, -18, \underline{-20}$$

$$831\text{Hz: } m = 150, \underline{152}, \underline{-16}, -18$$

$$907\text{Hz: } m = 156, 158, -12, -10$$

$$931\text{Hz: } m = 158, \underline{160}, -10, \underline{-8}$$

$$1007\text{Hz: } m = \underline{164}, 166, \underline{-4}, -2$$

1031Hz:  $m = 166, 168, -2, 0$

This results suggested that the with both static and dynamic eccentricity present the majority of the dynamic eccentricity components were compatible with the stator winding and that dynamic eccentricity was a function of static eccentricity for this motor. The only exceptions to this were the 907Hz and 1031Hz components whose pole-pairs were incompatible when the basic case of  $n_d = 1$  was taken, however, if  $n_d = 3$  (907Hz) and  $n_d = 5$  (1031Hz) then compatibility occurs. It is interesting to note with the pole-pair analysis that if  $n_s = 2$  (which is what made the static eccentricity components on their own compatible) and then dynamic eccentricity is then included  $n_d = 1$  or  $2$  then the pole-pairs associated with the dynamic eccentricity components are not compatible.

A summary of the findings is that with a concentric rotor the principal slot passing frequencies should not appear. With static eccentricity present and the basic pole-pair analysis applied ( $n_s = 1$ ) the pole-pairs associated with the principal slot passing frequencies are not modified to make them compatible with the stator winding unless  $n_s = 2$ . Purely dynamic eccentricity will not result in the dynamic eccentricity components appearing unless,  $n_d = 2$ . With static and dynamic eccentricity combined the dynamic eccentricity components will appear and increase in magnitude with increasing static eccentricity. The pole-pairs associated with the static eccentricity components cannot be calculated when static and dynamic eccentricity are present together. This analysis will be referred to as the on-site test and finite element results are presented.

## 7.4 On-Site Test Results

### 7.4.1 Introduction

The current spectra for two nominally identical motors, 'A' and 'B', were obtained during an on-site visit. It was known that motor B was being used for the vast majority of loads. The motors are not run at full-load at all times but are dependant on pumping rate required which in turn depends on other factors such as the capabilities of the tankers being loaded. A diagram showing the experimental set-up during the tests is show in Figure 7.1.

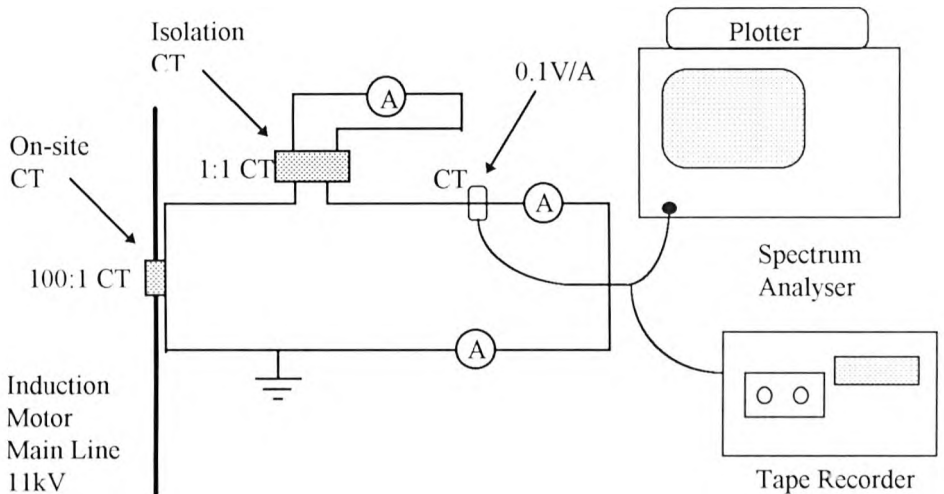


Figure 7.1 Experimental Set-up for On-Site Tests

The current transformer was identical to that used for the test-rig motor (0.1V/A output the same reference voltage was applied ( $10^{-6}$ ) for the dB to amps conversion). This CT was clipped round the secondary side of the on-site CT as shown in Figure 7.1. As a result, 40dB had to be added to the magnitudes of the current components displayed on the spectrum analyser (an additional 40dB is equivalent to a linear increase of 100). The magnitudes displayed on the spectra for the on-site tests were without the 40dB

included, magnitudes shown in tables, graphs and for comparison with the finite element analysis results had the 40dB added to them.

### 7.4.2 Current Spectra for Motors A and B

On the day of the on-site tests the motors were running at 744rpm which was obtained from the frequency of the principal rotor slot passing components in the current spectra using Equation 2.2. The current spectra for motors A and B are shown in Figures 7.2 and 7.3 respectively.

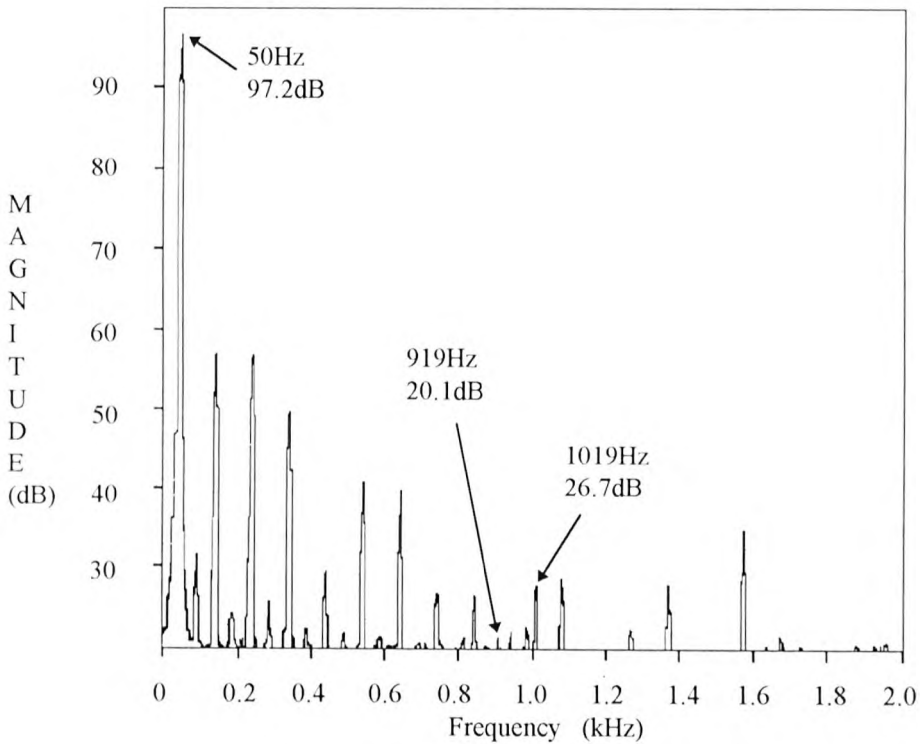


Figure 7.2 Current Spectra for Motor A

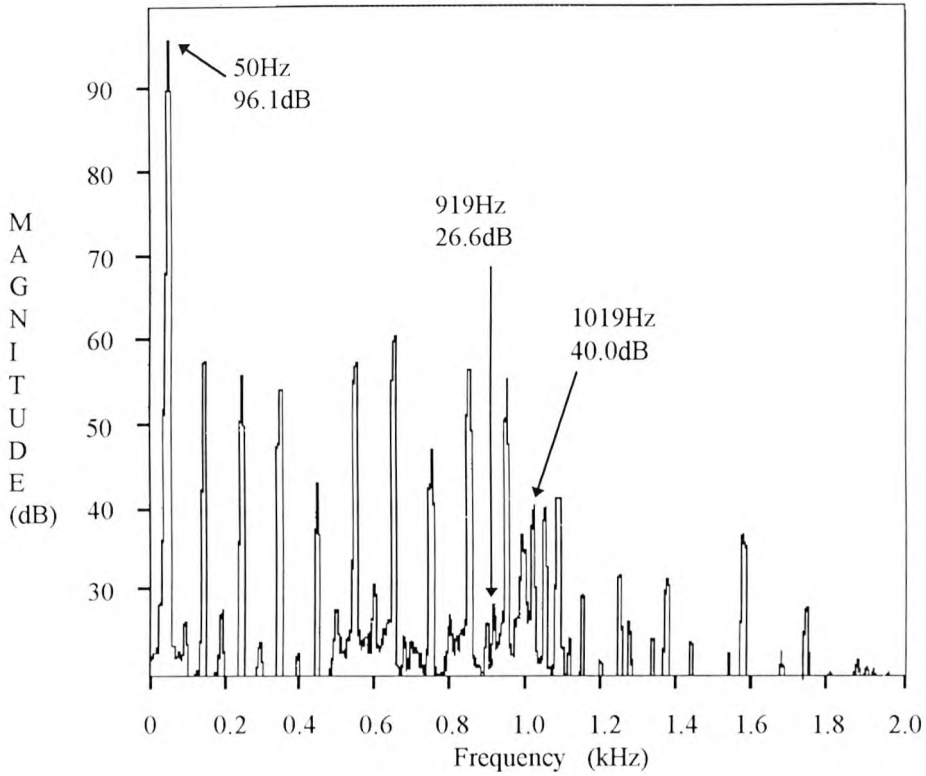


Figure 7.3 Current Spectra for Motor B

The fundamental current magnitude from the current spectra for the motors was, motor A = 72.4A and motor B = 63.8A. Frequency components at 919Hz and 1019Hz as predicted by Equation 2.2 were clearly present in the spectra and were higher in magnitude for motor B. For instance, the 1019Hz component increased by 13.3dB. This suggested that the airgap eccentricity level was higher for motor B which tied in with motor B being used for the majority of loads, that is, a much heavier duty cycle. By performing a zoom spectrum around these components the dynamic eccentricity components were clearly present as shown in Table 7.3.

Frequency (Hz)	Motor A (dB)	Motor B (dB)	<i>Difference</i> (dB)	Motor A (mA)	Motor B (mA)	<i>Difference</i> (mA)
807Hz (de)	38.9	58.3	19.4	0.88	8.2	7.32
<b>819Hz (se)</b>	<b>60.0</b>	<b>63.9</b>	<b>3.9</b>	<b>10.0</b>	<b>15.7</b>	<b>5.7</b>
831Hz (de)	53.8	61.8	8.0	4.9	12.3	7.4
907Hz (de)	45.8	48.8	3.0	1.95	2.75	0.8
<b>919Hz (se)</b>	<b>60.1</b>	<b>66.6</b>	<b>6.5</b>	<b>10.1</b>	<b>21.4</b>	<b>11.3</b>
931Hz (de)	34.9	52.2	17.3	0.56	4.1	3.54
1007Hz (de)	48.3	62.1	13.8	2.6	12.7	10.0
<b>1019Hz (se)</b>	<b>66.7</b>	<b>80.0</b>	<b>13.3</b>	<b>21.7</b>	<b>100</b>	<b>78.3</b>
1031Hz (de)	37.4	52.1	14.7	0.74	4.0	3.26

Table 7.3 Magnitude of Current Components for Motors A and B from On-site Tests

Inspection of Table 7.3 reveals that the dynamic eccentricity components were clearly present in the spectra. They were also higher in magnitude for motor B than for motor A, following the trend displayed by the static eccentricity components. For instance, the 807Hz was 19.4dB larger and the 931Hz was 17.3dB larger. The 907Hz and 1031Hz components were clearly present in the spectra, the basic pole-pair analysis predicted that the pole-pairs associated with these components would not be compatible with the stator. The appearance of these components could be due to winding asymmetries present in the on-site motors or to the component actually being compatible which the pole-pair analysis failed to predict. This is further discussed as the finite element results are presented. It is reasonable to conclude that static and dynamic eccentricity were present in both motors and that the airgap eccentricity level in motor B was higher. These results are discussed further in the next section.

### 7.4.3 Discussion and Conclusions on On-Site Results

The 1019Hz component was clearly the most prominent in both motors, other independent tests obtained a similar result [21]. The basic pole-pair analysis cannot unambiguously predict the pole-pairs associated with the static eccentricity components when both static and dynamic were present together. However, assuming the pole-pairs predicted for static only, with  $n_s = 2$  (second order static eccentricity), and investigating the winding factors associated with these pole-pairs provided interesting results. The pole-pairs calculated indicated that the components were compatible with the stator winding. The winding factors associated with the compatible pole-pairs are tabulated in Appendix 5, Section A5.3. The largest winding factor and associated pole-pair for each static eccentricity component are shown in Table 7.4.

Frequency Component (Hz)	Pole-Pairs for largest winding factor	Winding Factor associated with pole-pairs
819	152, 16	0.0584
919	160, 8	0.0313
1019	164, 4	0.9319

Table 7.4 Winding Factors for Static Eccentricity Components

The winding factor for the 1019Hz component was 15.9 times larger than that for the 819Hz component which accounted for its larger magnitude for both motors. The factor for the 819Hz component was larger than for the 919Hz component but the 819Hz component was 0.1dB less for motor A. The 919Hz was the larger by 2.7dB compared to 819Hz for motor B. This suggested that either there were slight differences between the windings or at higher levels of airgap eccentricity factors other than the winding factors came into play.

Investigating the pole-pairs and the winding factors for the dynamic eccentricity components revealed behaviour that was more predictable. The 831Hz component was larger than the 931Hz by 18.9dB for Motor A and 9.6dB for Motor B. The winding factor associated with the pole-pairs for the 831Hz component was 0.0584 compared to only 0.0313 for the 931Hz component.

Of course all the foregoing discussion is based on the pole-pairs predicted by the basic mmf and permeance wave analysis. This basic analysis, due to assumptions, has been shown not to model the true situation. However, the results clearly indicated once again the ability of on-line current monitoring to detect airgap eccentricity in the industrial situation.

## **7.5 Finite Element Analysis**

### **7.5.1 Introduction and Initial Result**

The finite element model and control files were compiled using the details described earlier in this Chapter and in Appendix 5. An initial run was performed to verify the finite element analysis of the motor and the values of the parameters used. Initially a full load condition of 742rpm was modelled with 35% static and 5% dynamic eccentricity. The finite element analysis outputted a figure of total rms input current of 107.5A at a power factor of 0.79 lag. This value of current was slightly higher than the rated value of 103A, however, the percentage difference is only + 4.3%. The power factor also was favourable with the nameplate value of 0.78 lag. It is possible that with further time to investigate the parameters used that this difference could have been decreased. However, the motor parameters provided by the manufacturer had to be assumed to be accurate in value. The induced emf spectrum contained the frequency components of interest as shown later, verifying that the finite element analysis was modelling the effects of airgap eccentricity on the motor. Analysis for different airgap eccentricity levels at 742rpm and then 744rpm were then performed. The majority of the finite

element analysis was performed at 742rpm before the on-site visit was arranged. Further analysis was then performed after the visit at 744rpm to compare these results with the on-site test results and the finite element analysis at 742rpm. Further runs at 744rpm would have been interesting, however, time did not permit that and enough results were obtained for a comparison with the on-site test data. Although all the frequency components from 519Hz to 1019Hz were present only the 819Hz, 919Hz and 1019Hz are the focus of the discussion.

## **7.5.2 Airgap Eccentricity Results for Finite Element Analysis at 742rpm**

### **7.5.2.1 Static and Dynamic Eccentricity Variations**

These results focused on increasing static eccentricity with a fixed level of 5% dynamic eccentricity. The pole-pair analysis predicted that the dynamic eccentricity components were a function of the static eccentricity level in the motor, that is, the dynamic components would increase with static eccentricity even though the dynamic eccentricity level remained constant. In the industrial situation it is more likely for the static eccentricity level to increase unnoticed than the dynamic eccentricity. The rotating unbalanced forces with dynamic eccentricity can be very high, for example, 600N for a 4 pole 15kW 3-phase induction motor [102]. As described for the test-rig motor, higher dynamic eccentricity was audibly noticeable. Analysis was performed for a fixed level of dynamic eccentricity with the static level increasing from 5%, 20%, 35%, 50% and finally 65%.

The spectra of the emf from the finite element analysis for 5% static with 5% dynamic and then 35% static with 5% dynamic eccentricity are shown in Figures 7.4 and 7.5, respectively.

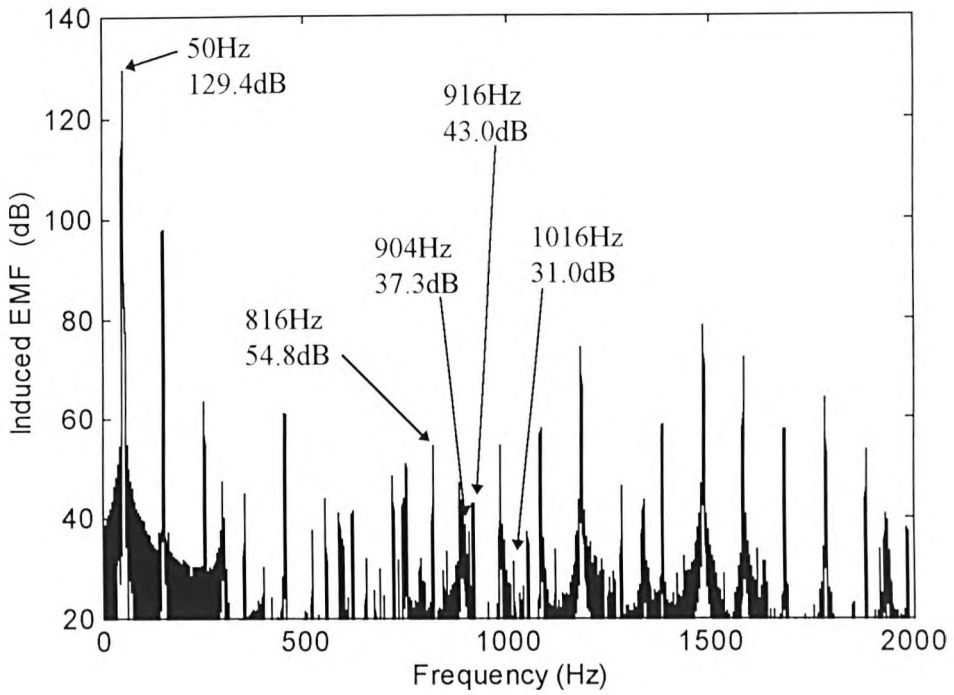


Figure 7.4 EMF Spectrum from FE for 5% Static and 5% Dynamic Ecc. 742 rpm

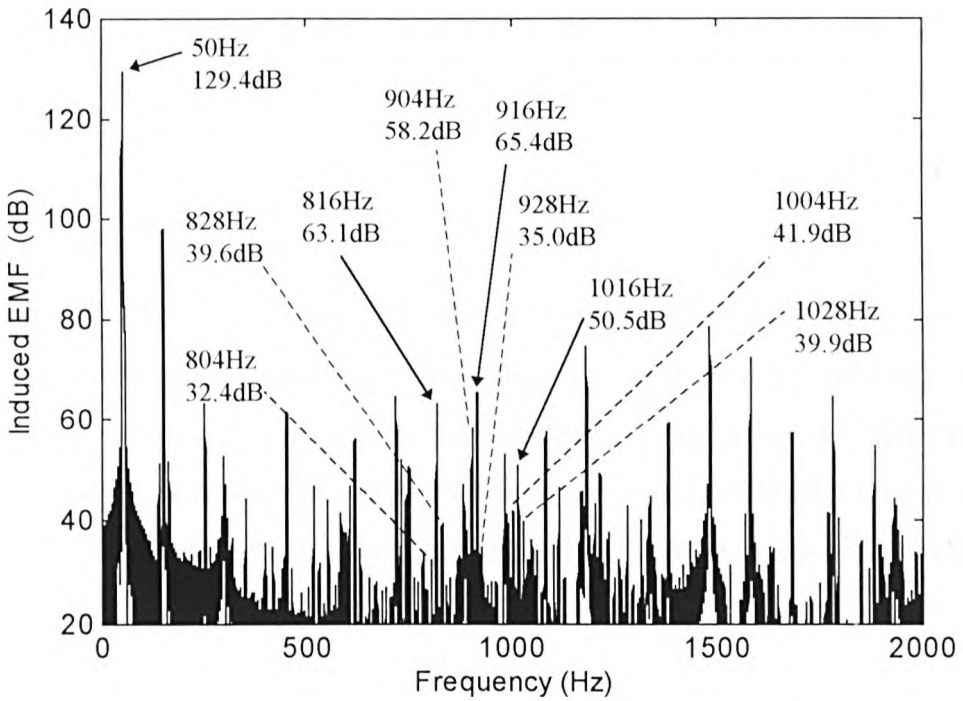


Figure 7.5 EMF Spectrum from FE for 35% Static and 5% Dynamic Ecc. 742 rpm

The principal rotor slot passing frequencies which are a function of static eccentricity were clearly present in both spectra and they increased in magnitude with the increase in static eccentricity. For instance, the 916Hz increased by 22.4 dB. Several of the dynamic eccentricity components were present with 5% static and 5% dynamic although they were low in magnitude (904Hz at 37.3dB, 1028Hz at 25.0dB). The 1004Hz and 1028Hz were present in the spectra in Figure 7.4, however, with the size of plot they could not be highlighted clearly. However, with the 20% increase in static eccentricity with fixed dynamic eccentricity of 5% these components increased considerably and the others that were not present in the 5% static with 5% dynamic spectrum became visible. The 904Hz increased by 20.9dB and the 1028Hz by 14.9dB. The 904Hz component, which has the same pole-pairs as the 907Hz component and the 1028Hz component which has the same pole-pairs as the 1031Hz, were clearly present in the finite element results despite the basic pole-pair analysis prediction that these components would not be compatible. Their presence in the spectra from the on-site motors could have been due to winding asymmetries, however, a perfect winding is modelled in the finite element analysis which suggests that the pole-pairs associated with these components were after all compatible with the stator. If the pole-pair analysis is extended with  $n_d = 3$  (904Hz) and  $n_d = 5$  (1028Hz) then compatibility can occur. The 804Hz which was not visible in the 5% static with 5% dynamic spectrum occurred at 32.4dB with 35% static eccentricity.

These results clearly showed the dependence of the dynamic eccentricity components on the level of static eccentricity. This illustrates that the basic pole-pair analysis, despite its limitations for specific components, does have its application to approximately predict the effect of the two forms of airgap eccentricity on one another. This level of understanding of the components behaviour with airgap eccentricity would be useful when applying on-line current monitoring practically.

The same procedure as for the test-rig motor was followed to calculate the current magnitudes of the frequency components from the emf. The supply voltage was

considered to be a short circuit at the high frequencies of interest. The values used for the stator resistance and stator end-winding leakage reactance in the circuit to calculate the current are shown in Appendix 5, Section A5.1. It was found that for the 50Hz component that a small uncertainty ( $\approx 0.3\text{dB}$ ) in positioning the cursor to obtain the magnitude of the 50Hz emf resulted in vast differences in the calculated current (over 25A). However, the 50Hz component of the current produced by the finite element analysis was obtained from the frequency spectrum of the current signal, as was performed for the test-rig motor. The 50Hz current component was 140.1dB which is equivalent to 103.5A. This is less than the total rms current outputted of 107.5A, as would be expected as the latter figure includes the magnitude of all frequency components. Figure 7.6 shows the increase in the magnitude of the calculated current components over the range of static eccentricity levels investigated.

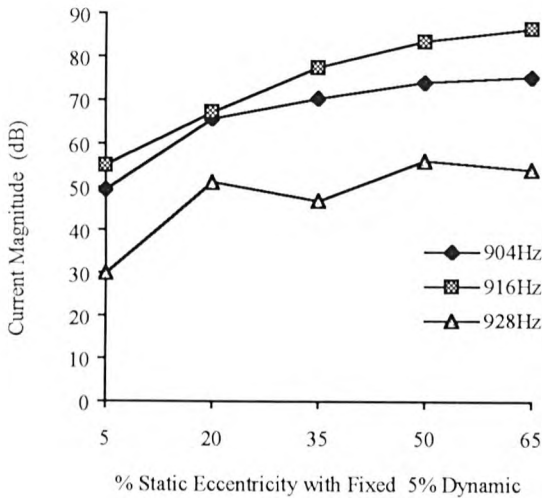


Figure 7.6 Increase in Magnitude of Current Components with Increasing Static Eccentricity and Fixed Dynamic Eccentricity

Table 7.5 shows the complete set of results for the calculated current components in dB at the different airgap eccentricity levels modelled. Inspection of this table reveals that the static eccentricity components consistently increased with the increasing static eccentricity. Overall the dynamic eccentricity components followed the same pattern, a general increase in magnitude, however, there was the occasional instance where the

magnitude decreased. This was visible from the 928Hz component in Figure 7.6. In Table 7.5 the 804Hz decreases from 52.1dB to 45.5 dB as the static eccentricity level increased from 20% to 35%. The largest increase for all the dynamic eccentricity components seemed to be in the earlier stages of static eccentricity increases, i.e., from 5% to 20% static. After this point, although the components on the whole increased in magnitude the overall increase from 20% to 65% static eccentricity was less than the increase for the first stage 5% to 20%. For instance, the 928Hz increased by 21.2dB from 5% to 20% static eccentricity and only 4.4dB from 20% to 65% static eccentricity. The static eccentricity components did not exhibit this trend with the increase in their magnitude being similar with each 15% increase in the static eccentricity. The 1019Hz component (744rpm) and associated dynamic eccentricity components were most prominent in the spectra from the on-site test results. The finite element results did not follow this trend. In fact the 1016Hz (742rpm) was smaller than both the 816Hz and 916Hz components. This difference will be discussed further during the comparisons of the on-site results and the finite element analysis for 744rpm.

- not visible	Current Magnitude in dB /mA for the Given Static and Dynamic Ecc. Level				
Frequency (Hz)	5% se 5% de	20% se 5% de	35% se 5% de	50% se 5% de	65% se 5% de
804 de	-	52.1	45.5	52.5	59.7
816 se	67.7 / 24.3	75.2 / 57.5	76.1 / 63.8	80.4 / 104.0	87.9 / 248.3
828 de	-	54.1	52.4	58.6	53.8
904 de	49.4	65.6	70.3	74.0	75.2
916 se	55.0 / 5.6	67.2 / 22.9	77.4 / 74.1	83.8 / 154.9	86.3 / 206.5
928 de	29.9	51.1	46.9	55.9	59.1
1004 de	38.2	52.3	53.0	59.9	59.1
1016 se	42.1 / 1.27	55.2 / 5.75	61.6 / 12.0	67.5 / 23.7	70.6 / 33.9
1028 de	36.0	53.6	50.9	56.2	55.6

Table 7.5 Calculated Current Components at 742rpm for Static and Dynamic Combinations

### 7.5.2.2 Static Eccentricity Variations

Although the condition of purely static eccentricity would be never be achieved in a real motor, the finite element analysis was used to model 10% and then 35% purely static eccentricity. This was to further investigate the findings of the pole-pair analysis. The independence of the static eccentricity components from the presence of dynamic eccentricity was also investigated. The calculated current magnitudes for these two conditions are shown in Table 7.6.

Frequency Component (Hz)	Current Magnitude (dB) 10% Static Eccentricity	Current Magnitude (dB) 35% Static Eccentricity
804 de	-	-
816 se	67.8	76.2
828 de	-	-
904 de	-	53.1
916 se	56.8	77.8
928 de	-	-
1004 de	-	-
1016 se	46.9	62.4
1028 de	-	-

Table 7.6 Calculated Current Magnitudes for 10% and 35% Static Eccentricity,  
742rpm

The dynamic eccentricity components were not present with 10% static eccentricity even when the display was reduced to 20dB for the emf spectrum, that is over 110dB down on the fundamental (in noise). Inspection of Table 7.6 shows that the static eccentricity components were independent of the level of dynamic eccentricity present in the motor. For both cases the magnitudes of the static eccentricity components did not differ from those obtained when the same level of static eccentricity was modelled

with 5% dynamic eccentricity present. At 35% static the current magnitude of the 916Hz was 77.8dB and with 35% static with 5% dynamic eccentricity the magnitude was 77.4dB. The differences were within processing tolerances.

The fact that the 904Hz dynamic eccentricity component appeared with 35% static eccentricity was a very interesting result. There was physically no dynamic eccentricity included in the model so the presence of the dynamic eccentricity component must have been due to the static eccentricity.

The basic pole-pair analysis with  $n_s = 1$  predicted that with the static eccentricity the pole-pairs associated with the principal rotor slot passing frequencies were incompatible with the stator winding. The components were clearly present in the spectra and as the finite element analysis did not model second order effects like supply or winding asymmetries their appearance could not be due to these factors. When the pole-pair analysis was extended to  $n_s = 2$  the pole-pairs became compatible, that is, with second order static eccentricity which the basic analysis did not include. Similar results were obtained for test-rig motor analysis, in that when the analysis was taken further compatibility occurred as the finite element and experimental results indicated. The effects of second order static eccentricity are inherently included in the finite element analysis as the actual rotor slot shape is modelled.

### **7.5.3 Airgap Eccentricity Results for Finite Element Analysis at 744rpm**

Two levels of airgap eccentricity were modelled, 5% static with 5% dynamic and 35% static with 5% dynamic. The purpose of the investigation at this speed was to compare the results at reduced speed with the finite element results at 742rpm and for comparison with the on-site test results. As expected at lighter load the total rms line current to the motor was less, 86.9A at 0.762 power factor. The 50Hz component of the current signal produced by the analysis was obtained at 138.4dB which is equivalent

to 83.2A. This was higher than the 50Hz magnitude obtained during the on-site tests, motor A = 72.4A and motor B = 63.8A for the same speed of 744rpm. This was a larger difference than for the 50Hz component at 742rpm. There were of course tolerances on both the finite element and on-site test results. The tolerance for the finite element results was realistically less than 1dB (0.3 to 0.4dB in practice). However, there is a 1dB tolerance on the experimental results which is equivalent to  $\pm 12.2A$ . If an error of this magnitude was present in the on-site test values for the 50Hz component then this would significantly reduce the difference.

The magnitudes of the static and dynamic eccentricity components decreased as expected with the lighter load and in certain cases became too small to be clearly visible in the emf spectra. In the results presented later, all components that were clearly visible are presented. Figure 7.7 shows the decrease in the magnitude of the emf components for 35% static eccentricity and 5% dynamic eccentricity as the speed increased from 742rpm to 744rpm. The principal rotor slot passing frequencies are presented, the same trend was observed with the dynamic eccentricity components that were visible.

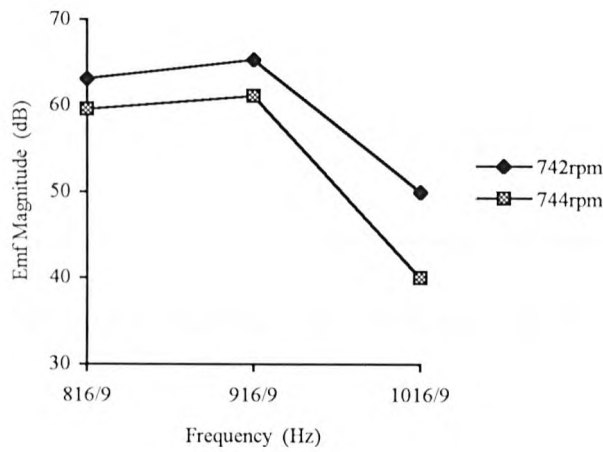


Figure 7.7 Magnitudes of the EMF Components at a Fixed Airgap Eccentricity Level (35% Static with 5% Dynamic) for 742rpm and 744 rpm

The current components were calculated for the two levels of airgap eccentricity investigated at 744rpm and the results are shown in Tables 7.7 and 7.8. When calculating the current magnitudes two equivalent circuits were used. Firstly, as before, only the stator resistance and stator end-winding leakage reactance were included. Another value of current was then calculated using the above circuit values but with a value for the supply impedance included. This was to model the on-site test situation as it was estimated that a mainly reactive supply impedance of  $j0.55\Omega$  was present. This was included in the circuit and resulted in the calculated current magnitudes being slightly smaller. During the discussions which follow only the current values calculated with the supply impedance are considered, the current magnitudes in Tables 7.5 and 7.6 did not include the supply impedance.

Frequency (Hz)	FE Emf Magnitude(dB)	Calculated Current $R_s + L_{es}$ (dB)	Calculated Current $R_s + L_{es} + L_{supply}$ (dB)
819 (se)	50.3	65.2	63.3
919 (se)	39.7	53.5	51.6
1019 (se)	24.8	37.9	35.8
807 (de)	36.8	51.8	49.8
1007 (de)	24.8	37.9	35.8

Table 7.7 Calculated Current Magnitudes for 5% Static with 5% Dynamic at 744 rpm

Frequency (Hz)	FE Emf Magnitude(dB)	Calculated Current $R_s + L_{es}$ (dB)	Calculated Current $R_s + L_{es} + L_{supply}$ (dB)
819 (se)	59.5	74.3	72.4
919 (se)	61.1	74.9	73.0
1019 (se)	40.0	52.9	51.0
907 (dc)	56.7	70.8	68.9
1007 (de)	37.1	50.2	48.2

Table 7.8 Calculated Current Magnitudes for 35% Static with 5% Dynamic at 744 rpm

All components clearly increased with the increase in static eccentricity, 819Hz by 9.1dB, 1007Hz by 12.2dB. In terms of a comparison between the finite element current magnitudes and those obtained from the on-site tests Figure 7.8 graphically shows where all the results are positioned with respect to each other. It has to be remembered that the level of airgap eccentricity in the on-site motors was not known and could lie anywhere between the two levels modelled or in fact be greater.

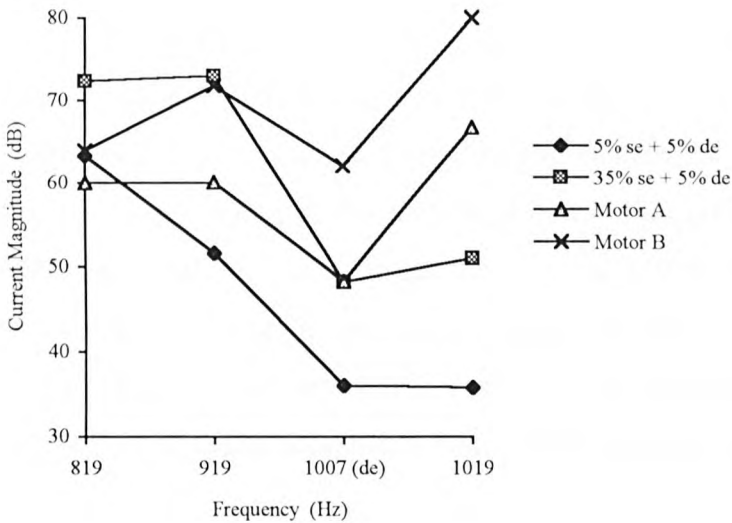


Figure 7.8 Current Magnitudes from the On - Site Tests (Motors A and B) and from the Finite Element Analysis at 744rpm (5%se + 5%se and 35%se + 5%de)

Inspection of the graph reveals that the agreement between calculated and measured current magnitudes was rather sporadic. There was no consistent agreement, for example, the finite element results for 35% static with 5% dynamic eccentricity agreeing with those for motor B. Table 7.9 presents the above magnitudes and the 807Hz component that was visible in the spectra for 5% static with 5% dynamic eccentricity.

Frequency (Hz)	Motor A (dB)	Motor B (dB)	FE 5% se + 5% de (dB)	FE 35% se + 5% de (dB)
819 (se)	<b>60.0</b>	<b>63.9</b>	<b>63.3</b>	<b>72.4</b>
919 (se)	60.1	66.6	51.6	73.0
1019 (se)	66.7	80.0	35.8	51.0
807 (de)	38.9	58.3	49.8	- (not visible)
907 (de)	45.8	48.8	-	68.9
1007 (de)	<b>48.3</b>	62.1	36.0	<b>48.2</b>

Table 7.9 Comparison of Finite Element and On-Site Test Current Components

The agreement for motor B and the lower level of finite element results is good for the 819Hz component (0.6dB different), however, for the 919Hz component the motor B magnitude is 6.4dB less than that obtained from the finite element for 35% static with 5% dynamic eccentricity. For motor A the 1007Hz is only 0.1dB greater than the FE magnitude at 35% static with 5% dynamic but then for the 819Hz the agreement is better between the motor A magnitude and the FE magnitude for 5% static with 5% dynamic eccentricity. There is no consistency in the results, however, it has to be remembered that the level of airgap eccentricity in the on-site motors was unknown.

The finite element analysis was predicting the magnitude of the components in the same region as those obtained from on-site test measurements which was a very positive result in terms of applying the technique to a large motor. As discussed earlier, the

1019Hz and associated dynamic eccentricity components were predominant in the finite element spectra compared to the on-site test spectra. Some of the other components predicted by the finite element analysis were reasonably close to experimental values which gave confidence in the analysis. However, the 1019Hz was consistently less for both levels of modelled airgap eccentricity than either the current magnitudes for motor A or B. This component was a function of second order saturation ( $n_{sa} = 2$ ) and a possible explanation is that the finite element modelling of saturation at this level was not in line with what was happening in the actual motors. Another explanation is that this component is also a function of the fifth time harmonic of the stator mmf ( $n_{os} = 5$ ) and no saturation ( $n_{sa} = 0$ ). Consequently, if this fifth harmonic is larger for the on-site motors than in the finite element analysis then the 1019Hz component would be larger in magnitude. The accuracy of the on-site results are also very dependent on the linearity of the on-site CT's. It is possible that for frequencies, for example, above 1000Hz that the CT's became non-linear, investigation of this would require another on-site visit.

In terms of the accuracy of the calculation of all the current magnitudes it was thought that the AC resistance of the stator (which is not included in the finite element model) could be having an effect on the magnitudes of the calculated current components. Unfortunately, this resistance would be higher at the higher frequencies, e.g. at 1019Hz compared to 819Hz which would not increase the magnitude of the 1019Hz component. However, the motor designers were consulted and the method described in Appendix 5, Section A5.4 was followed to calculate the AC resistance of the stator at the different frequencies of interest. It was found that the AC resistance at 1019Hz was  $15.3\Omega$ , the original total impedance (including the supply) was  $56\Omega$ , by using the AC stator resistance, instead of the DC value of  $0.649\Omega$ , this increased to  $58.3\Omega$ . In terms of the effect on the actual component magnitude, at 35% static with 5% dynamic the magnitude was 51dB, including the AC resistance decreased this to 50.7dB. This is a negligible difference and the AC resistance was deemed to have a negligible effect on the magnitude of the current components.

#### **7.5.4 Conclusion on Finite Element Analysis of Large Motor**

Overall the finite element analysis of the large motor was successful. The fundamental current was in good agreement with the rated value for full load and for the values obtained during the on-site tests for reduced load. The frequency components predicted by Equation 2.2 and obtained experimentally were present in the induced emf spectra and the effect of a change in speed of 2rpm was successfully modelled. The magnitude of the current components were in the same region as those obtained from the on-site tests. An accurate comparison between experimental and predicted current magnitudes for a known level of airgap eccentricity was not possible, however, the results obtained were very positive. A technique that was applied to a 11kW motor was successfully transferred up to a 1.45MW motor. Other than the 1019Hz component, the finite element analysis components exhibited the same behaviour as the on-site test results and what was suggested by the basic pole-pair analysis. With both forms of the fault present the static eccentricity components increased in magnitude with increasing static eccentricity. The dynamic components also increased in magnitude despite the dynamic eccentricity level not changing which indicated their dependence on the static eccentricity level.

### **7.6 Conclusion**

Once again the value of on-line current monitoring in the industrial situation has been proven worthwhile. The magnitudes of the airgap eccentricity components were clearly higher in motor B compared to motor A which indicated a higher level of airgap eccentricity. This tied in with the heavy usage of motor B and the thoughts of on-site personnel. The finite element analysis was successfully applied to the larger motor with the expected frequency components being present in the induced emf spectra. The magnitude of the predicted current components were in the same region as those

obtained on-site. The fundamental current and power factor were in good agreement with rated values and on-site results.

The application of the finite element analysis to model large industrial based motors is the area of this research that the majority of further work would be focused. The next Chapter details the objectives of further work in general related to the entire research programme and specifically in the area related to large industrial based motors.

# Chapter 8

## Conclusion

### 8.1 Achievement of Objectives

The objectives of this project, as detailed in Chapter 1, have been successfully achieved and new contributions to knowledge have been made as summarised below.

The critical appraisal of the classical mmf and permeance wave approach to predict the current components (frequency and magnitude) which are a function of airgap eccentricity revealed that the method accurately calculates the frequencies at which these components occur. Experimental results, for a 11kW test rig motor and a larger industrial based motor, showed that the magnitude of these components increased with increasing airgap eccentricity. However, an attempt to predict the magnitudes of the current components as a function of the airgap eccentricity level was largely unsuccessful as simplifications in the analysis resulted in inconsistent agreement between calculated and measured values. This was only attempted for the 11kW test-rig motor and was not applied to a large industrial induction motor.

Finite element analysis has been widely used to model induction motors and inherently overcomes many of the limitations of the classical approaches. It has been used to

model airgap eccentricity, however, the application of finite element analysis to investigate the current components and predict their magnitude as a function of the airgap eccentricity level had not been attempted. The successful achievement of this as presented in the thesis, has contributed to new knowledge in the area.

The finite element analysis was initially applied to a 11kW test-rig motor and the motor was successfully modelled with the fundamental current component at the expected value. The effect of high resistance joints in the rotor on the value of rotor bar conductivity used in the analysis was discovered. This had been a problem when trying to get the fundamental current at the expected value. The introduction of airgap eccentricity into the model was successful, the frequency components predicted by the mmf and permeance wave approach were present and increased in magnitude with increasing levels of airgap eccentricity.

Consistently good agreement was obtained between the calculated and the measured current magnitudes for given levels of airgap eccentricity. The combination of static and dynamic eccentricity as occurs in practice was successfully modelled. This was a considerable improvement on the achievements of the classical approach. Limitations in the mmf and permeance wave approach for calculating the pole-pairs of the flux waves associated with the airgap eccentricity components were discovered. The conclusion reached was that the pole-pair analysis can be used in a cautious fashion to gain a basic idea of the compatibility with the stator winding and dependability of static and dynamic eccentricity on each other. The finite element approach was shown to overcome the ambiguities in the classical approach and the results tied in with what was obtained experimentally.

The finite element investigations of the rotor slot design and the number of rotor bars successfully modelled the effects on the current components of these variations. The purpose of these investigations was to further the knowledge of the effects of these factors on the current magnitudes with airgap eccentricity variations. This was

particularly valuable in terms of monitoring different motors in industry. For instance, it was found that for the same increase in static eccentricity, the current components with a semi-closed rotor slot increased by three times more than those with a open rotor slot design.

The application of the finite element analysis to model a large industrially based motor was an important and successful part of this research. The classical approach to predict the current component magnitudes was never applied to a large induction motor and the application of finite element analysis to model these frequencies components and predict their magnitude for a large industrial motor was a new contribution. On-site tests on two 1.45MW three phase motors operating in industry further verified the application of on-line current monitoring in the industrial situation with the current components being larger for the motor that was thought to have a higher than normal level of airgap eccentricity. The finite element analysis of the motor was successful as the mains component was of the correct level and the airgap eccentricity components were present in the spectra. The finite element analysis verified the dependence of the dynamic eccentricity components on the static eccentricity level. This confirmed the experimental results and the general predictions of the pole-pair analysis. The calculated current magnitudes were in the same region as those obtained from the on-site tests. An exact comparison could not be made as the level of airgap eccentricity in the motors was unknown.

Overall this research has contributed to the understanding and quantification of airgap eccentricity in three phase induction motors. The classical approach was revisited and the advantages and limitations investigated. A finite element analysis has been successfully applied to both a small test-rig and a large industrially based motor. The airgap eccentricity components were modelled and for the test-rig motor consistently good agreement was obtain between measured and calculated magnitudes for a known level of airgap eccentricity. For the industrial motor the initial results were very encouraging as the predicted current magnitudes were at the same level as those

obtained on-site. The additional investigations into the effects of rotor design provided valuable information in terms of monitoring different motors in industry.

## **8.2 Suggestions for Future Work**

An immediate follow on from the work presented in this thesis would be the further investigation of the industrial based motor. The reason for the 1019Hz component being less prominent in the finite element analysis spectra than in the on-site test results needs to be established. Another on-site visit to check the frequency response of the on-site CT's would be required to eliminate CT non-linearity as the reason. A frequency spectrum for the busbar voltage supplying the motors could also be obtained. This voltage could then be applied to the finite element analysis which would be more realistic than the ideal voltage waveform currently assumed by the analysis. Due to computational restrictions the number of nodes available to generate the mesh was restricted. Although an adequate resolution was still obtained it might be possible, with another CPU, to increase the node number to more accurately model the flux distribution around the slots. It would also be valuable to perform further solutions at different levels of static and dynamic eccentricity with the view to try and match a modelled set of magnitudes with those obtained from the on-site tests.

Although not included in this thesis the author performed an additional finite element analysis on a small 10kW three phase induction motor during the project duration. The results of which are presented in a paper by Thomson et al [109]. Once again the finite element analysis predicted the results obtained experimentally and good agreement was obtained in terms of the current magnitudes for both the 50Hz and airgap eccentricity components. The basic pole-pairs analysis was again shown to be inaccurate in its predictions. This was a verification of the application of the technique to small motors. It would be valuable to model another larger industrial based motor to further investigate the capabilities of the approach.

In the longer term there is no reason why for a commonly used motor design that a finite element analysis could not be performed at different levels of airgap eccentricity to provide a database of current magnitudes related to specific levels of airgap eccentricity. Instead of monitoring a motor over time to look for relative increases in the component magnitudes, a one-off spectrum could be obtained and the magnitudes compared to the database. In order to monitor reliable frequency components that are not dependant on second order effects like winding asymmetry, a pole-pair analysis to provide an approximate estimation of the pole-pairs associated with the frequencies together with a finite element analysis and a calculation of the harmonic pole-pairs of the stator would be required. With increasing CPU power the time for finite element analysis is steadily decreasing and the availability of 3-dimensional modelling (even more accurate) is becoming increasingly a more practical option in terms of time and costs. Of course the database idea would require the co-operation of the motor manufactures in terms of the details of their designs. However, many manufacturers now perform finite element analysis as part of their design process and in fact they could compile such a database for airgap eccentricity without supplying design details to an outside source. Motors could then be supplied with guidelines for acceptable levels of the current components, with load taken into account, so that once the magnitudes reach a certain level then the operators know that the motor needs to be checked.

## References

- [1] S. Williamson, "The Induction Motor - a state-of-the-ark technology ?", *Power Engineering Journal*, Vol. 10, No. 6, December 1996, pp 247-255.
- [2] A. Hughes, "Electric Motors and Drives", *Newnes*, Reprint 1997, pp. 152.
- [3] M. S. Sarma, "Electric Machines Steady-State Theory and Dynamic Performance", *West Publishing Company*, 2nd Edition 1994, pp. 297.
- [4] P. J. Tavner, B. G. Gaydon and B. A. Ward, "Monitoring Generators and Large Motors", *IEE Proceedings*, Vol. 133, Pt. B, No. 3, May 1986, pp. 169-179.
- [5] W. H. Ross, "Condition Monitoring of Electrical Machines in ScottishPower", *IEE Colloquium on 'Condition Monitoring of Electrical Machines*, Digest No. 1995/019, January 1995, pp. 3/1-2.
- [6] D. R. Rankin, "The Industrial Application of Phase Current Analysis to Detect Rotor Winding Faults in Squirrel Cage Induction Motors", *Power Engineering Journal*, Vol. 9, No. 2, April 1995, pp. 77-86.
- [7] R. G. Courtney, "Machinery condition monitoring - a user's perspective", *IEE Colloquium on 'Condition Monitoring of Electrical Machines*, Digest No. 1995/019, January 1995, pp. 1/1-2.
- [8] K. Schneider, "Condition Monitoring", *Electrical Review*, January 1989, pp. 21-23.
- [9] A. H. Bonnett and G. C. Soukup, "Cause and Analysis of Stator and Rotor Failures in Three-Phase Squirrel-Cage Induction Motors", *IEEE Transactions on Industrial Applications*, Vol. 28, No. 4, July/August 1992, pp. 921-937.
- [10] D. G. Edwards, "Planned Maintenance of High Voltage Rotating Machine Insulation based upon Information Derived from On-Line Discharge Measurements", *Life Management of Power Plants*, IEE Conference publication No. 401, 12 - 14th December 1994, pp. 101-107.
- [11] W. T. Thomson and D. R. Rankin, "Case Histories of Rotor Winding Fault Diagnosis in Induction Motors", *2nd International Condition Monitoring Conference*, March 1987.
- [12] R. A. Leonard and W. T. Thomson, "Vibration and Stray Flux Monitoring for Unbalanced Supply and Inter-Turn Winding Fault Diagnosis in Induction Motors", *International Conference on Condition Monitoring*, April 1984, pp. 340-354.
- [13] R. R. Schoen, T. G. Habetler, F. Kamran and R. G. Bartheld, "Motor Bearing Damage Detection Using Stator Current Monitoring", *IEEE Transactions on Industrial Applications*, Vol. 31, No. 6, November/December 1995, pp. 1274-1279.
- [14] Motor Reliability Working Group, "Report of Large Motor Reliability Survey of Industrial and Commercial Installations, Part 1", *IEEE Transactions on Industrial Applications*, Vol. IA-21, No. 4, July/August 1985, pp. 853-864.
- [15] W. T. Thomson, N. D. Deans, R. A. Leonard and A. J. Milne, "Condition Monitoring of Induction Motors for Availability Assessment in Offshore Installations", *4th Euredata Conference*, Venice, Italy, 1983.
- [16] O. V. Thorsen and M. Dalve, "Condition Monitoring Methods, Failure Identification and Analysis for High Voltage Motors in Petrochemical Industry", *8th International Conference on Electrical Machines and Drives*, IEE Conference publication No. 444, 1-3th September 1997, pp. 109-113.
- [17] M. M. (Thys) Botha, "Electrical Machine Failures, Causes and Cures", *8th International Conference on Electrical Machines and Drives*, IEE Conference publication No. 444, 1-3th September 1997, pp. 114-117.

- [18] Discussions with John Middlemiss, Chief of Electrical Machine Design, Peebles Electric, Edinburgh.
- [19] J. R. Cameron, "Vibration and Current Monitoring for On-line Detection of Airgap Eccentricity in Induction Motors," *PhD thesis RGIT*, 1987.
- [20] J. R. Cameron, W. T. Thomson and A. B. Dow, "Vibration and Current Monitoring for Detecting Airgap Eccentricity in Large Induction Motors," *Proceedings IEE*, Vol. 133, Pt. B, No. 3, May 1986, pp. 155-163.
- [21] W. T. Thomson, D. R. Rankin and D. G. Dorrell, "On-Line Current Monitoring to Diagnose Airgap Eccentricity - an Industrial Case History of a Large High Voltage Induction Motor," *IEEE International Conference on Electrical Machines and Drives*, May 1997, pp. MA 2-4.1 - MA 2-4.3.
- [22] J. R. Cameron, W. T. Thomson and A. B. Dow, "On-Line Current Monitoring of Induction Motors - A Method for Calculating the Level of Airgap Eccentricity," *Proceedings IEE, 3rd EMDA Conference*, IEE No. 282, pp. 173-178.
- [23] A. Gray and J. G. Pertsch, "Critical Review of the Bibliography on Unbalanced Magnetic Pull in Dynamo-Electric Machines," *Transactions AIEE*, Vol. 37, Part II, 1918, pp. 1417-1424.
- [24] E. Rosenberg, "Magnetic Pull in Electric Machines," *Transactions AIEE*, Part 2, 1918.
- [25] A. Covo, "Unbalanced Magnetic Pull in Induction Motors with Eccentric Rotors," *Transactions AIEE*, 1954.
- [26] S. Williamson and M. A. S. Abdel-Magied, "Unbalanced Magnetic Pull in Induction Motors with Asymmetrical Rotor Cages," *2nd International Conference on Electrical Machine Design and Application*, 1985.
- [27] S. A. Swann, "Effect of Rotor Eccentricity on the Magnetic Field in the Airgap of a Non-Salient-Pole Machine," *Proceedings IEE*, Vol. 110, No. 5, 1963.
- [28] W. Freise and H. Jordan, "Unbalanced Magnetic Pull in 3-Phase A.C. Machines," *ETZ-A* 83 No. 9, Translation CE Trans 7836, 1962.
- [29] M. Osama and T. A. Lipo, "A New Induction Machine Model for Analysis of Eccentric Rotor Magnetic Pull," *Symposium on Power Electronic, Electrical Drives, Advanced Electrical Machines*, Taormina Italy, June 1994, pp. 173-177.
- [30] A. Arkkio and O. Lindgren, "Unbalanced Magnetic Pull in a High-Speed Induction Motor with an Eccentric Rotor," *International Conference on Electrical Machines (ICEM 94)*, Vol. 1, pp 53-58.
- [31] M. Bradford, "Misalignment of Rotating Machines, Determination of Unbalanced Magnetic Pull," *Electrical Review*, 1966, Vol. 178.
- [32] M. Bradford, "Unbalanced Magnetic Pull in a 6-pole Induction Motor," *Proceedings IEE*, 1968, Vol. 115, No. 11.
- [33] G. B. Rai, "Airgap Eccentricity in Induction Motors," *ERA Report* 74-1188.
- [34] T. Bratoljic and P. Vrkljan, "Magnetic Forces Created by Rotor Eccentricity in Electrical Machines," *The Brown Boveri Review*, 1967, Vol. 54, No. 9.
- [35] R. Belmans, A. Vandenput and W. Geysen, "Influence of Unbalanced Magnetic Pull on the Radial Stability of Flexible-Shaft Induction Machines," *Proceedings IEE*, 1987, Vol. 134, Pt. B, No. 2.
- [36] W. R. Finley and R. R. Burke, "Proper Specification and Installation of Induction Motors," *IEEE Industry Applications Magazine*, January/February 1997, pp. 56-69.
- [37] W. T. Thomson, J. R. Cameron and A. B. Dow, "On-Line Diagnostics of Large Induction Motors," *Vibrations and Audible Noise in Alternating Machines*, Edited by Belmans, Binns, Geysen and Vandeput, Kluwer Academic Publishers, 1988.

- [38] A. J. Ellison and S. J. Yang, "Effects of Rotor Eccentricity on Acoustic Noise from Electrical Machines," *Proceedings IEE*, Vol. 118, No. 1, 1971, pp. 174-184.
- [39] S. P. Verma and R. Natarajan, "Effects of Eccentricity in Induction Motors," *Proceedings of the International Conference on Electrical Machines*, Budapest, Hungary, September 1982, pp. 930-933.
- [40] S. Fruchtenicht, E. Pittuis and H. Seinsch, "A Diagnostic System for Three-Phase Asynchronous Machines," *Proceedings 4th EMDA Conference*, IEE, London, 1989, No. 310, pp. 163-171.
- [41] J. Penman, M. N. Dey, A. J. Tait and W. E. Bryan, "Condition monitoring of Electrical Drives," *Proceedings IEE*, Vol. 133, Pt. B, No. 3, May 1986, pp. 142-148.
- [42] W. T. Thomson and D. Rankin, "Case Histories of Rotor Winding Fault Diagnosis in Induction Motors," *Proceedings International Conference on Condition Monitoring*, University College Swansea, April 1987, pp. 798-819.
- [43] W. T. Thomson, "On-Line Monitoring to Detect Electrical and Mechanical Faults in Three-Phase Induction Motors," *IEE Conference Proceedings on Life Management of Power Plants*, no. 401, December 1994, pp. 66-74.
- [44] G. B. Kilman and J. Stein, "Induction Motor Fault Detection via Passive Current Monitoring," *Proceedings International Conference on Electrical Machines (ICEM'90)*, August 1990, pp. 13-17.
- [45] R. R. Schoen, B. K. Lin, T. G. Habetler, J. H. Schlag and S. Farag, "An Unsupervised, On-Line System for Induction Motor Fault Detection using Stator Current Monitoring," *IEEE Transactions on Industrial Applications*, Vol. 31, No. 6, November/December 1995, pp. 1280-1286.
- [46] J. Penman and C. M. Yin, "The Application of Artificial Neural Networks in Identifying Faults in Induction Machines," *International Conference on Electrical Machines (ICEM'92)*, Manchester, Vol. 3, pp. 1256-1260.
- [47] F. Filippetti, G. Franceshini and C. Tassoni, "Neutral Networks Aided On-Line Diagnostics of Induction Motor Rotor Faults," *IEEE Transactions on Industry Applications*, Vol. 31, No. 4, July/August 1995, pp. 892-899.
- [48] S. J. Yang, "Low-Noise Electrical Motors," *IEE Monographs in Electrical and Electronic Engineering*, Oxford Science Publications, 1981.
- [49] A. Stavrou and J. Penman, "The On-Line Quantification of Airgap Eccentricity in Induction Machines," *International Conference on Electrical Machines, (ICEM'94)*, pp. 261-266.
- [50] D. G. Dorrell, W. T. Thomson and S. Roach, "Combined Effects of Static and Dynamic Eccentricity on Airgap Flux Waves and the Application of current Monitoring to Detect Dynamic Eccentricity in 3-Phase Induction Motors," *Proceedings of IEE Electrical Machines and Drives Conference (EMD'95)*, IEE No. 412, pp. 151-155.
- [51] S. Salon, M. DeBortoli, D. Burrow and C. Slavik, "Calculation of Circulating Current between Parallel Winding in Induction Motors with Eccentric Rotors by Finite Element Method," *Proceedings of International Conference on Electrical Machines (ICEM'92)*, pp. 371-375.
- [52] H. A. Toliyat, M. S. Arefeen and A. G. Parlos, "A Method for Dynamic Simulation and Detection of Air-Gap Eccentricity in Induction Machines," *30th IEEE Industry Applications Society Annual Meeting*, Orlando 1995, Vol. 1, pp. 629-636.
- [53] R. Hirvonen, "On-Line Condition Monitoring of Defects in Squirrel Cage Motors," *International Conference on Electrical Machines, (ICEM'94)*, pp. 267-272.
- [54] A. J. M. Cardoso and E. S. Saraiva, "Computer-Aided Detection of Airgap Eccentricity in Operating Three-Phase Induction Motors by Park's Vector Approach," *IEEE*

*Transactions on Industry Applications*, Vol. 29, No. 5, September/October 1993, pp. 897-901.

- [55] W. T. Thomson, "On-Line Current Monitoring to Diagnose Shaft Misalignment in Three-Phase Induction Motor Drive Systems," *Proceedings International Conference on Electrical Machines (ICEM'94)*, pp. 238-243.
- [56] D. G. Dorrell, W. T. Thomson and S. Roach, "Analysis of Airgap Flux, Current and Vibration Signals as a Function of the Combination of Static and Dynamic Airgap Eccentricity in 3-Phase Induction Motors," *30th IEEE Industry Applications Society Annual Meeting*, Orlando 1995, Vol. 1, pp. 563-570.
- [57] W. Freize and H. Jordan, "Unilateral Magnetic Pulls in Three-Phase Machines," *ETZ-A*, Vol. 83, No. 9, Translation C.E. 7836, 1962.
- [58] G. Kron, "Equivalent Circuits of Electric Machines," *Dover Publications*, USA, 1967.
- [59] R. R. Schoen and T. G. Habetler, "A New Method of Current Based Condition Monitoring in Induction Machines Operating Under Arbitrary Load Conditions," *Electric Machines and Power Systems*, Talyor and Francis, 1997, pp. 141-152.
- [60] R. R. Schoen and T. G. Habetler, "Evaluation and Implementation of a System to Eliminate Arbitrary Load Effects in Current-Based Monitoring of Induction Machines," *IEEE Industry Applications Conference 1996*, Vol. 1, pp. 671-678.
- [61] Discussions with Research Supervisor W. T. Thomson and experimental investigations.
- [62] P. L. Alger, "The Nature of Induction Machines," *Gordon and Breach*, 1965.
- [63] B. Heller and V. Hamata. "Harmonic Field Effects in Induction Machines," *Elsevier Scientific Publishing Company*, 1977.
- [64] A. Arkkio, "Unbalanced Magnetic Pull in Cage Induction Motors - Dynamic and Static Eccentricity," *International Conference on Electric Machines (ICEM 1996)*, Vigo, Spain, Vol. 1, pp. 192-197.
- [65] J. C. Mercier, L. Durantay and J. Enon, "Finite Element Computation of the Magnetic Fields and Forces in an Induction Machine at its Rated Point with Simulation of Electromechanical Defects," *International Conference on Electric Machines (ICEM 1994)*, Vol. 2, pp. 44-49.
- [66] M. J. DeBortoli, S. J. Salon, D. W. Burow and C. J. Slavik, "Effects of Rotor Eccentricity and Parallel Windings on Induction Machine Behaviour: A Study using Finite Element Analysis," *IEEE Transactions on Magnetics*, Vol. 29, No. 2, March 1993, pp. 1676-1682.
- [67] S. Salon, D. Burow, C. Slavik and M. DeBortoli, "Effects of Air Gap Ovality on Induction Machine Behaviour," *International Conference on Electric Machines (ICEM 1996)*, Vigo, Spain, Vol. 1, pp. 401-404.
- [68] W. T. Thomson, "On-Line Current Monitoing to Diagnose Shaft Misalignment in Three-Phase Induction Motor Drive Systems," *International Conference on Electric Machines (ICEM'94)*, pp. 238-243.
- [69] J. R. Brauer (editor), "What Every Engineer Should Know About Finite Element Analysis," *Marcel Dekker, Inc.*, 1988.
- [70] M. J. Turner, R. W. Clough, H. C. Martin and L. J Topp, "Stiffness and Deflection Analysis of Complex Structures," *Journal of Aeronautical Science*, Vol. 23, 1956, pp. 805-824.
- [71] O. C. Zienkiewicz and Y. K. Cheung, "Finite Elements in the Solution of Field Problems," *The Engineer*, Sept. 1965, pp. 507-510.
- [72] S. J. Salon, "Finite Element Analysis of Electric Machinery," *IEE Computer Applications in Power*, April 1990, pp. 29-32.
- [73] J. M. Steele, "Applied Finite Element Modelling," *Marcel Dekker, Inc.*, 1989.

- [74] X. Deng, S. Palko, T. Jokinen and E. Ritchie, "Rotor Faults Analysis of Induction Motors by Dynamic Model and Finite Element Method," *IEEE Power Technology Conference*, Stockholm, Sweden, pp. 368-372.
- [75] C. B. Rajanathan and D. S. Thompson, "Finite Element Analysis of an Induction Motor Operating under Phase Failure Conditions," *Universities Power Engineering Conference (UPEC '94)*, pp. 193-195.
- [76] S. Williamson and M. J. Robinson, "Calculation of Cage Induction Motor Equivalent Circuit Parameters using Finite Elements," *IEE Proceedings B Electric Power Applications*, Vol. 138, Iss. 5, pp. 264-276.
- [77] S. Williamson and M. C. Begg, "Calculation of the Resistance of Induction Motor End Rings," *IEE Proceedings*, Vol. 133, Pt. B, No. 2, March 1986, pp. 54-60.
- [78] R. DeWeerd, K. Hameyer and R. Belmans, "End Ring Inductance of a Squirrel-Cage Induction Motor using 2D and 3D Finite Element Methods," *IEEE Industry Applications Society Annual Meeting*, Oct. 1995, Vol. 1, pp. 515-522.
- [79] A. Arkkio and A. Niemenmaa, "Estimation of Losses in Cage induction Motors using Finite Element Techniques," *International Conference on Electrical Machines (ICEM'92)*, Manchester, Vol. 1, pp. 317-321.
- [80] Y. Ning, C. Zhong and K. Shao, "Saturation Effects in Three-Phase Induction Motors," *International Conference on Electric Machines (ICEM'94)*, pp. 133-137.
- [81] Y. Liao and T. A. Lipo, "Effect of Saturation Third Harmonic on the Performance of Squirrel-Cage Induction Machines," *International Conference on Electrical Machines (ICEM'92)*, Manchester, Vol. 1, pp. 278-282.
- [82] S. Williamson, "Induction Motor Modelling using Finite Elements," *International Conference on Electric Machines (ICEM'94)*, pp. 1-8.
- [83] T. S. Parkin and T. W. Preston, "Induction Motor Analysis using Finite Elements," *Proceedings of the 6th International Conference on Electrical Machines and Drives (EMDA)*, Oxford, 1993, pp. 20-24.
- [84] G. K. M. Khan, W. C. H. Yu and J. P. Sturgess, "Finite Element Analysis of Induction Motors for Rail Traction Applications," *International Conference on Electric Machines (ICEM'94)*, pp 33-38.
- [85] W. T. Thomson, R. A. Leonard, N. D. Deans and A. J. Milne, "Monitoring Strategy for Discriminating between Different Types of Rotor Defects in Induction Motors," *18th Universities Power Engineering Conference*, 1983, pp. 241-246.
- [86] Beng Degree Notes (2/3rd year) by W. T. Thomson of The Robert Gordon University, Aberdeen.
- [87] R. L. Boylestad, "Introductory Circuit Analysis," *Macmillan Publishing Company*, 6th edition, 1990.
- [88] M. G. Say, "Alternating Current Machines," *Longman Scientific and Technical*, 5th edition, 1983.
- [89] M. Kostenko and L. Piotrovsky, "Electrical Machines Vol II," *MIR Publishers*, 1977.
- [90] E. C. Barnes, "An Experimental Study of Induction Machine End-Turn Leakage Reactance," *AIEE Transactions*, vol. 70, 1951, pp. 671-679.
- [91] T. C. Lloyd, V. F. Giusti and S. S. L. Chang, "Reactances of Squirrel-Cage Induction Motors," *AIEE Transactions*, vol. 66, 1947, pp. 1349-1355.
- [92] V. B. Honsinger, "Theory of Winding Leakage Reactance," *AIEE Transactions*, August 1959, pp. 417-426.
- [93] R. DeWeerd, K. Hameyer and R. Belmans, "End Winding Leakage Calculation of a Squirrel-Cage Induction Motor for Different Load Conditions," *COMPEL - The*

*International Journal for Computation and Mathematics in Electrical and Electronic Engineering*, vol. 14, no. 4, pp 85-88.

- [94] N. M. Morris, "Electrical and Electronic Principles," *Longman Scientific and Technical*, 1980.
- [95] D. Halliday and R Resnick, "Physics, Part 2," *John Wiley and Sons Inc.*, 1960.
- [96] "Matlab User Manual", *The MathWorks Inc.* Natick, Mass. USA, 1992.
- [97] R. B. Randall and B. Tech, "Frequency Analysis," *Bruel & Kjaer*, 1987.
- [98] E. C. Ifeachor and B. W. Jervis, "Digital Signal Processing: A Practical Approach," *Addison-Wesley Publishing Company*, 1993.
- [99] "Windows to FFT Analysis (part 1)," Technical Review no. 3, 1987, *Bruel & Kjaer*
- [100] J. C. Moreira and T. A. Lipo, "Modelling of Saturation AC Machines Including Air Gap Flux Harmonic Components," *IEEE Transactions on Industry Application*, Vol. 28, No. 2, March/April 1992, pp. 343-349.
- [101] J. S. Hsu, S. P. Liou, B. T. Lin and W. F. Weldon, "Losses Influenced by Third-Harmonic Flux in Induction Motors," *IEEE Transactions on Energy Conversion*, Vol. 6, No. 3, September 1991, pp. 461-468.
- [102] A. Arkkio, "Unbalanced Magnetic Pull in Cage Induction Motors with Asymmetry in Rotor Structures," *Proceedings of the 8th International Conference on Electrical Machines and Drives EMD 1997*, IEE Conference Publication No. 444, pp. 36 - 40.
- [103] A. Ferrah, P. J. Hogben-Laing, K. J. Bradley, G. M. Asher and M. S. Woolfson, "The Effect of Rotor Design on Sensorless Speed Estimation using Rotor Slot Harmonics Identified by Adaptive Filtering using the Maximum Likelihood Approach," *IEEE Industry Applications Society Annual Meeting*, 1997, pp. 128-135.
- [104] S. Williamson and C. I. McClay, "Optimisation of the Geometry of Closed Rotor Slot for Cage Induction Motors," *IEEE Transactions on Industrial Applications*, Vol. 32, Issue 3, May-June 1996, pp. 560-568.
- [105] S. Palko, "The Effect of Slanted Stator and Rotor Teeth on Torque and Electromagnetic Losses in Cage Induction Motors," *Proceedings of the Symposium on Power Electronics, Electrical Drives, Advanced Electrical Motors*, Taormina, Italy, 1994, Vol. 1, pp. 185-187.
- [106] S. Salon, D. Burrow, C. Slavik and M. DeBortoli, "Effects of Slot Closure and Magnetic Saturation on Induction Machine Behaviour," *IEEE Transactions on Magnetics*, Vol. 30, Issue 5, Part 2, Sept. 1994, pp. 3697-3700.
- [107] J. Middlemiss, Chief of Electrical Machine Design, Peebles Electric, Edinburgh: Extensive written notes on the motor design details and equations for calculating the winding factors and the AC stator resistance.
- [108] J. Sturgess, GEC Alstom, Engineering Research Centre, Collaborating Company: Written details on calculating the effective core length and stacking factor when cooling ducts are present.
- [109] W. T. Thomson, A. Barbour, C. Tassoni and F. Filippeti, "An Appraisal of the MMF and Permeance Method and Finite Element Models to Study Static Air-gap Eccentricity and its Diagnosis in Induction Machines," *Proceedings of the International Conference on Electrical Machines ICEM'98*, Istanbul, September 1998, Vol. 3., pp. 218.2 - 218.7.

# **Appendix 1**

## **Test- Rig Motor Specification**

## A1.1 Test -Rig Motor Specification:

Parameter	Value
Power	11 kW
Frequency	50 Hz
Phase	3
Line Voltage	415 V
Full load current	20 A
Speed	1420 rpm
Poles	4
Connection	delta
Airgap length	22 thou (0.56mm)
Number of stator slots	36
Number of rotor slots	51
Skew	None
Full Load Operating Temp.	80°C

## A1.2 Stator Specification and Dimensions:

*Winding Data:*

Double layer

Number of slots/pole = 9

Number of slots/pole/phase, d = 3

Number of coils = 36

Number of turns/coil = 15

Number of series turns/phase, T = 180

Coil span = 8 slots

Fundamental distribution factor,  $k_{d1} = 0.96$

Fundamental pitch factor,  $k_{p1} = 0.9848$

Fundamental skew factor  $k_{z1} = 1$  (no skew)

### *General and Slot Dimensions*

Stator Core Material - Newcore 800

Inside diameter = 165.1mm

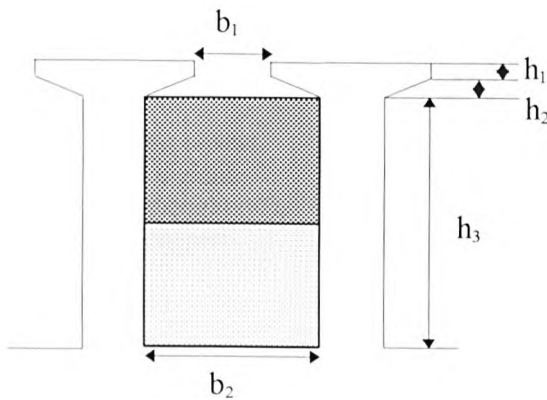
Outside diameter = 261.0mm

Axial length of core = 146.05mm

Pole pitch,  $\tau_p = 130.0\text{mm}$

Number of slots = 36

Slot pitch  $\tau_s = 14.4\text{mm}$



$$b_1 = 3.04\text{mm}$$

$$b_2 = 6.79\text{mm}$$

$$h_1 = 0.762\text{mm}$$

$$h_2 = 0.682\text{mm}$$

$$h_3 = 19.376\text{mm}$$

### A1.3 Rotor Specification and Dimensions:

Copper fabricated rotor: copper bars and end-rings brazed with soft solder joints

Rotor Core Material - Newcore 800

Rotor diameter = 164.54

Rotor shaft diameter = 56.8mm

Axial length of core = 146.05mm

Number of bars = 51

Full load speed (star connected 415V line) = 1322 rpm

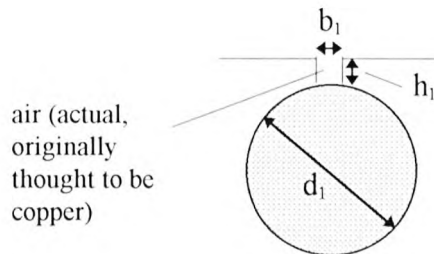
Full load slip (star connected 415V line) = 0.1187

Fundamental distribution factor,  $k_{d1} = 1$

Fundamental pitch factor,  $k_{p1} = 1$

Fundamental skew factor  $k_{z1} = 1$  (no skew)

*Bars:*

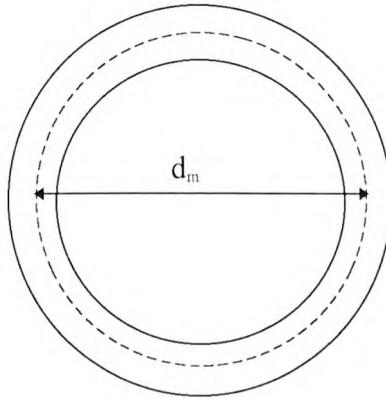


$d_1 = 7.0\text{mm}$

$b_1 = 0.6\text{mm}$  (actual, originally thought to be 1.27mm)

$h_1 = 0.40\text{mm}$

*End-Ring: (End View)*

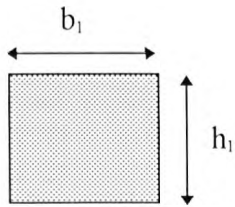


$d_m = \text{mean diameter} = 153.5\text{mm}$

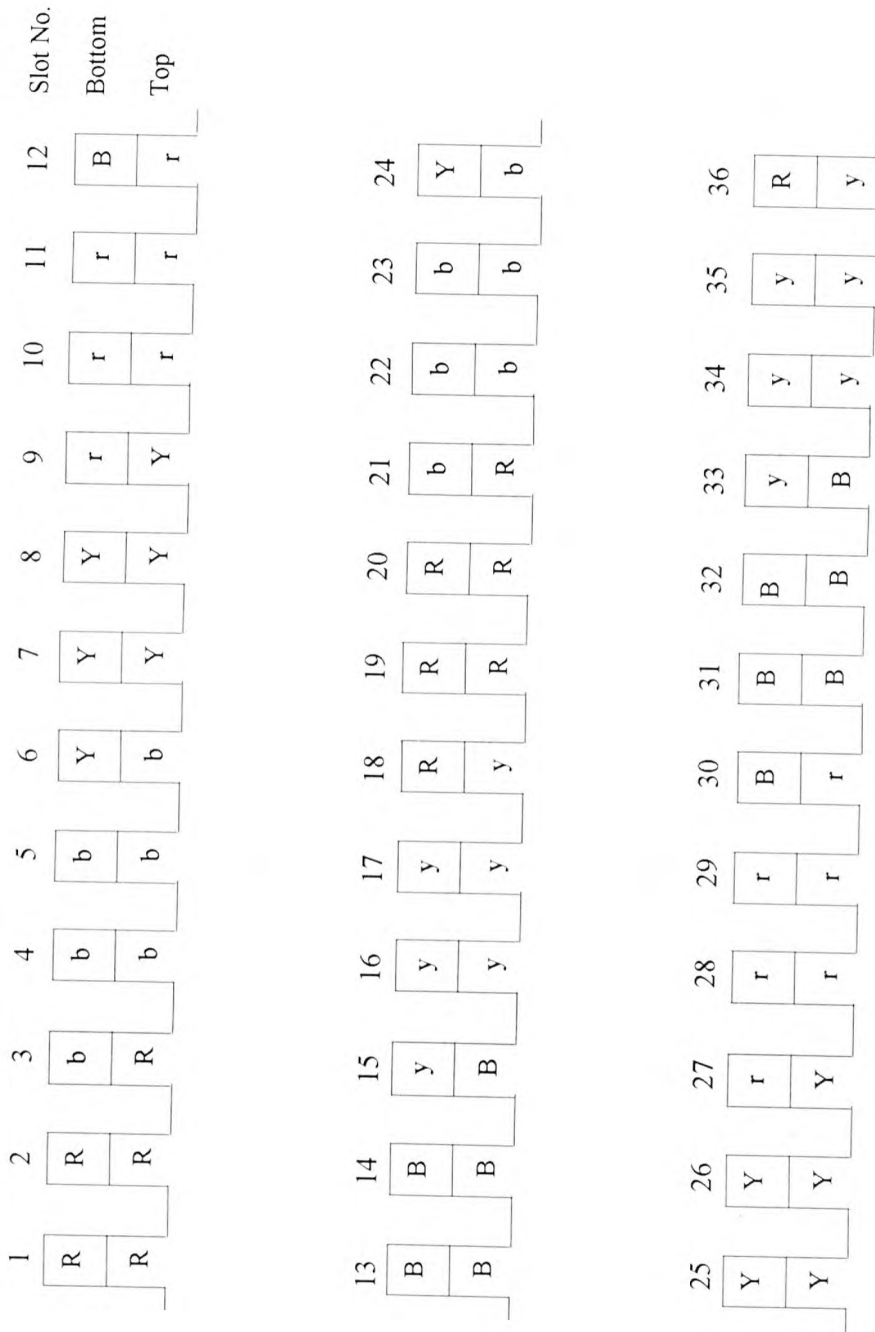
*Cross section through end-ring (approximately a square section):*

$b_1 = 13\text{mm}$

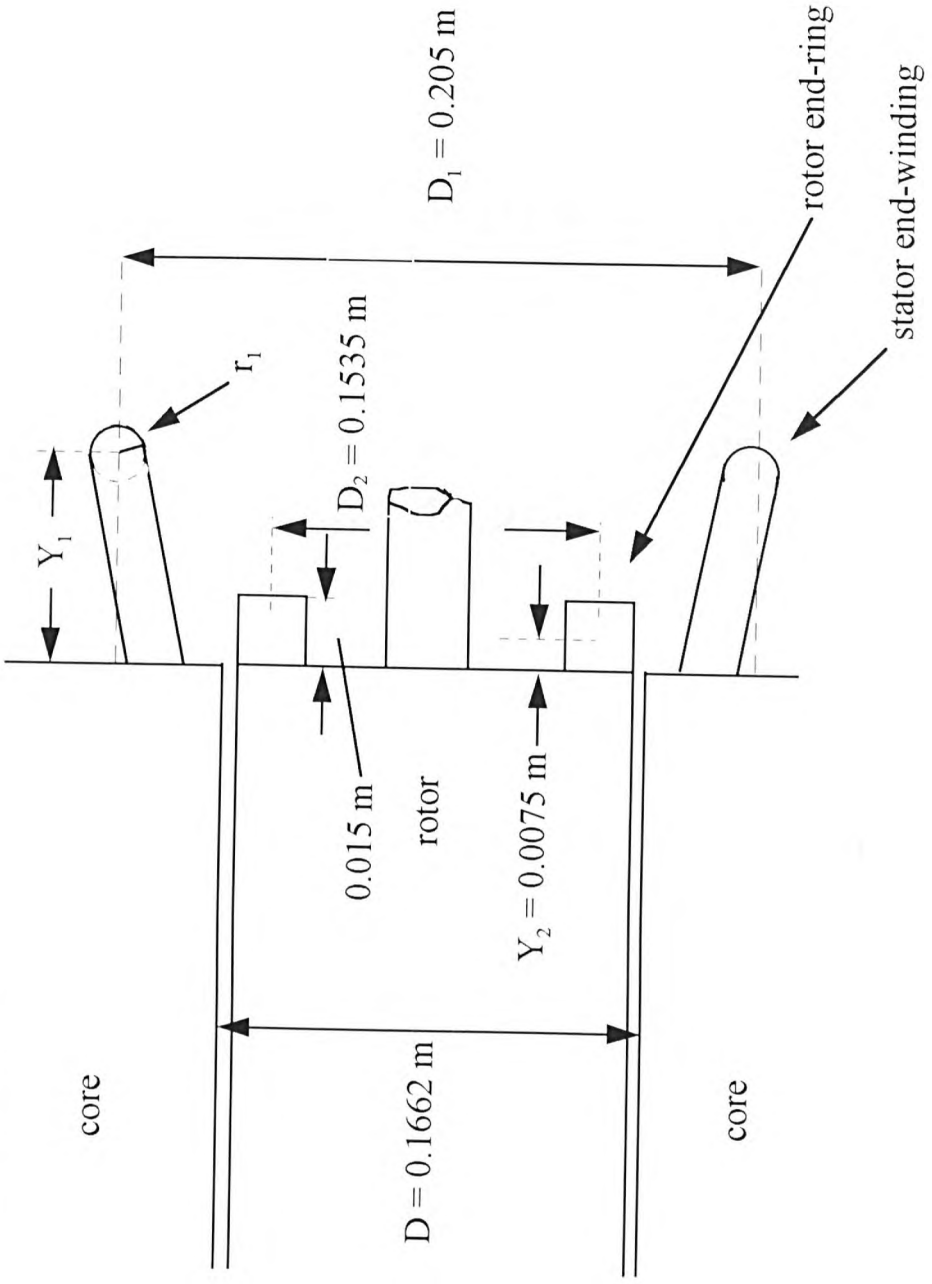
$h_1 = 15\text{mm}$



# A1.4 Stator Winding Layout



**A1.5 Diagram of Complete Stator and Rotor End-rings with Respect to Alger's Calculation for the Stator End-winding Leakage Reactance:**



# **Appendix 2**

## **Motor Parameter and Equivalent Circuit Calculations**

## Appendix 2.1 Calculation of No-Load Motor Parameters

As explained in Chapter 3.3.2 it was possible to use the exact equivalent circuit on no-load as the stator resistance was accurately measured and the stator inductance had been calculated from design details by Cameron [19]. This circuit is shown in Figure A2.1.

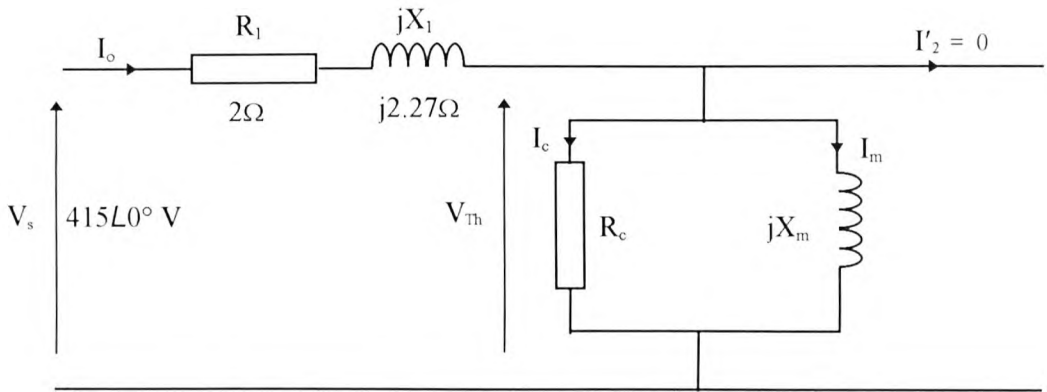


Figure A2.1 Exact Equivalent Circuit on No-Load

The results of the no-load test were (per phase values):

$$P_{in} = 390\text{W}, \quad V_{in} = 415\angle 0^\circ\text{V}, \quad I_o = 6.3\text{A}$$

The power factor of the no-load current  $I_o$  was calculated from:

$$P_o = V_{ph} I_o \cos \phi$$

$$390 = 415 \times 6.3 \cos \phi$$

$$\therefore pf = 0.149 \text{ lag}$$

$$\text{hence } \underline{I_o = 6.3 \angle -81.42^\circ}$$

this was required to calculate  $V_{Th}$  and hence  $R_c$  as  $R_c = \frac{V_{Th}^2}{P_c}$  where  $P_c$  is the power lost in the core and rotational and windage losses. The rotational and windage losses could not be separated from the core losses, however, it was reasonable to assume that they were negligible and that this power was lost in the core.

$$\begin{aligned}
P_c &= P_o - \bar{I}_o^2 R_1 \\
&= 390 - 6.3^2 \times 2 \\
&= \underline{\underline{310.62 \text{ W}}}
\end{aligned}$$

$$\begin{aligned}
\bar{V}_{TH} &= 415/\underline{0^\circ} - (2 + j2.77) 6.3/\underline{-81.42^\circ} \\
&= 415/\underline{0^\circ} - 3/\underline{48.62} \times 6.3/\underline{-81.42^\circ} \\
&= \underline{\underline{399.24 /1.464^\circ V}}
\end{aligned}$$

$$\text{hence } R_c = \frac{V_{Th}^2}{P_c} = \frac{399.11^2}{310.62} = \underline{\underline{513.13\Omega}}$$

The magnetising reactance was calculated from:

$$X_m = \frac{V_{Th}}{I_m} \quad \text{where} \quad \bar{I}_m = \sqrt{I_o^2 - I_c^2}$$

$$I_c = \frac{V_{Th}}{R_c} = \frac{399.24/\underline{1.464^\circ}}{513.14} = 0.778/\underline{1.464^\circ} \text{ A}$$

$$\therefore \bar{I}_m = \sqrt{6.3^2 - 0.078^2} = 6.252 \text{ A}$$

$$X_m = \frac{V_{Th}}{I_m} = \frac{399.24/\underline{1.464^\circ}}{6.252/\underline{90^\circ}} = \underline{\underline{j63.86\Omega}}$$

The value of  $j63.96\Omega$  for the magnetising reactance compared favourably with a value obtained from design details by Cameron of  $j62\Omega$  [19]. Therefore, the exact equivalent circuit on no-load is shown in Figure A2.2.

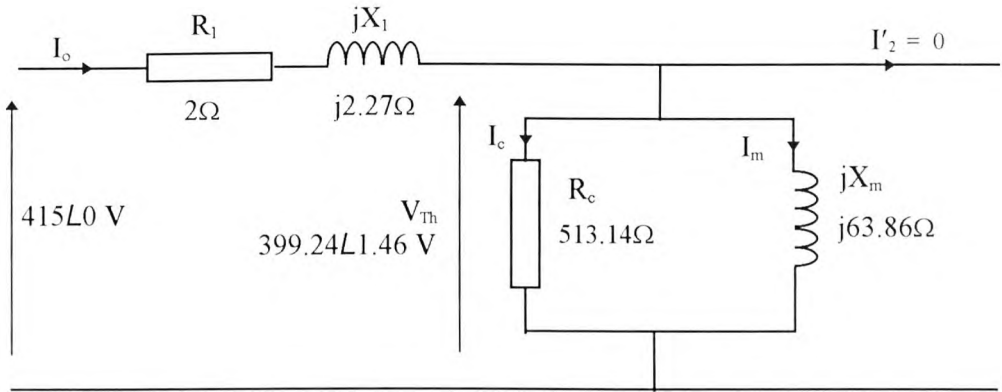


Figure A2.2 Complete Exact Equivalent Circuit on No-Load

## Appendix 2.2 Calculation of Locked Rotor Motor Parameters

The locked rotor results are shown in Table A2.1:

Phase	Power (W)	$I_L$ (A)	$I_{ph}$ (A)	$V_L$ (V)
Red (RY)	562.5	20	11.5	66.2
Yellow (YB)	572.25	20	11.5	67
Blue (BR)	552.5	20	11.5	65.25

Table A2.1 Locked Rotor Results for each Phase

From these results:

$$P_{ph} = I_{ph}^2 R_{eq} \quad \text{where} \quad R_{eq} = R_1 + R_2'$$

$$\therefore R_{eqR} = \frac{562.5}{11.5^2} = \underline{4.253\Omega}$$

$$\text{Similarly:} \quad R_{eqY} = 4.33\Omega \quad R_{eqB} = 4.178\Omega$$

The average equivalent resistance  $R_{eqAV} = 4.254 \Omega$  which results in  $R'_2 = 2.254 \Omega$  as  $R_1 = 2 \Omega$ . The average resistance is virtually the value of the red phase hence only the red phase was used to calculate  $jX_{eq}$ .

$$Z_{eqR} = \frac{V_{RY}}{I_{ph}} = \frac{66.2}{11.5} = 5.76 \Omega \quad \text{as} \quad X_{eqR} = \sqrt{Z_R^2 - R_{eqR}^2}$$

$$X_{eqR} = \sqrt{5.76^2 - 4.253^2} = \underline{\underline{j3.885 \Omega}}$$

Therefore as  $X_{eqR} = X_1 + X'_2$  and  $jX_1 = 2.27 \Omega$  then  $jX'_2 = \underline{\underline{1.615 \Omega}}$

Hence, the complete equivalent circuit is shown in Figure A2.3.

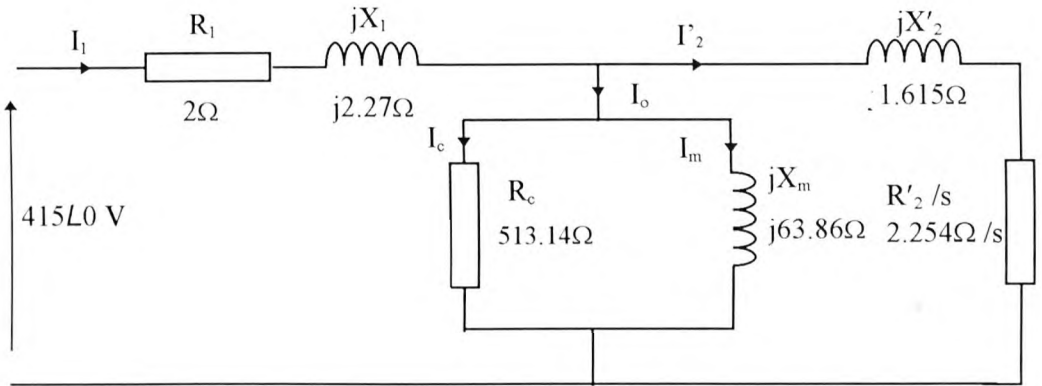


Figure A2.3 Complete Equivalent Circuit for Test-Rig Motor

### Appendix 2.3 Full-load 1420 rpm Equivalent Circuit Calculation

Using the derived equivalent circuit a performance calculation was performed at full-load 1420rpm to compare calculated values of motor current etc. with measured values.

To simplify the equivalent circuit and to calculate the referred rotor current  $I_2'$  a Thevenin equivalent circuit was used [87], the Thevenin voltage had already been calculated for the no-load test. Open circuiting the secondary side of the equivalent circuit meant the referred rotor side was seen as the load. The Thevenin voltage was then calculated across the load terminals as performed in the no-load test. This is shown in Figure A2.4.

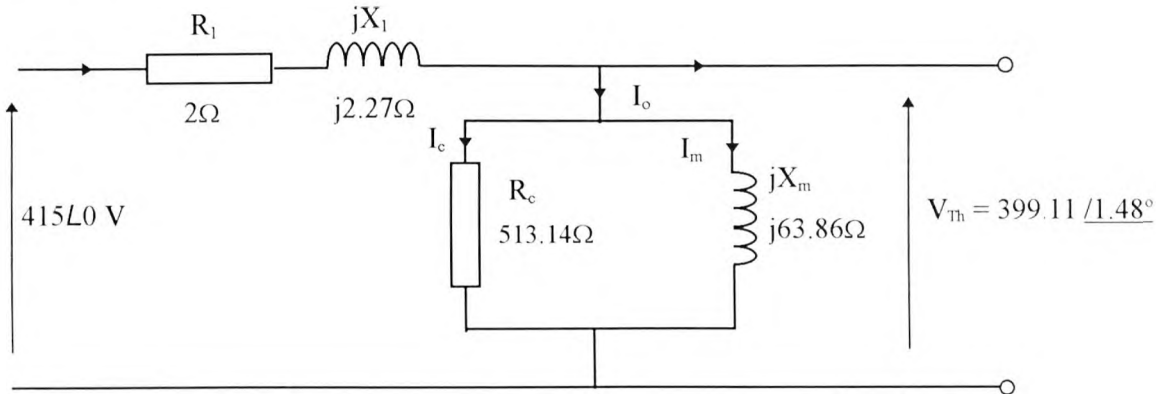


Figure A2.4 Calculation of Thevenin Circuit Parameters

By replacing the supply voltage (415V) with a short circuit the Thevenin impedance was calculated:

$$Z_{Th} = (2 + j2.27) // 513.14 // j63.86 = 2.91/50.1^\circ = \underline{\underline{1.86 + j2.22 \Omega}}$$

Hence the Thevenin equivalent circuit incorporated with the load is shown in Figure A2.5.

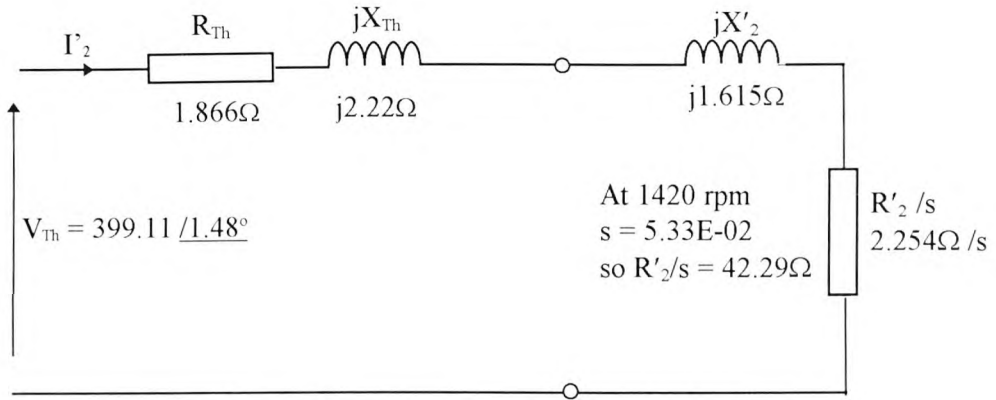


Figure A2.5 Thevenin and Load Circuits

Using this circuit  $I'_2$  was calculated:

$$\overline{I'_2} = \frac{V_{Th}}{Z_{Th}} = \frac{399.11/1.48^\circ}{42.29 + 1.86 + j2.22 + j1.615} = \underline{\underline{9/-3.496^\circ}}$$

Hence

$$P_o = 3 \times (\overline{I'_2})^2 \times R'_2 \left[ \frac{(1-s)}{s} \right]$$

$$= 3 \times 9^2 \times 2.254 \left[ \frac{(1 - 53.3E-03)}{5.33E-03} \right]$$

$$= \underline{\underline{9.728 kW}}$$

To calculate the input power and power factor the input current per phase had to be calculated:

$$V_{ph} = \bar{I}_1(R_1 + jX_1) + (\bar{I}_1 - \bar{I}_2)(R_c // jX_m)$$

$$415/\underline{0^\circ} = \bar{I}_1(2 + j2.27) + (\bar{I}_1 - 9/\underline{-3.578^\circ})(62.91/\underline{84^\circ})$$

$$\therefore \text{after reagraning } I_{1phase} = \underline{\underline{11.5/-33.5^\circ \text{ A}}}$$

$$I_L = 19.92/\underline{-33.5^\circ} \text{ A} \quad \text{and the power factor } \cos\phi = 0.834 \text{ lag}$$

$$P_{in} = \sqrt{3}V_L I_L \cos\phi = \sqrt{3} \times 415 \times 19.92 \times 0.834 = \underline{\underline{11.94 \text{ kW}}}$$

$$\text{The efficiceny is: } \eta = \frac{P_o}{P_{in}} \times 100 = \frac{9.728}{11.94} \times 100 = \underline{\underline{81.4\%}}$$

This value of efficiency was in line with another similar motor

## Appendix 2.4 Calculation of Effective Rotor Bar Conductivity

$$R'_2 = \frac{12(k_p k_d T_{ph})^2}{R} \left\{ r_{be} + \frac{R}{2p^2 \pi^2} r_e \right\} \quad (\text{A2.1})$$

where  $k_p$  = coil pitch factor = 0.9848

$k_d$  = distribution factor = 0.96

$T_{ph}$  = turns / phase = 180

$R$  = number of rotor bars = 51

$r_{be} = r'_{be}$  = effective rotor bar resistance

$p$  = pole pairs = 2

$r_e$  = end-ring resistance

$R'_2$  = referred rotor resistance = 2.254  $\Omega$  from locked rotor test

Hence by equating the end-ring resesitance to zero:

$$R_2' = 2.254 = \frac{12(0.96 \times 0.9848 \times 180)^2}{51} \{r_{be}' + 0\}$$

hence  $r_{be}' = r_{be} = \underline{330.8 \times 10^{-6} \Omega}$

To calculate the conductivity the resistivity had to be calculated:

$$r_{be}' = \frac{\rho_{eff} l}{A} \quad \text{where } A = \frac{\pi D^2}{4}$$

$r_{be}' =$  effective rotor bar resistance =  $330.8 \times 10^{-6} \Omega$

$\rho_{eff} =$  resistivity of bar material ( $\Omega m$ )

$l =$  length of bar = 146mm

$A =$  cross sectional area of bar ( $m^2$ )

$D =$  bar diameter = 6.985mm

$$\therefore \rho_{eff}' = \frac{330.8 \times 10^{-6} \times \pi \times 0.006985^2}{4 \times 0.146} = \underline{0.0868 \times 10^{-6} \Omega m}$$

$$\therefore \text{as } \sigma_{eff}' = \frac{1}{\rho_{eff}'} = \underline{1.115 \times 10^7 \text{ S/m}}$$

## Appendix 2.5 Calculation of Referred Rotor Resistance using the Standard Value for the Conductivity of Copper

Bar Resistance:  $r_{be} = \frac{\rho l}{A} = \frac{1.72 \times 10^{-8}}{\pi \times 0.003^2} \times 0.146 = \underline{8.88 \times 10^{-5} \Omega}$

End-ring Resistance:  $r_{er} = \frac{\rho l}{A} = \frac{1.72 \times 10^{-8} \times 2\pi \times 0.07675}{15 \times 13 \times 10^{-6}} = \underline{4.25 \times 10^{-5} \Omega}$

Substituting these values into Equation A2.1 the referred rotor resistance was calculated:

$$R'_2 = \frac{12(k_s k_d T_{ph})^2}{R} \left\{ r_{be} + \frac{R}{2p^2 \pi^2} r_e \right\}$$

$$R'_2 = \frac{12(0.96 \times 0.9848 \times 180)^2}{51} \left\{ 8.88 \times 10^{-5} + \frac{51}{2 \times 2^2 \times \pi^2} \times 4.25 \times 10^{-5} \right\}$$

$$= \underline{\underline{0.79 \Omega}}$$

This value is at 21°C, by using Equation A2.2 [95] this was transferred to 80°C to be comparable with the value from the locked rotor test:

$$R_2 = R_1 (1 + \alpha (\theta_2 - \theta_1)) \quad (A2.2)$$

$$= 0.79 (1 + 4 \times 10^{-3} (100 - 21))$$

$$= \underline{\underline{1.04 \Omega}}$$

where

$R_2$  = resistance at temperature  $\theta_2$  (21°C room temperature + 80°C motor temperature)

$R_1$  = resistance at temperature  $\theta_1$  (21°C room temperature)

$\alpha$  = temperature coefficient of resistance for copper

*(Note: In equation A2.2 the resistance terms can be directly replaced by the resistivity at the two temperatures as the resistance is linearly proportional to the resistivity. The resistivity of copper could then be changed to that at 80°C and the resistance for the bars and end-ring calculated. Equation A2.1 could then be used to calculate  $R'_2$  directly at 80°C. The same answer is obtained by both methods).*

# **Appendix 3**

**Matlab Based Spectrum Analysis  
Programs:  
Test Programs and Final Programs**

### Appendix 3.1 Code to Plot the FFT of a Generated Sinewave

```
t = 0:0.001:1;           % Generates time vector for producing
                          % sine wave i.e.  $f_s = 1000$  Hz
y = 100*sin(2*pi*50*t)   % Sine wave of magnitude 100 at 50 Hz
                          % 1001 data points
Y = fft(y,1001);        % FFT performed  $N = 1001$   $\Delta f = 1$  Hz
YY = abs(Y);            % Obtain magnitude of components i.e.
                          % remove complex part
f = 1000/1001*(1:500);  % Generate frequency axis
plot(f,YY(1:500));      % Plot spectrum
```

### Appendix 3.2 Code to Calculate the Conversion Factors for an FFT where $N=20,000$ , $f_s = 5000\text{Hz}$ and $\Delta f = 0.25\text{Hz}$

```
a = 1;                  % index into matrix for storing factors Conf5
j = 0;                  % loop index for generating dc signal
b = 1;                  % index into matrix containing dc signal
for j = 0:0.0002:1     % this loop generates a dc level  $f_s = 5000$  Hz
    y(b,1) = 100;      % magnitude 100
    b = b + 1;
end
x = fft(y,20000);      % FFT applied
X = abs(x);            % complex part removed
M = max(X);            % find size of peak due to component
MM = M/100;            % divide by original magnitude to find factor
Conv(a,1) = MM;        % store factor in matrix for 0 Hz (dc)

xf = 0.25;             % set first frequency for line 2 in spectrum
a = a + 1;             % increment position in storing matrix

% loop generates a signal at each line in the spectrum 0.25, 0.5..
2000Hz (xf)
```

```

for xf = 0.25:0.25:2000
    t = 0:0.0002:1;
    y = 100*sin(2*pi*xf*t);           % generates sinewave of xf Hz
    x = fft(y,20000);                % see code above for comments
    X = abs(x);
    M = max(X);
    MM = M/100;
    Conv(a,1) = MM;                  % factor stored
    a = a + 1;                       % increment position in storing
                                    matrix
end

```

### **Appendix 3.3 Code to Apply Conversion Factors to an FFT and Display the Spectrum with the Correct Frequency Axis**

This code applies the conversion factors to the matrix containing the FFT results.

```

a = 1;
for a = 1:8001                       % only first 2000 Hz required
    K1(a,1) = Plot(a,1)/Conv(a,1);
end

```

This divides the magnitude of each line up to 2000 Hz by the corresponding conversion factor and the values of magnitudes for the corrected spectrum are stored in matrix K1. The FFT could then be plotted against the frequency axis to display the corrected plot:

```

f = 5000/20000*(1:8001);           % 0-2000 Hz scale generated
plot(f,K1);

```

### Appendix 3.4 Code to Convert Linear Magitudes to dB

This code converts the results of the FFT from linear to dB.

```
a = 1;
for a = 1:8001
    K(a,1) = 20*log10(K1(a,1)/0.000001);
end
```

### Appendix 3.5 Code to Calculate the Factor x to Compensate for the Effects of Windowing

```
w1 = Kaiser(24480,9); % generate window coefficients
sum = 0; % hold value of running sum
i = 1; % index into matrix holding window coefficients
for i = 1:1:5001
    mult = w1(i,1) * w1(i,1); % w2(n)
    presentsum = mult + sum; % add to running total
    sum = presentsum % new running total
end
x = sqrt(5001/presentsum);
```

### Appendix 3.6 Program to Generate Spectrum of Current Signal

This test program generates the frequency spectrum of the current signal. The effects of the FFT, windowing and the conversion of the plot to a dB scale are incorporated.

```
w1 = Kaiser(24480,9); % generate window coefficients
y1 = y*0.7071*0.1*2.3; % change data to volts RMS and x
                        2.3
```

```

a = 1;
for a = 1:5001                                % apply window to data
    NW(a,1) = y1(1,a) * w1(a,1);
end
Y = fft(NW,20000);                            % FFT data
Plot = abs(Y);                                % remove complex part
a = 1;
for a = 8001                                    % apply conversion factors
    K1(a,1) = Plot(a,1) / Conv(a,1);
end
a = 1;
for a = 1:8001                                  % convert from linear to dB
    K(a,1) = 20*log10(K1(a,1)/0.000001);
end
f = 5000/20000*(1:8001);                      % generate frequency axis
plot(f,K);                                     % plot
axis([0 2000 0 120]);                         % display axis

```

### Appendix 3.7 Programs to Calculate Conversion Factors and Generate Spectrum of Current Signal with the Sampling Frequency Increased

```

% Calculates Conversion Factors
a = 1;                                         % index into matrix for storing factors Conf6
j = 0;                                         % loop index for generating dc signal
b = 1;                                         % index into matrix containing dc signal
for j = 0:0.0001:1                            % loop generates a dc level fs = 10000 Hz
    y(b,1) = 100;                             % magnitude 100
    b = b + 1;
end
x = fft(y,40000);                             % FFT applied
X = abs(x);                                   % complex part removed
M = max(X);                                   % find size of peak due to component

```

```

MM = M/100;                % divide by original magnitude to find factor
Confv(a,1) = MM;         % store factor in matrix for 0 Hz dc

xf = 0.25;                 % set first frequency for line 2 in spectrum
a = a + 1;                 % increment position in storing matrix

% loop generates a signal at each line in the spectrum 0.25, 0.5 ...
1500 (xf)

for xf = 0.25:0.25:1500
    t = 0:0.0001:1;
    y = 100*sin(2*pi*xf*t); % generates sine wave of xf Hz
    x = fft(y,40000);       % see code above for comments
    X = abs(x);
    M = max(X);
    MM = M/100;
    Confv(a,1) = MM;       % factor stored
    a = a + 1;             % increment position in storing
                           matrix
end

-----

% Plots Spectrum
w1 = Kaiser(24480,9);      % generate window coefficients
y1 = y*0.7071*0.1*2.3;    % change data to RMS and x 2.3
a = 1;
for a = 1:10001           % apply window to data
    NW(a,1) = y1(1,a) * w1(a,1);
end
Y = fft(NW,40000);        % FFT data
Plot = abs(Y);            % remove complex part
a = 1;
for a = 8001              % apply conversion factors
    K1(a,1) = Plot(a,1) / Confv(a,1);
end
a = 1;
for a = 1:8001            % convert from linear to dB

```

```

        K(a,1) = 20*log10(K1(a,1)/0.000001);
end
f = 10000/40000*(1:8001);           % generate frequency axis
plot(f,K);                           % plot
axis([0 2000 0 120]);                % display axis

```

### Appendix 3.8 Final Programs to Calculate Conversion Factors and Generate EMF and Current Spectrums for a Timestep of 3.9215e-05s

```

% This code calculates the conversion factors for the fft
a = 1;                                % index into matrix for storing factors
                                     Conhts
j = 0;                                % loop index for generating dc signal
b = 1;                                % index into matrix containing dc signal
for j = 0:3.9215E-05:0.959943985     % loop generates a dc level fs =
                                     25500 Hz
    y(b,1) = 100;                    % magnitude 100
    b = b + 1;
end
x = fft(y,102000);                   % FFT applied
X = abs(x);                           % complex part removed
M = max(X);                            % find size of peak due to component
MM = M/100;                            % divide by original magnitude to find factor
Conhts(a,1) = MM;                     % store factor in matrix for 0 Hz dc

xf = 0.25;                             % set first frequency for line 2 in spectrum
a = a + 1;                             % increment position in storing matrix

% loop generates a signal at each line in the spectrum 0.25, 0.5 ...
1500 (xf)

for xf = 0.25:0.25:2000
    t = 0: 3.9215E-05:0.959943985;
    y = 100*sin(2*pi*xf*t);           % generates sine wave of xf Hz

```

```

x = fft(y,102000);           % see code above for comments
X = abs(x);
M = max(X);
MM = M/100;
Conhts(a,1) = MM;           % factor stored
a = a + 1;                   % increment position in storing
                              matrix

end

% This code generates the frequency spectrum of an emf signal
% contained in matrix y
w1 = Kaiser(24480,9);        % generate window coefficients
y1 = y*0.7071*0.0005*2.3;    % change data to RMS, divide by
                              2000 and x 2.3

a = 1;
for a = 1:24480              % apply window to data
    NW(a,1) = y1(1,a) * w1(a,1);
end
Y = fft(NW,102000);          % FFT data
Plot = abs(Y);               % remove complex part
a = 1;
for a = 8001                 % apply conversion factors
    K1(a,1) = Plot(a,1) / Conhts(a,1);
end
a = 1;
for a = 1:8001               % convert from linear to dB
    K(a,1) = 20*log10(K1(a,1)/0.000001);
end
f = 25500/102000*(1:8001);   % generate frequency axis
plot(f,K);                   % plot
axis([0 2000 0 120]);        % display axis
xlabel('Frequency (Hz)');
ylabel('Induced EMF (dB)');

```

```

% This code generates the frequency spectrum of a current signal
contained in matrix y
w1 = Kaiser(24480,9);           % generate window coefficients
y1 = y*0.7071*0.1*2.3;         % change data to volts RMS,
                                and x 2.3

a = 1;
for a = 1:24480                 % apply window to data
    NW(a,1) = y1(1,a) * w1(a,1);
end
Y = fft(NW,102000);           % FFT data
Plot = abs(Y);                 % remove complex part
a = 1;
for a = 8001                    % apply conversion factors
    K1(a,1) = Plot(a,1) / Conhts(a,1);
end
a = 1;
for a = 1:8001                  % convert from linear to dB
    K(a,1) = 20*log10(K1(a,1)/0.000001);
end
f = 25500/102000*(1:8001);     % generate frequency axis
plot(f,K);                     % plot
axis([0 2000 0 130]);         % display axis
xlabel('Frequency (Hz)');
ylabel('Phase Current (dB)');

```

# **Appendix 4**

**Calculation of Test- Rig Motor Winding  
Factors and the  
Calculation of Finite Element Current  
Magnitudes from the EMF**

## Appendix 4.1 Test-Rig Motor Winding Factors

The overall winding factor is calculated from the product of the distribution factor ( $k_{dn}$ ) and the coil pitch factor ( $k_{pn}$ ) for a given harmonic order  $n$  [62] as shown below:

$$k_{wn} = k_{dn} \times k_{pn}$$

The distribution factor is calculated from:

$$k_{dn} = \frac{\sin \frac{mn\theta}{2}}{m \sin \frac{n\theta}{2}}$$

where  $\theta$  = slot pitch angle (electrical degrees)

$m$  = slots/pole/phase = 3

$n$  = harmonic order

$$\theta = \frac{2\pi}{S} \times p = 20^\circ \text{ where } S = \text{number of stator slots} = 36, p = \text{pole-pairs} = 2$$

Therefore, the distribution factor associated with a 14 pole-pair ( $n = 7$ ) flux waveform is:

$$k_{dn} = \frac{\sin \frac{3 \times 7 \times 20}{2}}{3 \sin \frac{7 \times 20}{2}} = -0.177$$

The distribution factor for 86 pole-pairs is the same.

The coil pitch factor was calculated from:

$$k_{pn} = \sin \frac{n\beta}{2} \quad \text{where } \beta = \text{coil pitch (160}^\circ\text{), } n = \text{harmonic number}$$

Therefore for a 14 pole-pair flux waveform the coil pitch factor is:

$$k_{pn} = \sin \frac{7 \times 160}{2} = -0.342$$

The coil pitch factor for 86 pole-pairs is the same.

$$\text{Therefore } k_w (14/86) = k_d (14/86) \times k_p (14/86) = -0.177 \times -0.342 = \underline{0.06} \text{ (low)}$$

$$\text{Similarly for 16 and 88 pole-pairs } k_d = -0.296 \text{ and } k_p = 0.898 \therefore k_w = \underline{-0.263} \text{ (larger)}$$

## **Appendix 4.2 Calculation of the Current Component Magnitudes from the Finite Element EMF Magnitudes using the Equivalent Circuit**

This appendix details the calculation performed to compute the current magnitude from the magnitude of a component in the induced emf spectrum from the finite element analysis. The equivalent circuit and procedure described in Chapter 3 is used and examples for the 50Hz and 1072Hz components are presented.

### **50Hz:**

At 50Hz the supply voltage  $V_s$  is included in the equivalent circuit where  $R_s = 2\Omega$  and  $X_{sewl} = 2\pi \times 50 \times 2.5\text{mH} = j0.785\Omega$ . The combined impedance of these two elements was  $2.15L \ 21.4^\circ\Omega$ . The equivalent circuit is shown in Figure A4.1.

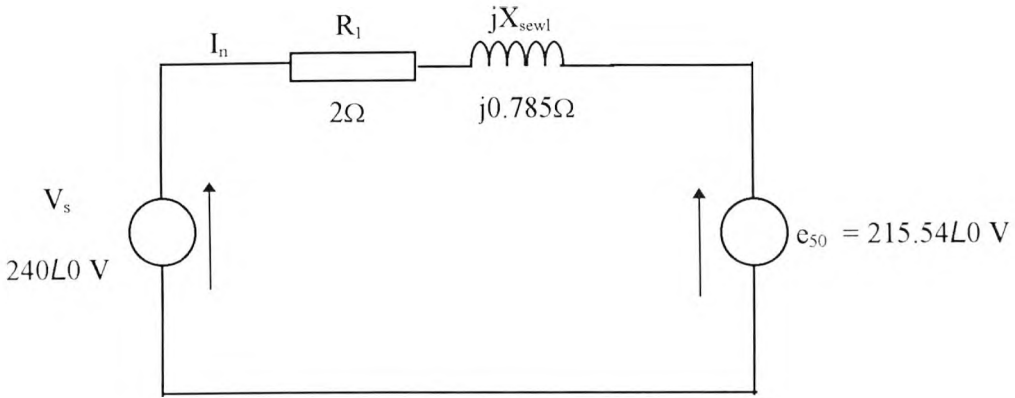


Figure A4.1 Equivalent Circuit at 50Hz

The value for the induced emf at 50Hz was obtained from the emf spectrum. The dB value of 100.65dB was converted to volts by the following process:

$$\text{antilog}(100.65/20) = 1.07 \times 10^5 \text{ and then } 1.07 \times 10^5 \times 1 \times 10^{-6} \times 2000 = \underline{215.54V}$$

This reversed the process of dividing the voltage by 2000 and applying a 100mV = 100 dB reference to the time domain induced emf signal. The angle was taken a 0° as the equivalent circuit calculations in Appendix 2 showed that the angle of the Thevenin voltage, which is equivalent to the emf induced across the stator winding, was only 1.464°. The current flowing at 50Hz was calculated by:

$$I = \frac{V_{res}}{R} = \frac{240L0 - 215.54L0}{2.15L21.4} = \underline{11.3L - 21.4 A}$$

To convert the 11.3A to dB the conversion factor of 0.1V/A (output of the current transformer) was applied and then the 100mV = 100 dB reference. Therefore:

$11.3 \times 0.1 = 1.13$ ,  $1.13 / 1 \times 10^{-6} = 1.13 \times 10^6$ . The log of this is then calculated and multiplied by 20 to give 121.0dB as the magnitude of the 50Hz current component in dB.

### 1072Hz:

A similar process is applied for the rotor slot passing frequencies except that here the supply voltage is seen as a short circuit. In this circuit  $X_{sewl} = 2\pi \times 1072 \times 2.5\text{mH} = j16.84\Omega$ . This shows the much larger effect of the stator end-winding leakage reactance at the higher frequencies compared to 50Hz. The combined impedance of these two elements was  $16.96\angle 83.2^\circ\Omega$ . The equivalent circuit is shown in Figure A4.2.

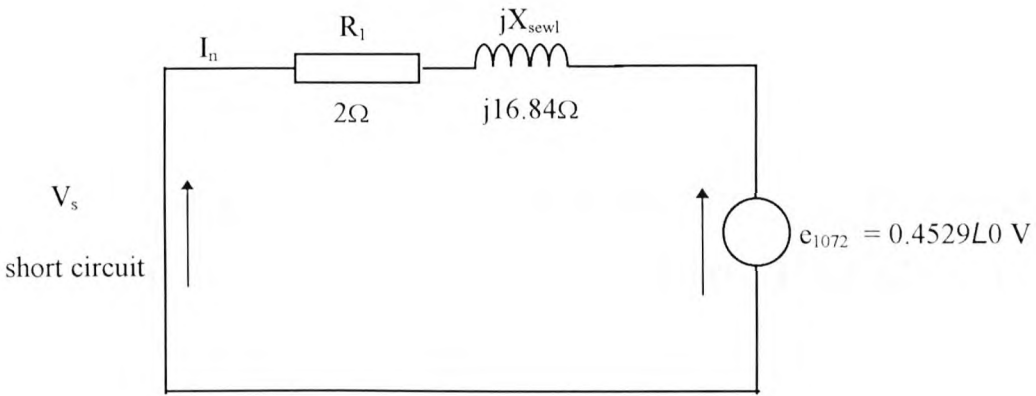


Figure A4.2 Equivalent Circuit at 1072Hz

The value for the induced emf at 1072Hz was 47.1dB in the emf spectrum which converted to volts is 0.4529V.

The current at this frequency is therefore:

$$I = \frac{V_{res}}{R} = \frac{0.4529L0}{16.96\angle 83.2} = \underline{0.0267\angle -83.2 A}$$

Converting this to dB as before gives the magnitude of the current component at 1072Hz, for 10% static eccentricity, as 68.5dB.

The same procedure was followed for the calculation of all the current component magnitudes.

# **Appendix 5**

**Large Industrial Motor Design Details and  
Calculation of Finite Element Parameters**

## A5.1 Large Motor Specification:

Parameter	Value
Power	1.45MW
Frequency	50 Hz
Phase	3
Line Voltage	11kV
Full load current	103 A
Speed	742 rpm
Poles	8
Connection	star
Airgap length	2.25mm
Number of stator slots	84
Number of rotor slots	62
Skew	None
Full Load Operating Temp.	80°C
Stator Resistance (21°C and 80°C)	0.507 Ω/phase 0.649 Ω/phase (FE value)
Stator End-Winding Leakage Reactance	7mH (2.2 Ω/phase)
Rotor Bar Conductivity	$2.56 \times 10^7$ S/m
Supply Impedance	$X_s = j0.55$ Ω/phase

## A5.2 Effective Core Length and Stacking Factor

The presence of radial ventilating ducts in the core meant that the values used in the finite element analysis had to be adjusted to take the ducts into account. With reference to Sturgess [108] the following equations were used to calculate the effective core length and stacking factor.

$$L_{eff} = L_{gross} - (n_{ducts} \times w_{duct}) + 2 \times gap \quad (A.1)$$

where:  $L_{eff}$  = effective lamination core length

$L_{gross}$  = Gross core length = 950mm

$n_{ducts}$  = number of radial ducts = 20

$w_{duct}$  = width of an individual radial duct = 10mm wide

gap = airgap length = 2.25mm

Substituting these values into Equation A.1 gave a value of effective core length of 754.4mm.

The effective lamination factor taking into account ventilating ducts and the actual stacking factor of the laminations can be calculated from Equation A.2 [107].

$$sf_{eff} = sf \times \frac{(L_{gross} - (n_{ducts} \times w_{duct}))}{L_{eff}} \quad (A.2)$$

where:

$sf_{eff}$  = effective stacking factor

sf = material stacking factor

$L_{eff}$  = effective lamination core length = 754.4mm

$L_{gross}$  = Gross core length = 950mm

$n_{ducts}$  = number of radial ducts = 20

$w_{duct}$  = width of an individual radial duct = 10mm wide

Substituting these values into Equation A.2 gave a value of effective stacking factor of 0.944.

### A5.3 Winding Factors for Large Motor Stator

Harmonic Order n	Pole-Pairs p	$k_{wn} = k_{pn} \times k_{dn}$
1	4	0.9319
2	8	0.0313
4	16	0.0584
5	20	0.0848
7	28	0.0 (k <sub>p7</sub> = 0)
8	32	0.0843
10	40	0.0762
11	44	0.0762
13	52	0.0843
14	56	0.0 (k <sub>p14</sub> = 0)
16	64	0.0848
17	68	0.0584
19	76	0.0313
20	80	0.9319
22	88	0.9319
23	92	0.0313
25	100	0.0584
26	104	0.0848
28	112	0.0 (k <sub>p28</sub> = 0)
29	116	0.0843
31	124	0.0762
32	128	0.0762
34	136	0.0843
35	140	0.0 (k <sub>p35</sub> = 0)
37	148	0.0848
38	152	0.0584

40	160	0.0313
41	164	0.9319
43	172	0.9319
44	176	0.0313
46	184	0.0584
47	188	0.0848
49	196	0.0 (k <sub>p49</sub> = 0)
50	200	0.0843

The above table was compiled by Middlemiss [107] using the equations shown below [107]. These were used to confirm the winding factors shown above.

*Distribution Factor:*

Since the number of slots/pole/phase was a non integer (m = 3.5) another approach had to be used to calculate the distribution factors for the harmonic orders (n). With 3.5 slots/pole/phase the coil grouping is 4, 3, 4, 3 etc., so that only a 4, 3 need be considered for assessment of the distribution factor.

$$\text{Slot pitch angle: } \theta = \frac{2\pi}{S} \times p = \frac{360}{84} \times 4 = \underline{17.14^\circ}$$

$$\text{For coil group 4: } k_{dn4} = \frac{\sin\left(\frac{4n\theta}{2}\right)}{4 \sin\left(\frac{n\theta}{2}\right)}$$

$$\text{For coil group 3: } k_{dn3} = \frac{\sin\left(\frac{3n\theta}{2}\right)}{3 \sin\left(\frac{n\theta}{2}\right)}$$

Hence, for n = odd integer (including 1):

$$k_{dn} = \frac{(4k_{dn4} + 3k_{dn3})}{7}$$

and for n = even integer:

$$k_{dn} = \frac{(4k_{dn4} - 3k_{dn3})}{7}$$

*Pitch Factor:*

The pitch factor is calculated as for the test-rig motor using:

$$k_{pn} = \sin\left(\frac{n\beta}{2}\right) \quad \text{where } \beta = \text{coil pitch} = 9 \times 17.14^\circ = 154.28^\circ$$

#### **A5.4 Calculation of the AC Resistance of the Stator at the Frequencies of Interest**

With reference to J. Middlemiss [107] the following procedure was followed to calculate the AC resistance of the stator. The AC resistance is calculated via the eddy current loss.

The terms used are:

H = Conductor Copper Depth (cms)

f = frequency (Hz)

a = width of copper across slot / slot width

b = core length / length of mean half turn

A = (1 - Fractional coil pitch) × 3

P = total number of conductors / slot

$$d = H \times 0.137 \sqrt{(f \times a)} \quad (\text{A.3})$$

$k$  = extra loss factor i.e. additional loss in terms of basic copper loss.

$$k = \frac{P^2(1 - A \times 0.187)d^4b}{9} \quad (\text{A.4})$$

and 
$$\frac{R_{AC}}{R_{DC}} = (1 + k)$$

It can be seen from Equation A.3 that  $d \propto \sqrt{f}$  and from Equation A.4 that  $k \propto d^4$ , hence,  $k \propto f^2$ . This means that the value  $k$  can be calculated for any frequency, for example:

$$\text{At } 1019\text{Hz, } k = 0.0544 \times \left(\frac{1019}{50}\right)^2 = 22.6$$

For the larger motor:

$$H = 0.355$$

$$f = 50$$

$$a = 8/15 = 0.533$$

$$b = 950/1812 = 0.524$$

$$A = (1 - 9/10.5) \times 3 = 0.429$$

$$P = 16$$

Substituting these values gives:

$$d = 0.251 \quad \text{and} \quad k = 0.0544$$

Hence, at 50Hz:

$$\frac{R_{AC}}{R_{DC}} = (1 + 0.0544)$$

Now the DC stator resistance at 80°C is 0.649 hence  $R_{AC} = 0.649(1 + 0.0544) = \underline{0.68\Omega}$

The value of stator resistance at 50Hz is only 0.031Ω larger than the value of DC resistance. This is a negligible difference. At 1019Hz the stator resistance becomes:

$$\frac{R_{AC}}{R_{DC}} = (1 + 22.6) \quad \text{Hence, } R_{AC} = 0.649(1 + 22.6) = \underline{15.3\Omega}$$

This is considerably higher resistance than before, however, as explained in the main text if this resistance is used instead of the 0.649Ω then the actual difference in current component magnitude is only 0.3dB less.

# **Appendix 6**

## **Published Papers**

Full References for the published papers presented in this appendix are shown below in order of appearance:

- [1] A. Barbour, "Analysis of Airgap Eccentricity in Induction Motors using Finite Elements," *Proceedings of The Robert Gordon University, Faculty of Science and Technology, Research '96, Engineering Monitoring and Maintenance*, March 1996, pp. 36-40.
  
- [2] W. T. Thomson and A. Barbour, "On-Line Current Monitoring and Application of Finite Element Method to Predict the Level of Static Airgap Eccentricity in Three-Phase Induction Motors," *IEEE Transactions on Energy Conversion*, May 1997.
  
- [3] A. Barbour and W. T. Thomson, "Finite Element Study of Rotor Slot Designs with Respect to Current Monitoring for Detecting Static Airgap Eccentricity in Squirrel-Cage Induction Motors," *Proceedings of the IEEE Industrial Applications Society Annual Meeting*, October 5 - 8, 1997.
  
- [4] A. Barbour and W. T. Thomson, "Finite Element Analysis and On-Line Current Monitoring to Diagnose Airgap Eccentricity in 3-Phase Induction Motors," *Proceedings of the IEE International Conference on Electrical Machines and Drives*, September 1997, pp. 150 - 154.
  
- W. T. Thomson, A. Barbour, C. Tassoni and F. Filippeti, "An Appraisal of the MMF and Permeance Method and Finite Element Models to Study Static Air-gap Eccentricity and its Diagnosis in Induction Machines," *Proceedings of the International Conference on Electrical Machines ICEM'98*, September 1998, Vol. 3, pp. 218.2-218.7.

# ANALYSIS OF AIRGAP ECCENTRICITY IN INDUCTION MOTORS USING FINITE ELEMENTS

Detection of airgap eccentricity in motors

A. BARBOUR

School of Electronic and Electrical Engineering, The Robert Gordon University, Aberdeen, Scotland

## Abstract

Static and/or dynamic eccentricity in an induction machine is the condition where the airgap is non-uniform in length between the stator and rotor. Consequently the flux in the machine is unbalanced and a force results that tries to pull the rotor over to the stator. Eccentricity can be observed by studying the behaviour of unique frequency components in the line current of the motor. The early detection of eccentricity is beneficial to users to prevent further degradation of the machine's condition.

The majority of research to date has treated static and dynamic eccentricity separately and used classical techniques to try to predict the frequency and magnitude of the components in the current due to eccentricity, however, the prediction of component magnitude was largely unsuccessful. The combination of static and dynamic has recently been considered and the frequency components due to eccentricity were successfully predicted, but this analysis did not calculate the magnitude of the components. The magnitude is important as from it the severity of the fault can be predicted.

To handle the increasingly complex analysis some researchers have begun to use Finite Element analysis (FE). However, none have used FE to model the frequency and magnitude of components in the machine current caused by eccentricity. It is the purpose of the work outlined in this paper to use a FE package to model a machine in order to predict the components in the current signal. Initially static eccentricity will be examined, then dynamic and finally a combination of the two forms. Initial results have been positive, the imbalance of flux in the machine due to eccentricity has been illustrated.

Keywords: Airgap, analysis, eccentricity, faults, finite elements, induction, monitoring, motor.

## 1 Introduction

Condition monitoring of electrical machines has been extensively adopted by industry today. The availability of techniques to detect the presence and degradation of faults has allowed machine users to make significant reductions in machine down times and financial savings as a result of the planned maintenance programmes that can be developed from information provided by monitoring systems.

Many techniques exist for condition monitoring of machines, the machine parameter being monitored and the type of fault detected vary dependent on the monitoring method as reviewed by Tavner et al [1]. The principle signals monitored are the machine current and vibration, the advantage being that they are non-invasive. Static and dynamic eccentricity can be detected by current and vibration monitoring [2], in addition to faults such as broken rotor bars and bearing wear.

The ability to detect eccentricity reliably is vital to machine operators as it causes excessive bearing wear. The stator core and windings are also subject to extra vibration and complete failure can occur if the rotor is actually pulled onto the stator. Eccentricity can be caused by incorrect bearing assembly during manufacture, worn bearings, a bent rotor shaft or operation at a critical speed creating rotor whirl.

Rotor eccentricity occurs in two forms in induction motors: static and dynamic eccentricity. Static eccentricity occurs when the rotor is rotating about its own axis but not about the stator axis, as shown in Figure 1.

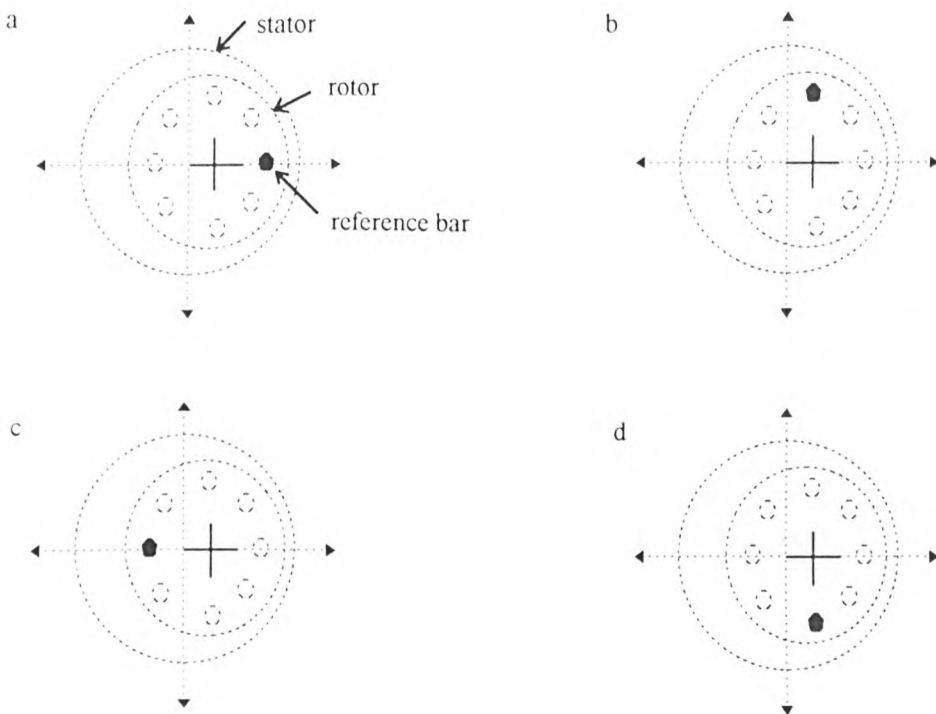


Fig. 1. Minimum airgap due to static eccentricity.

Dynamic eccentricity causes the rotor to rotate about the stator axis but not about its own axis, as shown in Figure 2.

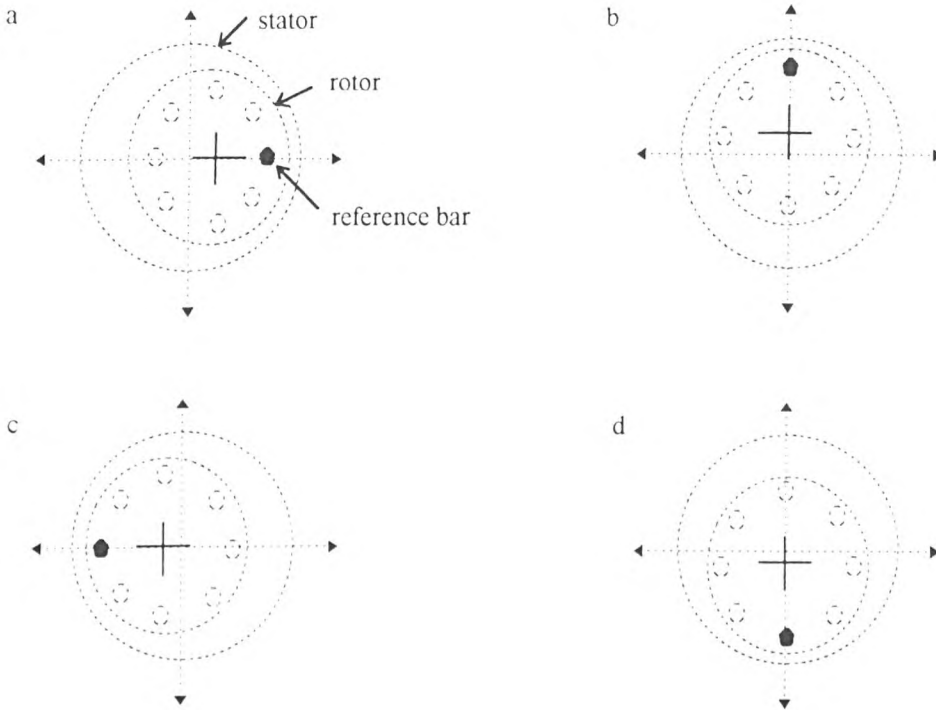


Fig. 2. Minimum airgap due to dynamic eccentricity.

Static eccentricity results in a constant unbalanced force directed along the axis of the minimum airgap and dynamic eccentricity results in a rotating unbalanced force. The rotating force can be detected using vibration analysis, however, the steady pull caused by static eccentricity cannot be detected using vibration monitoring, [3]. Current analysis can be used to detect the presence of both static and dynamic eccentricity as the distortion of flux in the airgap causes harmonics in the current signal to the motor. Previous studies, to simplify the complex analysis, have considered static and dynamic eccentricity to occur separately within a machine. This assumption creates a slightly artificial situation as manufacturing and assembly methods create an inherent level of eccentricity in the machine. This means that when dynamic eccentricity occurs then both types of eccentricity are present in the machine. It is a latter objective of this work to study the combination of both static and dynamic eccentricity together.

## 2 Research review

Interest has been shown in this area of machine fault since the early part of this century. The area splits into two branches; the calculation of the force between stator and rotor (unbalanced magnetic pull - UMP), and the detection of airgap eccentricity by monitoring machine current and /or vibration analysis.

The on-line diagnosis of airgap eccentricity was researched by Cameron et al [2]. He predicted and verified, via laboratory tests, that certain frequency components can occur in the current and vibration signals which are characteristic of airgap eccentricity in a three phase induction motor. Cameron [4] attempted to predict the magnitude of these components in the current spectrum to assess the severity of the fault. This was only partially successful since in a number of cases the difference between theoretical and experimental results was unacceptable. The application of Cameron's technique on industrial installations has not been successful since it is not possible to reliably determine the severity of either static or dynamic airgap eccentricity.

A successful monitoring strategy must be able to assess the severity of faults so that appropriate action can be taken to prevent a failure in the motor. This important criterion is not yet available with existing methods of detecting airgap eccentricity.

It is known that in practice there will always be an inherent level of static and dynamic eccentricity in a nominally good motor due to manufacturing tolerances. To simplify the complex analysis, previous researchers [4, 5, 6, 7] have considered either static or dynamic eccentricity but not the combination. Recent research by Dorrell [3] has shown that the combination of static and dynamic eccentricity produces lower order frequency components (rotational speed frequency sidebands around the supply frequency) in the current spectrum. The theoretical predictions have been verified by experimental tests but the analysis does not predict the magnitude of the frequency components, hence the severity of the fault cannot be quantified.

Due to the complexity of modelling the induction motor with different types and combinations of airgap eccentricity a more advanced modelling and analysis technique is required. DeBortoli et al [5] has used Finite Elements (FE) to study the effects of rotor eccentricity and parallel winding connections on induction motor behaviour. He concluded that circulating currents between parallel windings reduces the (UMP) due to static or dynamic eccentricity. No attempt was made to calculate the induced current components which are unique to the different types or combinations of airgap eccentricity. Arikio and Lindgren [6] used FE to calculate the forces acting on a rotor due to static eccentricity and Mercier et al [7] also used FE to predict the average forces in the airgap due to static or dynamic eccentricity.

## 3 Research objectives

This project will focus on the use of FE to calculate the magnitude and frequency of unique components in the airgap flux density waveform due to different types and combinations of eccentricity. The induced current components in the stator windings and supply current waveform will be calculated by applying the data from the FE to an equivalent circuit model. Previous research using FE has not provided this information and the end objective is to produce a reliable method for detecting airgap eccentricity in

three phase induction motors via on-line current monitoring. In detail the objectives are:

- Develop a FE model (based on a commercial FE package) of an induction motor with static eccentricity and hence determine the unique frequency components in the flux density waveform due to the fault.
- Apply data from above to an equivalent circuit model to calculate the components (frequency and magnitude) in the current due to static eccentricity and compare theoretical predictions with experimental results from an induction motor with static eccentricity.
- Further develop the FE model for dynamic and combinations of static and dynamic eccentricity.
- Apply data from this new model to an equivalent circuit to calculate the current components (frequency and magnitude) in the stator winding due to the fault and then compare theoretical predictions with experimental results from an induction motor with the same fault.

This work is still in its early stages, the next section outlines the work performed to date.

#### **4 Finite Element package and initial results**

The work is based around the FE package 'SLIM' developed by GEC Engineering Research Centre. It solves both electromagnetic and electrostatic problems. The package consists of three main parts: model generator, solver and post processing. Each part will be briefly described.

Using the model generator the stator and rotor can be constructed in 2-d (cross section in X-Y plane through machine) as shown in Figure 3.

# ON-LINE CURRENT MONITORING AND APPLICATION OF A FINITE ELEMENT METHOD TO PREDICT THE LEVEL OF STATIC AIRGAP ECCENTRICITY IN THREE-PHASE INDUCTION MOTORS

William Torbat Thomson, Senior Member IEEE and Alexandra Barbour  
The Robert Gordon University, Schoolhill, Aberdeen AB10 1FR, Scotland, UK

**Abstract** - The introduction reviews the real practical problems of airgap eccentricity in large 3-phase induction motors. On-line monitoring methods for diagnosing airgap eccentricity are also discussed and a state of the art review on the application of current monitoring to detect airgap eccentricity is presented. The limitations of the classical MMF and permeance wave approach for predicting the severity of airgap eccentricity are discussed. The time stepping finite element (FE) method and FFT analysis technique are used as 'analysis tools' to predict the frequency components in the current (Hz and dB) as a function of static airgap eccentricity. Excellent agreement is obtained between the measured and predicted frequency components (Hz) in the current spectra which are a function of static eccentricity. The FE method is also used to predict the magnitude (dB) of these frequency components in the current spectrum with different levels of static airgap eccentricity. These predictions are much closer to the measured values in comparison to previous attempts using the classical MMF and permeance wave approach. The contents of this paper will be of particular interest to the manufacturers and industrial users of three-phase induction motors.

## I. INTRODUCTION

### A. Review of Airgap Eccentricity in Induction Motors

In large, high-voltage, three-phase induction motors airgap eccentricity is kept to a minimum by good designs, stringent quality assurance and control standards, followed by comprehensive tests and high quality installation procedures. Unacceptable levels of airgap eccentricity are therefore uncommon in newly commissioned large induction motors. However, it is untrue to state that high levels of airgap eccentricity never occur after the motor is installed and has been running for a number of years. Experience with applying on-line diagnostic techniques to motors already in service has shown that problems can occur due to airgap eccentricity [1,2].

There are two types of airgap eccentricity, namely, static and dynamic and in practice both types can occur simultaneously. The former exists when the minimum airgap is fixed in space and is not a function of the rotor position, whereas the latter is a function of space and time as the rotor rotates. In a new motor, static airgap eccentricity is caused by a build up of manufacturing tolerances between the centre of the stator bore and the bearing centres. Dynamic eccentricity in a new motor is controlled by the total indicated reading (TIR) or "run-out" of the rotor. A typical TIR is 0.05 mm for a large induction motor (e.g. a 2 MW, 4-pole, 50 Hz, motor). It is generally accepted that an airgap eccentricity of up to 10% is permissible but manufacturers normally achieve a lower value to keep the unbalanced magnetic pull (UMP) between the rotor and stator core to a minimum and to reduce acoustic noise and vibration.

A typical airgap length in a 2 MW, 4-pole, induction motor is 2.5 mm with a permissible maximum tolerance of 10% eccentricity. This means that with a TIR of 0.05 mm on the rotor the static and dynamic eccentricities will have a maximum permissible level of 8.0% and 2.0% respectively. The setting of the airgap in a large induction motor has also to take into account the effect of lift in the plain bearings. An increase in static eccentricity can be caused by incorrect positioning of the stator core assembly or bearing centres at the commissioning stage or following a major repair. Although this is uncommon, it can happen in an industrial installation [2]. An increase in dynamic eccentricity can be produced by thermal bow of the rotor, instability in plain bearings or bearing wear. High levels of static eccentricity can also cause dynamic eccentricity due to UMP.

An extreme case of high airgap eccentricity levels can result in a rotor-to-stator rub and consequential damage to the stator core and high-voltage winding. This can result in motor failure and an expensive repair. Higher than normal levels of airgap eccentricity can produce high vibration levels at the bearings and subsequent bearing failure. It is important to emphasise that it is very difficult to quantify what is a high level of airgap eccentricity which results in a rotor-to-stator rub or a higher than normal level which can cause rotor dynamic problems or bearing wear. This will be unique to each motor design and its operational function.

Discussions with manufacturers suggests that an airgap eccentricity of 20% would be considered to be unacceptable and a level of 50% is considered to be a serious problem such that the motor should be immediately removed from service to rectify the problem.

### B. On-Line Diagnosis of Airgap Eccentricity

It is standard practice to monitor bearing vibration to detect rotor dynamic problems and bearing wear. Although bearing vibration increases due to an increase in airgap eccentricity the vibration components are not unique to static or dynamic airgap eccentricity. In industrial installations confusion can occur when bearing vibration increases and the vibration spectrum is being interpreted. For example, the vibration component at the rotational speed frequency can increase due to airgap eccentricity, mechanical imbalance in the rotor or because of problems in the mechanical load. Hence, it can be difficult to diagnose the real problem.

The stator core vibration spectrum will change due to static or dynamic eccentricity. For example, it has been shown that vibration components due to rotor slotting will increase in magnitude due to static airgap eccentricity and unique components will appear due to dynamic eccentricity as presented in reference [3]. However, the degree of severity of airgap eccentricity has not been predicted due to the complexity of modelling electromagnetic forces and the mechanical response of the stator core for each motor which is being monitored. It is also difficult to apply stator core vibration monitoring in an industrial installation.

Airgap and axial flux signals can be analysed to detect components which are a function of airgap eccentricity but the magnitude (webers) of these components has not been quantified as a function of the fault severity [4,5]. It is extremely difficult to convince the operators of large induction motors to remove motors from service to fit airgap search coils, hence, this method is not really a practical option and is not popular with the users of induction motors. Access to the motor is also required to fit an axial flux search coil and in a large, high-voltage induction motor the coil should be installed around the shaft inside the outer steel frame to ensure that a reliable signal is sensed. This means the motor has to be stopped to fit the coil and would require special approval in an industrial installation, consequently, the operators prefer a monitoring method which is completely non-invasive and does not disturb the drive system.

The use of current monitoring is now extensively used to detect broken rotor bars [6,7,8] and operators are keen that airgap eccentricity can also be detected via current spectrum analysis due to the ease in which a clip-on current transformer can be used to sense the signal. Access to the

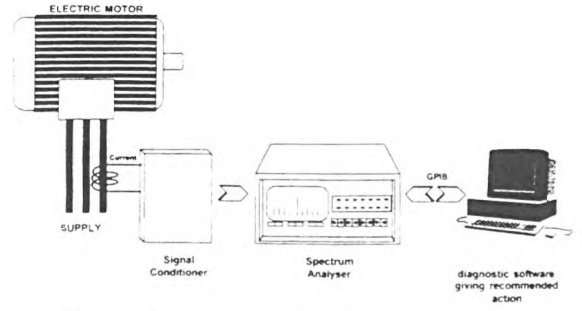


Fig. 1. On-line current monitoring system

motor is not required and the current can be sensed in the switchgear room without any disturbance to the operation of the motor. A typical on-line current monitoring system is shown in Fig. 1, as presented in reference [6].

### C. Analysis of the Current Signal

By using the MMF and permeance wave approach it has been shown that specific components (equation (1)) can occur in the flux density waveform which are a function of rotor slotting, and static and dynamic eccentricity [2,9]. The pole pairs associated with these flux waves can be calculated using equation (2) as shown in references [2,9]. It has also been shown that these rotating flux waves can induce corresponding current components in the stator winding [1,2] but the number of pole pairs of the flux waves and the stator winding factors need to be included when predicting the actual current components which will be induced:

$$f_{cc} = f_1 \left[ (R \pm n_d) \left( \frac{(1-s)}{p} \right) \pm n_{ws} \right] \quad (1)$$

$$m = (R \pm S \pm n_s \pm n_d \pm 2n_{sa} p \pm n_{or} p) \quad (2)$$

$f_{cc}$  = frequency components which are a function of airgap eccentricity (Hz)

$f_1$  = supply frequency (Hz)

$R$  = number of rotor slots

$S$  = number of stator slots

$n_d$  = zero for static and one for dynamic eccentricity

$s$  = slip

$p$  = pole-pairs

$n_{ws}$  = 1, 3, 5, 7

$m$  = pole-pair number of flux waves

$n_s$  = static eccentricity integer

$n_d$  = dynamic eccentricity integer

$n_{sa}$  = saturation integer

$n_{or}$  = rotor space harmonic integer

To predict the severity of airgap eccentricity requires the magnitude (in amps) of the induced current components to be calculated as a function of airgap eccentricity. Previous research involved the calculation of resistances and reactances at these frequencies using design details and classical formulae to develop an equivalent circuit taking into account the high frequencies given by equation (1), as presented in reference [10]. This approach proved to be only partially successful since the difference between calculated and measured magnitudes (in amps) of the various frequency components was 7.1% for some of the components, whereas, others differed by as much as 300% for a given level of static eccentricity as shown in reference [2]. A similar set of results was obtained for dynamic eccentricity.

However, it is still possible to detect an increase in static eccentricity via current monitoring by detecting an increase in the magnitude of the rotor slot passing frequencies ( $n_d = 0$ ), but a base line survey of the motor is really required at the commissioning stage or the motor has to be monitored over a period of time as stated in reference [2]. If the current components due to dynamic eccentricity ( $n_d = 1$ ) are obvious in the current spectrum then it can be stated that airgap eccentricity is present. This is based on industrial case histories where current monitoring has detected airgap eccentricity as is shown in reference [11]. However, it is still not possible to reliably predict if the problem is due to an increase in static or dynamic eccentricity. It has also been shown that when static and dynamic eccentricity occur simultaneously, as can occur in practice, then additional components (equation (3)) can be induced in the current signal as proved in reference [12]. However, the magnitude of these components has not been predicted as a function of the fault severity.

$$f_e = f_1 \pm f_r \quad (3)$$

$f_r$  = rotational speed frequency of the rotor (Hz)  
 $f_e$  = components which are a function of static and dynamic eccentricity (Hz)

At present it is possible to use on-line current monitoring to detect airgap eccentricity and to diagnose a serious problem [11], however, the type of eccentricity cannot be reliably diagnosed and an accurate prediction of the severity of the problem is still not possible.

The main objectives of the research work reported in this paper are as follows:

- To model a 3-phase induction motor using the time stepping finite element analysis method as a function of static airgap eccentricity.

- To use the results from the FE model to compute the Fourier spectrum of the current time domain signal to identify the components (frequency and amplitude in amps) which are a function of static airgap eccentricity.
- To compare theoretical predictions with measured results.

The ultimate goal is to provide industry with a reliable on-line current monitoring system for detecting the magnitude of static or dynamic eccentricity and combinations of both types of eccentricity.

## II. APPLICATION OF THE FINITE ELEMENT METHOD

To predict the magnitude (in amps) of the components given by equation (1) requires an accurate model and it is proposed that the time stepping finite element method is used to calculate the induced EMF time domain waveform in the stator winding as a function of static eccentricity. It will then be possible to calculate the current waveform using an equivalent circuit to model stator end - winding leakage inductance and stator resistance per phase. The induced EMF waveform can be analysed via an FFT signal processing programme in MATLAB to identify the frequency components and their corresponding magnitude in volts or dB. Since the components given by equation (1) are at high frequencies due to rotor slotting effects a time stepping FE solution is required for the following reasons, as specified in reference [13]:

- Airgap permeance variations due to slotting can be modelled.
- Localised saturation can be modelled using instantaneous rather than time averaged reluctivities.
- Rotor movement is automatically incorporated.

The time step must be sufficiently small to ensure that the effects of slotting and static airgap eccentricity are accurately modelled in order that the EMF waveform includes the high frequency components. There are a number of excellent papers on the theory of time stepping FE analysis of 3-phase induction motors [13-16], and it is suffice to state that the analysis used to produce the results in this paper is based on the method reported in references [15,16].

Prior to using FE analysis to provide quantitative results for the level of static eccentricity it is sensible to study the product of the MMF and permeance waves to predict the frequency components in the flux density waveform. This combined approach was used to predict the primary flux density harmonics produced by stator and rotor core ovality

and is reported in references [17,18]. This work showed that the magnitude and frequency of ovality flux density harmonics can be calculated using a time stepping FE analysis. It is worth noting that these were the primary harmonics due to static and dynamic airgap eccentricity and occurred at the supply frequency and the supply frequency plus twice the rotational speed frequency of the rotor. The influence of stator slot permeance harmonics was also presented. These results showed that the time stepping FE method can be used to quantify the relative effects of airgap eccentricity on certain components in the flux density waveform. The force waves were also predicted as a by-product of these primary flux density waves ( $B^2$ ) due to airgap ovality. However, the theoretical predictions were not compared with actual experimental results and it is worth noting that the higher frequency components which are a function of the number of rotor slots and static airgap eccentricity (equation (1)) were not the subject of the results presented in references [17,18].

The use of the time stepping FE method to predict the magnitude of the components given by equation (1) is the focus of this paper to provide a more reliable on-line current monitoring system to detect airgap eccentricity.

### III. EXPERIMENTAL RESULTS AND FINITE ELEMENT PREDICTIONS

#### A. Introduction

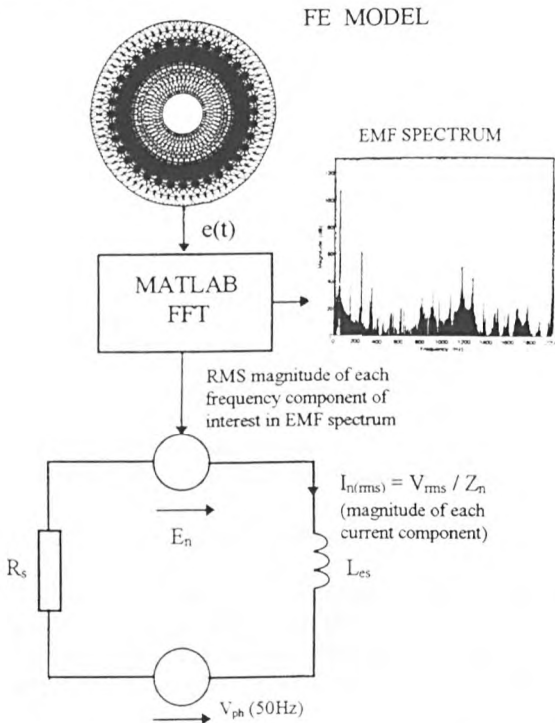


Fig. 2. Procedure for FE Analysis and Calculation of Current Components

- $R_s$  = stator resistance per phase ( $2 \Omega \pm 0.01 \Omega$ )
- $L_{es}$  = stator end - winding leakage inductance per phase ( $2.5 \text{ mH} \pm 0.2 \text{ mH}$ )
- $V_{ph}$  = supply volts (240 V RMS)
- $e(t)$  = induced EMF time domain waveform (volts)
- $E_n$  = RMS magnitude of frequency component in EMF spectrum (volts)
- $I_n$  = Resulting current for component n (amps)
- $Z_n$  = Impedance at that frequency n (ohms)
- $n$  = relevant frequency component

The experimental test-rig motor was an 11 kW, 415 V, 50 Hz, 4-pole, 1420 rpm, 20 A, delta-connected, 3-phase, squirrel-cage induction motor with 36 stator and 51 rotor slots. A copper fabricated rotor was designed and constructed with unskewed slots as reported in reference [19], however, the experimental test-rig motor was still constructed using components provided by a manufacturer (i.e. stator core assembly, 51 slot rotor laminations, rotor shaft etc.). In the majority of large induction motors the rotors are unskewed, hence the reason for using a specially designed unskewed rotor. Full design details of the motor and the method of introducing static and dynamic eccentricity into the special test rig are given in references [2,10] and [12] respectively.

The procedure to predict the magnitude of the current components using a combination of time stepping FE, a stator equivalent circuit and MATLAB's signal processing package is shown in the schematic diagram of Fig. 2. It should be mentioned that the signal processing software in MATLAB was improved to obtain a dynamic range of 80 dB and a frequency resolution of 0.25 Hz for the induced EMF spectrum (0-2 kHz).

#### B. Experimental Results

Large, high-voltage, induction motors are normally always connected in star hence the laboratory test-rig motor was connected for this mode of operation. Although this meant the motor was operating at a reduced voltage and power the results are still perfectly valid. The measured line current spectra for the motor operating with 8-10% (tolerance limit) and 50% static eccentricity under the same load conditions (full-load current of 11.5 A) are presented in Fig. 3 and Fig. 4. These results show that the frequency components predicted by equation (1) have increased in magnitude by 12.2 to 13.2 dB. A plot of dB versus static eccentricity for the various frequency components which are a function of static eccentricity is presented in Fig. 5.

An increase of 10 dB is equivalent to approximately a three times increase in absolute units. This confirms that these components can be used to identify an increase in static eccentricity, however, the real challenge is to reliably predict the level of static eccentricity from a single

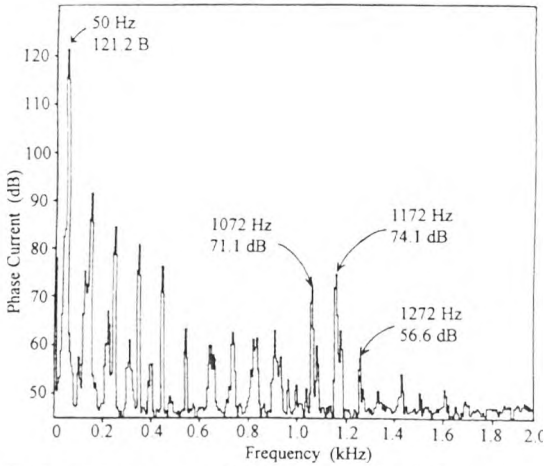


Fig. 3. Current spectrum with 10 % static eccentricity in the experimental motor (1322 rpm, 11.5 A, 415 V, star-connected). Calibration: 100 mV=100 dB on the spectrum analyser and the CT and voltage to current converter produced 0.1V/amp.

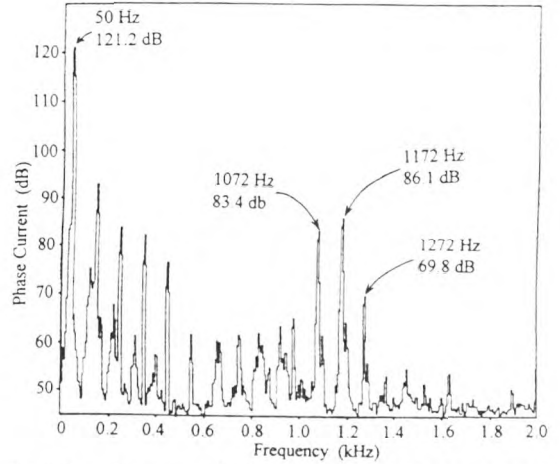


Fig. 4. Current spectrum with 50 % static eccentricity in the experimental motor (1322 rpm, 11.5 A, 415 V, star-connected). Calibration: 100 mV=100 dB on the spectrum analyser and the CT and voltage to current converter produced 0.1V/amp.

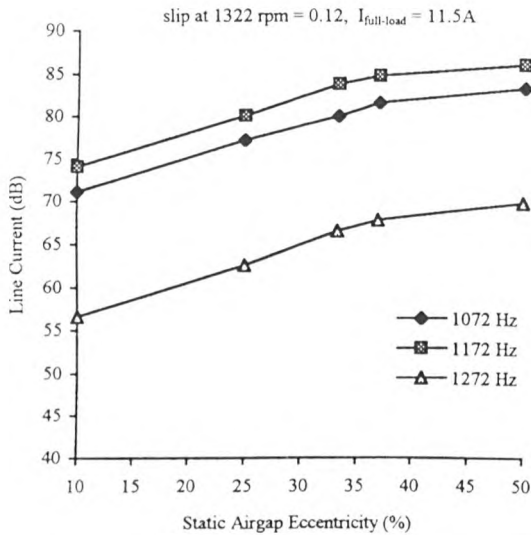


Fig. 5. Magnitude of current components versus static airgap eccentricity

measurement. At present, an historical record is required to detect an increase in the magnitude of these components but it is often the case in industry that this has not been achieved prior to a problem developing.

### C. Finite Element Predictions

A two-dimensional time stepping FE method was used and the required data inputted to the analysis. This included data such as the dimensions of the modelled motor, stator and rotor winding design, supply volts, rotor

bar conductivity and speed of operation, in addition to the FE mesh which models a two-dimensional cross section of the motor with various levels of static airgap eccentricity. In order to determine the conductivity of the rotor bars a locked rotor test was performed on the experimental motor to be modelled. Since the FE model is two-dimensional the rotor end ring resistance is not included, however, its resistive effect can be included by increasing the rotor bar resistance. The locked rotor test was used to determine the referred rotor resistance per phase ( $R'_2$ ). The locked rotor measurements were taken when the temperature of the rotor cage was the same as that obtained after a 3-hour full load test (i.e.  $80^\circ\text{C} \pm 2^\circ\text{C}$ ). Using the equation in reference [20] and equating the end ring resistance to zero an effective rotor bar resistance was calculated, (see appendix 1). An exact equivalent circuit was deduced from experimental tests and design calculations [1] and a comparison between calculated and measured full-load currents, power factors and input powers produced a difference of 4%, 3% and 1.4% respectively. Hence, the effective rotor bar conductivity calculated from the referred rotor resistance  $R'_2$  is validated. This value was used as the effective rotor bar conductivity for the FE analysis.

The time step in the FE analysis was calculated on the basis that at least twenty steps were required for each tooth pitch to ensure the calculated time domain EMF  $e(t)$  waveform (Fig. 2) contains the high frequency components which are a function of slotting and static airgap eccentricity. This resulted in a short time step of  $39.2 \mu\text{s}$  and the FE model had 11,105 elements and 6406 nodes since the complete motor has to be modelled when a non-uniform airgap is being studied. An estimate of the end-winding stator leakage inductance was based on the exact

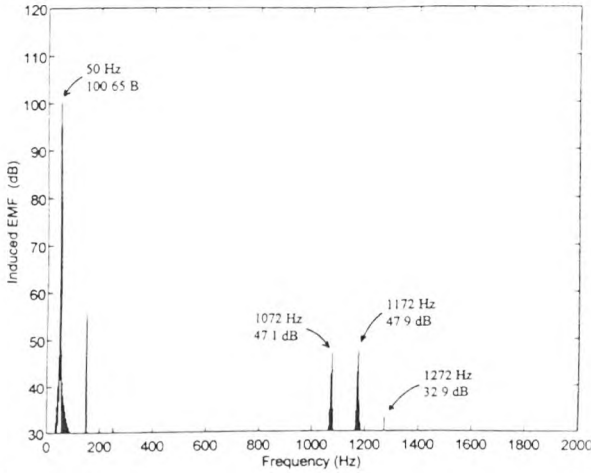


Fig. 6. Induced EMF Spectrum from FEA (see Fig. 2 for analysis) of motor with 10 % static eccentricity

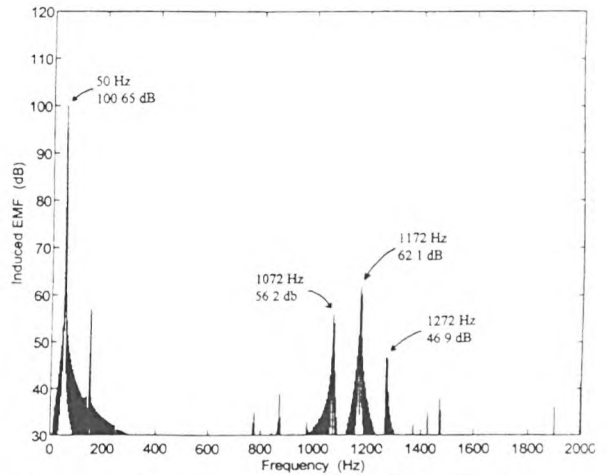


Fig. 7. Induced EMF Spectrum from FEA (see Fig. 2 for analysis) of motor with 50 % static eccentricity

TABLE I. Comparison between the measured and predicted (FE analysis) magnitudes of the 50 Hz supply component of current and current components which are a function of static airgap eccentricity

<ul style="list-style-type: none"> <li>• Experimental test conditions: SCIM, 415 V, star-connected, 11.5 A, 4-pole, 50 Hz, 1322 rpm, <math>s=0.12</math>, 51 rotor slots.</li> <li>• Spectrum analyser: 80 dB dynamic range, <math>\Delta f = 2.5</math> Hz resolution (0-2 kHz), 100 dB = 100 mV, CT signal to volts : 0.1 V/A.</li> <li>• Measured frequencies (m)- predicted components from equation (1) - spectrum analyser display of current from test rig motor.</li> <li>• Calculated frequencies and magnitudes in dB (c) - from FE analysis procedure shown in Fig. 2</li> </ul>												
m - measured		c - calculated		se - static eccentricity (%)			diff. - difference					
se (%)	50 Hz (m)	50 Hz (c)	dB diff	$f_{ec}$ (m) $n_{ws} = -1$ 1072 Hz	FEA (c) 1072 Hz (dB)	dB diff	$f_{ec}$ (m) $n_{ws} = +1$ 1172 Hz	FE (c) 1172 Hz	dB diff	$f_{ec}$ (m) $n_{ws} = +3$ 1272 Hz	FE (c) 1272 Hz	dB diff
	(dB)	(dB)	(dB)	(dB)	(dB)	(dB)	(dB)	(dB)	(dB)	(dB)	(dB)	(dB)
10	121.2	121.0	0.2	71.1	68.5	2.6	74.1	68.6	5.5	56.6	52.9	3.7
25	121.2	121.0	0.2	77.2	73.5	3.7	80.1	76.5	3.6	62.6	59.9	2.7
50	121.2	121.0	0.2	83.3	77.7	5.6	86.1	82.7	3.4	69.8	66.8	3.0

formulae proposed in reference [21] which includes the mutual flux linkage between the rotor end-rings and the stator end - winding. The stator resistance per phase was measured after a 3-hour heat run at full load using a four terminal resistance measurement instrument (digital read out). The values for the end winding stator leakage inductance and the stator resistance per phase were required to calculate the relevant current components using the procedure shown in Fig. 2. Finite element models were created for the experimental motor with 10%, 25% and 50% static eccentricity respectively. The analysis was carried out for full-load speed which corresponds to the experimental tests at full-load current (11.5 A) and a speed of 1322 RPM. Fig. 6 and Fig. 7 show the induced EMF spectra for 10% and 50% static eccentricity. A comparison of theoretical and experimental results is presented in Table

I and sample calculations are given in appendix 2 for the interpretation of Figures 3, 4, 6, 7 and the analysis procedure presented in Fig. 2.

#### D. Summary of Results.

A comparison between the predicted and measured value of current at 50 Hz shows that the magnitudes differ by 0.2 dB thus validating the parameters used in the FE analysis. The FE results have produced an accurate prediction of the frequency components (Hz) which are a function of static eccentricity. This is verified by comparing the frequency components at 1072 Hz, 1172 Hz and 1272 Hz in Fig. 3 and Fig. 6 and Fig. 4 and Fig. 7. These components are identical to those predicted by equation (1) from the MMF and permeance wave approach.

However, the main focus of this paper is to predict the magnitude (dB) of these components and it is here that the results provide an original contribution.

The difference in dB between the predicted and measured values of the current component at 1272 Hz with a static eccentricity of 10% and 50% is 3.7 dB and 3.0 dB respectively. With respect to on-line condition monitoring this is a reasonable estimate considering that previous attempts using the MMF and permeance wave approach were very inconsistent as presented in reference [1]. Inspection of Table I shows that the difference between the magnitude of the predicted and measured components is between 2.6 dB and 5.6 dB. In terms of absolute values in amps it can be argued that there is still a substantial difference between some of the predicted and measured values.

However, it is important to note that the increase in magnitude (dB) of the predicted frequency components was 9.2 to 14.1 dB with an increase of 40% static eccentricity whereas the experimental results produced an increase of 12.2 to 13.2 dB. It is emphasised that the increase is of the same order and is encouraging for a first attempt at using time stepping FE analysis to predict the severity of static airgap eccentricity via an on-line current monitoring strategy.

#### IV. CONCLUSIONS AND FURTHER WORK

The time stepping FE method has accurately predicted the frequency components in the current spectrum which are a function of static airgap eccentricity and the simulations were verified by experimental results. Of particular importance is the application of the FE method to predict the magnitudes of these current components as a function of the degree of severity of static eccentricity. The results show that the analysis has produced a good estimate of their magnitudes in dB.

There is still a need to improve the accuracy of the FE predictions. For example, the FE mesh could be refined in the airgap region, however, it is considered that the time step of 39.2  $\mu$ s is sufficiently small to provide the required accuracy and this was verified by the accurate prediction of the frequency components (Hz) in the current signal. In the FE analysis the three-phase supply was considered to be perfectly balanced and to consist of only the supply frequency. In practice the three-phase line voltages differed by 1 to 2% and the third, fifth, seventh, and ninth harmonics were each 1% of the actual supply frequency voltage to the experimental motor. For normal analysis these effects would be considered negligible but for the prediction of high frequency current components which are a function of static eccentricity, slotting, saturation, winding design and MMF time harmonics then it is

probably necessary to include supply voltage influences. It is interesting to note that the fifth, and seventh harmonics are negligible in the EMF spectrum predicted by the FE analysis compared to the components which are a function of static eccentricity and is due to the pure sinusoidal supply voltage which was used in the FE model.

Future research will focus on improving the accuracy of the FE predictions and to evaluate the simulations when current monitoring is applied to large motors operating in industrial installations. This will support the work on current monitoring to detect static eccentricity as reported in reference [11]. The FE method will also be extended to include dynamic airgap eccentricity and combinations of both types.

Finally, it is accepted that the CPU time for time stepping FE simulations for this type of problem can be lengthy. This is due to the small time step and the substantial number of complete cycles required from the FE analysis to subsequently perform an accurate high resolution FFT on the induced EMF time domain signal. Since the complete motor has to be modelled a lengthy computational time is unavoidable.

#### V. ACKNOWLEDGEMENTS

The authors wish to thank GEC ALSTHOM ENGINEERING RESEARCH CENTRE, STAFFORD for providing the FE analysis programme (FEMTA) for the research project. Dr. J. P. Sturgess and Dr. T. W. Preston are sincerely thanked for their advice and support as industrial advisors on the project.

#### VI. REFERENCES

- [1] J. R. Cameron, "Vibration and Current Monitoring for On-line Detection of Airgap Eccentricity in Induction Motors," *Ph.D thesis RGIT*, 1987.
- [2] J. R. Cameron, W. T. Thomson and A. B. Dow, "Vibration and Current Monitoring for Detecting Airgap Eccentricity in Large Induction Motors," *Proceedings IEE*, vol. 133, pt. B, no. 3, May 1986, pp. 155-163.
- [3] W. T. Thomson, J. R. Cameron and A. B. Dow, "On-line Diagnostics of Large Induction Motors," *Vibrations and Audible Noise in Alternating machines*, Edited by Belmans, Binns, Geysen and Vandenput, Kluwer Academic Publishers, 1988.
- [4] S. Fruchtenicht, E. Pittuis and H. Seinsch, "A Diagnostic System for Three-phase Asynchronous Machines," *Proc. 4th EMDA Conference*, IEE, London, UK, 1989, no. 310, pp. 163-171.
- [5] J. Penman, M. N. Dey, A. J. Tait and W. E. Bryan, "Condition Monitoring of Electrical Drives," *Proceedings IEE*, vol. 133, pt. B, no. 3, May 1986, pp. 142-148.
- [6] W. T. Thomson and D. Rankin, "Case Histories of Rotor Winding Fault Diagnosis in Induction Motors," *Proceedings Int. Conf. on Condition Monitoring*, University College Swansea, April 1987, pp. 798-819.
- [7] W. T. Thomson, "On-Line Current Monitoring to Detect Electrical and Mechanical Faults in Three-Phase Induction Motors," *IEE Conference Proceedings on Life Management of Power Plants*, no. 401, December 1994, pp. 66-74.
- [8] G. B. Kliman and J. Stein, "Induction Motor Fault Detection via Passive Current Monitoring," *Proceedings Int. Conf. Electrical Machines (ICEM '90)*, August 1990, pp. 13-17.

- [9] S J Yang, *Low-noise Electrical Motors*, Oxford University Press, 1981.
- [10] J. R. Cameron, W. T. Thomson and A. B. Dow, "On-line Current Monitoring of Induction Motors - A Method for Calculating the Level of Airgap Eccentricity," *Proceedings IEE, 3rd EMDA Conference*, IEE no. 282, London 1989, pp. 173-178.
- [11] W. T. Thomson, D. Rankin and D. G. Dorrell, "On-line Current Monitoring to Diagnose Airgap Eccentricity - An Industrial Case History of a Large High-Voltage Three-Phase Induction Motor," *Proceedings of an IEEE -International Conference on Electrical Machines and Drives*, Wisconsin, USA, May 1997 (paper accepted for publication).
- [12] D. G. Dorrell, W. T. Thomson and S. Roach, "Analysis of Airgap Flux, Current and Vibration as a Function of the Combination of Static and Dynamic Airgap Eccentricity in 3-Phase Induction Motors," *IEEE Industry Applications Society Meeting - Conference Proceedings*, Orlando, Florida, October 1995, pp. 563-570.
- [13] S. Williamson, "Induction Motor Modelling Using Finite Elements," *Proc. ICEM '94*, Paris, September 1994, vol. 1, pp. 1-8.
- [14] S. J. Salon and J. M. Schneider, "Hybride Finite Element Boundary Integral Formulation of the Eddy Current Problem," *IEEE Trans*, vol. mag-18, no. 2, 1982, pp. 461-466.
- [15] T. W. Preston, A. B. J. Reece and P. S. Sangha, "Induction Motor Analysis by Time Stepping Techniques," *IEEE Transactions on Magnetics*, vol. 24, no. 1, January 1988, pp. 471-474.
- [16] G. K. M. Khan, W. C. H. Yu and J. P. Sturgess, "Finite Element Analysis of Induction Motors for Rail Traction Applications," *Proc. ICEM '94*, Paris, September 1994, vol. 2, pp. 33-38.
- [17] S. Salon, M. DeBortoli, D. Burrow and C. Slavik, "Calculation of Circulating Current Between Parallel Winding in Induction Motors with Eccentric Rotors by Finite Element Method," *Proc ICEM '92*, Manchester, UK, 1992, pp. 371-375.
- [18] S. Salon, D. Burrow, C. Slavik and M. DeBortoli, "Effects of Air Gap Ovality on Induction Motor Behaviour," *Proc. ICEM '96*, Vigo, September, 1996, vol. 1, pp. 401-404.
- [19] W. T. Thomson, R. A. Leonard, N. D. Deans and A. J. Milne, "Monitoring Strategy for Discriminating Between Different Types of Rotor Defects in Induction Motors," *18th UPEC Proceeding*, University of Surrey, Guildford, Surrey, UK, 1983, pp. 241-246.
- [20] M. G. Say, *Alternating Current Machines*, Fifth Edition, Pitman, 1983.
- [21] P. L. Alger, *The Nature of Induction Machines*, Gordon and Breach, Science Publishers, New York and London.

## VII. APPENDICES

### APPENDIX 1

$$R'_2 = \frac{12(k_{s1}k_{d1}T_{ph})^2}{R} \left\{ r_{be} + \frac{R}{2p^2\pi^2} r_e \right\}$$

$R'_2 = 2.25 \Omega$  from locked rotor test,  $k_{s1} = 0.96$  (coil span 8/9),  $k_{d1} = 0.9848$ ,  $T_{ph} = 180$ ,  $R = 51$ . With  $r_e =$  end ring resistance = 0 then  $r_{be} = r'_{be} =$  effective rotor bar resistance =  $330 \mu\Omega$ . Hence  $r'_{be} = 0.0868 \mu\Omega\text{-m}$ ,  $\sigma'_{rbe} = 11.52 \text{ MSm}^{-1}$  value of rotor bar conductivity used in FE analysis.

### APPENDIX 2

#### Interpretation of Fig. 3 and Fig. 4 - Experimental results

CT: 0.1V/A: Analyser 100 mV = 100 dB (calibration signal); reference voltage: 1μV. Hence, Fig. 3 - component at 50 Hz = 121.2 dB.

$I = \{ \text{antilog} (121.2 / 20) \times 1\mu\text{V} \} / 0.1\text{V/A} = 11.48 \text{ A}$  (compared to the current measured from an ammeter 11.5 A).

#### Interpretation of Fig. 6 and Fig. 7: FE Analysis and FFT procedure shown in Fig. 2.

$E_{n(50 \text{ Hz})} = 100.65 \text{ dB}$ ; a divide by 2000 factor is applied to the signal  $e(t)$  and for compatibility with the FFT spectrum analyser calibration signal (100 mV = 100 dB) produces comparable scales on Figures 3 and 4 with 6 and 7. From MATLAB FFT Fig. 6 -  $E_n = 2000 \times 1\mu\text{V} \{ \text{antilog} (100.65 / 20) \} = 215.5 \text{ V}$ .

Hence,  $I_n = (240-215.5) / Z_{n(50\text{Hz})} = 11.37 \text{ A}$ ; supply impedance is negligible reference [1]. Phase difference between  $V_{ph}$  and  $E_n$  at 50 Hz is negligible - confirmed from exact equivalent circuit calculations.

Hence, the dB value given in Table I is given by the following:

$$\text{dB} = 20 \log\{(11.37 \times 0.1\text{V/A}) / 1\mu\text{V}\} = 121 \text{ dB (current)}$$

Similarly for 1272 Hz in Fig. 7 at 50% static eccentricity

$$E_{n(1272 \text{ Hz})} = 0.44\text{V}; Z_{n(1272 \text{ Hz})} = 20 \Omega; I_n = 0.0219 \text{ A}$$

$\text{dB} = 20 \log\{(0.0219 \times 0.1\text{V/A}) / 1\mu\text{V}\} = 66.8 \text{ dB}$  as presented in Table I. Supply volts is a short circuit at all high frequency components.

## VIII. BIOGRAPHY



Professor Thomson (SM' 94) was born in the Scottish village of Alyth, Perthshire, in 1946. In 1973 he graduated from the University of Strathclyde with a B.Sc. Honours in Electronic and Electrical Engineering specialising in electrical machines and power systems. He began working as a research engineer with Hoover Ltd in Glasgow and in 1977 was awarded an M.Sc. by research for a thesis on "Vibration and Noise in Small Power Motors". From 1977 to '79 he lectured at the Hong Kong Polytechnic during which time he carried out consultancy work on vibrations in rotating machines. In 1979, he was appointed as a lecturer at Robert Gordon's Institute of Technology (now The Robert Gordon University) and in 1983 was promoted to a Senior Lecturer. In 1989, he was appointed as the University's first Reader, followed in 1990 by a professorship in Electrical Engineering. His main interests are in electrical machines, and in particular, condition monitoring of induction motor drive systems. He has been collaborating with industry on major research projects for the past seventeen years and has also published over fifty papers on the on-line diagnosis of fault mechanisms in induction motors. In 1992, a product which was developed with industry, received the Queen's Award for Technological Achievement. Professor Thomson is a fellow of the IEE and a Chartered Engineer.



Alexandra Barbour was born in Aberdeen, Scotland in November 1973. She received a BEng (Hons.) degree in Electronic and Electrical Engineering from The Robert Gordon University, Aberdeen in July 1995. She commenced employment as a research assistant at The Robert Gordon University in August 1995. The title of her research project is: "The analysis of 3-phase Induction Motors for the Reliable Diagnosis of Static and Dynamic Eccentricity". Miss. Barbour is an associate member of the IEE.

# FINITE ELEMENT STUDY OF ROTOR SLOT DESIGNS WITH RESPECT TO CURRENT MONITORING FOR DETECTING STATIC AIRGAP ECCENTRICITY IN SQUIRREL - CAGE INDUCTION MOTORS

A. Barbour and W. T. Thomson, Senior Member, IEEE  
School of Electronic and Electrical Engineering, The Robert Gordon University  
Schoolhill, Aberdeen AB10 1FR, Scotland

**Abstract** - Previous research using the mmf and permeance wave approach and experimental investigations has established that there are specific frequency components in the input current signal to an induction motor which are a function of static eccentricity, rotor slotting and saturation. The magnitudes of these components increase as the level of static eccentricity increases. The work reported in this paper applies finite element analysis to model a motor with static eccentricity to predict the severity of the fault from the magnitudes of these current components. The finite element results are compared with measured results from the test-rig motor being modelled and the agreement between them is found to be consistently closer than was achieved on previous attempts using the mmf and permeance wave approach. The finite element analysis is also used to determine what effect rotor slotting has on the magnitude of these components in relation to the overall changes in magnitude due to increasing static eccentricity levels. Different rotor slot designs were modelled (open, closed, semi-closed) and it was found that in terms of on-line current monitoring of induction motors the effect of different rotor slots on the magnitudes of the components was significant. This study has provided valuable information in terms of monitoring different motors in industry with the severity of the fault at different stages.

## I. INTRODUCTION

### A. Airgap Eccentricity

Airgap eccentricity is a fault mechanism which can occur in induction motors where the airgap between the stator and rotor is no longer uniform. The condition can take two forms each with a different effect on the airgap in the motor and in practice both forms are normally present in a motor simultaneously. Static airgap eccentricity exists when the position of the minimum airgap is fixed in space and time, whereas with dynamic eccentricity, the position of the minimum airgap rotates with the rotor. The condition is caused by a build up of manufacturing and assembly tolerances and by wear in motor components during service. In newly commissioned motors the fault is kept to a minimum due to good engineering designs and assembly procedures and a typical level of airgap eccentricity in a new

motor would be 5% - 10%. However, the application of on-line current monitoring to motors in industrial situations (1) and (2) has shown that when a motor has been in service for a number of years the level of airgap eccentricity can increase considerably by up to 40%, (3). Bearing wear, rotor or stator structure movement and thermal bow of the rotor are all problems that can occur with motors in service which lead to an increase in the level of airgap eccentricity. High levels of static eccentricity can cause dynamic eccentricity due to the unbalanced magnetic pull and in a worst case the rotor can actually be pulled onto the stator resulting in complete motor failure.

### B. On-Line Diagnosis of Airgap Eccentricity using Current Monitoring

It has been shown (1) and (2) that there are specific frequency components present in the airgap flux waveform which are a function of rotor slotting, saturation and airgap eccentricity. This work was based on classical techniques using the mmf and permeance wave approach. These components can be induced in the stator winding, and hence the line current of the motor, if the pole-pairs associated with these flux waveforms and the stator winding factors are taken into account. Equation (1) is derived from the mmf and permeance wave approach and is used to calculate the frequency components in the current spectrum.

$$f_{ec} = f_1 \left[ (R \pm n_d) \left( \frac{(1-s)}{p} \right) \pm n_{ws} \right] \quad (1)$$

- $f_{ec}$  = frequency components which are a function of airgap eccentricity (Hz)
- $f_1$  = supply frequency (Hz)
- $R$  = number of rotor slots
- $n_d$  = zero for static and one for dynamic eccentricity
- $s$  = slip
- $p$  = pole-pairs
- $n_{ws}$  = 1, 3, 5, 7, time harmonic of the stator mmf

The frequency components which are a function of airgap eccentricity are present in the current signal to the motor. By monitoring the frequency spectrum of the line current an indication of the presence of airgap eccentricity can be obtained. As the severity of the fault increases the magnitude of these frequency components in the current increase. In an industrial installation the current spectrum is monitored using a clip-on current transformer around one of the input line conductors and a spectrum analyser. This can be done from the switchgear room so access to the motor is not required which makes it popular with motor operators. By monitoring the current spectrum over time it is possible to detect high levels of airgap eccentricity and if the component magnitudes are seen to increase then it can be stated that the severity of the fault is increasing (2) and (3). However, it is not possible to reliably quantify the severity of the fault, i.e. this motor has x% eccentricity from the magnitudes of these current components. This would be of considerable interest to operators in the development of planned maintenance programs as discussions with manufactures suggest that a level of 20% eccentricity would be considered unacceptable and a level of 50% would be considered serious enough for immediate removal of the motor from service. It is appreciated that airgap eccentricity problems can be detected by stator core vibration (4), airgap and axial flux signals, (5) and (6) respectively, however, current monitoring is the least invasive to implement in the industrial environment.

#### *C. Limitations of the MMF and Permeance Wave Approach in Comparison to a Finite Element Analysis Approach*

Equation (1) is derived from the classical mmf and permeance wave approach (1, 2). This takes the flux density in the airgap to be the product of the mmf and permeance. The permeance term represents the permeance variation around the airgap due to rotor and stator slotting, saturation and airgap eccentricity. When determining the permeance variation over the slots it assumes a totally open square sided slot in order to simplify the complex analysis. This approach can therefore not be used to investigate the effects on the current component magnitudes due to the actual rotor slot shape. To take into account the distortion of the airgap flux density wave due to saturation the airgap length was increased, effectively increasing the reluctance. This approach was based on empirical formulae and simplifications so consequently the true effects of saturation are only partially modelled. As reported in (7) an attempt was made to predict the magnitudes of the current components for a specific level of airgap eccentricity using this approach. However, the differences between calculated and measured magnitudes varied from 3% to 300%. The poor agreement and inconsistency can be attributed to the above simplifications in the mmf and permeance wave approach. As the results in this paper show, a finite element

analysis of the motor to predict the magnitudes of the current components produces consistently better agreement between calculated and measured results. With a finite element analysis the true slot shape is modelled and instantaneous rather than time averages values of reluctivities are used to model localised saturation. Consequently, a detailed investigation of the effects of rotor slot shape variations is possible.

#### *D. Previous Finite Element Analysis of Airgap Eccentricity and Research Objectives of this Paper*

Finite element techniques have been used to analyse airgap eccentricity problems. They were used to calculate the forces acting on a rotor due to static eccentricity (8) and the average forces in the airgap due to static or dynamic eccentricity (9). Work reported in (10) investigated the effects on low order harmonics in the airgap flux density waveform due to static and dynamic eccentricity. Finite elements have also been used to investigate the optimum rotor slot shape for maximum efficiency (11) and the effects of slanted stator and rotor teeth on torque and electromagnetic losses (12). The work of (13) used a finite element model to investigate the effects of stator slot closure on the permeance variations in the airgap. The airgap flux density and force waves produced by the finite element analysis revealed that when the stator slots were closed the airgap flux density and force waves due to stator slotting decreased and those due to saturation increased. However, finite elements have not been used to predict the magnitudes of the frequency components in the current spectrum which are a function of rotor slotting, saturation and static airgap eccentricity. The effect of different rotor slot shapes on the magnitude of these components has not been investigated. Consequently, this paper focuses on the application of a two-dimensional time-stepping finite element analysis to investigate the aforementioned points and in brief the objectives are to:

- Use a time stepping finite element analysis to model a 3-phase induction motor with static eccentricity.
- Use the finite element results to calculate the current components which are a function of static airgap eccentricity, rotor slotting and saturation (frequency and magnitude) in the current spectrum and compare the predictions with experimental results from the test-rig motor being modelled.
- Investigate the effect of open, semi-closed and totally closed rotor slots on the magnitudes of these current components in comparison to the effect of static eccentricity using the finite element analysis.

These investigations will lead to the prediction of the level of static eccentricity present in the motor from the magnitudes of these specific components in the current spectrum. They will also determine how much of an effect the rotor slot shape has on the magnitudes of these current components in comparison to the changes in magnitudes observed when the eccentricity level is increased. This will lead to a better understanding of airgap eccentricity in relation to current monitoring of different types of motors in industry. The finite element analysis method used in this paper is reported in (14) and (15). It has already been used to analyse airgap eccentricity problems and it produced good agreement between calculated and measured current components for models of static eccentricity and combinations of static and dynamic eccentricity as reported in (16). Rotor slot shapes were not investigated in that paper.

## II. EXPERIMENTAL RESULTS

### A. Procedure

The test-rig motor used for the experimental tests and finite element models had the following specification: 3-phase, 415V, 50Hz, 4-pole, 1420 rpm, 20A, delta connected squirrel-cage motor with 36 stator and 51 rotor slots. As the majority of large motors are star connected and have unskewed rotors the stator was star connected and an unskewed copper fabricated rotor was used. Static airgap eccentricity was introduced into the test-rig in a controlled fashion as reported in (1). A clip-on current transformer was used to monitor the line current to the motor. This had an output of 0.1V/A which was inputted to a spectrum analyser with a input reference voltage of 100mV = 100dB.

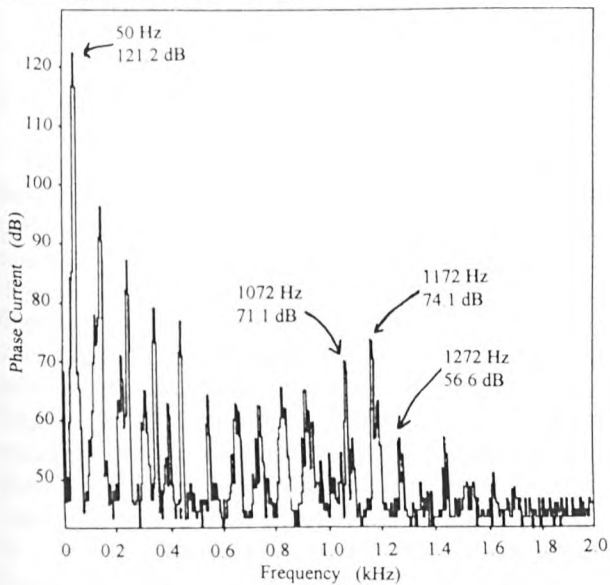


Fig. 1. Current Spectrum from experimental motor with 10% static eccentricity, full-load 1322 rpm.

A tolerance of approximately  $\pm 1$ dB was present in the experimental results.

### B. Static Eccentricity Variations

The test-rig motor had a nominal airgap length of 0.02 inches (0.508mm) and had a tolerance limit of 10% static (0.0508mm) with 5% dynamic (0.0254mm). Hence, the inherent level of static eccentricity in the motor was 10% and an upper limit of 50% static was used for safe operation. The level of inherent dynamic eccentricity was low and since combinations of static and larger levels of dynamic eccentricity are not being discussed in this paper, the dynamic eccentricity was considered negligible. The current spectra from the experimental motor for 10% static and then 50% static eccentricity are shown in Figures 1 and 2 respectively. This was for the full-load condition of 11.5A at 1322 rpm. The components which are a function of rotor slotting, saturation and static eccentricity are calculated from equation (1) and they occur at 1072Hz ( $n_{ws} = -1$ ), 1172Hz ( $n_{ws} = 1$ ) and 1272Hz ( $n_{ws} = 3$ ). They are clearly present in both spectrums and for a 40% increase in the static eccentricity level they increased in magnitude by more than 10dB which in linear terms is an increase of more than 3.16 times. These components are clearly a function of the level of static eccentricity present in the motor. The effect on the magnitudes of these components for different levels of static eccentricity is shown in Figure 3. With the motor running on lighter loads the magnitudes of these components decreased as expected, however, they are still obvious in the current spectrum. Figure 4 shows the decrease in the magnitudes of the components with load for a fixed level of 25% static eccentricity. Load variations are of interest as a motor may not always be operating at full-load.

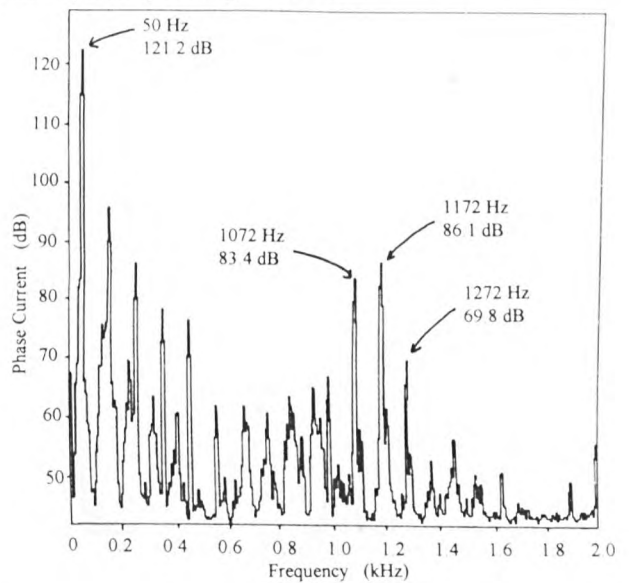


Fig. 2. Current Spectrum from experimental motor with 50% static eccentricity, full-load 1322 rpm.

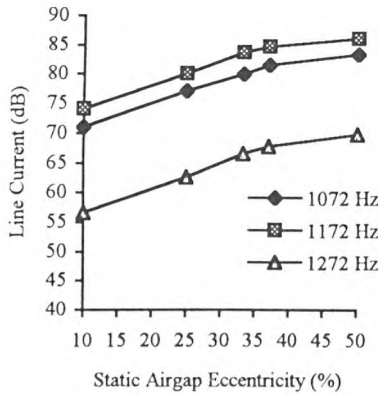


Fig. 3. Magnitude of current components versus static eccentricity, experimental results.

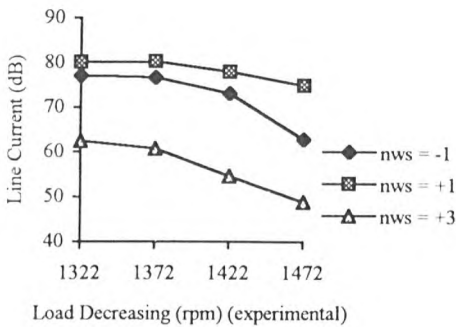


Fig. 4. Effect of load on the magnitude of the static eccentricity components, experimental results.

### III. APPLICATION OF FINITE ELEMENTS TO INVESTIGATE STATIC AIRGAP ECCENTRICITY

#### A. Procedure

The time-stepping finite element analysis predicted the time domain induced emf waveform. An FFT analysis was performed to identify the unique components predicted by equation 1 and obtained from the experimental results (Figures 1 and 2). The magnitudes of the emf components of interest in the spectrum were then applied to an equivalent circuit using the principle of superposition in order to calculate the magnitude of the current at those particular frequencies. The equivalent circuit modelled the stator resistance and the stator end-winding leakage reactance per phase and at these high frequencies the supply voltage was considered to be a short circuit. The emf signal was divided by 2000 and a reference of 100dB = 100mV was applied to display the emf spectrum on a dB scale. The calculated current components were converted to dB by dividing the

signal by 0.1 and applying a reference of 100dB = 100mV, hence, the calculated current components in dB can be directly compared with the magnitudes of the experimental current components in dB. The components of interest in the emf waveform were at high frequencies so a short time step of 39.2μs was used to ensure that they were modelled. To model the airgap variation due to static eccentricity the entire motor had to be modelled which resulted in the mesh containing 6406 nodes and 11,105 elements. To model static eccentricity the rotor was left on (0,0) and the stator was shifted by the required distance away from the centre axis of the motor. This results in a minimum airgap which is fixed in both space and time.

#### B. Static Eccentricity Variations

Models of the test-rig motor were created for 10%, 25% and then 50% static eccentricity (0% dynamic) and the finite element analysis was performed. The emf spectrums from the finite element analysis of the motor with 10% and then 50% static eccentricity can be seen Figures 5 and 6 respectively.

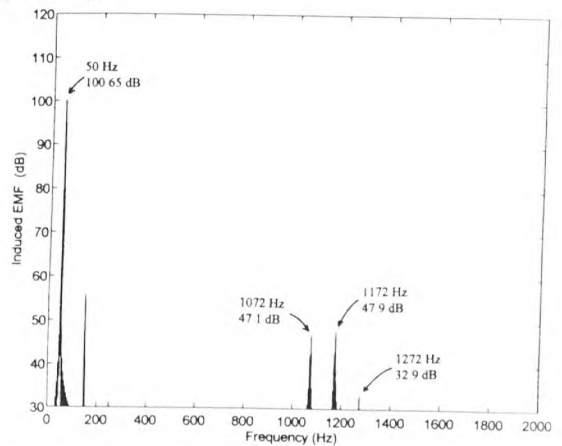


Fig. 5. EMF spectrum from FE analysis for 10% static eccentricity at 1322 rpm.

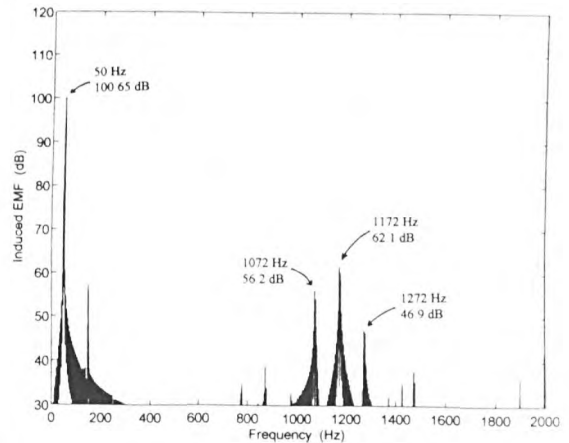


Fig. 6. EMF spectrum from FE analysis for 50% static eccentricity at 1322 rpm.

TABLE I. COMPARISON BETWEEN THE MEASURED AND PREDICTED (FE ANALYSIS) MAGNITUDES OF THE 50 HZ SUPPLY COMPONENT OF CURRENT AND THE CURRENT COMPONENTS WHICH ARE A FUNCTION OF STATIC AIRGAP ECCENTRICITY

m - measured se (%)	c - calculated			se - static eccentricity (%)			diff. - difference (Semi-closed slot 1.27mm with copper)					
	50 Hz (m) (dB)	50 Hz (c) (dB)	dB diff (dB)	1072 (m) (dB)	1072 (c) (dB)	dB diff (dB)	1172 (m) (dB)	1172 (c) (dB)	dB diff (dB)	1272 (m) (dB)	1272 (c) (dB)	dB diff (dB)
10	121.2	121.0	0.2	71.1	68.5	2.6	74.1	68.6	5.5	56.6	52.9	3.7
25	121.2	121.0	0.2	77.2	73.5	3.7	80.1	76.5	3.6	62.6	59.9	2.7
50	121.2	121.0	0.2	83.3	77.7	5.6	86.1	82.7	3.4	69.8	66.8	3.0

The components predicted by equation (1) are clearly present in the spectra and their magnitude can be seen to increase for a 40% increase in static eccentricity. Table I shows the comparison of the experimental and calculated current magnitudes for 10%, 25% and 50% static eccentricity. The difference between the measured and calculated 50Hz component was only 0.2dB thus validating the finite element analysis of the motor and the equivalent circuit used to predict the current component magnitudes. The difference between the magnitudes for the components which are a function of static eccentricity range from 2.6 to 5.6dB. In real current terms this might appear to be a substantial difference, however, compared to the difference between the measured and calculated results produced by the classical mmf and permeance wave approach the finite element analysis has produced a much closer agreement between the measured and calculated values. The overall increase in the magnitudes of the experimental and finite element results for the 40% increase in static eccentricity was of the same order. The range of increase for experimental components was 10.2 to 13.2dB compared with 9.2 to 14.1dB for the calculated components.

#### IV. APPLICATION OF FINITE ELEMENTS TO INVESTIGATE THE EFFECT OF ROTOR SLOT SHAPE ON COMPONENTS DUE TO STATIC ECCENTRICITY

##### A. Introduction

As mention before the components which are a function of the static eccentricity level are also a function of rotor slotting and saturation. The purpose of this investigation is to apply the finite element method to determine what effect the shape of the rotor slots has on the magnitudes of these components as a factor in the overall changes observed when the static eccentricity level is increased. This will lead to a better understanding of airgap eccentricity in terms of current monitoring of different motors in industry. Three types of rotor slot shape were investigated as shown in Figure 7. The semi-closed slot was modelled in several different configurations with a gap of 1.27mm or 0.6mm and air or copper filling the slot gap. The variation in the material in the slot was to investigate the effect on the

components when the gap between the copper conductor and the rotor surface was filled with air or copper up to the rotor surface. The finite element analysis was performed for different rotor slot designs at 0%, 10% and 25% static eccentricity.

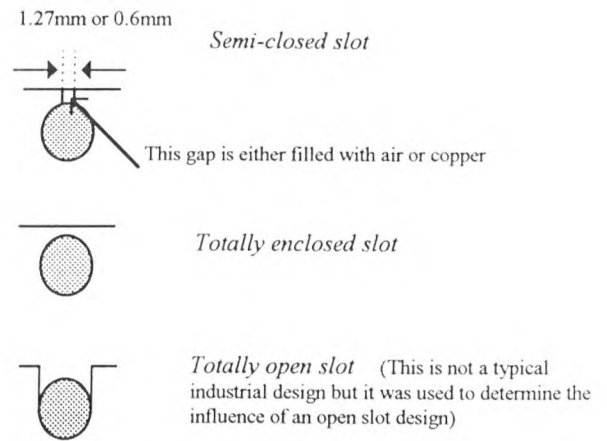


Fig. 7. Rotor Slot Shapes Investigated.

##### B. Rotor Slot Variations at 0% Static Eccentricity

An analysis of different rotor slot designs with 0% static eccentricity was performed. As no static eccentricity was being modelled the magnitudes of the components are only due to rotor slotting and saturation. These 'healthy' motor spectrum magnitudes can then be compared to those with static eccentricity, for the same slot design, in order to determine what portion of the magnitude of the components is due purely to static eccentricity. Three slot designs were modelled at 0% eccentricity and the variation in magnitudes of the components is shown in Table II.

TABLE II. MAGNITUDE OF COMPONENTS DUE TO DIFFERENT SLOT SHAPES MODELLED AT 0% STATIC ECCENTRICITY

0% static Frequency Hz	Slot shape		
	Semi- closed 1.27mm Cu	Totally open	Totally closed
1072	62.1	56.3	62.3
1172	54.3	56.5	57.4
1272	44.8	47.7	47.0

These results will be referred to again when determining what portion of the component magnitudes is due only to static eccentricity. Inspection of Table II shows that changing the slot shape to totally open or totally closed had an effect on the magnitude of the components. For instance, the 1072 Hz component decreased by 5.8dB when the slot design was changed from semi-closed to totally open, however, when the design was changed from semi-closed to totally closed it increased by 0.2dB. The 1172Hz and the 1272Hz increased in magnitude by 2.2 and 2.9dB respectively when the design goes from semi-closed to totally open but they remained constant to within 1dB when totally open and totally closed slot magnitudes were compared.

### C. Rotor Slot Variations at 10% Static Eccentricity

The analysis performed at 10% static eccentricity focuses on the effects of variations in the design of the semi-closed slot as Table III illustrates.

TABLE III. MAGNITUDE OF COMPONENTS DUE TO DIFFERENT SEMI-CLOSED SLOT SHAPES MODELLED AT 10% STATIC ECCENTRICITY

10% static	Slot shape		
Frequency Hz	Semi- closed 1.27mm Cu	Semi- closed 1.27mm air	Semi- closed 0.6 mm air
1072	68.5	68.2	67.9
1172	68.6	68.6	68.6
1272	52.9	52.9	54.4

Inspection of the results indicate that changing the material in the gap between the rotor conductor and the rotor surface from copper to air for the same slot width had a very small or no effect on the magnitudes of the components. This was expected as the magnetic properties of copper are very similar to those of air, hence, the analysis is confirmed to be modelling this change accurately. The reduction in the width of the slot gap from 1.27mm to 0.6mm had an insignificant effect on the 1072Hz and the 1172Hz components, however, the 1272Hz increased in magnitude by 1.5dB. The 1272Hz component is calculated when  $n_{ws} = 3$  (stator mmf time harmonic). The 3rd stator mmf time harmonic is predominantly produced by saturation effects (17), hence the 1272Hz component magnitude is dependant on saturation to a greater extent than the 1072Hz ( $n_{ws} = 1$ ) and 1172Hz ( $n_{ws} = -1$ ). Decreasing the slot width (i.e. closing the slot more) increased the magnitude of the component due to saturation.

A comparison of the component magnitudes for the 1.27mm copper filled semi-closed slot modelled with 0% and then 10% reveals that the magnitude of the components for 0% static eccentricity (Table II) were considerable less than those for 10% static eccentricity (Table III) as would be expected. Each frequency component increased in magnitude by a different amount when the static eccentricity level

increased from 0% to 10%. The 1072Hz increased by 6.4dB whereas the 1172Hz increased by 12.3dB. Inspection of Table I shows that the increase in each component for a increase of 10% to 25% static eccentricity was less spread out ranging from 5 to 7.9dB. A similar trend was noticed when the static eccentricity increased from 25% to 50%, each component increased in the range of 4.2 to 6.9dB. These results revealed that in the earlier stages of the fault each component increased by a considerably different amount for the same increase in static eccentricity but at higher levels of the fault, each component increased by approximately the same amount for the same increase in static eccentricity.

### D. Rotor Slot Variations at 25% Static Eccentricity

The results for variation in rotor slot designs modelled at 25% static eccentricity are shown in Table IV.

TABLE IV. MAGNITUDE OF COMPONENTS DUE TO DIFFERENT SEMI-CLOSED SLOT SHAPES MODELLED AT 25% STATIC ECCENTRICITY

25% static	Slot Shape			
Frequency Hz	Semi- closed 1.27mm Cu	Semi- closed 0.6 mm air	Totally open	Totally closed
1072	73.5	72.9	63.0	72.3
1172	76.5	76.5	63.6	74.5
1272	59.9	61.7	51.8	55.9

Changing the slot gap from copper to air with a constant gap of 1.27mm was not repeated as it clearly had no significant effect on the component magnitudes. The results for the variation in the width of the semi-closed slot at 25% eccentricity confirmed the observations at 10% static eccentricity in that only the magnitude of the 1272Hz component was affected which increased by 1.8dB.

Changing the slot shape from semi-closed 1.27mm copper to totally open decreased the 1072Hz component by 10.5dB. This is a considerably larger change than was noticed at 0% static where it decreased by 5.8dB. The 1172Hz and the 1272Hz decreased at 25% by 12.9dB and 8.1dB respectively compared to an increase of 2.2dB for the 1172Hz and 2.9dB for the 1272Hz at 0% static eccentricity.

Changing the rotor slot from semi-closed 1.27 mm copper to totally closed at 25% static decreased the 1072Hz component by 1.2dB, decreased the 1172Hz by 2dB and decreased the 1272Hz by 4dB. At 0% eccentricity this change in slot design increased the 1072Hz by 0.2dB, increased the 1172Hz by 3.1dB and increased the 1272Hz by 2.2dB.

Changing the slot from totally open to totally closed at 25% resulted in the 1072Hz increasing by 9.3dB, the 1172Hz increasing by 10.9dB and the 1272Hz increasing by 4.1dB. This is in comparison to the results at 0% static where

changing the slot from open to closed increased the 1072Hz by 6dB, the 1172Hz increased by 0.9dB and the 1272Hz decreased by 0.7 dB.

A comparison of the range of increase for the components with the semi-closed 1.27mm copper and the totally open and totally closed slot designs can be made from Tables II and IV. Table V shows the increase in magnitude of each component as the static increases from 0 to 25% for the different rotor slot designs.

TABLE V. COMPARISON OF THE INCREASES IN COMPONENT MAGNITUDES FOR A 25% INCREASE IN STATIC ECCENTRICITY FOR THE DIFFERENT ROTOR SLOT DESIGNS

Increase in component magnitudes			
0-25% Static increase	Semi-closed 1.27 mm copper	Totally Open	Totally Closed
1072 Hz	11.4	6.7	10.0
1172 Hz	22.2	7.1	17.1
1272 Hz	15.1	4.1	8.9

Table V shows that the design of rotor slot has a large effect on how much the component magnitudes increase for an increase in static eccentricity from 0 to 25%. The 1072Hz for the semi-closed and totally closed were the only components that increased a similar amount. The totally open slot showed considerably less of an increase than the totally closed and in particular the semi-closed slot design.

#### E. Discussion on the Rotor Slot Variation Results

The investigations into the effects of rotor slot shape on the components which are a function of rotor slotting, saturation and static eccentricity revealed that changes in rotor slot design have a significant effect on the magnitudes of these components. There is clearly a complex relationship between rotor slotting, saturation and static eccentricity and their combined effect on the magnitudes of the current components. The difference in the magnitude of the components for the different rotor slot designs was less at 0% static eccentricity than at 25% static. For instance, the 1172Hz component increased by 0.9dB at 0% as the slot design changed from totally open to totally closed, whereas, at 25% this component increased by 10.9dB. The higher levels of static eccentricity had a significant effect on the behaviour of the component magnitudes.

The investigations of the semi-closed slot design at 10% and then 25% static eccentricity revealed that changing the slot gap filling from copper to air had no significant effect on the components and when the slot gap was reduced from 1.27mm to 0.6mm it was only the 1272Hz which was affected - increased by 1.5dB and 1.8dB respectively. This is small in comparison to the increases in component magnitudes with static eccentricity and it is also very close to

the tolerance of approximately  $\pm 1$ dB for the experimental measurement of the component magnitudes.

The results in Table V show that the amount each component increased for the same increase in static eccentricity is very dependant on the rotor slot shape. In an industrial situation if a motor with a totally open rotor slot design is being monitored then the increase in the component magnitudes is considerably less than would be observed for a motor with a semi-closed rotor slot.

## V. CONCLUSIONS

The work reported in this paper has successfully applied finite element analysis to an induction motor with static airgap eccentricity in order to analyse the frequency spectrum of the input current to the motor. The frequency components in the current spectrum which are a function of rotor slotting, saturation and static eccentricity were present as predicted by classical theory and obtained experimentally. The finite element analysis was also used to predict the magnitude of these components in order to quantify the severity of static eccentricity. Consistently, better agreement was obtained between predicted and experimental magnitudes than was achieved previously using the mmf and permeance wave approach. For instance, the 1072Hz component for 10% static eccentricity was 2.6dB different from the experimental magnitude. This improvement is due to the accuracy in which the finite element method models the motor, whereas the classical approach has to make assumptions in order to simplify the complex analysis.

The finite element investigation of the rotor slot designs has revealed that the rotor slot design has a considerable effect on the magnitudes of the current components especially when static eccentricity is present. The rotor slot design also effects the size of the increase in the magnitudes of the components for the same increase in static eccentricity. For an increase of 25% (0 to 25%) static eccentricity the 1172Hz component increased by 22.2dB for the semi-closed slot compared to an increase of only 7.1dB for the totally open slot. The information gained from this analysis is of considerable value in terms of on-line current monitoring of different motors in industry.

For future work it is intended to investigate the effect of the number of rotor bars on the magnitude of the current components. Design details for a large motor operating in industry will be used in the finite element analysis to study airgap eccentricity problems and predicted results will be compared with on-site tests.

## ACKNOWLEDGEMENTS

The authors wish to thank GEC ALSTHOM ENGINEERING RESEARCH CENTRE, STAFFORD for

access to the FE package FEMTA. Dr. J. P. Sturgess and Dr. T. W. Preston are sincerely thanked for their advice and support as industrial advisors on the project.

#### REFERENCES

- [1] J. R. Cameron, "Vibration and Current Monitoring for On-line Detection of Airgap Eccentricity in Induction Motors," *PhD thesis RGIT*, 1987.
- [2] J. R. Cameron, W. T. Thomson and A. B. Dow, "Vibration and Current Monitoring for Detecting Airgap Eccentricity in Large Induction Motors," *Proceedings IEE*, vol. 133, pt. B, no. 3, pp. 155-163, May 1986.
- [3] W. T. Thomson, D. R. Rankin and D. G. Dorrell, "On-line Current Monitoring to Diagnose Airgap Eccentricity - an Industrial Case History of a Large High Voltage Induction Motor," *IEEE - International Conference on Electrical Machines and Drives*, pp. MA2-4.1 to MA2-4.3, May 1997.
- [4] W. T. Thomson, J. R. Cameron and A. B. Dow, "On-Line Diagnostics of Large Induction Motors," *Vibrations and Audible Noise in Alternating Machines, 1988*, Edited by Belmans, Binns, Geysen and Vandeput, Kluwer Academic Publishers.
- [5] S. Fruchtenicht, E. Pittuis and H. Seinsch, "A Diagnostic System for Three-phase Asynchronous Machines," *Proc. 4th EMDA Conference*, IEE, no. 310, pp. 163-171, 1989.
- [6] J. Penman, M. N. Dey, A. J. Tait and W. E. Bryan, "Condition Monitoring of Electrical Drives," *Proceedings IEE*, vol. 133, pt. B, no. 3, pp. 142-148, May 1986.
- [7] J. R. Cameron, W. T. Thomson and A. B. Dow, "On-line Current Monitoring of Induction Motors - A Method for Calculating the Level of Airgap Eccentricity," *Proceedings IEE, 3rd EMDA Conference*, IEE no. 282, pp. 173-178, 1989.
- [8] A. Arkkio and O. Lindgren, "Unbalanced Magnetic Pull in a High Speed Induction Motor with an Eccentric Rotor," *Proc. ICEM*, vol. 1, pp. 53-58, 1994.
- [9] J. C. Mercier, L. Durantay, J. Enon and C. Aubertin, "Finite Element Computation of the Magnetic Fields and Forces in an Induction Machine at its Rated Point with Simulation of Electromagnetic Defects," *Proc. ICEM*, vol. 2, pp. 44-49, 1994.
- [10] S. Salon, D. Burrow, C. Slavik and M. DeBortoli, "Effects of Air Gap Ovality on Induction Motor Behaviour," *Proc. ICEM '96*, vol. 1, pp. 401-404, 1996.
- [11] S. Williamson and C. I. McClay, "Optimisation of the Geometry of Closed Rotor Slot for Cage Induction Motors," *IEEE Trans. Industrial Applications*, vol. 32 issue 3, pp. 560-568, May-June 1996.
- [12] S. Plako, "The Effect of Slanted Stator and Rotor Teeth on torque and Electromagnetic Losses in Cage Induction Motors," *Proceedings of the Symposium on Power Electronics, Electrical Drives, Advanced Electrical Motors*, Taormina, Italy, vol. 1, pp. 185-187, June 1994.
- [13] S. Salon, D. Burrow, C. Slavik and M. DeBortoli, "Effects of Slot Closure and Magnetic Saturation on Induction Machine Behaviour," *IEEE Trans. on Magnetics*, vol. 30, issue 5, pt. 2, pp. 3697-3700, Sept 1994.
- [14] T. W. Preston, A. B. J. Reece and P. S. Sangha, "Induction Motor Analysis by Time Stepping Techniques," *IEEE Trans. on Magnetics*, vol. 24, pt. 1, pp. 471-474, 1988.
- [15] G. K. M. Khan, W. C. H. Yu and J. P. Sturgess, "Finite Element Analysis of Induction Motors for Rail Traction Applications," *Proc. ICEM '94*, vol. 2, pp. 33-38, 1994.
- [16] A. Barbour and W. T. Thomson, "Finite Element Analysis and On-Line Current Monitoring to Diagnose Airgap Eccentricity in 3-Phase Induction Motors," *IEE Electrical Machines and Drives Conference*, Cambridge, September, 1997.
- [17] J. C. Moreira and T. A. Lipo, "Modelling of Saturated AC Machines Including Air Gap Flux Harmonic Components," *Trans. IEEE 90/CH2935*, pp. 37-44, May 1990.

# FINITE ELEMENT ANALYSIS AND ON-LINE CURRENT MONITORING TO DIAGNOSE AIRGAP ECCENTRICITY IN 3-PHASE INDUCTION MOTORS

A Barbour and W T Thomson

The Robert Gordon University, Aberdeen

**Abstract** - This paper applies finite element analysis to predict the frequency components in the current signal which are a function of airgap eccentricity in a 3-phase squirrel-cage induction motor. The magnitude of the components and hence the severity of the fault are predicted and compared with experimental results for static and combinations of static and dynamic eccentricity. Closer agreement is consistently found between calculated and measured magnitudes in comparison to previous attempts using the mmf and permeance wave approach.

## INTRODUCTION

**Airgap Eccentricity** : This occurs in induction motors when the airgap between the stator and rotor is non-uniform. Eccentricity can occur in two forms, namely static (fixed position minimum airgap) and dynamic (rotating minimum airgap), and in practice both occur simultaneously. Static and dynamic eccentricity is caused by assembly and manufacturing tolerances but is kept to a minimum (typically 5 - 10%) due to good designs and high manufacturing standards. High levels of airgap eccentricity are not normally a problem in new motors, however, it is known that problems such as bearing wear, thermal bow, rotor or stator structure movement, can occur with motors in service, Cameron (1) and Cameron et al (2).

**Diagnosis of Airgap Eccentricity using On-line Current Monitoring** : This paper focuses on the analysis of the current to identify frequency components which are a function of static or dynamic eccentricity and their combination. Current monitoring is popular with motor operators because the signal is sensed via a clip-on transformer in the switchgear room and access to the motor is not required, Rankin (3). Other techniques can be used to diagnose airgap eccentricity, such as stator core vibration (Thomson et al (4)), airgap and axial flux signals Fruchtenicht et al (5) and Penman et al (6), respectively. By using the mmf and permeance wave approach it has been shown that there are specific frequency components in the current spectrum which are a function of rotor slotting and static and dynamic eccentricity (1) and (2). Equation 1 is derived from the mmf and permeance wave approach and is used to calculate the frequency components in the current (1).

$$f_{ec} = f_1 \left[ (R \pm n_d) \left( \frac{(1-s)}{p} \right) \pm n_{ws} \right] \quad (1)$$

- $f_{ec}$  = frequency components which are a function of airgap eccentricity (Hz)  
 $f_1$  = supply frequency (Hz);  $R$  = no. of rotor slots  
 $n_d$  = zero for static and one for dynamic eccentricity  
 $s$  = slip;  $p$  = pole-pairs;  $n_{ws} = 1, 3, 5, 7$

It is the frequency components predicted by equation 1 which are studied in this paper. To predict the severity of the fault the magnitude of these components has to be calculated as a function of the level of eccentricity. At present, monitoring the current can detect the presence of abnormal levels of airgap eccentricity, (2) and Thomson et al (7), but the severity of the fault cannot be reliably quantified.

## Finite Element Analysis and Research Objectives :

Finite element analysis has been used to analyse airgap eccentricity, as reported in reference (8) Salon et al, it was used to analyse the effect of static and dynamic eccentricity on low order harmonics in the airgap flux density waveform. However, the identification and quantification of the high frequency components in the current due to rotor slotting, static or dynamic eccentricity and their combination was not investigated. The work reported in the paper uses a time stepping finite element analysis method as reported in (9,10) and the objectives are to:

- Use time stepping finite element analysis to model a 3-phase induction motor with static, dynamic and combinations of both forms of eccentricity.
- Use the finite element results to calculate the components (frequency and magnitude) in the current spectrum.
- Compare the calculated components with measured components from the experimental motor being modelled.

## EXPERIMENTAL RESULTS

**Procedure** : A 3-phase, 11kW, 415V, 50 Hz, 4 pole, 1420 rpm, 20A, delta-connected squirrel-cage motor with 36 stator and 51 rotor slots was used for the tests. An unskewed copper fabricated rotor was used and the stator was star connected because large motors are mainly unskewed and connected in star. The current

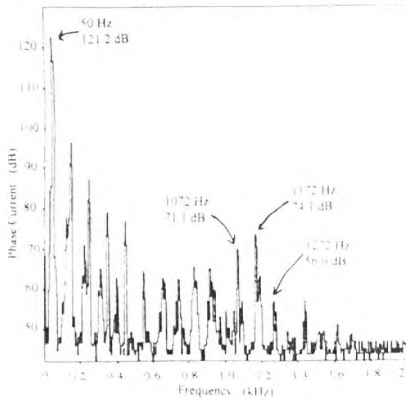


Fig. 1. Current spectrum for 10% static and 5% dynamic eccentricity, full load 1322 rpm; experimental.

signal was monitored using a current transformer (output 0.1V/A) which was fed to a spectrum analyser with a reference input of 100mV = 100dB. Airgap eccentricity was introduced into the test-rig in a controlled manner as reported in (1). A tolerance of approximately 1dB was present in the experimental measurements.

**Fixed Dynamic and Variable Static Eccentricity :**

The current spectra from the motor with 10% and then 50% static eccentricity are shown in Figures 1 and 2. This was for the full load condition (11.5A, 1322rpm) with a minimum, nominal level of 5% dynamic eccentricity. The components which are a function of static eccentricity predicted by equation 1 are at 1072Hz, 1172Hz, 1272Hz ( $n_d = 0$ ). Each component increased by more than 10dB which is a linear increase of more than 3.16 times the original magnitude. The increase in the magnitude of the components with increasing static eccentricity is illustrated in Figure 3. The effect of load variation on the magnitudes of the components is shown in Figure 4 for a fixed value of 25% static and nominal 5% dynamic eccentricity. The components which are a function of static eccentricity change in frequency with load so they are referred to as the components calculated with  $n_{ws} = 1$ ,  $n_{ws} = -1$ ,  $n_{ws} = 3$ ,  $n_d = 0$  for each. As expected, with reduced current flowing in the rotor winding the magnitude of the components decreased, however, the initial rate of decrease is low between 1322 to 1372 rpm. The results presented in Figure 4 are important since a motor may not always be operating at full-load in industry.

**Variations in Combinations of Static and Dynamic Eccentricity :**

Equation 1 also predicts frequency components which are a function of dynamic eccentricity when  $n_d = \pm 1$ , these appear either side of the components due to static eccentricity provided the pole number of the flux waveforms can induce current in the stator winding. The previous results, Figures 1-4, with varying levels of static eccentricity were obtained with a nominal value of 5% dynamic eccentricity, the

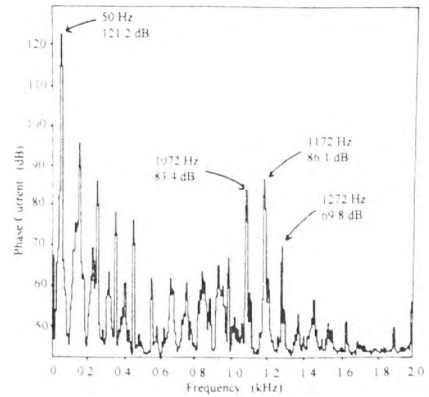


Fig. 2. Current spectrum for 50% static and 5% dynamic eccentricity, full load 1322 rpm; experimental.

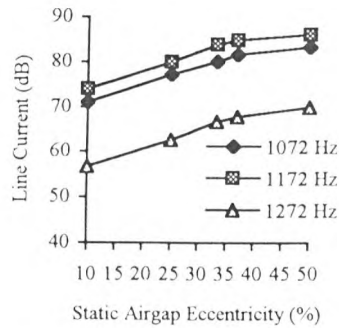


Fig. 3. Magnitude of current components versus static airgap eccentricity; experimental results.

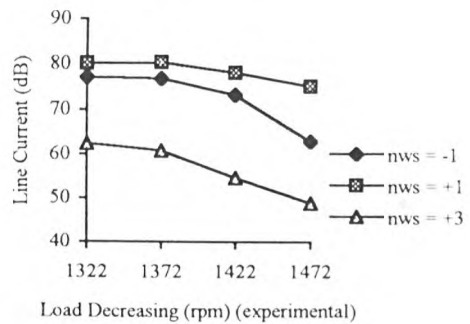


Fig.4. Effect of load on static eccentricity components.

dynamic level was then increased to 25% and two levels of static eccentricity (10% and 25%) were investigated. Table 1 shows the increase in the dynamic eccentricity components with the change from 5% to 25% dynamic eccentricity (fixed static of 10%) in the test-rig motor. These components, in particular those with  $n_d = 1$ , are clearly dependant on the dynamic eccentricity level, for instance, the component at 1094 Hz increased by 20.4dB and the 1194Hz component increased by 18.4dB for a 20% increase in dynamic eccentricity. This is clear evidence of the effect of dynamic eccentricity (20dB = 10 times linear). The effect on the components with a fixed level of dynamic (25%) with increasing static was investigated, Figures 5 and 6 and Table 1 show the spectra of the current for

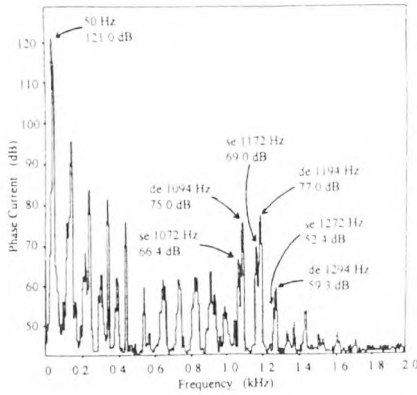


Fig. 5. Current spectrum for 10% static with 25% dynamic full-load 1322 rpm; experimental results.

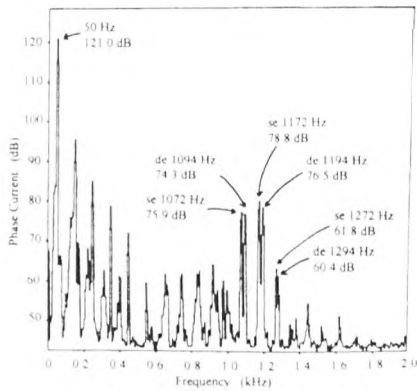


Fig. 6. Current spectrum for 25% static with 25% dynamic full-load 1322 rpm; experimental results.

10% static with 25% dynamic and 25% static with 25% dynamic respectively. With a 15% increase in static and a fixed dynamic of 25% the static eccentricity components increased in magnitude and the dynamic components remained approximately at the same level. For instance, the 1172 Hz (static component) increased by 9.8dB and the 1194Hz decreased by 0.5dB, whereas the 1194Hz component increased by 18.4dB when dynamic eccentricity was increased from 5% to 25%. The effect of load variations on these components for fixed static (25%) and dynamic (25%) eccentricity levels is shown in Figure 7.

## FINITE ELEMENT RESULTS

**Procedure :** The time domain induced emf waveform was predicted from the time stepping finite element analysis. An FFT of the emf was used to identify the frequency components due to airgap eccentricity as predicted by classical theory (equation 1). Using the principle of superposition each emf component magnitude was used in an equivalent circuit which modelled the stator resistance and stator end-winding leakage reactance in order to calculate the magnitude of the current at that particular frequency. At the high frequencies the supply voltage was considered to be a short circuit. To display the spectrum on a dB scale the

Freq. Comp. (Hz)	$n_{ws}$	$n_d$	Mag. (dB) 10% se 5% de	Mag. (dB) 10% se 25% de	Mag. (dB) 25% se 25% de
50	-	-	121.0	121.0	121.0
de 1050	-1	-1	50.8	44.4	41.8
se 1072	-1	0	67.0	66.4	75.9
de 1094	-1	+1	54.6	75.0	74.3
de 1150	+1	-1	40.4	39.7	42.8
se 1172	+1	0	70.8	69.0	78.8
de 1194	+1	+1	59.0	77.0	76.5
de 1250	+3	-1	31.1	44.6	37.7
se 1272	+3	0	55.6	52.4	61.8
de 1294	+3	+1	51.2	59.3	60.4

TABLE 1. Magnitudes of current components from test-rig motor for combinations of static and dynamic eccentricity; se - static, de - dynamic.

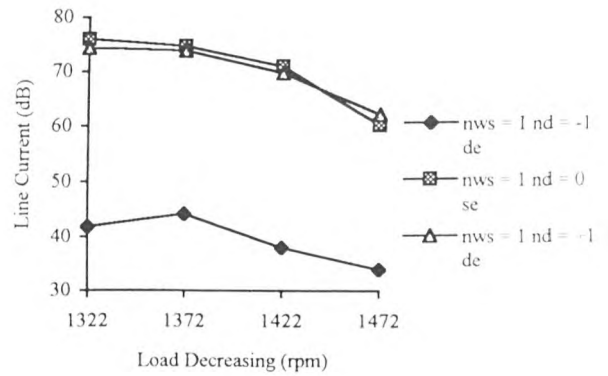


Fig.7. Effect of load on static (se) and dynamic (de) eccentricity components; experimental results.

emf signal is divided by 2000 and a reference of 100dB=100mV was used. To convert the calculated current components to dB the signal was divided by 0.1 and a reference of 100mV=100dB was used. This means that the computed current components in dB can be directly compared with the experimental current magnitudes in dB from the spectrum analyser. The complete motor had to be modelled to analyse the airgap variation which resulted in the mesh containing 6406 nodes and 11,105 elements. Since the emf waveform contained high frequency components due to slotting and eccentricity a small time step of 39.2 $\mu$ s was used. This was calculated based on approximately 20 steps for each rotor slot. To model static eccentricity the stator model was shifted off centre and the rotor was left centred on (0,0). For dynamic eccentricity and combinations of both types, shift vectors were used, one for each form of eccentricity, which resulted in the required variation of the airgap length for the different fault combinations.

**Simulations of Static Eccentricity and Comparison with Experimental Results :** Time stepping finite element analysis was performed on models of the motor with 10%, 25% and then 50% static eccentricity for the

full load speed (1322 rpm) with 0% dynamic eccentricity. Figures 8 and 9 show the emf spectrum of the motor with 10% and then 50% static eccentricity. The components predicted by equation 1 are present and they clearly increase in magnitude, Table 2 shows the comparison between the calculated and measured magnitudes of the current components. Inspection of Table 2 reveals that the magnitude of the calculated 50 Hz component is within 0.2dB of the experimental, this validates the FE analysis of the motor. A comparison of the measured and calculated magnitudes show that they differ by 2.6 to 5.6 dB. This may seem to be a considerable difference in real current terms, however, the agreement between calculated and measured magnitudes is consistently closer than was achieved in reference (1) and the overall change for the experimental and calculated magnitudes is of the same order, 12.0 to 13.2dB experimentally compared with 9.2 to 14.1dB from the finite element analysis.

**Simulations of Static and Dynamic and Comparison with Experimental Results :** Initially 25% dynamic with 0% static eccentricity at 1322 rpm was modelled to verify that the analysis was modelling dynamic eccentricity. The emf spectrum still contained the components which are a function of the magnitude of static eccentricity since these components are primarily due to rotor slotting. The components which are a function of dynamic eccentricity were present as predicted by equation 1. The magnitude of the static eccentricity components was smaller than was later obtained when modelling 25% dynamic with static

eccentricity present. This was expected since the magnitude of the static eccentricity components present in the 25% dynamic and 0% static eccentricity spectrum were only due to rotor slotting and not the additional presence of static eccentricity. Finite element analysis was then performed for 10% static with 25% dynamic and then 25% static with 25% dynamic. The spectra of the emf waveform for the two fault conditions are shown in Figures 11 and 12. The frequencies of the components in the emf are the same as those predicted by equation 1 (classical theory) and obtained from experimental tests. With the increase in static eccentricity the static eccentricity components increased and the upper dynamic components remained approximately constant. Table 3 shows the comparison between measured and calculated current component magnitudes for 10% static and 25% dynamic eccentricity. Good agreement is obtained, for instance, the dB difference between the calculated and measured values for the 1050Hz and 1194Hz (de components) was 2.2dB and 1.7dB, respectively. The difference in dB for the static eccentricity component at 1072Hz was only 0.6dB.

### Conclusions

The application of finite element analysis has facilitated the prediction of the magnitude of current components which are a function of static or dynamic airgap eccentricity in a 3-phase squirrel-cage induction motor. Of particular significance is that the finite element method has predicted the magnitude of current

TABLE 2. Comparison between the measured and predicted (FE analysis) magnitudes of the 50 Hz supply component of current and current components which are a function of static airgap eccentricity

m - measured (x% se with 5% de)				c - calculated (se only)			se - static eccentricity (%)			diff - difference		
se (%)	50 Hz (m) (dB)	50 Hz (c) (dB)	dB diff (dB)	1072 (m) (dB)	1072 (c) (dB)	dB diff (dB)	1172 (m) (dB)	1172 (c) (dB)	dB diff (dB)	1272 (m) (dB)	1272 (c) (dB)	dB diff (dB)
10	121.2	121.0	0.2	71.1	68.5	2.6	74.1	68.6	5.5	56.6	52.9	3.7
25	121.2	121.0	0.2	77.2	73.5	3.7	80.1	76.5	3.6	62.6	59.9	2.7
50	121.2	121.0	0.2	83.3	77.7	5.6	86.1	82.7	3.4	69.8	66.8	3.0

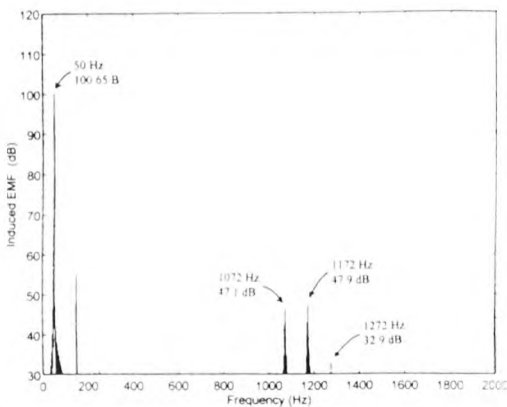


Fig. 8. EMF spectrum from FE analysis for 10% static at 1322 rpm.

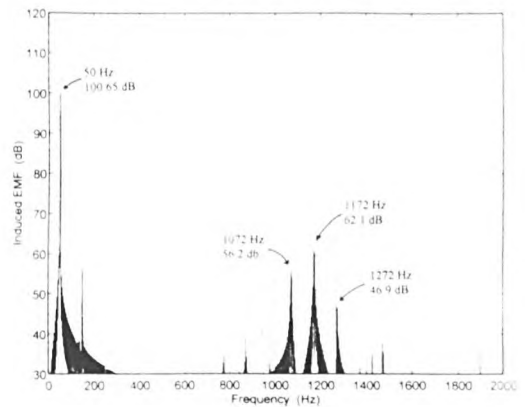


Fig. 9. EMF spectrum from FE analysis for 50% static at 1322 rpm.

Component (Hz)	Exp. Mag. (dB)	FE Cal. Mag. (dB)	dB difference
50	121.0	120.7	0.3
de 1050	44.4	46.6	2.2
se 1072	66.4	67.0	0.6
de 1094	75.0	72.4	2.6
de 1150	39.7	39.9	0.2
se 1172	69.0	68.9	0.1
de 1194	77.0	78.7	1.7

TABLE 3. Comparison of experimental and calculated component magnitudes for 10% se and 25% de eccentricity.

components when a combination of static and dynamic eccentricity is present, which is the case in all industrially based induction motors. Good agreement was obtained between the predicted and measured results in the context of applying on-line current monitoring to detect abnormal levels of airgap eccentricity and an estimation of the degree of severity of the fault condition. For example, the experimental results showed that the dynamic eccentricity component at 1194Hz increased by 18dB when dynamic eccentricity was increased by 20% with a fixed static of 10%. The time stepping finite element analysis predicted that the 1194Hz dynamic eccentricity component was 78.7dB compared to the measured value of 77dB. Hence, the difference of 1.7dB between experimental and predicted absolute values for a given static and dynamic combination is negligible compared to the increase of 18dB due to the increase in actual dynamic eccentricity. These predictions have hitherto not been possible using existing monitoring strategies and the classical mmf and permeance wave approach. Research is continuing to improve the accuracy of predictions and to consider the influence of different slot designs. The analysis will also be applied to large induction motors operating in industry and a comparison made with on-site tests.

### Acknowledgements

The authors wish to thank GEC ALSTHOM ENGINEERING RESEARCH CENTRE, STAFFORD for access to the FE package FEMTA. Dr. J. P. Sturgess and Dr. T. W. Preston are sincerely thanked for their advice and support as industrial advisors on the project.

### References

1. Cameron, J. R., 1987 "Vibration and current monitoring for on-line detection of airgap eccentricity in induction motors," Ph.D thesis RGII.
2. Cameron, J. R., Thomson, W. T., and Dow, A. B., 1986, "Vibration and current monitoring for detecting airgap eccentricity in large induction motors," Proceedings IEE vol. 133, part B, 3, 155-163.
3. Rankin, D. R., 1995, "The industrial application of phase current analysis to detect winding faults in

squirrel cage induction motors", IEE PEJ, vol 9, no 2, 77-86.

4. Thomson, W. T., Cameron, J. R., and Dow, A. B., 1988, "On-line Diagnostics of Large Induction Motors," Vibrations and Audible Noise in Alternating machines, Edited by Belmans, Binns, Geysen and Vandepuut, Kluwer Academic Publishers.
5. Fruchtenicht, S., Pittuis, E. and Seinsch, H., 1989, "A Diagnostic System for Three-phase Asynchronous Machines," Proc. 4th EMDA Conference, IEE, 310, 163-171.
6. Penman, J., Dey, M. N., Tait, A. J. and Bryan, W. E., 1986, "Condition monitoring of electrical drives", Proc. IEE, vol. 133, part B, 3, p 142-148.
7. Thomson, W. T., Rankin, D. R., and Dorrell, D. G., May 1997, "On-line current monitoring to diagnose airgap eccentricity - an industrial case history of a large high voltage induction motor", IEEE - International Conference on Electrical Machines and Drives.
8. Salon, S., Burrow, D., Slavik, C. and DeBortoli, M., 1996, "Effects of Air Gap Ovality on Induction Motor Behaviour," Proc. IECM '96, vol. 1, 401-404.
9. Preston, T. W., Reece, A. B. J. and Sangha, P. S., 1988 "Induction Motor Analysis by Time Stepping Techniques," IEEE Transactions on Magnetics, vol. 24, 1, 471-474.
10. Khan, G. K. M., Yu W. C. H. and Sturgess, J. P., "Finite Element Analysis of Induction Motors for Rail Traction Applications," Proc. IECM' 94, vol. 2, 33-38.

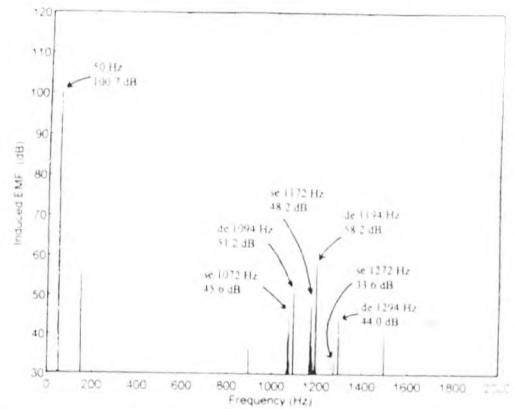


Fig. 10 EMF spectrum from FE analysis for 25% dynamic with 10% static at 1322 rpm.

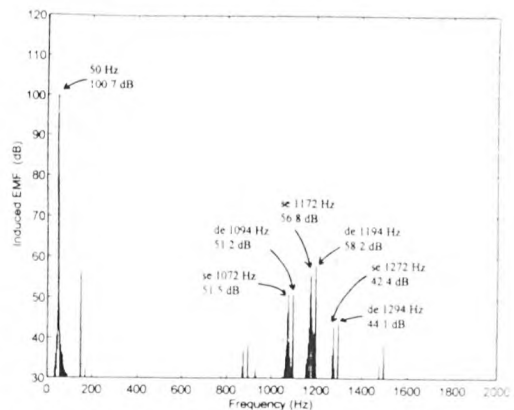


Fig. 11 EMF spectrum from FE analysis for 25% dynamic with 25% static at 1322 rpm.

# AN APPRAISAL OF THE M.M.F.-PERMEANCE METHOD AND FINITE ELEMENT MODELS TO STUDY STATIC AIR-GAP ECCENTRICITY AND ITS DIAGNOSIS IN INDUCTION MACHINES

W. T. Thomson and A. Barbour - The Robert Gordon University Aberdeen Scotland

C. Tassoni - Università di Parma Italy

F. Filippetti - Università di Bologna Italy

**Abstract:** Industry is now using on-line current monitoring as the preferred method to diagnose problems such as broken rotor bars, airgap eccentricity and shorted turns in stator windings (low voltage) of three phase induction motors. The main advantage of this method is that it is non-invasive since the sensor is a current transformer. This paper will focus on the complexity of analysing the current signal and the interrelationships between airgap flux density, induced e.m.f. and the current spectra. Experimental results and analyses using the m.m.f. - permeance wave model will be compared with finite element simulations as a function of airgap eccentricity. An appraisal between theoretical predictions and experimental results is presented.

## 1. Introduction

Current spectrum analysis is an accepted strategy for condition monitoring of induction motors [1-5]. Fault mechanisms can be diagnosed via the identification of unique components in the current spectrum which are characteristic of the fault. The m.m.f.-permeance wave analysis has shown that specific frequency components in the airgap flux density, induced e.m.f. and current are a function of slotting, airgap eccentricity, time and space harmonics [1,4,6-9]. However, the classical analysis assumes perfect symmetry of the winding distribution, magnetic circuit and supply voltage. The airgap flux density components can induce current components in the stator winding provided there is compatibility between the pole-pair number of the specific flux component and a harmonic pole-pair number of the stator winding.

In practice, induction motors are not perfectly symmetrical and the supply voltages are not normally exactly balanced. It has been observed from laboratory experiments and on-site case histories that current components can be induced due to airgap eccentricity [1, 4] which, by the classical m.m.f. - permeance wave analysis, should not be induced assuming perfect magnetic and winding symmetry.

Experimental results from a spectrum analysis of the flux density, induced e.m.f. and current will be presented and compared with predictions from the m.m.f.-permeance wave analysis. It will be shown that the analysis of the signals from a practical induction motor is more complex than the classical m.m.f. - permeance wave analysis suggests. Finite element simulations and m.m.f. - permeance wave models will be compared with experimental results

## 2. Permeance - m.m.f. wave analysis

Many researchers have investigated the effects which airgap eccentricity can produce in the induction motor current via m.m.f. - permeance wave models [1,4,6-10]. Experimental evidence has clearly shown that sideband current components positioned at  $f \pm fr$  frequencies (often detectable in a healthy motor) can be due to mechanical phenomena or a combination of inherent static and dynamic airgap eccentricity [8].

However, when only dynamic eccentricity is modelled this will not lead to these components being predicted. This is due to the fact that with only dynamic eccentricity then the pole pairs for the  $f \pm fr$  flux components are  $p \pm 1$  and these waves cannot induce an e.m.f. or current in a  $p$  - pole pair stator winding [11]. Recent publications have proved, via theoretical analysis and experimental verification, that a combination of static and dynamic eccentricity does produce these current components [8]. This is due to the inter-modulation between static and dynamic eccentricity flux waves which produces waves at  $f \pm fr$  having  $p$ - pole pairs. If only these two components are monitored it is not possible to discriminate between static and dynamic eccentricity [4].

Experimental results from laboratory work and industrial case histories have verified that static eccentricity can change the magnitude ( in amps or dB ) of the classical rotor slot passing frequencies ( sometimes referred to as the principal rotor slot passing frequencies ) and these can be used to identify an increase in static eccentricity [1,4]. However, the problem with only observing these components is that a base line survey is required for trending their increase but it has been shown that an increase in static eccentricity can cause the  $f \pm fr$  current components to increase with a fixed inherent dynamic eccentricity [4]. The combination of monitoring different components can therefore lead to a more reliable diagnosis.

The principal rotor slot passing frequencies are the well known lines at frequencies  $f \pm Rf_r$  [1,4,6-11] which can be present in the current spectrum due to air gap permeance variations caused by rotor slotting. These components have also been given special attention since they can be utilised to determine the rotor slip for mains and inverter fed induction motor drives [12]. Due to complex phenomena which are the sources of these components an in-depth understanding of their origins is required. A substantial contribution can be found in [12] and a similar approach is presented in this paper to further clarify the

fundamental causes of flux components due to slotting and which are also a function of airgap eccentricity. According to the classical rotating field model the air gap flux density is a product of the m.m.f. and airgap permeance [10]. The temporal and spatial harmonics of rotor and stator m.m.f.s and complex permeance wave functions give rise to numerous flux waves [1]. Consider only the waves which can induce e.m.f.s and currents at frequencies  $f \pm Rf_r$ , hence only the fundamental spatial and temporal stator harmonic need to be considered, i.e.

$$F_1(\theta, t) = F_1 \cos(p\theta - \omega t) \quad (1)$$

responsible for the induced frequency  $f$ , and the permeance harmonic with  $R$  pole pairs which rotates at a speed of  $2\pi f_r$ . The interaction between these two waves causes two flux density waves seen by the stator windings at frequencies  $f \pm Rf_r$ . The e.m.f.s induced by the flux density wave depend on machine dimensions and winding characteristics, the main one being the pitch factor which can vary between zero and one.

As proposed in [12], the main parameter to be considered is the wave pole pair number which if a full-pitch winding is considered, will enable the conditions for a zero winding factor to be identified. Consider the variables which determine the pole pair number of the flux waves at  $f \pm Rf_r$ . The initial pole pair numbers are  $p \pm R$  and other possibilities are found by adding new phenomena. Static eccentricity adds pole pairs at  $\pm n_{se}$  ( $n$  harmonic order), the stator slotting at  $\pm S$  (only the first harmonic is considered), and where appropriate, the anisotropy of the lamination steel  $\pm 2$  (only the first harmonic is considered). In conclusion, the possible pole pair numbers can be expressed as:

$$p_i = p \pm R \pm n_{se} \pm S \pm 2 \quad (2)$$

Therefore  $p/p$  will be one of the possible pole pairs referred to the fundamental pole pair  $p$ . The pitch factor contribution for a full-pitch winding can be expressed as:

$$\xi_i^* = \sin[0.5\pi(p/p)] \quad (3)$$

and will be zero pole by pole if  $p/p$  is even, and zero for the  $p$  series winding if  $p/p$  is fractional. The pitch factor contribution to the winding factor will be 1 only if  $p/p$  is odd. Under this condition the winding factor could be zero due to certain skew or distribution factors. Additionally, a pole pair number multiple of three will produce zero sequence conditions and no induced currents

An attempt is now made to show a correlation between certain motor parameters and the amplitude of slot current component amplitudes:  $I_1$  at  $(f-Rf_r)$ Hz, and  $I_2$  at  $(f \pm Rf_r)$ Hz referred to the fundamental component  $I_0$  in the no-load operating condition of the motor. A semi-closed rotor slot design can cause a decrease in amplitude (which varies in the range 0.05/0.15 [13]) of the fundamental flux density wave, referred to  $B_0$  in the unsaturated condition and with a slot-opening/airgap depth ratio in the range 1/2. If a reference value of 0.1 is considered with respect to this ripple in the flux density

waveform, then the two rotating fields at frequencies  $f \pm Rf_r$ , have corresponding amplitudes of  $B_1/B_0 = B_2/B_0 = 0.05$ .

Consider the contribution of other phenomena which causes additional permeance variations. Assume that  $K$  is the amplitude of the Fourier component of the additional term, with reference to ideal conditions, the amplitude of the new, four flux density combined waves is

$$B_i/B_0 = (K/2) \cdot 0.05 \quad (4)$$

The flux linkage for a full-pitch winding due to a flux density wave with amplitude  $B_i$  and  $p/p$  odd pole pair will be:

$$\lambda_i/\lambda_0 \cong 0.025 K (p/p)_i \xi_i \quad (5)$$

where  $\xi_i$  is the distribution and skew factor and  $\lambda_0$  is the fundamental linkage flux. The consequent ratio between the e.m.f.  $E_i$ , whose amplitude is  $2\pi(f \pm Rf_r)\lambda_i$ , and  $E_0$  whose amplitude is  $2\pi f\lambda_0$ , is

$$E_i/E_0 \cong 0.025 K \xi_i (p/p)_i [(f \pm Rf_r)/f] \quad (6)$$

While the frequencies are  $f \pm Rf_r$ , assuming that  $(f \pm Rf_r)/f \cong R/p$  the previous ratio becomes:

$$E_i/E_0 \cong 0.025 K \xi_i (R/p)_i \quad (7)$$

At these frequencies it is reasonable to assume that the motor p.u. impedance  $z_{pu}$  is given by the leakage reactance (about 0.25 for the supply frequency) and for the components of interest is:

$$z_{pu} \cong 0.25 (R/p) \quad (8)$$

Therefore the p.u. current referred to the rated current is:

$$I_i/I_{rat} = (E_i/E_0) / z_{pu} \quad (9)$$

or with reference to the no-load current (about  $I_{rat}/5$ )

$$I_i/I_0 = (E_i/E_0) (p/R) 20 \quad (10)$$

that is, considering the previous relationships:

$$I_i/I_r \cong 0.5 K \xi_i (p/p)_i \quad (11)$$

According to this relationship the main parameters which influence the slot harmonic currents in the no-load operating condition are the distribution and skew factor  $\xi_i$  and the value  $K$  related to the phenomena which gives rise to a pole pair number compatible with a stator winding harmonic pole pair number. If the slot-fundamental pole pair combination does not allow slot harmonic currents to be induced, but in practice the currents are present due to airgap eccentricity, then the amplitude of the two currents (having computed  $\xi_i$  and  $p_i$ ) should give an approximate estimation of  $K$ , and a sensible estimate for the level of static airgap eccentricity

### 3. Experimental results - spectra of flux density, induced e.m.f. and current

Hall probes and search coils sensed the instantaneous flux density and induced e.m.f. waveforms respectively and an FFT of the flux density, e.m.f. and stator current signals enabled the  $f \pm Rf_r$  components to be identified.

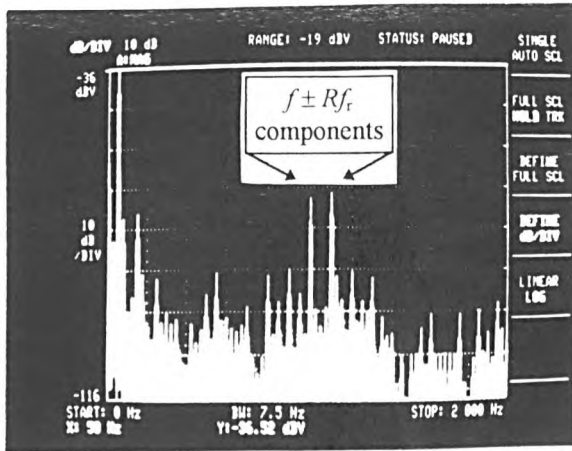


Fig. (1a) FFT spectrum of flux density waveform

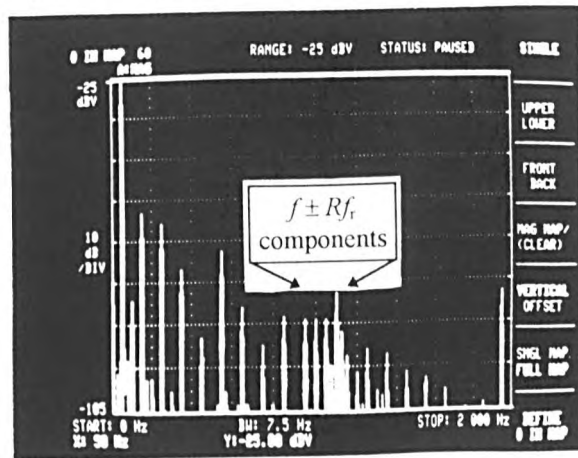


Fig. (1b) FFT spectrum of induced e.m.f. per phase

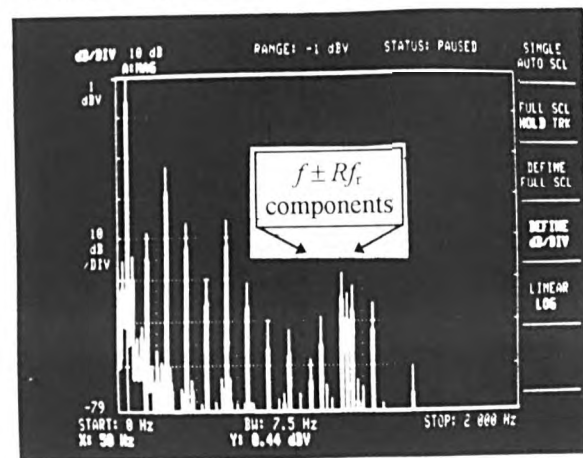


Fig. (1c) FFT spectrum of stator current

The motor was in a nominally healthy state hence only inherent electrical, magnetic and mechanical asymmetries are present. The motor data is presented in appendix (1). Since it has  $p=2$ ,  $R=42$  and a full pitched, stator winding this means that  $p/p$  is equal to  $(p \pm R)/p = 20$  and  $22$  are incompatible with the stator winding harmonic pole pairs. The rotor slot passing frequencies which are clearly visible in the e.m.f. and current spectra at frequencies  $(50 \pm 42)50/2 = 1000/1100\text{Hz}$  (assuming the slip value is approximately zero in the no-load condition at rated voltage), must therefore be caused by the superposition of rotor slotting with other phenomena. Note the actual frequencies measured via the FFT were 998 and 1098 Hz for  $I_1$  and  $I_2$  respectively.

Fig. 1 a, b, c presents an overview of flux density, e.m.f. and current spectra in the range 0-2kHz for the motor operating in no-load supplied at rated volts and frequency. These results were measured via a high quality, commercially produced spectrum analyser and present a clear picture of the rotor slot passing frequencies. For clarity, Figure (2) shows an FFT current spectrum using an on-line LABVIEW based diagnostic system [14] and the high dynamic dB range and narrow frequency resolution further confirms the presence of the  $f \pm Rf_r$  components. Stator slotting adds an even number ( $S=48$ ) to the pole pair number per fundamental pole pair hence the pitch factor is also zero [1, 12].

The first static eccentricity harmonic adds  $\pm 1/2$  to the pole pair number per fundamental pole pair, therefore the chording factor becomes zero when the total, series connected stator phase winding is considered. The static eccentricity second harmonic adds  $\pm 1$  as does the lamination anisotropy (the stator laminations are manufactured from strips of sheet steel hence asymmetry can be present), [12]. Therefore, these phenomena can be the causes of induced e.m.f.s and currents in the stator winding at  $f \pm Rf_r$  which are evident in the experimental results: (Figs. (1b) and (1c)).

The numerical values (r.m.s.) for the flux density, e.m.f. and current components ( $f \pm Rf_r$ )Hz can be compared with the theoretical estimates given in section (2). To observe the influence of saturation, results were also taken at different voltages. The percentage values of the flux density versus supply voltage are shown in Fig.3. The saturation introduces a dissymmetry in the components:  $B_1$  at  $(f-Rf_r)$  decreases, while  $B_2$  at  $(f+Rf_r)$  increases and is a function of the different shape in the flux density behind the rotor slot. As anticipated the two values are very close up to the rated volts (220V).

The percentage amplitude of the e.m.f.s  $E_1$  and  $E_2$  and of the currents  $I_1$  and  $I_2$ , all referred to the fundamental component, versus supply voltage are reported in Fig. 4. A constant shape for the variables is expected but at low voltage the slip cannot be assumed to be zero on no-load and for voltages above the rated value saturation starts to have a dominant influence. In addition, the current is referred to a fundamental component which increases with saturation.

Near the rated voltage, the numerical values of e.m.f.s and current are in agreement with the simplified relationship [10] being  $p/R=2/42$  (approximately 0.05), which is  $I_1/I_2 \approx E_1/E_2$  and  $I_2/I_1 \approx E_2/E_1$ .

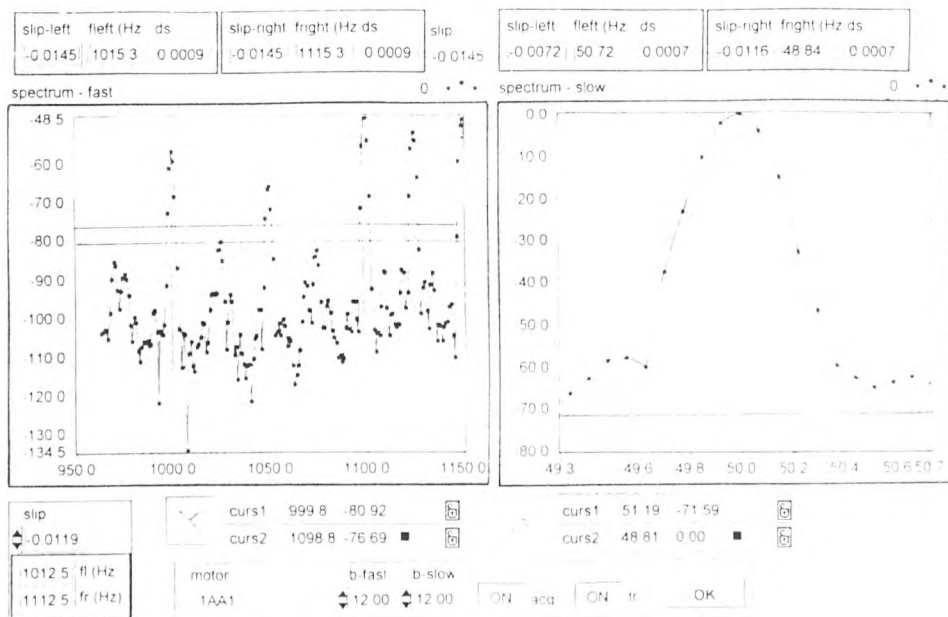


Fig. (2) FFT current spectrum via LABVIEW

Equation (7) can be used as an indirect indication of the second harmonic of static eccentricity and lamination asymmetry. For the first slot harmonic (19th) the winding factor  $\xi_1=0.2$  and for the second one (43th)  $\xi_2=0.96$ , equation (7) gives respectively the two values  $K=22\%$  and  $K=13\%$  (It is to be noted that according to equation (7) the two e.m.f. value should have the ratio  $\xi_1/\xi_2$ ; if so, the values of  $K$  will be the same). This result can be interpreted as an asymmetry of approximately 15%-20% static eccentricity.

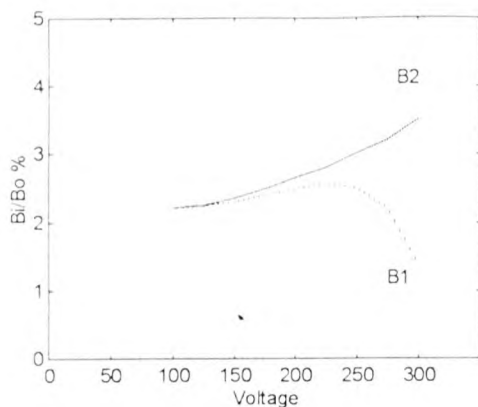


Fig.3 - Percentage values of the flux density versus supply voltage.

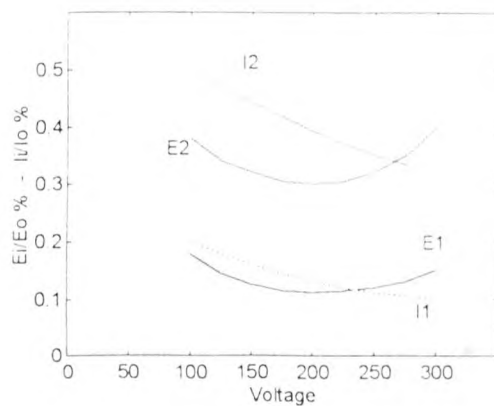


Fig.4 - Percentage amplitudes of e.m.f.s  $E_1$  and  $E_2$  and of the currents  $I_1$  and  $I_2$ .

#### 4. Finite Element Simulations

A time stepping, two dimensional finite element model was used to predict the current waveform as a function of load and airgap eccentricity [9]. An FFT of the time domain current signal is computed via MATLAB [9]. Calibration of the FFT spectrum gives a reference of 100 dB equal to 100 mV and a conversion to current of 0.1V/amp for comparisons with nameplate data and experimental results. The speed is the input variable which describes the load condition and the simulation predicts the current waveform when the motor is fed from a sine wave, symmetrical voltage supply.

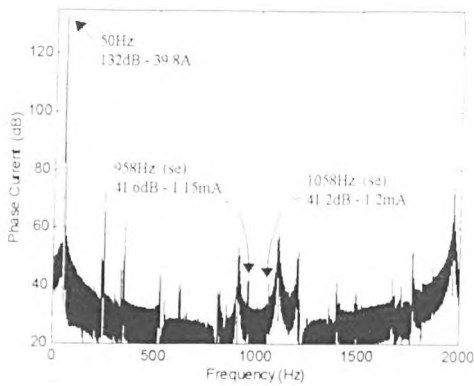


Fig. (5): FFT spectrum, 0% static (se) and dynamic (de) eccentricity, full-load condition (1440 r.p.m.).

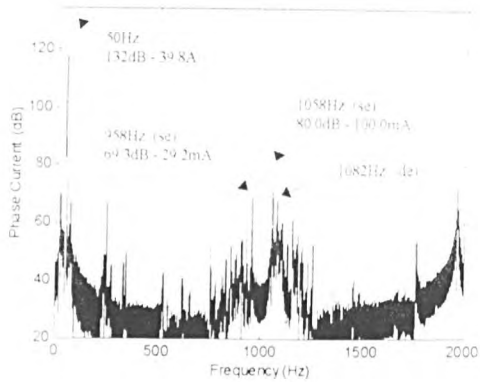


Fig. (6): FFT spectrum, 25% static (se) and 5% dynamic (de) eccentricity, full-load condition (1440 r.p.m.).

The nominal full-load current and speed is 40 amps at 1440 r.p.m. The finite element prediction of the current at 50 Hz was 132 dB ( $\pm 0.5$ dB) which is 39.8 A ( $\pm 2.2$  A) and is within  $\pm 5.5\%$  of the rated value thus validating the finite element simulation for the fundamental component of current. A comparison between the spectra (for full-load) presented in figures (5) and (6) clearly demonstrates the difference in the magnitude of the first order frequency components of current which are a function of airgap eccentricity. For example, the components at 958 Hz and 1058 Hz have increased by 27.7 dB and 38.8 dB respectively with an increase of 25% static eccentricity (with a nominal 5% dynamic eccentricity) from the nominally zero static airgap eccentricity level. With respect to the m.m.f. - permeance wave analysis the pole pair numbers for the 958 Hz and 1058 Hz components with zero airgap eccentricity are not compatible with any of the harmonic pole pair numbers for this stator winding (based on symmetry, pole-pairs =  $p/6c \pm 1$ , slots/pole/phase equals an integer,  $c=0, 1, 2, \dots$ ). Hence the classical theory states that no e.m.f. or current can be induced in this stator winding with zero airgap eccentricity. This is the case for the finite element result in figure (5) since the magnitude of the 958 Hz and 1058 Hz components was 1.15 mA and 1.2 mA respectively which is in the noise level of the FFT

compared to the full - load current of 39.8 A (132 dB) at 50 Hz.

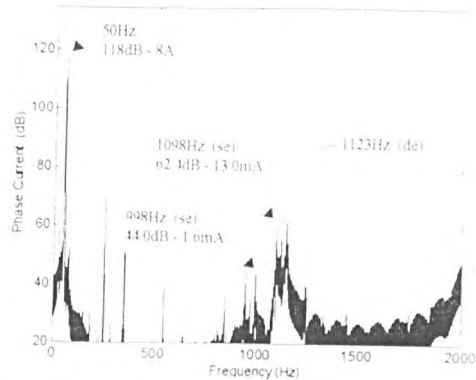


Fig. (7): FFT spectrum, 12.5% static and 5% dynamic eccentricity, no-load condition (1499 r.p.m.).

With the introduction of static eccentricity the m.m.f. - permeance analysis gives odd pole pairs for these frequencies which are not compatible with any of the stator winding harmonic pole pairs, hence no e.m.f. or current can be induced when first order static eccentricity is modelled. However, the finite element result in figure (6) clearly shows that these components are present (27.7 dB and 38.8 dB higher than with zero static eccentricity) and the experimental tests at no-load also confirm their presence. See Fig. (1c) - note the higher frequencies due to the lower slip at no-load. A further study using the m.m.f. - permeance wave model has already shown that if second order static eccentricity (etc) is modelled then additional pole pair numbers associated with these components are present which are compatible with a number of the harmonic pole pairs from the stator winding. The winding factors for these pole pairs are not equal to zero. Fig. (7) gives the finite element result for the motor operating on no-load (1498/1499 r.p.m.) with 12.5% static and 5% dynamic eccentricity. The components at 958 Hz and 1058 Hz have increased to 998 Hz and 1098Hz since the speed has increased to 1498/1499 r.p.m. and the slip has decreased from 4% to approximately 0.1%. As expected the magnitude in dB or amps has decreased due to the reduction in static eccentricity and load. A comparison with the experimental results in Figs. (1a,b,c) confirms the presence of these components and verifies the finite element simulations.

## 5. Discussion and Conclusions

The finite element solution automatically models all the relevant complexities [9] but it is useful to understand the physical phenomena which produces the particular components and it is here that the m.m.f. - permeance wave analysis is advantageous. For example, second order static eccentricity effects (etc see section 3) need to be modelled to prove that pole pairs (compatible with stator harmonic pole pairs) associated with the 958 Hz and 1058 Hz flux components are present such that current components can be induced in this stator winding. To obtain an understanding requires a study of the m.m.f.

- permeance wave model and it is insufficient to just accept the final result produced from the finite element simulation. The hypothesis from the m.m.f. - permeance wave analysis, taking into account second order eccentricity (etc), was verified by finite element simulations and experimental results.

It should be noted that the finite element simulations (compare Figs. 5 and 6) verifies that the components due to dynamic eccentricity are also present and that with an increase in static eccentricity, this also results in an increase in magnitude (amps) of the dynamic eccentricity components. This phenomenon was also observed from previous experimental results [1,4,9]. Theoretical predictions using the m.m.f. - permeance wave model have also shown that their is modulation between static and dynamic eccentricity flux components which can cause an increase in the dynamic eccentricity components with an increase in static eccentricity [6,8]. A prediction of the magnitude of these components (in amps) with a combination of static and dynamic eccentricity has not been previously presented using the m.m.f. - permeance wave model. This is due to the difficulty of obtaining accurate values for all the variables and assumptions required for modelling the slot shapes, magnetic non-linearity and localised tooth saturation. It is in this respect that the finite element is more powerful and versatile since it can predict the current components (frequency and magnitude in amps) with combinations of static and dynamic airgap eccentricity.

## 6. Acknowledgements

The authors wish to thank GEC ALSTHOM ENGINEERING RESEARCH CENTRE, STAFFORD, ENGLAND, for access to their time stepping finite element package (FEMTA). Dr. J. P. Sturgess and Dr. T. W. Preston are sincerely thanked for their advice and support as industrial advisors on Miss Alexander Barbour's Ph. D programme of study.

## References

1. J.R. Cameron, W.T. Thomson and A.B. Dow: "Vibration and Current Monitoring for Detecting Airgap Eccentricity in Large Induction Motors," Proceedings IEE, Vol. 133, pt B, pp 155-163, May, 1986.
2. F. Filippetti, G. Franceschini and C. Tassoni: "Neural Networks Aided On-Line Diagnostics of Induction Motor Rotor Faults," IEEE Trans, on Industry Applications, Vol. 31, No.4, July-August, pp 892-899, 1995.
3. G.B. Kliman and J. Stein: "Induction Motor Fault Detection via Passive Current Monitoring," ICEM'92, Cambridge, MA, Aug. 1990, pp 13-17.
4. W.T. Thomson, D.R. Rankin and D.G. Dorrell: "On-Line Current Monitoring to Diagnose Airgap Eccentricity - an Industrial Case History of a Large High Voltage Induction Motor," IEEE International Conf. on Electrical Machines and Drives, pp MA2-4.1 - MA2-4.3, May, 1997.
5. F. Filippetti, G. Franceschini, C. Tassoni and P. Vas: "AI Techniques in Induction Machines Diagnosis Including the Speed Ripple Effect," IEEE Trans. on Industry Applications, Vol. 34, No. 1, Jan/Feb, 1998.
6. S. Stavrou, J. Penman: "The On-line Quantification of Air gap Eccentricity in Induction Machines", Proc. ICEM'94, pp. 261-264, Paris, 1994.
7. T. J. Sobczyk, P. Vas, C. Tassoni: "Models for Induction Motors with Air-gap Asymmetry for Diagnostic purpose," Proc. ICEM '96, pp 79-84, Vigo, 1996.
8. D. G. Dorrell, W. T. Thomson, S. Roach: "Analysis of Air-gap Flux, Current and Vibration Signals as a Function of the Combination of Static and Dynamic Eccentricity in three phase Induction motors." PROC. IEEE-IAS'95, pp.563-570, Orlando, 1995.
9. A. Barbour, W. T. Thomson: "Finite Element Study of Rotor Slot Designs with respect to Current Monitoring for detecting Static Air-gap Eccentricity in Squirrel-cage Induction Motors" PROC. IEEE-IAS'97, pp.112-119, New Orleans, 1997.
10. P. L. Alger: "The Nature of Induction Machines", ed. Gordon&Breach, 1969.
11. S. Fruchericht, E. Pittuis, H. Seinsch: "A Diagnostic System for Three-Phase Asynchronous Machines", Proc. IEE, 4th EMDA Conference, No. 310, London, UK, 1989, pp 163-171.
12. A. Ferrah, P. J. Hogben-Laing, K. J. Bradley, G. M. Asher, M. S. Woolfson: "The Effect of Rotor Design on Sensorless Speed Estimation using Rotor Slot Harmonics Identified by Adaptive Filtering using the Maximum Likelihood Approach. PROC. IEEE-IAS'97, pp.128-135, New Orleans, 1997.
13. W. Suisky: "Berechnung Elektrischer Maschinen", Ed. Springer Verlag, Wien, 1987.
14. A. Cavallini, F. Filippetti, G. Franceschini, S. Pirani: "Global Instrument for On-Line Induction Motor Integrity Assessment" IEEE Int. Symp. Stockholm Power Tech. Stockholm, June 1995.

## Appendix (I)

Design details of motor	
Rated power	10kW
Rated line volts	220V
Rated current	40A
No-load current	10A
Rated frequency	50Hz
Rated slip	0.04
Pole pairs	2
Stator slots	48
Rotor slots	42
Stator turns phase	56
Single layer winding coil pitch	1
Conductors slot	7
Stator bore diameter	210mm
Stator core length	180mm
Rotor diameter	209mm)
Nominal airgap length	0.5mm ( ± 0.05mm)
Stator resistance	0.14Ω
Rotor equivalent resistance	0.19Ω
Stator reactance	0.45Ω
Rotor equivalent reactance	0.05Ω
Magnetising reactance	11.9Ω
Steel Newcore 800	
HC copper conductors in rotor	
Stator winding: standard copper	
Rotor double cage design but only outer cage was used - round copper bars.	

Comments: The reader can contact the authors to obtain full stator and rotor core designs including all slot dimensions.